Integrated interpretation of 3D seismic data using seismic attributes to understand the structural control of methane occurrences at deep gold mining levels: West Wits Line Goldfield, South Africa

Mbali Mkhabela

Supervisors:

Dr Musa Manzi, Dr Grant Bybee, and Prof. Tamiru Abiye

A thesis submitted to the
Faculty of Science, University of the Witwatersrand
in fulfilment of the requirements for the degree of

Master of Science

School of Geosciences

University of the Witwatersrand

DECLARATION

I, Mbali Mkhabela, declare that this thesis is my own, unaided work. It is being submitted for the Degree of Master of Science at the University of the Witwatersrand, Johannesburg. It has not been submitted before for any degree or examination in any other University.

Mbali Mkhabela

Date: 08 November 2017 **Location**: University of the Witwatersrand, Johannesburg

ABSTRACT

At a number of gold mines in South Africa, the presence of methane gases has been encountered when drilling into faults and/or dyke structures extending to depths beyond 4.5 km. Methane gas has been reported to have migrated through structures from within the basin to the mine working environments (~3.0 km depths) and caused explosions. The Booysens Shale is considered one of the possible source rocks for hydrocarbons and it forms the footwall to the gold-bearing Ventersdorp Contact Reef (VCR, ~ 1.5 m thick). The Booysens Shale lies at depths between 3.5 km and 4.5 km below land surface and can be best described as the base of the divergent clastic wedge which thickens westward, hosting the quartzite and conglomerate units that sub-crop against the VCR towards the east of the gold mining areas.

Geometric attributes (dip and dip azimuth) and instantaneous attributes (phase, frequency and envelope) computed for the Booysens Shale and Ventersdorp Contact Reef horizons (interpreted from 3D prestack time migrated data acquired in the Witwatersrand goldfields) provide insight into structures that extend from the Booysens Shale into the overlying mining level, the Ventersdorp Contact Reef. These attributes provide high-resolution mapping of the structures (faults, dykes, and joints) that have intersected both the Ventersdorp Contact Reef and Booysens Shale horizons. Volumetric fault analysis using the ant-tracking attribute incorporated with methane gas data also show the continuity and connections of the faults and fracture zones possibly linked to methane gas and fluid migration.

Correlation between the known occurrence of fissure water and methane with geologically- and seismically-mapped faults show that steeply dipping structures (dip>60°) are most likely to channel fracture water and methane. $\delta^{13}C$ and $\delta^{2}H$ isotope results suggest that the methane gas (and associated H_2 and alkanes) from the goldfields, particularly along seismically delineated faults and dykes, have an abiogenic origin produced by water-rock reactions. Isotopic data derived from adjacent goldfields also suggests the possibility of mixing between microbial

hydrocarbons (characterized by highly depleted δ^2H_{CH4} values) and abiogenic gases. It is, therefore, possible that the propagation of these structures, as mapped by 3D seismics and enhanced volumetric attributes, between Booysens Shale and Ventersdorp Supergroup provide conduits for mixing of fluids and gases encountered at mining levels.

The study may provide new evidence for the notion of hydrocarbons, particularly CH_4, having migrated via faults and dykes from depth, within the Witwatersrand Basin, to where they are intersected at mining levels. The research gives new insight into mixing between microbial and abiogenic end-members within hydrogeologically isolated water pockets.

"What profit has the worker from that which he labours? I have seen the God-given task with which the sons of men are to be occupied. He has made everything beautiful in its time. Also, He has put eternity in their hearts, except that no one can fathom the work that God has done from beginning to end…" – Ecclesiastes 3:11-13

ACKNOWLEDGEMENTS

To God Almighty, my Rock, Shield, Comforter, and Shepard without Whom I would not have been able to start and complete this work.

I would like to thank my supervisor, Dr. Musa Manzi. Your guidance, objections to and approval of my work have built me up both academically and personally. I would also like to thank Dr. Stephanie Enslin-Scheiber; your input was invaluable.

I wish to express my appreciation to AngloGold Ashanti Ltd. for availing the Western Ultra Deep Levels 3D seismic data as well as borehole data that were used in the study. In addition, many thanks go to Sibanye Gold Ltd. for providing borehole core log and deviation data from the Driefontein gold mine. My gratitude goes out to Prof. Tullis Onstott of Princeton University and Prof. Esta van Heerden of the University of Free State for availing the methane borehole and gas composition data. Many thanks to IHS Global Inc. for granting licences for the IHS Kingdom Suite seismic interpretation software, as well as Schlumberger for granting licences for Petrel, a seismic interpretation and modelling software. I would also like to thank the Wits Seismic Research Centre, funded by Shell SA Ltd. and CGG, for providing research facilities to conduct this research.

I would like to acknowledge and express my gratitude towards the financial support I received throughout my MSc. This includes Thuthuka Funding (NRF), CIMERA (Centre of Excellence for Integrated Mineral and Energy Resource Analysis), Golder Associates, and CGG.

To my family, especially, my mom, this one is for you. Thank you for the love and support and occasionally, the food.

Last but definitely not least, I wish to convey my heart-felt gratitude towards my husband, Arthur Moya, for praying with and for me, for the light that you have been and to many more adventures in the world of love and science together. God bless you, my Love.

CONTENTS

LIST OF FIGURES

LIST OF TABLES

1. INTRODUCTION

1.1 Motivation and Objectives

The Archaean Witwatersrand Basin, situated in South Africa, is the second largest gold province in the world. It is a well-preserved and extensively studied sedimentary basin with a 130-year-old gold mining history (Moon, et al., 2006). The mines exploit tabular gold-bearing ore bodies (locally known as reefs) and mining occurs anywhere between approximately 1 and 4 km depths. Mining in the region occurs at depths of up to 4 km below the surface of the Earth, making the gold mines of the Witwatersrand Basin the deepest mines in the world. The depth to which mining occurs and the structural complexity of the basin pose substantial risks to the lives of gold miners, and this is reflected by the high level of fatalities and injuries recorded by gold mines in the area (Roberts & Schweitzer, 1999).

According to annual reports published by the Department of Mineral Resources (DMR), the Gauteng mining sector experienced the highest number of injuries and fatalities, with gold mining averaging the highest incidences between 2006 and 2013 (Department of Mineral Resources, 2013). In the years prior to that, statistics showed that although there has been a general decline in the number of mine-related injuries and fatalities, there is a steady increase in methane gas explosions (Cook, 1998; Biffi & Cook, 2002).

Methane gas in mine workings has been reported in a number of coal, platinum and gold mines in South Africa. The sources of the gas leading to explosions in these mines vary (Cook, 1998; Biffi & Cook, 2002). Until 1999, the occurrence of explosions associated with flammable gas in hard rock mines was minimal, overshadowed by those that frequently occurred in collieries. In July 1999, a gas explosion occurred that resulted in eighteen casualties at the Mponeng mine, in the Far West Rand Goldfield. The following year, a major disaster involving a flammable gas explosion occurred at Beatrix gold mine on 15 May 2000 in which twelve mineworkers lost their lives. These incidents increased awareness of the risks associated with methane gas explosions, and measures have been modified and put into place to mitigate these risks (Sibanye Gold Ltd., 2014). However, due to the sporadic and unpredictable nature of gas explosions, some of these measures have dwindled or become obsolete. This is particularly true in areas where mining has ceased. The motivation for this study is to understand the pathways of methane gas from possible sources to sinks using seismic and isotopic data to avoid future explosions.

The hypothesis for research is as follows: The methane found at depth in mining levels in the West Wits Line Goldfield travels via faults and dykes (geological structures) that cross-cut key hydrocarbon-bearing lithologies.

The main objective of the study is to identify possible sources of methane, and detect faults and dykes that may be responsible for transmitting the methane to mining levels in the West Wits Line Goldfield. This will be achieved using seismic attributes applied to the 1995 Western Ultra Deep Levels (WUDLs) 3D pre-stack time migrated (PSTM) seismic data. Seismic attributes are used to enhance subtle structural features in the seismic data that cannot be detected by conventional interpretation methods. Seismic attributes include complex-trace attributes (e.g., instantaneous phase, frequency, and envelope), horizon-based attributes (e.g., dip, dip azimuth and edge-detection), and volumetric attributes (e.g., ant tracking and coherence). The research aims to answer the following questions:

- How well do seismic attributes enhance fault detection compared to conventional seismic interpretation?
- Do all the geological structures that cross-cut mining levels provide pathways for methane gas?
- How continuous and inter-connected are these structures?

- Is there any correlation between these structures and known occurrences of methane data in the mines?

1.2 Location and overview of mining operations in the study area

The mines of interest to the study are part of the West Rand and the West Wits Line, also known as Carletonville, Goldfields. The goldfields are located on the north-western edge of the Witwatersrand Basin and south-west of the city of Johannesburg, Gauteng, South Africa (Figure 1.1). The mines include the Driefontein, Mponeng, TauTona, Kusasalethu and Deelkraal gold mines. The 3D seismic survey, which covers a significant portion of the West Wits Line and to a lesser extent, the West Rand goldfields, extends over an area of approximately 300 km^2, in an ENE-WSW direction (Figure 1.2).

Mponeng and TauTona are gold mines, collectively known as the West Wits Line operations, are operated by AngloGold Ashanti Limited. Mponeng, the world's deepest gold mine, uses sequential-grid mining to exploit the Ventersdorp Contact Reef (VCR) at depths between 2.4 and 3.9 km. The Mponeng lease area is constrained to the north by the TauTona and Savuka gold mines, to the east by Sibanye's Driefontein gold mine and to the west by Kusasalethu gold mine, which is operated by the Harmony Gold Mining Company. Mining in TauTona takes place at depths of between 1.85 and 3.45 km. The mine has a three-shaft system, supported by secondary and tertiary shafts and, in 2007, embarked on the process of converting from longwall to scattered-grid mining; 80% of stoping production is carried out using sequential grid mining. The increasingly complex geology, seismicity and the unsuitability of longwall mining, given the occurrence of geological structures, drove the change in mining method to improve safety. The two gold mines currently employ a total of 10 905 people and have mining rights that expire in 2036 (AngloGold Ashanti Limited, 2013; 2015).

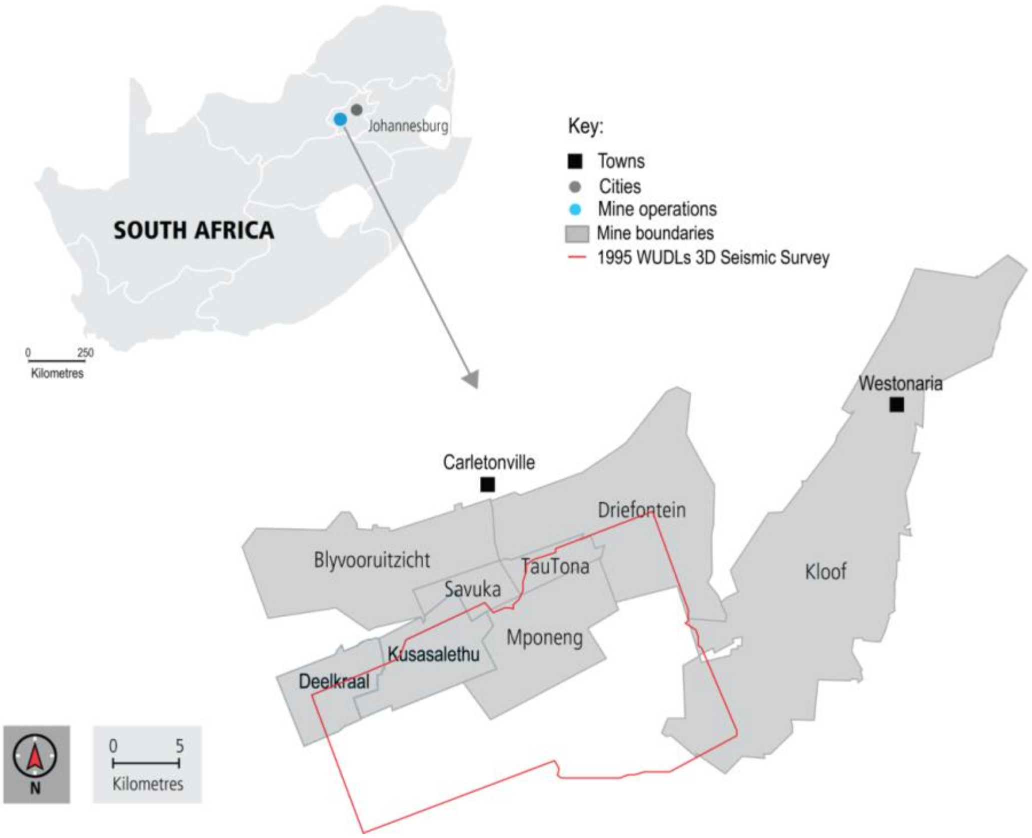

Figure 1.1: Study area showing mine lease areas including the Driefontein, Mponeng, TauTona, Kusasalethu, and Deelkraal gold mines. These mines are located approximately 65 km from South Africa's economic hub, the city of Johannesburg. The extent of the 1995 WUDLs 3D seismic survey is outlined in red.

The Kloof-Driefontein Complex (KDC) is a large, well-established shallow to ultra-deep level gold mine that is accessed from surface through a number of shafts to its deepest working levels (~3.35 km below surface). It comprises eleven producing shaft systems and five metallurgical plants. KDC exploits three primary reefs, namely, the Carbon Leader Reef (CLR), Ventersdorp Contact Reef (VCR), and Middelvlei Reef (MR). The CLR represents most of the current mineral reserves in the west of the mining lease, and the VCR represents the majority of the current mineral reserves in the east of the mining lease. Driefontein, the main gold mine of interest, currently employs 11 721 people and the life of mine is estimated to the span for the next 20 years, terminating in 2037 (Sibanye Gold, 2012a, b).

The Kusasalethu gold mine, operated by Harmony Gold Limited, is an amalgamation of the Elandsrand and Deelkreel gold mines, is located approximately 17 km southwest of Mponeng gold mine. This mine comprises two vertical shafts, a rock/ventilation and man/material shaft, as well as two sub-vertical rock/service and ventilation shafts. Mining of the VCR occurs between 2.2 km and 3.3 km below the Earth's surface (Harmony Gold Mining Company Limited, 2015).

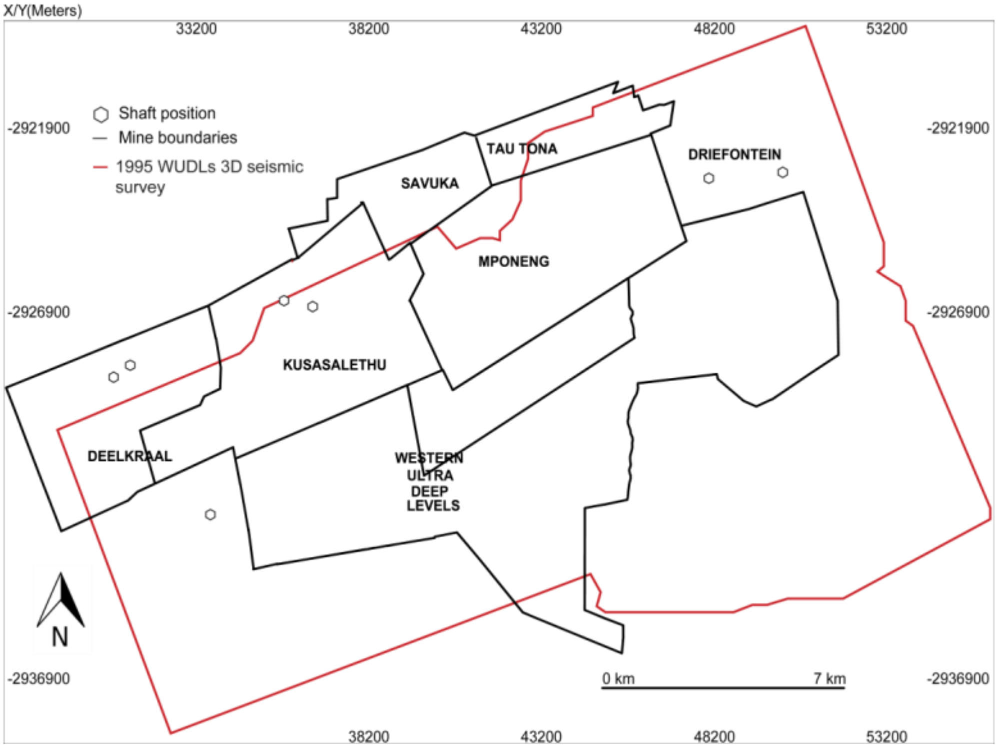

Figure 1.2: Map of the extent of the 1995 WUDLs 3D seismic survey (outlined in red) and the mines (black boundaries) covered by the survey.

2. GEOLOGY AND STRUCTURAL SETTING

Mineral exploration in South Africa generally occurs in rocks that are described as “hard rock”. These rocks are characterized by high seismic velocities and sometimes, complex deformational histories. The geology of the Witwatersrand Basin is very complex and characterized by multiple events of structural deformation, as well as different metamorphic grades at different places. The following section gives a detailed description of the geology of the Witwatersrand Basin as well as the over- and under-lying geology and structural framework of the West Wits Line Goldfield.

2.1 Geology

2.1.1 Archaean Basement (Kaapvaal Craton)

The Kaapvaal Craton is a stable continental crust made up of 3.7 to 3.1 Ga greenstone belts and tonalite-trondjhemite-granodiorite intrusions (Robb, et al., 2006). Late Archaean to Palaeoproterozoic tectonics resulted in the accretion of terranes along the flanks of the craton. The development of these terranes was contemporary to the deposition of four significant meta-sedimentary and volcanic sequences: the Dominion Group, the Witwatersrand, Ventersdorp, and Transvaal supergroups on the basement rocks (Figure 2.1; De Wit, et al., 1992; Robb, et al., 2006).

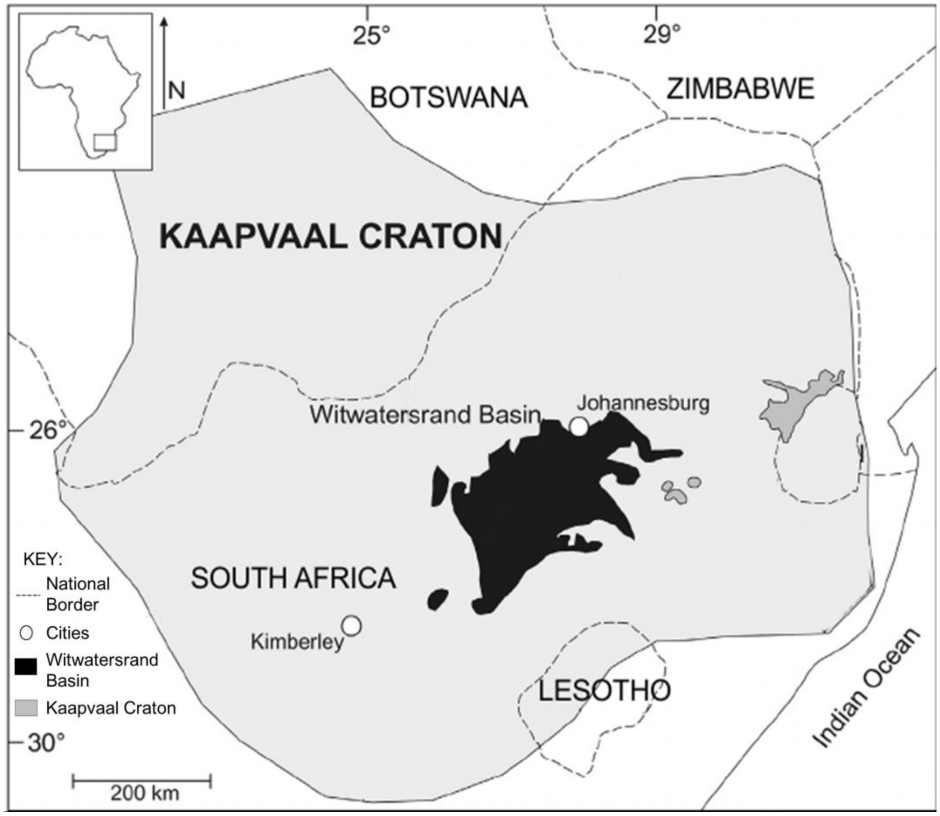

Figure 2.1: A map showing the extent of the Kaapvaal Craton (grey area) and the approximate size of the Witwatersrand Basin (black shaded area) within it. The craton covers almost all northern South Africa and portions of Lesotho and Botswana (after Viehmann et al., 2015).

2.1.2 Dominion Group

The deposition of fluvial sediments followed by the extrusion of mafic and felsic volcanics represents the stratigraphy of the Dominion Group. The poorly exposed group is divided into the Rhenosterspruit, Rhenosterhoek, and uppermost Syferfontein formations and is up to 2 km thick. It unconformably overlies basement rocks (Crow & Condie, 1987; Armstrong , et al., 1991; Marsh, 2006).

2.1.3 Witwatersrand Supergroup

The Dominion Group is overlain by the Witwatersrand Supergroup. The onset of the deposition of sediments in the Witwatersrand Basin (Figure 2.2) is dated at approximately 2.98 Ga, with sedimentation ceasing at around 2.81 Ga (Kositcin & Krapez, 2004, U–Pb detrital zircon SHRIMP). During this period, arenaceous and argillaceous sediments of the lower West Rand Group and upper Central Rand Group were deposited. The sediments deposition was controlled by varying palaeo-sedimentary environments and later underwent greenschist facies metamorphism, subsequently creating a 7 to 8 km thick, 350 by 200-km wide succession (Figures 2.2 and 2.3; Armstrong, et al., 1991; Moon, et al., 2006).

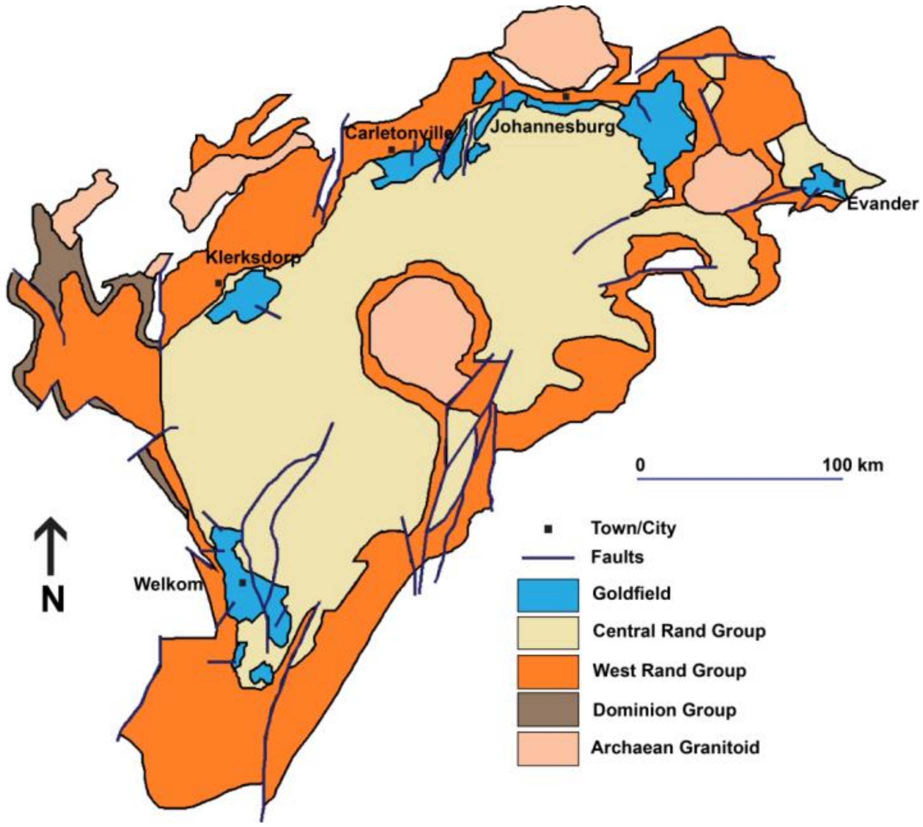

Figure 2.2: The simplified geology of the Witwatersrand Basin as well as the main geological groups (after Gibson & Jones, 2002; Manzi, et al., 2013a). The goldfields (blue polygons) generally lie along the collar of the basin and mining occurs mostly within the Central Rand Group.

2.1.3.1 West Rand Group

Sediments of the West Rand Group were deposited in distal fluvio-deltaic and shoreface to offshore sedimentary environments. These comprise equiproportional amounts of shale and quartzite, capped by the only igneous unit in the West Rand Group, the basaltic andesite known as the Crown Formation. Most of the Kaapvaal Craton was inundated at the time of the deposition of the sediments of the group (Stanistreet & McCarthy, 1991; Coward, et al., 1995; McCarthy, 2006).

The group is divided into the Hospital Hill, Government, and Jeppestown subgroups. The lowermost sediments of the Hospital Hill Subgroup lie unconformably over the lavas of the Dominion Group. The sequence, comprising orthoquartzites, siltstones and iron formations, was deposited in foreshore and shoreface sedimentary environments. Apart from the few conglomerate reefs located close to the top of the sequence (associated with fluvial, regressive depositional settings), the Hospital Hill Subgroup marks a period of major transgression from the south-west in the basin (Robb & Meyer, 1995; McCarthy, 2006). Rocks of the Government and Jeppestown subgroups were deposited in a range of depositional settings. The diamictites, iron formations, and conglomerates represent a significant period of glaciation and multiple periods of major sea level rise. The subgroups are representative of a transition from extremely unstable and then later stable tectonic conditions in the craton (McCarthy, 2006).

2.1.3.2 Central Rand Group

The Central Rand Group, where nearly all the gold mining in the basin occurs, disconformably overlies the West Rand Group (Moon, et al., 2006). Aside from gold-bearing conglomerates, other rock types making up the group (characterised by multiple unconformities) include coarse-grained quartzites and minor siltstone units, all deposited under fluvial and marine settings (McCarthy, 2006). The group splits into the Johannesburg and Turffontein subgroups.

Two palaeo-sedimentary environments characterise the stratigraphy of the Central Rand Group: braid-plains and alluvial fans. The Johannesburg Subgroup sequence is characterised by alternating quartzite (dominant) and conglomerate units deposited in a fluvial braid-plain environment. The stratigraphy is marked by multiple erosional surfaces associated with periods of non-deposition as well as placer development. Reworking of placer sediments by incised valleys that cut-through the erosional surfaces resulted in the deposition of thin gravel units. These matrix-dominated, pebbly lags can be identified by thin layers of carbonaceous material (referred to as bitumen or kerogen) and one such example is the economically significant, Carbon Leader Reef (Buck & Minter, 1985; Mossman, et al., 2008).

The peneplains were subsequently inundated as sea levels in the basin rose, resulting in the further concentration of heavy minerals and laterally developed mineralized reefs across the basin. The deposition of these reefs is variable across the basin with tectonic processes having a significant effect on the rates of sedimentation and deposition, as well as the concentration of mineralization (Robb, 2005). The Booysens Shale marks the top of the Johannesburg Subgroup, and separates the two subgroups. The shale bed is laterally extensive and is a significant stratigraphic marker that is discussed later in the chapter.

The upper Turffontein Subgroup is categorized by prograding braid-plains and alluvial fans, in which the latter culminated in massive conglomerates and boulders beds at the top of the sequence. Pyrite-laden sand and shale units are typical of the reefs that underwent multiple periods of erosional degradation (Kingsley, 1987). The Elsburg, Kloof, Libanon, and Kimberley Reefs of the Johannesburg Subgroup and the Bird, North and Carbon Leader, and Middelvlei Reefs of the Turffontein Subgroup are all the auriferous conglomerates mined in the basin (McCarthy, 2006).

For the purposes of the seismic interpretation component of the study, two stratigraphic units are of importance. The Ventersdorp Contact Reef (VCR) is part of the lithostratigraphic formation, the Venterspost Formation. The formation has yet to be assigned to either the Witwatersrand or Ventersdorp Supergroup, although there has been significant evidence that designates it to the Ventersdorp Supergroup (Hall, et al., 2004). The VCR corresponds to a transition from the quartzites of the Central Rand Group and overlying 3 km thick volcanics of the Klipriviersberg Group of the Ventersdorp Supergroup. The significant contrast in acoustic impedances makes it a strong seismic reflector in the seismic data. The depth at which the VCR occurs ranges approximately 2 to 4 km below surface (Manzi, et al., 2012). The Booysens Shale is a 75-m thick, regionally extensive unit separating the Johannesburg and Turffontein Subgroups and was deposited during basin-wide transgression (Phillips & Law, 1994). Its lateral extensiveness and seismic reflective nature make it a suitable marker for seismic interpretation (McCarthy, 2006; Manzi, et al., 2013a).

2.1.4 Ventersdorp Supergroup

The Ventersdorp Supergroup is an 8-km thick, volcano-sedimentary sequence that unconformably overlies the Central Rand Group. Rocks of this largely meta-volcanic sequence have been dated at minimum and maximum ages of approximately 2.71 and 2.60 Ga, respectively (Armstrong , et al., 1991; van der Westhuizen, et al., 1991). The supergroup is made up of the Klipriviersberg, Platberg, and Pniel groups. The Klipriviersberg Group comprises the continental flood basalts and komatiites and forms the basal rocks of the Ventersdorp Supergroup. These lavas erupted over a short period and preserve the mineralized VCR. The subsequent Platberg Group comprises an upward-fining succession of sediments and volcanics. It is characterized by dominantly porphyritic (and subordinate amygdoidal) mafic and felsic volcanics. The greywacke, quartzite, carbonate, and chert units making up the top of the Platberg Group represent the varying sedimentary environments at the time of deposition of these sediments. The uppermost Pniel Group is divided into a lower sedimentary package of conglomerates, sandstones, shales, and limestones (the Bothaville Formation) and an upper unit of amygdaloidal pillow basalts (Allanridge Formation) (Crow & Condie, 1988).

2.1.5 Transvaal Supergroup

The Ventersdorp Supergroup is unconfomably overlain by the rocks of the Transvaal Supergroup. The supergroup, which was deposited around 2.65 and 2.06 Ga, is preserved in three structural basins: The Griqualand West and Transvaal basins in central and northern South Africa, respectively, and the Kanye Basin in Botswana (Eriksson & Altermann, 1998). The groups correlate along stratigraphy and have varying names in each basin. The Transvaal Basin is divided into the Chuniespoort and Pretoria groups. Rock types of the lower Chuniespoort Group include dolomites, shales, and ironstones deposited in shallow to deep marine settings. The compartmentalized (by dykes and sills) carbonates of the Malmani Subgroup, the largest karstic aquifer in South Africa, are largely responsible for flooding that occurs at mining levels in the underlying Witwatersrand Basin (Eriksson & Altermann, 1998; Ngcobo, 2006). The overlying Pretoria Group is a 6 to 7 km thick (at its thickest) volcano-sedimentary sequence made up of mudstone-sandstone units, andesite, and subordinate conglomerate beds and carbonates (Els, et al., 1995).

The Black Reef (BLR) Formation marks a seismic reflective interface between the overlying dolomites of the Chuniespoort Group and underlying Ventersdorp basalts (Figure 2.3). The formation has a maximum thickness of 30 m in the Transvaal Basin and is located at the base of the lower Chuniespoort Group. It comprises an upward-fining conglomerate to sandstone sequence followed by inter-bedded shale and dolomite beds (Els, et al., 1995; Eriksson & Altermann, 1998).

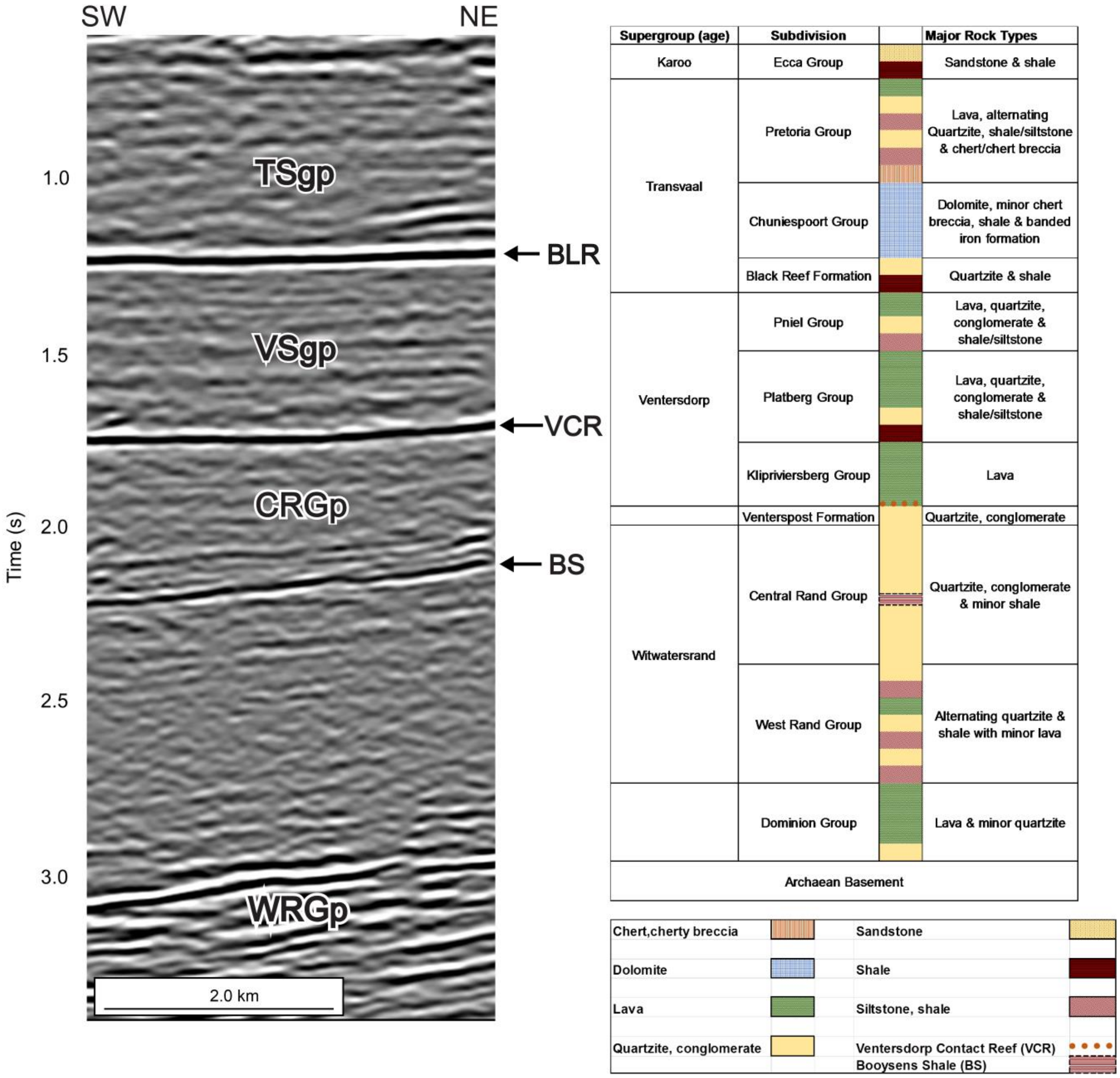

Supergroup (age)	Subdivision		Major Rock Types
Karoo	Ecca Group		Sandstone & shale
Transvaal	Pretoria Group		Lava, alternating Quartzite, shale/siltstone & chert/chert breccia
	Chuniespoort Group		Dolomite, minor chert breccia, shale & banded iron formation
	Black Reef Formation		Quartzite & shale
Ventersdorp	Pniel Group		Lava, quartzite, conglomerate & shale/siltstone
	Platberg Group		Lava, quartzite, conglomerate & shale/siltstone
	Klipriviersberg Group		Lava
	Venterspost Formation		Quartzite, conglomerate
Witwatersrand	Central Rand Group		Quartzite, conglomerate & minor shale
	West Rand Group		Alternating quartzite & shale with minor lava
	Dominion Group		Lava & minor quartzite
Archaean Basement			

Chert,cherty breccia	▥	Sandstone	🟨
Dolomite	🟦	Shale	🟥
Lava	🟩	Siltstone, shale	🟥
Quartzite, conglomerate	🟨	Ventersdorp Contact Reef (VCR) Booysens Shale (BS)	•••• ▤

Figure 2.3: Stratigraphy of sequences overlying the Kaapvaal Craton (Archaean Basement), namely the Witwatersrand (separated into the Central Rand Group – CRGp – and the West Rand Group – WRGp), Ventersdorp (VSgp), Transvaal (TSgp), and Karoo Supergroups. Strong seismic reflectors are shown on the seismic section and these are the Booysens Shale (BS), Ventersdorp Contact Reef (VCR), and the Black Reef (BLR) (modified after Jones, 2003).

2.2 Structural Framework

The structural evolution of the basin is a crucial factor in understanding the distribution and transmission of gas and fissure water transporting dissolved gas into mining levels. The tectonic history is therefore noteworthy although it is not described in depth. The following chapter summarises the tectonic history of the West Wits Line Goldfield and reports on the possible dyke systems that have intruded into the goldfield.

2.2.1 Structural Overview of the West Wits Line Goldfield

Geological sequences in the West Wits Line Goldfield take on two different general orientations. They are SE-dipping in the south-west of the goldfield and S-dipping on the north-eastern end. The goldfield has a complex structural history characterized by regional-scale folding of the meta-sedimentary units and drag-folding related to major faults in the basin (Myers, et al., 1990; Jolley, et al., 1999; Gibson, et al., 2000; Jolley, et al., 2004)

The numerous fault and fracture arrays also record a multi-deformational history within the basin (Figure 2.4). The Bank and West Ran Faults are first-order faults transecting most of the stratigraphy of the Witwatersrand and Ventersdorp Supergroups. The Bank and West Rand Faults are part of a westward-dipping thrust system that was active for approximately 200 Ma (Dankert & Hein, 2010). The Bank Fault has been described as a reverse fault that later reactivated as a normal fault and accommodated listric block rotation (in the kilometre range) prior to the deposition of the Transvaal Supergroup. It is flanked by the Bank anticline to the west and the Kloof syncline to the east. The Bank Fault does not breach the base of the Transvaal Supergroup. This implies that the minimum relative age for fold-thrust formation began late during the deposition of the West Rand Group and proceeded until after the deposition of the Central Rand Group (ca. 2.9–2.7 Ga; Gibson, et al., 2000; Dankert & Hein, 2010; Manzi, et al., 2013).

Another significant fault that has been identified in this region is the Master Bedding Fault (MBF). It is a 1 to 50 m wide fault zone that is sub-parallel to bedding. The MBF has been identified by Fletcher and Gay (1972) as a gravity-driven, dominantly cataclasitic, decollement zone with a normal sense of displacement that hosts brecciated and mylonitic rock fragments. The MBF crosscuts the Witwatersrand Basin and it was initiated prior to the deposition of the VCR, if not during the deposition of the Transvaal Supergroup sequences (Dankert & Hein, 2010).

Thrust systems in the Elandsrand (Kusasalethu) mining area (in west of the goldfield) are linked arrays of fore-, back-, and under-thrusts. These have throws that mostly range between 1 to 10 m, occasionally 30 to 50 m and rarely up to 100 m. Furthermore, Jolley, et al. (2004) suggested that the thrust system has three parallel NE/SW-trending, thin-skinned imbricate zones (up to 800 m wide) connected by NNW/SSE-striking thicker-skinned lateral ramps. These thrust imbricates are associated with ultracataclasites, thrust deformation features and most importantly, higher gold grades linked to the presence of hydrocarbons (Robb, et al., 1997; Drennan & Robb, 2006). Thrust-related deformation at the Ventersdorp Supergroup lavas/VCR contact in the Elandsrand gold mine has been observed by Jolley, et al. (1999, 2004). Jolley, et al. (1999) identified three stages associated with the formation of these thrust systems: (1) early thrust-related deformation dominated by layer parallel shear, (2) southeast-verging kilometre-scale thrust spread up towards the Ventersdorp Supergroup lavas resulting in steep mineralised fracture formation, and (3) propagation of the major thrust to crosscut and join with the Ventersdorp Supergroup lavas/VCR contact leading to widespread imbrication due to sediment shortening beneath the lavas.

Work done by Manzi, et al. (2012) to detect faults transecting the auriferous VCR and BLR mining levels identifies four, second-order faults within the Western Ultra Deep Levels (WUDLs)/Driefontein block relevant to the study area. This includes NNE-trending faults in line with the Bank Fault, variably oriented faults (identified as K1 to K3) that are particularly prominent at VCR mining level and the K4 fault, which lies west of Driefontein gold mine.

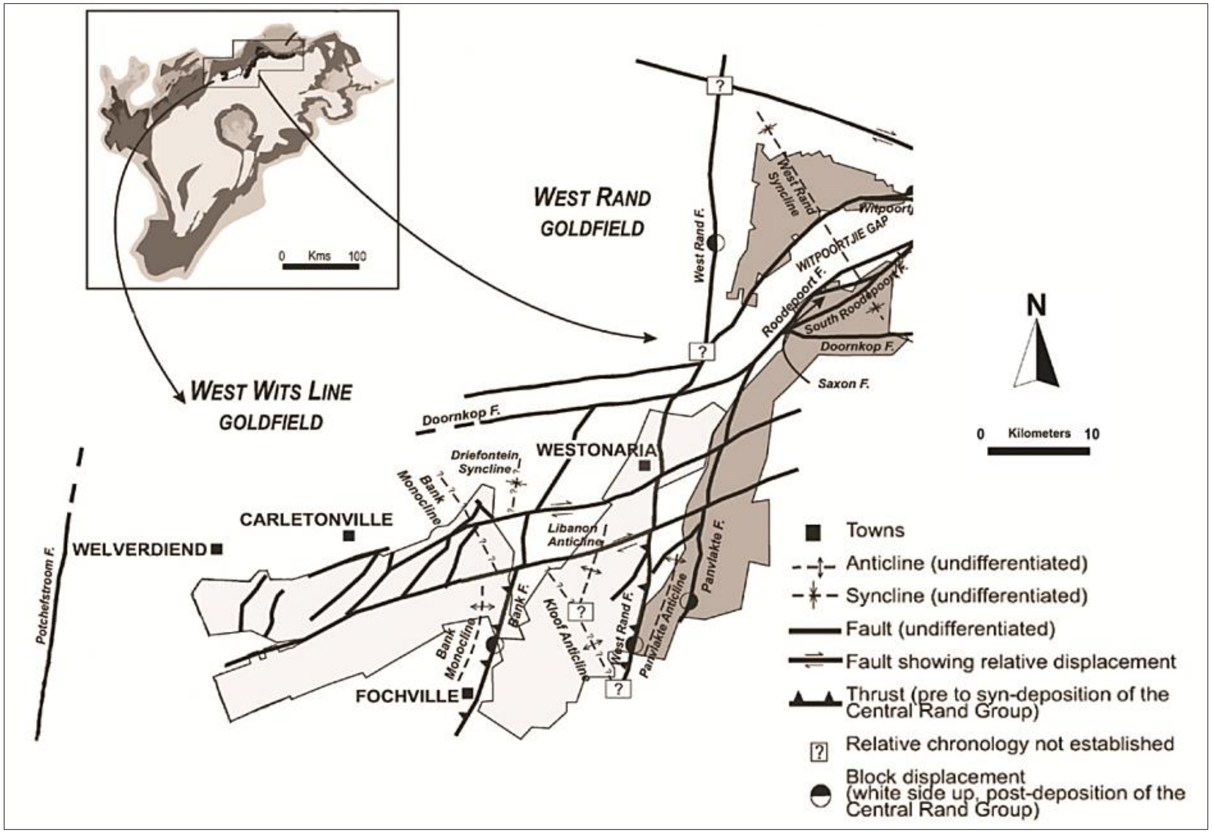

Figure 2.4: First-order structures (faults that have vertical displacements between 400 m and 2.5 km) that crosscut the West Wits Line and West Rand Goldfields. The major fault that separates the West Rand and West Wits Line Goldfield is the Bank Fault (labelled Bank F; after Dankert & Hein, 2010). The area shaded light grey denotes the West Wits Line Goldfield, and the darker shade of grey, the West Rand Goldfield.

2.2.2 Dykes intruding the Witwatersrand Basin

Multiple types of dykes associated with different intrusive events crosscut the goldfields of the Witwatersrand Basin. In the West Wits Line Goldfield several large dykes contribute to dividing the goldfield into a series of compartments. These dykes have different impacts on mining:

- Dykes can either impede or act as conduits for lateral groundwater flow. Dykes that impede flow either disrupt or compartmentalize the formation through which the groundwater flows; such dykes are usually unweathered and massive. If the structure becomes fractured or weathered, it may act as an aquifer, channelling water through it. In the case of the West Rand Goldfield, these dykes crosscut the water-bearing, overlying Malmani dolomites, forming an aquifer that has been responsible for flooding events in the West Rand and West Wits Line Goldfields (Barnard & Baran, 2000; Cook, 2003; Ngcobo, 2006).

- Intrusive events increase the geothermal gradient. An increase in temperature with depth plays a significant role in facilitating prime conditions for methanogenic reactions as well other flammable gases (Einsele, et al., 1980; Duddy, et al., 1994).
- The intrusion of dykes may result in the re-activation of faults (Magee, et al., 2014; Cox, et al., 2015).

Geochemical analyses of these dykes have been useful in designating them into the respective magmatic events with which they are associated. From a geochronological point of view, the data are sparse, and dating is done relatively. A study by Litthauer (2009) identified four events that were responsible for dyke intrusion into the West Rand and West Wits Line Goldfields and they are as follows:

2.2.2.1 Ventersdorp Supergroup lavas

The volcano-sedimentary sequence of the Ventersdorp Supergroup includes tholeiitic basalt dykes that have a mild calc-alkaline affinity which intrude the underlying Witwatersrand stratigraphy with extrusion of lavas occurring approximately 2.71 Ga ago (Schweitzer & Kroner, 1985; Bowen, et al., 1986). Most of the dykes have undergone greenschist facies metamorphism, and hydrothermal alteration indicated by the presence of secondary minerals. They have been largely interpreted as feeders to the overlying Klipriviersberg Group lavas and are part of a 200-km wide, NE-trending dyke swarm related to the Ventersdorp rifting event (Figure 2.5; Anhaeusser, 2006; Litthauer, 2009; Meier, et al., 2009).

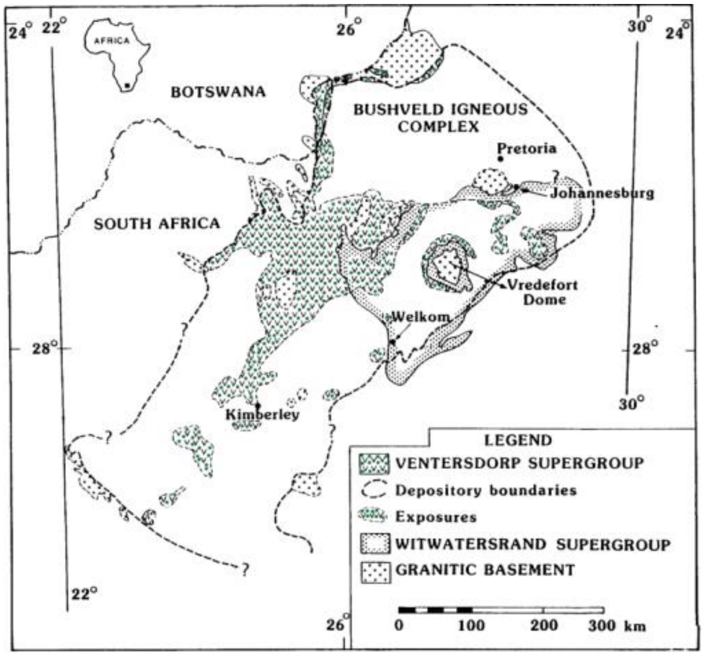

Figure 2.5: The geological map showing the extent and exposures of the Ventersdorp Supergroup. The supergroup comprises mainly volcanic rocks with most outcrops identified north-west and centrally within the Witwatersrand Basin (after van der Westhuizen et al., 1999).

2.2.2.2 Bushveld Complex

The Bushveld Complex is considered the world's largest, best preserved layered mafic intrusion. It covers an area of 65 000 km^2 in the central part of the Kaapvaal Craton with commencing approximately 2.06 Ga ago (Figure 2.6; Cawthorn, et al., 1981). More than one magma injection has been responsible for the emplacement and development of the complex and consequently these multiple injections are associated with their individual sets of sills (Cawthorn, et al., 1981; Cawthorn, et al., 2006). A complex suite of sills ranges from quench-textured micropyroxenites, norites, pyroxenites to heterogeneously contaminated norites (Cawthorn, et al., 1981). These sills intruded into the surrounding

Transvaal Supergroup and may have intruded into the underlying Witwatersrand Supergroup and Vredefort Dome area.

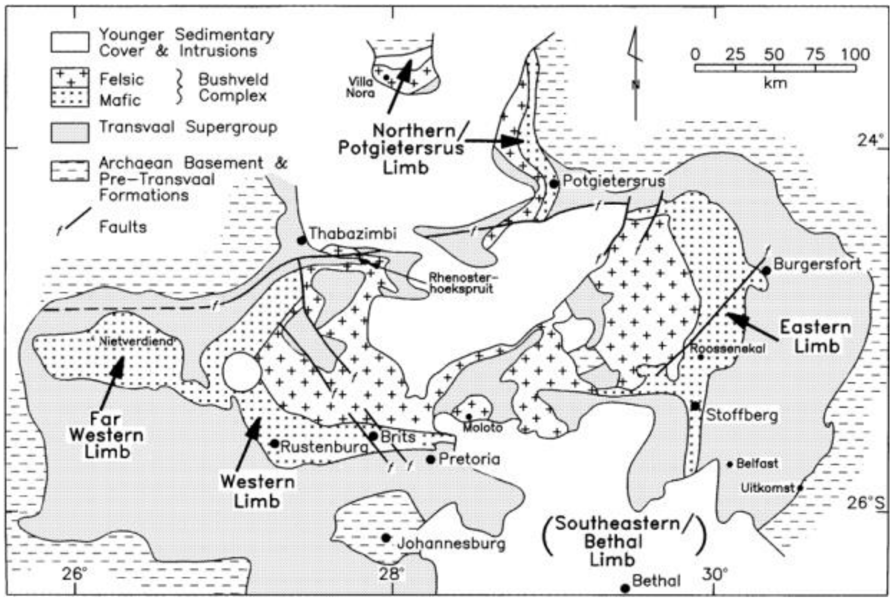

Figure 2.6: Map showing the main body of the Bushveld Igneous Complex. The saucer-shaped complex comprises mafic and felsic rocks, and is divided into the Western, Far Western, Northern, Eastern and South-Eastern limbs, according to its spatial distribution (Cawthorn & Walraven, 1998).

2.2.2.3 Pilanesberg dyke swarm

The Pilanesberg Complex is possibly the best preserved and one of the largest alkaline complexes in the world. It is a radial intrusion with a 28-km diameter, covers an area of 625 km^2, and is situated at the centre of the Kaapvaal Craton. The intrusion is associated with a NW- trending dyke swarm extending as far as the border of Botswana to about 120 km south of Johannesburg (Figure 2.7). Many of the dykes have ages dated at ~1.39 Ga. They are composite, with marginal zones of fine-grained dolerite intruded while still hot by slightly younger syenite and nepheline syenite in the centre. Notable Pilanesberg-aged dykes intruding into the West Rand and West Wits Line Goldfields are the Venterspost and Gemspost dykes (Verwoed, 2006; Cawthorn, 2015).

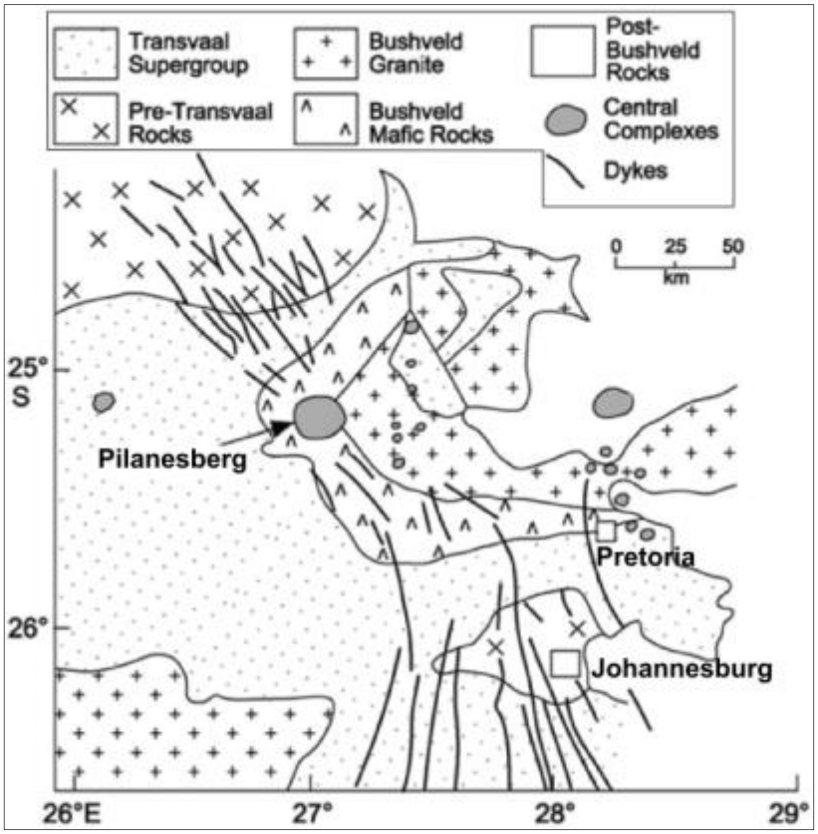

Figure 2.7: A map showing the Pilanesberg Complex and dykes extending from the alkaline complex. The dykes outlined in the image extend for approximately 390 km; they span outward from the radial complex from the border of Botswana, in the north-west, to about 120 km south of Johannesburg (after Cawthorn, 2015).

2.2.2.4 Karoo dolerite suite (~183 Ma)

The interconnected dykes and sills of the Karoo dolerite suite represent the intrusive feeder system that resulted in the formation of the Drakensberg Group approximately 183 Ma ago. The suite is associated with multiple dyke events and represents one of the youngest set of intrusive bodies that intruded into the Witwatersrand Basin (Figure 2.8; Duncan & Marsh, 2006; Neumann, et al., 2011).

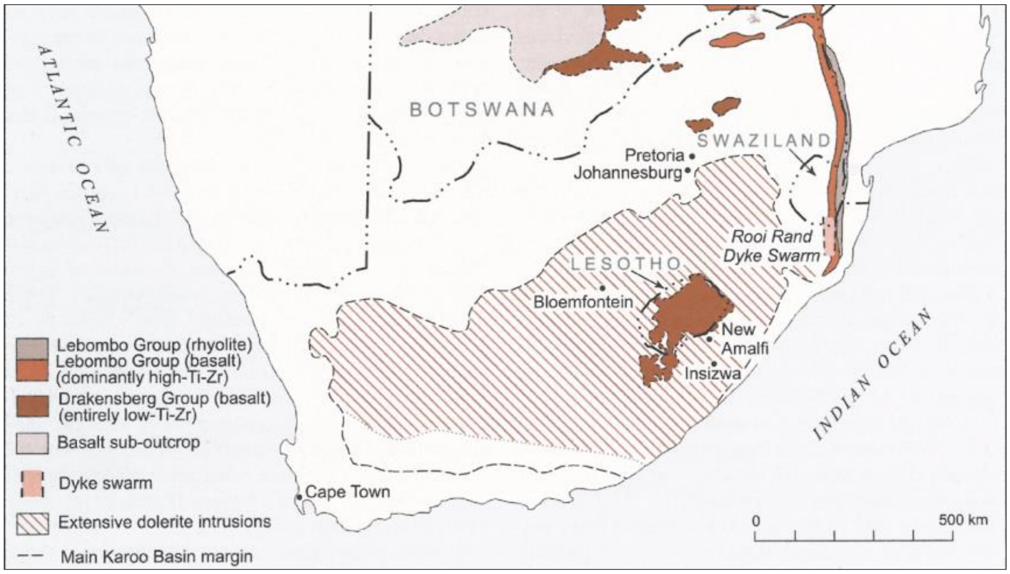

Figure 2.8: Intrusive events associated with the Karoo Supergroup, particularly the Karoo dolerite suite**.** Igneous rocks of the Karoo Supergroup (the Lebombo and Drakensberg Groups) are both mafic and felsic and cover a significant portion of southern Africa (after Duncan and Marsh, 2006).

3. METHANE GAS IN THE WITWATERSRAND BASIN

3.1 Sources of methane at subsurface

Natural gas emitted from the Earth comprises approximately 60-90% hydrocarbons. The hydrocarbon component of natural gas is made up of the simplest, most abundant alkane, methane (CH_4), and higher hydrocarbons such as ethane (C_2H_6), propane (C_3H_8), and butane (C_4H_{10}). The higher hydrocarbons, denoted with the collective annotation C^{2+}, generally make up less than 10% of total hydrocarbon composition (Rojey, 1997; Hoefs, 2009).

The lightness of hydrocarbons (lighter than air) allows the gas to infiltrate through porous rock strata and permeable geological features such as faults and dykes. Migration is impeded by the intersection of the gas with an impermeable rock layer. This eventually results in the accumulation of the gas in what is termed as a 'gas pocket'. Most of these pockets are associated with oil fields and, if large and productive enough, the natural gas is extracted and used as a fossil fuel (Verweij, 1993).

Distinguishing between different sources of hydrocarbons has been the focus of many studies related to oil and gas exploration. Different processes result in the production and migration of methane but there are fundamentally two distinct sources of methane found at depth: a biogenic source and an abiogenic source (Schoell, 1984; Verweij, 1993). Figure 3.1 gives a diagrammatic overview of the main sources of methane on Earth.

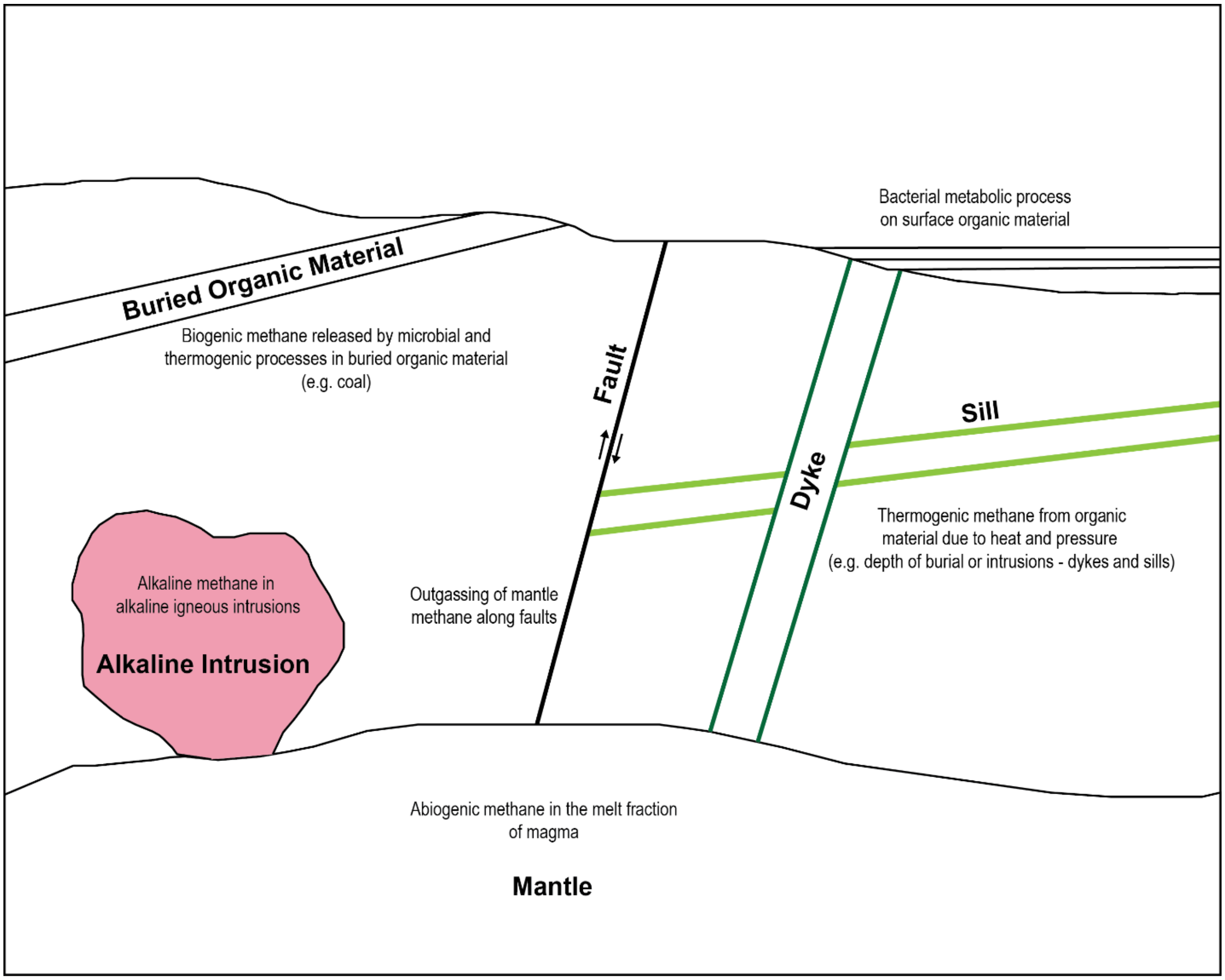

Figure 3.1: The possible sources of methane on Earth. The processes of methane generation at depth include, but are not limited to, magmatic activity that results in the intrusion of igneous bodies such as alkaline complexes, dykes and sills, and bacterial and thermogenic processes occurring in buried organic matter. Faults and dykes are significant agents of methane migration from depth to surface (after Cook, 1998).

Processes that produce biogenic methane are divided into two categories: 1) Microbial methanogenesis involves a process where microorganisms produce methane as a by-product of their metabolic and respiratory activities, and 2) thermogenesis, where the deep burial and heating of organic matter with time results in the production of methane (Schoell, 1988; Sherwood Lollar, et al., 2008). Several geological processes result in the production of abiogenic hydrocarbons.

Processes involving these two kinds (biogenic and abiogenic) of methanogenic production are not mutually exclusive and mixing often occurs between the two end-members (Figure 3.2). This results in a somewhat unclear indication of the source of the gas. As the following section will highlight, distinguishing the origin of methane requires an inter-disciplinary approach.

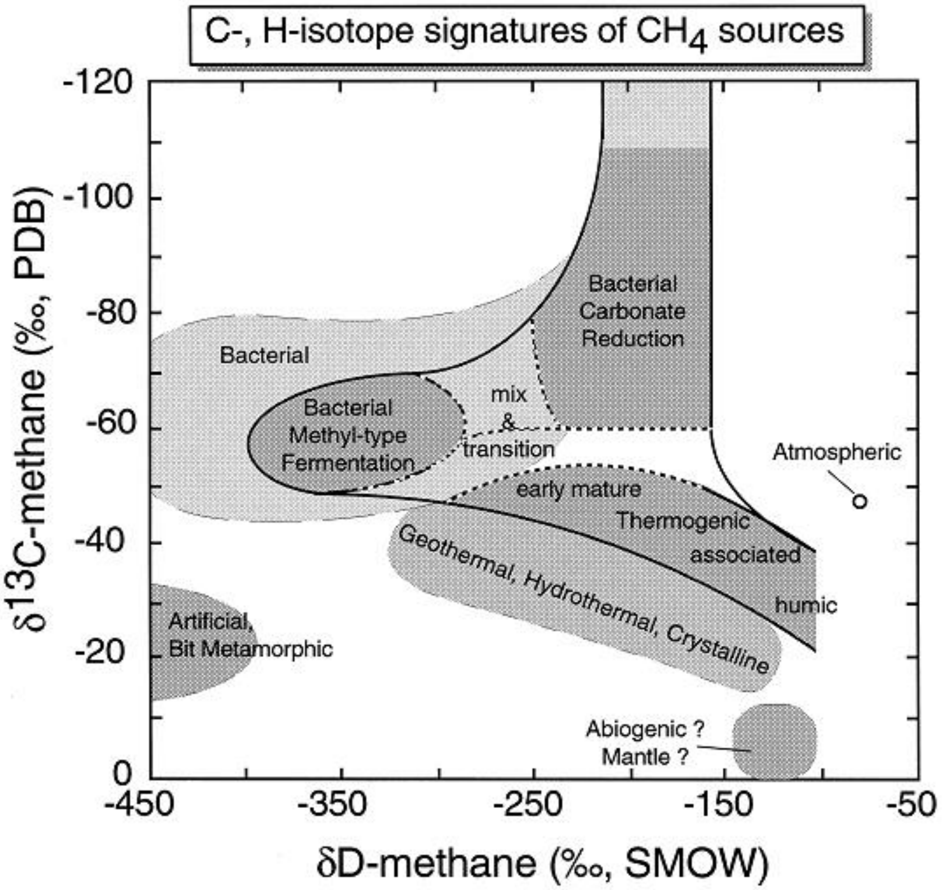

Figure 3.2: Variations in the $\delta^{13}C$ and H isotope signatures of different sources of methane. The grey areas represent the different fields in which the different types of methane fall based on their isotopic signatures. Biogenic sources, such as those produced by bacterial methyl-type fermentation and carbonate reduction, are generally ^{13}C-enriched. The abiogenic end-member, produced through geothermal, hydrothermal, and metamorphic processes, is more $\delta^{13}C$-depleted (Whiticar, 1999).

3.1.1 Biogenic methane

Approximately 20% of global natural gas accumulations comprise gas that is biogenic in origin. Biogenic methane is the product of the respiratory and fermentative processes associated with microorganisms. Methanogenesis by these microbes occurs under anaerobic conditions and primarily through two metabolic reactions: the reduction of carbon dioxide (CO_2) and “acetate” fermentation (Rice & Claypool, 1981; Whiticar, 1999).

CO_2 reduction occurs in sulphate-free, marine sediments and is most common in older sediments and gas fields. It is the dominant pathway for bacterial methane formation through the reaction:

$$CO_2 + 8H^+ + 8e^- \rightarrow CH_4 + 2H_2O$$

Acetate fermentation involves the decomposition of acetate resulting in the production of methane and carbon dioxide as is noted in the reaction below:

$$^{14}CH_3COOH \rightarrow {}^{14}CH_4 + CO_2$$

This process is more common in shallow, freshwater aquifers (Whiticar, 1999). Microbial activity results in methane isotope fractions that are depleted in ^{13}C. CO_2-reduction prone sediments are more depleted in ^{13}C than biogenic gases formed through acetate fermentation. The values range between -110 and -50‰ for the former, and between -65 to -50‰ for the latter reaction (Hoefs, 2009).

Sherwood Lollar, et al. (2008) confirm that CO_2 reduction is the most dominant process by which methane is produced in Precambrian shields. A useful tool in distinguishing between CO_2 reduction and acetate fermentation processes is through the analysis of hydrogen isotopes. Biogenic gas is significantly depleted in δD, where marine sediments (associated with CO_2 reduction) measure values between -250 and -170‰ and between -400 and -250‰ for freshwater sediments (Figure 3.2). The source of hydrogen for these reactions is also considerably different. Hydrogen for CO_2 reduction is derived from formation water and it is the methyl group in the acetate fermentative process that provides hydrogen for the reaction (Whiticar, et al., 1986; Whiticar, 1999).

3.1.2 Thermogenic methane

Complex organic material and diagenetic processes are key factors in the production of thermogenic methane. Increased temperatures favour the breaking up of ^{12}C-^{13}C bonds resulting in higher ^{13}C values during chemical reactions such as cracking and hydrogen disproportionation in kerogen (complex organic material; Kotelnikova, 2001; Hoefs, 2009). Thermogenically-derived methane, unlike biogenic methane, is enriched in ^{13}C. Values range between -50 and -20‰. Freshwater sediments have higher ^{13}C concentrations versus their marine end-member. In the case of thermogenic gases, δD levels are dependent on the level of maturity of kerogen and not the actual source of the H_2 (as is the case with biogenic gases; Schoell, 1988; Hoefs, 2009).

In other words, thermogenic and biogenic methane are differentiable by their ^{13}C content. The latter has the lower ^{13}C levels than the former. Within the biogenic end members, it can be concluded that methane resulting from CO_2 reduction has a low ^{13}C but enriched δD compared to methane from acetate fermentation.

3.1.3 Abiogenic methane

The production of abiogenic methane results from a number of on-going geological processes in the Earth. A review paper compiled by Etiope and Sherwood Lollar (2013) identifies nine different sources of abiotic methane outlined in Table 3.1.

Table 3.1: The three classes for the sources of abiogenic methane are magmatism, late-magmatism, and gas-water-rock reactions. There are a number of processes that are responsible for the production of abiogenic methane in the Earth, with gas-water-rock reactions being the most dominant mode of methane formation (after Etiope and Sherwood Lollar, 2013).

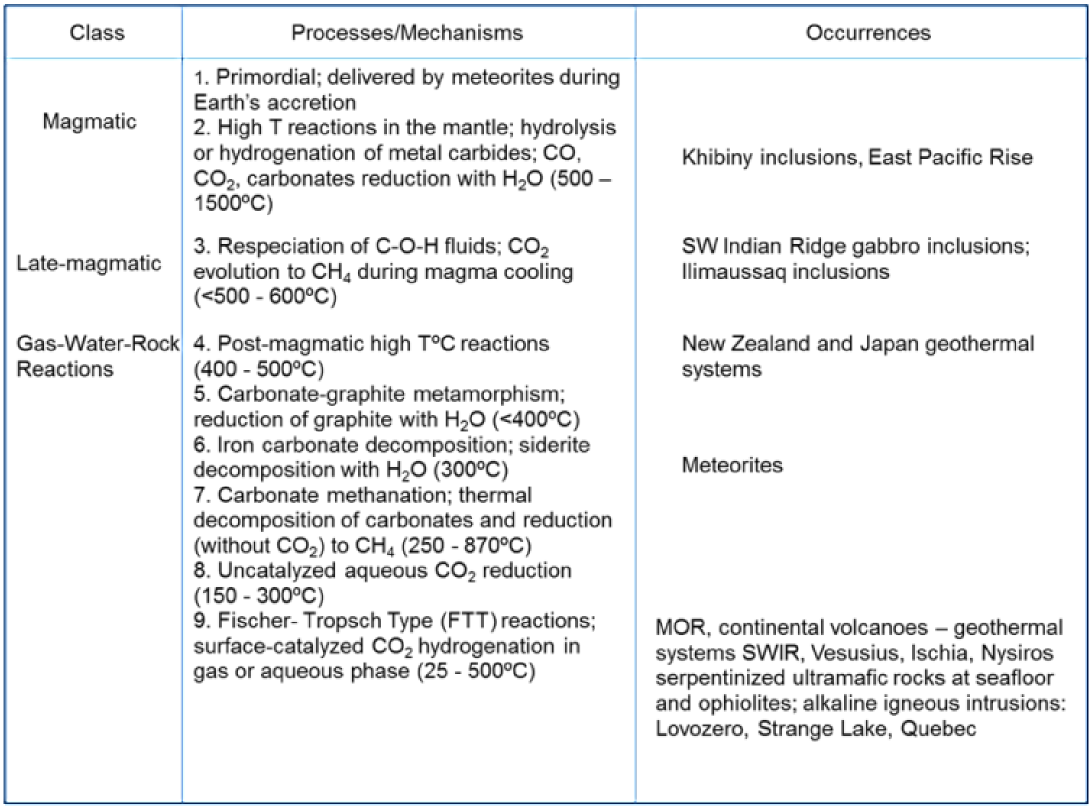

Class	Processes/Mechanisms	Occurrences
Magmatic	1. Primordial; delivered by meteorites during Earth's accretion 2. High T reactions in the mantle; hydrolysis or hydrogenation of metal carbides; CO, CO_2, carbonates reduction with H_2O (500 – 1500°C)	Khibiny inclusions, East Pacific Rise
Late-magmatic	3. Respeciation of C-O-H fluids; CO_2 evolution to CH_4 during magma cooling (<500 - 600°C)	SW Indian Ridge gabbro inclusions; Ilimaussaq inclusions
Gas-Water-Rock Reactions	4. Post-magmatic high T°C reactions (400 - 500°C)	New Zealand and Japan geothermal systems
	5. Carbonate-graphite metamorphism; reduction of graphite with H_2O (<400°C)	
	6. Iron carbonate decomposition; siderite decomposition with H_2O (300°C)	Meteorites
	7. Carbonate methanation; thermal decomposition of carbonates and reduction (without CO_2) to CH_4 (250 - 870°C)	
	8. Uncatalyzed aqueous CO_2 reduction (150 - 300°C)	
	9. Fischer- Tropsch Type (FTT) reactions; surface-catalyzed CO_2 hydrogenation in gas or aqueous phase (25 - 500°C)	MOR, continental volcanoes – geothermal systems SWIR, Vesusius, Ischia, Nysiros serpentinized ultramafic rocks at seafloor and ophiolites; alkaline igneous intrusions: Lovozero, Strange Lake, Quebec

Mantle-derived methane is one of the most significant sources of abiogenic methane. The following factors established by Jenden, et al. (1994) highlight the key characteristics of abiogenic sources of methane derived from the mantle:

- Methane (CH_4) derived from microbial or organic activity is assumed to have been produced later than mantle-derived methane making the source of the former kind of methane a juvenile one. This observation is indicated by the enriched $\delta^{13}C$ values (more than -25‰).
- Low C^{2+} ratios.

- The $\delta\ ^{13}C$ value decrease in the order CH_4, C_2H_6, and C_3H_8. This is a process known as isotopic reversal (Horita & Berndt, 1999).
- A $^3He/^4He$ ratio, where R/Ra is greater than 0.1, indicative of mantle-derived helium. R is the $^3He/^4He$ ratio found in rocks whereas Ra is the present day atmospheric $^3He/^4He$ ratio which is a constant measured at 1.38×10^{-6} (Jenden, et al., 1994).

Rare gases such as helium and neon also have distinctive isotope signatures that have been used to characterize mantle-derived gases. Mantle-derived gases were earlier largely associated with mid-ocean ridge basalts but have since also been identified in continental settings. These mantle gases found in continental basins have been related to continental extension and lithospheric thinning (Sherwood Lollar, et al., 1994). Mechanisms for the presence of mantle methane in the crust include, but are not restricted to, the intrusion of ultramafic rocks and the associated magmatic and hydrothermal fluids moving through geological structures into the upper lithosphere (Sherwood Lollar, et al., 1993; Fruh-Green, et al., 2001).

Alternative sources from which non-biological methane can be derived include water-gas-rock interaction with the surrounding geology over millions of years, serpentinization of olivine from mafic igneous bodies, and the metamorphism of graphite-bearing rocks (Hall & Bodnar, 1990; Etiope & Sherwood Lollar, 2013).

Sherwood Lollar, et al. (2008) noted that it is relatively easy to differentiate between the two biological end-members. It is, however, not as easy to distinguish between biogenic and abiogenic sources of methane because the parameters that separate the two entities are not well defined. There is not much clarity pertaining to the characterization of abiogenic methane. The carbon isotope values derived from the reduction of CO_2 to form methane typical of a mantle source are very low (-4‰ per mil). These values tend to overlap with microbially produced methane. Another distinguishing factor for abiogenic methane is the characteristic decrease in $\delta^{13}C$ values as the hydrocarbons increase, i.e. CH_4 to C_2H_6 to C_3H_8 (Jenden, et al., 1994; Horita & Berndt, 1999).

3.2 Methane in the Witwatersrand Basin

Methane usually comprises more than 50% of the gas composition in gold mines in the West Rand and West Wits Line Goldfields. Some of the most crucial studies regarding the presence of hydrocarbons in the basin have been conducted because of the high gold and uranium grades that have been associated with carbon seams (Gray, et al., 1998; Spanenberg & Frimmel, 2001; Mossman, et al., 2008).

Several different sources have been proposed for the presence of the methane found at mining levels. Jackson (1957) originally proposed that the methane originated from eroded or overlying coal seams of the Karoo sequence. However, other proposed sources of hydrocarbons in the Witwatersrand Basin include:

- Compositional and isotopic studies of the hydrocarbons in the Archaean basin suggest that the origin of methane and higher hydrocarbons (such as ethane, butane, and propane) can be largely attributed to microbial respiratory and metabolic processes. This Precambrian-isolated microbial activity accounts for approximately 80% of this type (biogenic) of methane found in the basin mainly derived from colonies of microbial algal mats over the surface of the clastic sediments of the Witwatersrand Basin (Hallbauer & van Warmelo, 1974; Ward, et al., 2004; Sherwood Lollar, et al., 2006; Mossman, et al., 2008).
- Kerogens disseminated in shale units in the Witwatersrand Supergroup (Robb, et al., 1997; Gray, et al., 1998).
- Sources outside of the Witwatersrand Basin such as shales of the Wolkberg Group or overlying carbonates at the base of the Chuniespoort Group in the Transvaal Supergroup (Robb, et al., 1997).
- Hydrocarbons hosted in brines associated with the Mississippi Valley type Pb-Zn deposits in the Transvaal Basin (Roberts, et al., 1993).

Diagenetic processes such as burial, metamorphism and the associated hydrothermal fluids have led to the thermal alteration of organic matter that may have resulted in the release of gaseous hydrocarbons into the basin. The mobility of these gases through faults and fractures results in isotopic fractionation, which is used to differentiate the sources of the hydrocarbon. The migration of hydrocarbons through rock strata may result in lowered $\delta^{13}C$ values; this is due to continued fractionation as the gases move through the strata (Spanenberg & Frimmel, 2001). Such an example is that of hydrocarbons derived from the Transvaal Supergroup that may traverse into the rocks of the Witwatersrand Supergroup versus those that are indigenous to sediments in the Witwatersrand Basin. Spanenberg and Frimmel (2001) showed that alkanes derived from Transvaal dolomites were isotopically lighter (i.e. depleted in $\delta^{13}C$) than hydrocarbons associated with reef bitumen, gold-bearing conglomerates that contain carbonaceous material. The term bitumen specifically refers to either *in situ* fossils of algae that colonized sedimentary beds or the residual products of liquid hydrocarbons. Isotopic data showed that the hydrocarbons which circulated with hydrothermal fluids through the dolomites and Ventersdorp Supergroup lavas and into the Witwatersrand bituminous reefs, were isotopically different, outlining the distinct difference in the sources of hydrocarbons within the strata.

Biogenic and abiogenic hydrocarbon end-members have been identified in the Witwatersrand Basin. Biogenic methane is linked to microbial methanogenesis and associated with shallow, palaeometeoric groundwater with residence times between 10 000 years and 5 million years. Sites that exhibit methane of an abiogenic origin are almost exclusively associated with groundwater that has older residence times (10 to 25 million years). The fissure water is also associated with deeper, more saline aquifers in the basin. Gas and groundwater geochemistry points to extensive gas-water-rock interaction initiating and catalysing abiogenic methanogenesis (Lippmann, et al., 2003). Carbon fractionation in Fischer-Tropsch reactions has been associated with gas-water-rock interaction. In the simplest terms, the Fischer-Tropsch chemical processes involve the hydrogenation of CO or CO_2 to produce liquid hydrocarbons and have been identified as the main method responsible for some of the abiogenic methane emanating from sites in the basin (Sherwood Lollar, et al., 2008).

Determining the origin of methane requires a basic interdisciplinary approach involving microbiology, geology, geophysics, and isotope chemistry. Compositional and isotopic (namely $\delta^{13}C$ and $\delta^{2}H$) analysis and calculation of the ratio between methane and higher hydrocarbons (CH_4/C_{2+}) may be used to trace the possible source(s) of methane.

4. THE SEISMIC REFLECTION METHOD

Seismic reflection is one of the numerous geophysical exploration methods used in the oil and gas as well as mining industries. As with any branch of exploration, the topics and sub-topics related to the method are vast, however, for the purposes of this study, a few topics have been considered and they are as follows:

- An introduction to the seismic reflection method and how it works.
- The advantages and disadvantages of using the method and how this has been used globally in the oil and gas and mining industries, and more specifically, in South Africa.
- Seismic attributes and their applications in enhancing seismic data.

4.1 Background on the seismic reflection method and its applications

The seismic reflection method works on the basic principle of the propagation and behaviour of sound energy (waves) as it travels through the subsurface. It is a measure of the time it takes for that energy to travel from a known locus on the surface, through the subsurface and reflect to the surface, where it is detected by multiple receivers (known as geophones) located at surface (Figure 4.1). The geophones measure the slightest ground movement and the sound energy created is then converted to voltage, which is directly proportional to velocity, thus giving a recordable seismic response. The time taken for the wave to go down and reflect again is known as the two-way-travel (TWT) time (Kearey, et al., 2002; Herron, 2011).

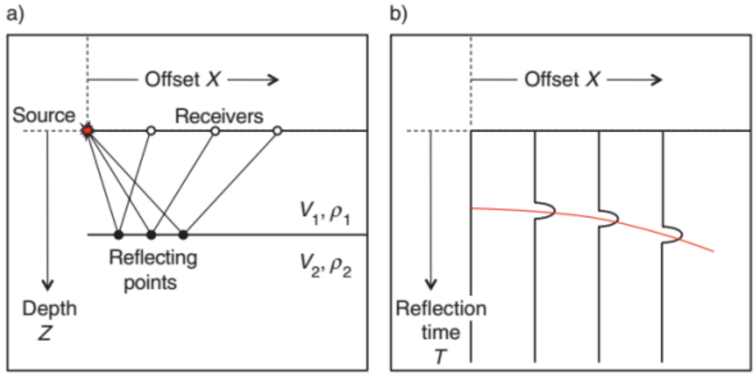

Figure 4.1: (a) A simple illustration of the propagation of seismic waves from the source, to the reflective interface, and back up to multiple receivers (geophones), where a record of the two-way-travel (TWT) time (b) is recorded.

The response of a seismic wave is measured using the two physical properties of the rock layers at the subsurface – the density of the geological layer and the velocity at which the seismic wave moves through media. The degree of reflection or transmission of the seismic energy is dependent on the acoustic impedance contrast (Z) at the boundary between rock layers (Figure 4.2) and is given by equation 4.1:

$$Z = \rho \times V \tag{4.1}$$

where Z is the acoustic impedance contrast, ρ is the density and V is the seismic velocity.

These physical properties determine whether an interface, characterized by sedimentary bedding planes, unconformities, and/or pore-fill, will be seismically reflective or not. Acoustic impedance contrast (Z) cannot be directly related to any physical rock property but it has been noted that it is directly proportional to the hardness of the rock, i.e. more compressed rocks have higher Z-values. A greater contrast at the interface of two layers would result in a greater amount of energy being reflected. It remains, however, that at rock interfaces; a large portion of the energy is transmitted rather than reflected. The amount of energy that is reflected at a rock layer interface is defined as the reflection coefficient (R; equation 4.2). Energy that is not reflected back to surface but transmitted (T) deeper into the Earth is expressed by equation 4.3. The transmitted energy is important in the detection of deeper interfaces at surface (Veeken, 2007; Herron, 2011).

$$R = \frac{\rho_2 v_2 - \rho_1 v_1}{\rho_2 v_2 + \rho_1 v_1} = \frac{Z_2 - Z_1}{Z_2 + Z_1} \tag{4.2}$$

$$T = 1 - R \tag{4.3}$$

where R is the reflection coefficient and T, the transmission coefficient.

The following can be deduced about the wave behaviour of a normal incident pulse at the interface of two layers, bearing in mind that $-1 \leq R \leq +1$ (Figure 4.2):

- From the equation 4.2, it is apparent that R will be a positive number when $V2 > V1$, and a negative number when $V2 < V1$. A positive R means that the polarity of the reflected wave will be the same as that of the incident wave. A negative R means that the polarity of the reflected wave will be the opposite of the incident wave.
- If R is zero, the incident ray will be completely transmitted. This implies that there is no contrast in the acoustic impedance (i.e. $Z_1 = Z_2$), even if the densities and velocities of the two layers are different.

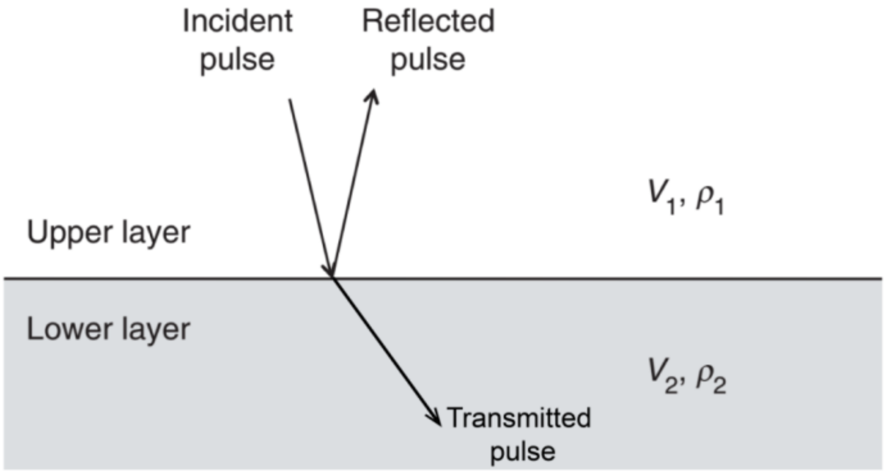

Figure 4.2: An illustration of the reflection and transmission of seismic waves depicted as the incident pulse. The proportion of the reflected energy versus the transmitted energy is dependent on the acoustic impedance contrast between the upper and lower layers. The greater the contrast, the greater the amount of energy that will be reflected (after Herron, 2011).

The reflected pulses are recorded on surface and displayed on a seismograph as seismic traces (otherwise known as wiggly lines). A trace is a depiction of the seismic energy from depth that is reflected back to a single receiver on the surface of the Earth. The information about the TWT and seismic velocities enables geophysicists to reconstruct wave paths and produce an image of the subsurface (Kearey, et al., 2002; Bacon, et al., 2007). Figure 4.3 is a depiction of how rock layers are related to Z, R, and the resultant seismic trace. An increase in Z, which would in turn result in an increase in R, at the boundary between two layers, is identified as a positive change in polarity at the point that coincides with the boundary along the seismic trace. The opposite is true if Z and R decrease at a rock interface, then the polarity is negative. Polarity is important in the seismic interpretation process and two standards are used to describe the polarity of seismic data: the European standard or the American standard. The concept of polarity is described in more detail in Chapter 5.1.2.

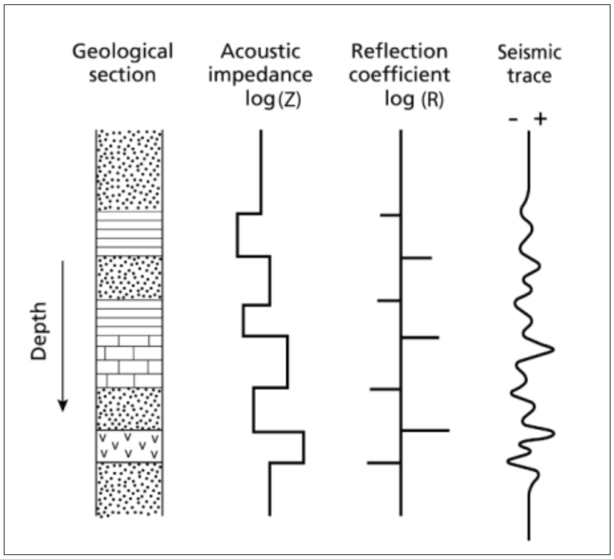

Figure 4.3: The relationship between stratigraphy, the acoustic impedance contrasts (Z) from one lithology to the next and the related reflection coefficients (R). If the Z increases from one layer to the next, this results in an increase in R. This in turn affects the polarity of the seismic trace – an increase in Z and a positive R implies positive polarity, while a decrease in Z and negative R results in a negative polarity (after Kearey, et al., 2002).

4.2 Seismic processing

The reconstruction of wave paths to produce an image of the subsurface is a part of the seismic reflection workflow known as seismic processing. The details of the seismic processing are beyond the scope of this thesis except for one component that is relevant to the study – the migration of seismic data. The purpose of the migration is to move dipping events to their correct locations in the subsurface. This can be done before (pre-) or after (post-) stacking – the process of combining shot records that have a common reflection point to produce a single seismic trace. There are two types of migration processes that can be applied to seismic data: pre- and post-stack migration. Post-stack depth migration (PSDM) was initially considered a more cost effective but time-consuming option than pre-stack time migration. However, the advancement of migration algorithms and the availability of more disk space at a lower cost have resulted in a greater preference in pre-stack migration as a mode for the migration of seismic datasets (Yilmaz, 1987; Etgen, et al., 2009).

4.3 The application of seismic reflection data in South Africa

The seismic reflection method is currently one of the most widely used geophysical methods for exploration. This geophysical exploration method was patented in 1917 but the first exploration survey was acquired in Oklahoma, United States of America, in 1921 (Weatherby, 1940). The seismic reflection method only became popular in the 1930s and was predominantly used for oil and gas exploration. Data acquisition was initially constrained to 2D seismic surveys within marine environments, with the first survey being acquired in the 1950s. With the growth of digital and processing techniques and the advancement of workstation technology, the seismic reflection method has evolved into the 3D, land seismic survey arena. The first 3D seismic surveys were carried out in 1970s and the geophysical method has since gained more popularity in crustal research and mineral exploration within continental basins (Weatherby, 1940; Davies, et al., 2004; Trickett, et al., 2005).

The cost of acquiring seismic data is significant – it is currently one of the most expensive geophysical methods used for exploration – but the advantages of the method far outweigh the disadvantages. One advantage of using seismic reflection is the increased confidence and accuracy in reservoir and ore body delineation and therefore reduced exploration risk. Another advantage is that advancements in computer technology have resulted in a decreased cost (over time) in acquisition and processing of 3D seismic data but improved data quality (Davies, et al., 2004). The use of 3D seismic reflection to identify and constrain ore reserves in hardrock environments is young compared to its application in the oil and gas industry. Although the seismic exploration method has been building up significant momentum in oil and gas exploration, imaging of sedimentary-hosted mineral deposits only picked up in the 1980s. This was because the data acquisition and processing techniques had not been properly altered to fit hardrock environments. Secondly, although the reflection seismology was good at imaging the deep crustal structures (as far down as the Moho), high-resolution imaging of the upper crust fell short. Another problem was that mining houses, particularly in South Africa, considered the method too expensive and restrictive in the types of mineralization that could be imaged. This changed, however, in 1983 when the Gold Division of Anglo America took the plunge, and accumulated an extensive 2D seismic survey collection along with seven 3D seismic surveys across the Kaapvaal Craton. This is known to be the most extensive seismic project to date (Milkereit & Eaton, 1998; Pretorius, et al., 2003; Stevenson, et al., 2003).

A number of studies have been done regarding 3D seismic surveys in hardrock environments, i.e. areas of crystalline rocks characterized by high densities and velocities have been driven by mineral resource exploration. The application of the geophysical method has been largely based on ore body delineation, mining development and planning, as well as the structural and stratigraphic controls of mineralization. In South Africa, the gold and platinum industries have been the greatest recipients of the 3D seismic reflection method, where it has become an integral part of mine planning and development. Probably the most significant component of the application of reflection seismics has been the use of seismic attributes to enhance particular features in seismic data (Salisbury, et al., 1997; Jolley, et al., 2004; Dehghannejad, et al., 2012; Manzi, et al., 2012; Ahmadi, et al., 2013; Manzi, et al., 2013a; Manzi, et al., 2013b; Manzi, et al., 2015).

4.3.1 Western Ultra Deep Levels 3D seismic reflection survey

The original 1995 WUDLs post-stack depth migrated 3D seismic data were interpreted by Manzi, et al. (2013a). However, the pre-stack time migrated data (PSTM) have been used in this study to maximize the usefulness of the time-dependent seismic attributes to enhance the structural interpretation. Manzi et al. (2012) provide a detailed description of the processing steps carried out for these data set but that is beyond the scope of this thesis. The difference in the time versus depth migrated data is that most seismic attribute techniques are functions of time and frequency, not depth. This is particularly the case with the application of complex trace attributes (e.g., instantaneous phase, instantaneous frequency, and envelope), which are time-dependent techniques used to identify particular features in seismic data.

The WUDLs 3D survey is a 6-second two-way-time (TWT) seismic dataset; this equates to approximately 12 km in depth when using the average seismic velocity of 6500 m/s. The data show the mapping of stratigraphy from surface down to the base of the Witwatersrand Supergroup. The 3D seismic data were acquired in 1995 by AngloGold Ashanti Ltd. with the purpose of imaging major gold-bearing horizons: the Ventersdorp Contact Reef (VCR) and the Black Reef (BLR). The entire sequence comprises meta-sedimentary, basic and mafic rocks that are characterised by high velocities (Gibson, 1997; Manzi, et al., 2012; Manzi, et al., 2015). The high velocities (5200 m/s to 6500 m/s) in the data are indicative of the highly consolidated nature of the rocks of the Witwatersrand Basin and overlying volcano-sedimentary basins. These are described as hardrock because they are mechanically hard and therefore exhibit high seismic velocities, which are indicative of resistant crystalline rocks. The detection of an interface between two layers requires that at least 6% of the incident energy be reflected (Kearey, et al., 2002). Such is the case with the contact between the quartzites of the Central Rand Group and overlying Klipriviersberg lavas of the Transvaal Supergroup as well as the contact between the Booysens Shale Formation and overlying quartzites of the Central Rand Group.

4.4 Seismic attributes

A seismic attribute has been described by Chopra and Marfurt (2005) as “a quantitative measure of a seismic characteristic of interest.” The application of seismic attributes is an integral part of seismic interpretation. Seismic attributes have been used since the 1930s to derive information from the seismic data, such as faults and changes in lithology, which is not immediately evident or prominent using the basic observations of the seismic data on the amplitude displays. Over 55 seismic attributes now exist, and this has been the result of the substantial development in computer technology and increased data storage capacity at reduced costs. Attributes can either be applied to a specific seismic event (reflector) or to the entire seismic 2D line or 3D volume (Brown, 1996; Chopra & Marfurt, 2005). The use of seismic attributes has become standard practice in the seismic interpretation process. In the Witwatersrand Basin, seismic attribute analysis has been useful in identifying gold-bearing reefs and fault systems, particularly those that were below seismic resolution, which is a quarter of the dominant wavelength, i.e. 25 m (Manzi, et al., 2012; 2015).

There are a number of studies conducted in the gold mining exploration in the Witwatersrand involving the use of probably the simplest seismic attribute – amplitude display. For example, Manzi, et al. (2012; 2013a,b) reprocessed 3D seismic data sets acquired in the West Wits Line and West Rand goldfields, which effectively improved the quality of the data, and applied a number of different types of seismic attributes to enhance the imaging of gold-bearing reefs, faults and fault continuity. The authors further used seismic attributes to investigate the relationship between methane gas and water-bearing structures affecting mine safety and productivity in the West Rand and West Wits Line Goldfields.

Although there is a detailed classification of seismic attributes, the attributes that have been used in this study are simply divided into horizon-based and volumetric attributes. The horizon-based attributes are instantaneous phase, instantaneous frequency, envelope, dip, dip azimuth, and edge-detection. These attributes were applied to 3D seismic data from the West Wits Line Goldfield to detect and compare stratigraphic and structural relationships between the BS (i.e. a possible source of methane) and the overlying VCR (i.e. a gold-bearing reef or mining level). Ant tracking is a volumetric attribute that is used to detect any structural links between the BS, VCR and methane sampled data points. Chapters 4.4.1 and 4.4.2 provide a detailed description and application of these seismic attributes.

4.4.1. Horizon-based attributes

4.4.1.1 Complex trace analysis - Instantaneous attributes

Complex trace analysis can be described as the transformation of time seismic data in order to derive new information about the seismic signal. The complex trace is the sum of the real seismic trace, T(t), and the Hilbert transform of the real trace, iH(t), as expressed in equation 4.4:

$$CT(t) = T(t) + iH(t) \tag{4.4}$$

Where CT(t) is the complex trace, T(t) is the seismic trace, and H(t) is the Hilbert Transform of T(t), a 90° phase shift of T(t).

Complex trace analysis separates and measures two quantities of a signal: the amplitude and the phase of the data. Instantaneous amplitude (envelope) and phase are the basic attributes and the rest are derived by differentiation, averaging, combination, or transformation. All instantaneous attributes provide important information regarding the seismic data. Instantaneous amplitude measures reflection strength in time. This attribute is primarily used to visualize regional characteristics such as structure, sequence boundaries, thickness, and lithology variations. In some cases, bright and dim spots can be gas indicators. Tuning characteristics can be observed using this attribute, and may help to identify reservoirs on a local scale. Instantaneous frequency is the rate of change of instantaneous phase from one time sample to the next (first vertical derivative of the phase). It is used for visualizing regional depositional patterns. In some cases, high frequency absorption can cause shadow zones beneath condensate and gas reservoirs. Frequency tuning can indicate changes in bed thickness (possibly pinchouts, onlaps, or downlaps). Spikes indicate noise or discontinuous points where frequency can become zero, negative or anomalously large. Instantaneous phase enhances the continuity of events by ignoring the amplitude information in time samples. It is the magnitude part of each pair of polar values, produced by applying a Hilbert transform to the original seismic trace.

Instantaneous phase is expressed in degrees, usually from -180 (trough) to +180 (peak) or +180 (trough) to 0 (peak). It is used for the regional visualization of stratigraphic relationships (prograding reflections, onlaps, pinchouts, etc.). In some cases, fluid contacts are isolated and phase reversals can indicate down-dip gas limits (Rijks & Jauffred, 1991; Taner, et al., 1979). The mathematical expressions and key features given by instantaneous attributes are tabulated below (Table 4.1).

Table 4.1: The mathematical expressions of the amplitude, instantaneous phase, frequency, and envelope attributes, and the key features that they highlight.

Attribute	Equation	Application
Amplitude (Envelope)	$E(t) = [T^2(t) + H^2(t)]^{0.5}$	Voids Fluids (oil, gas and or water) Intrusions
Instantaneous Phase	$\Phi(t) = \lvert \arctan(t)/T(t) \rvert$	Lateral continuity Unconformities
Instantaneous Frequency	$F(t) = d(\Phi(t))/dt$	Change in bed thickness Change in lithology

where $\Phi(t)$- time-dependent instantaneous phase; $H(t)$ is the Hilbert Transform of $T(t)$; $T(t)$ is the seismic trace; $F(t)$ is instantaneous frequency; and $E(t)$ is the envelope (Subrahmanyan & Rao, 2008).

4.4.1.2 Geometric attributes

Geometric attributes are mathematical functions that resolve surface features on picked events, i.e. horizons. They show disturbances in bed continuity such as edges and faults on the surface as well as geometrical features such as the orientation of a bed namely dip and azimuth. The geometric attributes used in this study include dip, dip azimuth, and edge-detection. These attributes can be applied to detect a particular geological feature or reservoir property, and to delineate structural or stratigraphic features from which basin evolution can be inferred (Chopra & Marfurt, 2005). A single attribute may be applied to a dataset but, in some instances, more than one attributes may be applied to the data provided they are independent of each other. In order not to create bias interpretation, Kalkomey (1997) advises that when applying the attributes, they must enhance different physical properties.

4.4.1.2.1 Dip and dip-azimuth

Dip and azimuth attributes are the function of the variability in inclination and direction, respectively, of the time gradient from one time interval to the next (Figure 4.4; Rijks & Jauffred, 1991). Dip and dip-azimuth can be mathematically expressed as follows:

$$\text{Dip}=\sqrt{(dt/dx)^2+(dt/dy)^2} \qquad (4.5)$$

$$\text{Dip Azimuth}=\arctan((dt/dx)/(dt/dy)) \qquad (4.6)$$

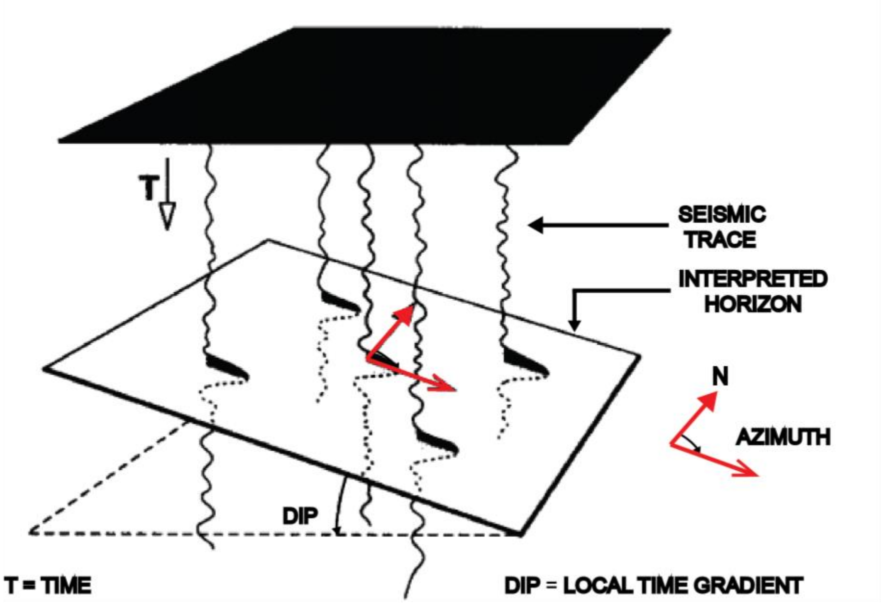

Figure 4.4: A visual representation of how dip and azimuth are extracted from an interpreted horizon (after Rijks & Jauffred, 1991).

Computing dip and azimuth on an interpreted horizon is useful in resolving faults and flexures on an interpreted horizon. Colour plays an integral part in representing the discontinuities and subtle undulations along the picked surface, representing values that range between 0 and 90° for dip and 0 to 360° for dip azimuth. The effectiveness of these attributes in detecting faults depends on the difference in dip angle or dip direction along the horizon on each side of the fault. The dip and dip azimuth attributes are also dependent on the signal-to-noise ratio of the data. Dalley, et al. (1989) provide two recommendations when using these attributes. The first is to use automated picking when interpreting a chosen reflector. This will ensure that the surface is picked along the same phase, thus reducing background noise. The second recommendation is that where a fault, characterized by a disturbance along a reflector, is encountered, it should be picked as part of the horizon. The fault will appear as a lineament along the surface, characterized by a relatively high dip and an anomalous azimuth.

4.4.1.2.2 Edge-detection

The edge-detection attribute is a useful means of detecting edges or discontinuities along surfaces (horizons). In most instances, if a feature is continuous and appears to vertically displace the seismic surface, then it is most likely to be a fault. This attribute combines the variations in dip and dip-azimuth that have been normalized to the local noise of the picked horizon grid. It picks up even the slightest variations in the signal amplitudes - an optimal method to detect faults that are below the seismic resolution limit (Randen, et al., 2001). The edge-detection attribute highlights, with the help of the manipulation of the colour bar, finer details such as cross-cutting relationships and fault continuity. The attribute can detect faults that cross-cut the gold-bearing horizons of the West Wits Line Goldfield with throws as little as 5 m (Manzi, et al., 2012; Manzi, et al., 2013b).

4.4.2 Volumetric seismic attributes

Volumetric attributes are attributes applied on an entire 3D seismic volume. There are many types of volumetric attributes including curvature, coherence, variance, chaos, and ant-tracking (Randen, et al., 2001; Chopra & Marfurt, 2007). The ant-tracking attribute, in particular, is used in this study to examine the extent of faulting and fault connectivity.

4.4.2.1 Ant-tracking

Fault interpretation on noisy and/or poor seismic data requires manual fault picking because the faults would be difficult to identify with confidence through auto-picking (Ngeri, et al., 2015). This is considered a tedious task that is plagued by the biases of the interpreter. Ant-tracking is a fault detection technique developed by Schlumberger and implemented in the Petrel software package. The ant-tracking workflow incorporates edge-detection techniques, such as chaos and variance, to identify and track faults throughout the volume (Cox & Sietz, 2007; Godfrey & Ran, 2008; Ngeri, et al., 2015). The algorithm enhances the detection of geological features that are most likely to be faults. The process works analogously to ants in nature: ants use swarm intelligence to accomplish tasks; they identify the most efficient path to find food and to their nests through the most traversed paths using pheromones. In the ant-tracking technique swarm intelligence uses computer-coded agents to identify, track, and sharpen faults in the seismic volume. The paths that have the most electronic 'pheromones' are most likely faults (Khair, et al., 2012; Farghal & Zoback, 2014; Wang, et al., 2014).

The process of computing the ant-tracking technique to the seismic volume is divided into four parts: conditioning or filtering, edge-detection, edge enhancement, and interpretation. Conditioning removes the attenuated noise by using various filters. The most popular method of conditioning the data is through structural smoothing. This is done by applying a Gaussian filter, which seeks to remove random noise while preserving the edges (faults)

(Ngeri, et al., 2015). The edges in the data can be detected using variance and chaos attributes measurements.

Variance and chaos attributes are edge-detection techniques that are applied during the ant-tracking workflow (Baytok & Pranter, 2013). Variance measures the dissimilarity of the local amplitude of each voxel in the data to differentiate edges from noise (Farghal & Zoback, 2014). It is versatile in that the user can define vertical and horizontal windows to allow for vertical smoothing and noise suppression. This option is data and objective dependent. When the variance volume is used as input for the ant-tracking, potential identification of constant discontinuities is enhanced (Baytok, 2010).

Chaos, on the other hand, measures the degree of randomness in the dip and azimuth of the data. It searches for chaotic signals and identifies the presence and extent of edges in data. The chaos attribute is sensitive to noise; thus, it has the potential to enhance both faults and noise in the data (Baytok, 2010). This attribute, therefore, works best on data with high signal-to-noise ratio. For an in-depth description of these attribute (Baytok, 2010).

The ant-tracking technique is poor when not coupled with other fault enhancing techniques such as variance and chaos. A seismic volume in which the variance or chaos attribute has been applied prior to the application of the ant-tracking attribute produces a volume showing the mapping of major fault systems. Edge enhancement is achieved by distributing ants within the seismic volume following the application of the chaos or variance attributes to the volume (Khair, et al., 2012; Farghal & Zoback, 2014). A full description of the parameters as applied at each step in the ant-tracking workflow is given in Chapter 5.3.2.

5. DATA AND METHODOLOGY

5.1 Seismic interpretation

Seismic interpretation is the analysis of seismic data to infer subsurface geology. Information that can be inferred from seismic interpretation includes geological structures and subsurface physical properties that can be used to create seismic models. The interpretation of seismic data is preceded by the acquisition and processing of the data. Interpretation of 3D seismic data involves identifying laterally continuous seismic reflectors and picking these at every inline and crossline in seismic sections, as well as along time or depth slices. The term inline refers to the direction in which the receiver cables are placed during seismic acquisition. The inline coordinates increase from west to east. The crossline direction, on the other hand, moves from south to north, perpendicular to the inline direction (Bacon, et al., 2007). Constraining the interpreted seismic horizons with borehole log data, surface and subsurface mapping increases the confidence in the final geological model. Confident interpretation relies on seismic data that are of good quality, the accuracy and quantity of supplementary borehole data, and the experience of the interpreter. This chapter provides a detailed description of the techniques used in this study to interpret the WUDLs 3D seismic data.

5.1.1 Seismic borehole correlation

Three hundred and fifty boreholes were used to verify the position of the BS and VCR at depth (Figure 5.1). Most of the boreholes lie within the Mponeng area with a few spread-out across the other mines. Although most boreholes intersected the Booysens Shale in the Mponeng, TauTona, and Kusasalethu gold mines, there were no boreholes that contained log information about the shale unit in the Driefontein and Deelkraal gold mines. Of the 350 boreholes, three boreholes (LIB 16, 19 and 35) are used below to illustrate the relationship between the Booysens Shale and the VCR (Figure 5.2) in the eastern portion of the seismic survey area. Figure 5.2 shows the intersection points (true vertical depth (TVD) seismic) for the BS and VCR. The position of the VCR was previously interpreted and corroborated with borehole data by Gibson, et al. (2000) and later by Manzi, et al. (2012). The boreholes had a depth mistie ranging between 20 and 35 m.

As numerous as the borehole dataset was, there was no downhole geophysical data available that provided information about the seismic response of the BS. This hindered the ability to create an accurate synthetic seismogram representing the seismic response of the BS, as well as for the over- and under-lying lithologies.

Another limitation of the borehole data is their sparseness (~ 1 km apart) in the western portion of the West Wits Line Goldfield (Figure 5.1). However, numerous boreholes could be used to correlate the BS and VCR within the AngloGold Ashanti gold mines (Mponeng and TauTona gold mines) as well as in the Driefontein gold mine. However, in the Kusasalethu and Deelkraal survey areas the interpretation relied mainly on the reflector continuity because there are only four boreholes that fall within these areas. Therefore, the tracking of the BS horizon in these areas was dependent on the strength of the reflector, few borehole data, as well as the location of the reflector as identified previously by other authors (Gibson, et al., 2000; Jolley, et al., 2004).

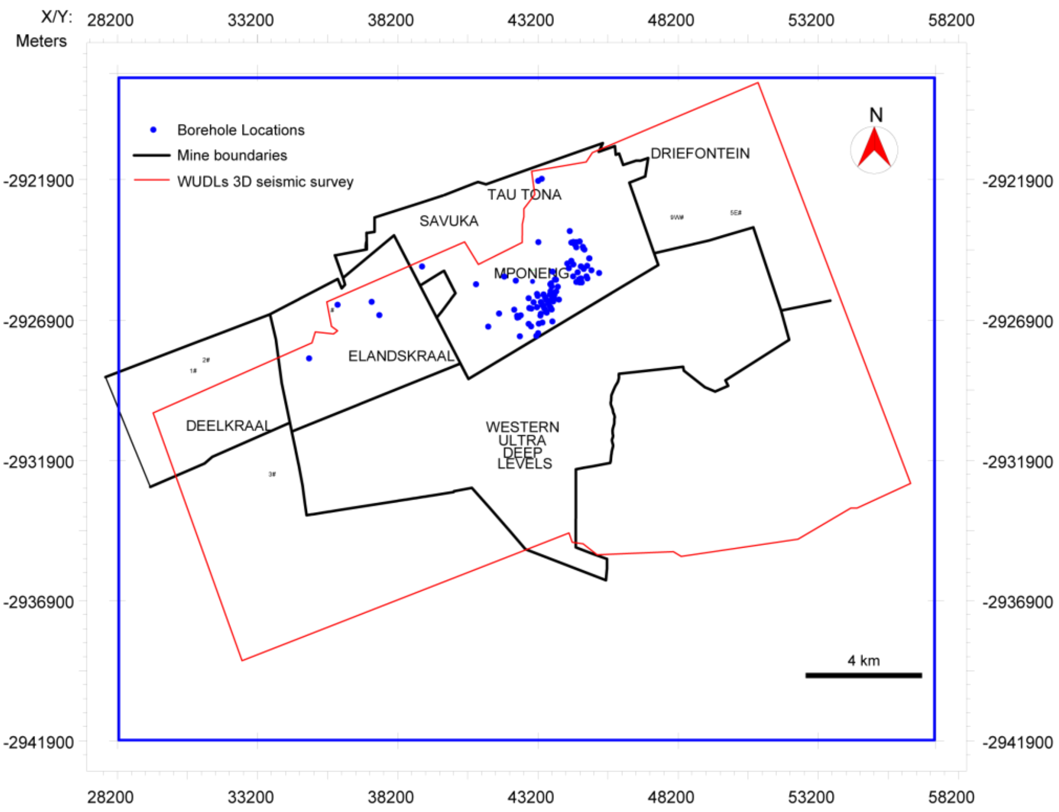

Figure 5.1: Survey area showing the location of the boreholes that intersected Booysens Shale (BS) and Ventersdorp Contact Reef (VCR) horizons. Of the 350 boreholes containing core log data, only four formation tops were available to correlate the position of the BS in the Kusasalethu gold mine and there is no borehole data available for the position of the BS in the Driefontein gold mine.

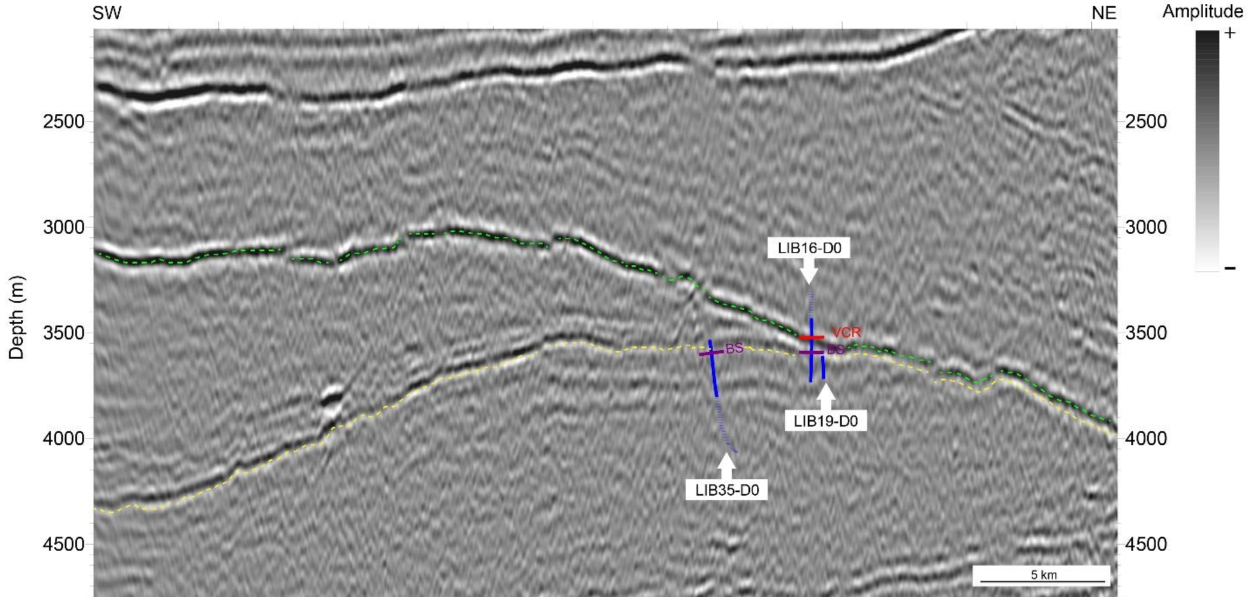

Figure 5.2: Crossline 1314 showing the boreholes LIB35-D0, LIB16-D0, and LIB19-D0 used to locate the stratigraphic position of the Booysens Shale (BS) and Ventersdorp Contact Reef (VCR). The seismic section shows that the distance between the BS and VCR decrease towards the NE of the survey.

5.1.2 Horizon interpretation

The BS and VCR horizons were interpreted using both 3D auto-picking and manual picking. Manual picking was used where the continuity of the horizon could not be easily tracked due to the low quality of the data, particularly at the edges of the survey area or where there was increased structural complexity. The horizons were selected based on their geological significance and/or a strong reflector that had a constant phase. Seismic sections were initially interpreted at wide-line spacing, i.e. every tenth crossline and inline of the 3D volume. This was done in order to map first-order scale structures. Once a wide grid of picks was completed, infill picks were made at close line spacing that enabled detailed structural interpretation. Acoustic impedance contrast decreases from the flood basalts of the Klipriviersberg lavas to the quartzites of the Central Rand Group. This resulted in the VCR being picked as a “hard” event, i.e. a peak. The transition from the quartzites to the BS is characterised by an increase in acoustic impedance contrast and the BS was therefore interpreted as a “soft event” or trough (Simm & Bacon, 2014) (Figure 5.3). The European standard of picking, where the peak is identified as positive amplitude (as opposed to the American standard where positive amplitude is defined by a trough), was used for the picking process. Picking was mostly restricted to the central part of the survey because of the deterioration in seismic resolution due to structural complexity and, on the southern end of the survey area, due to low fold of coverage.

The position of the BS was constrained using borehole data that had intersected both the BS and the VCR horizons. The reflector strength of the VCR enabled continuous, smooth picking for most of the West Wits Line Goldfield. The surface was, however, re-picked using the 3D-seeded auto-picking. In areas of uncertainty or poor resolution, manual picking was used.

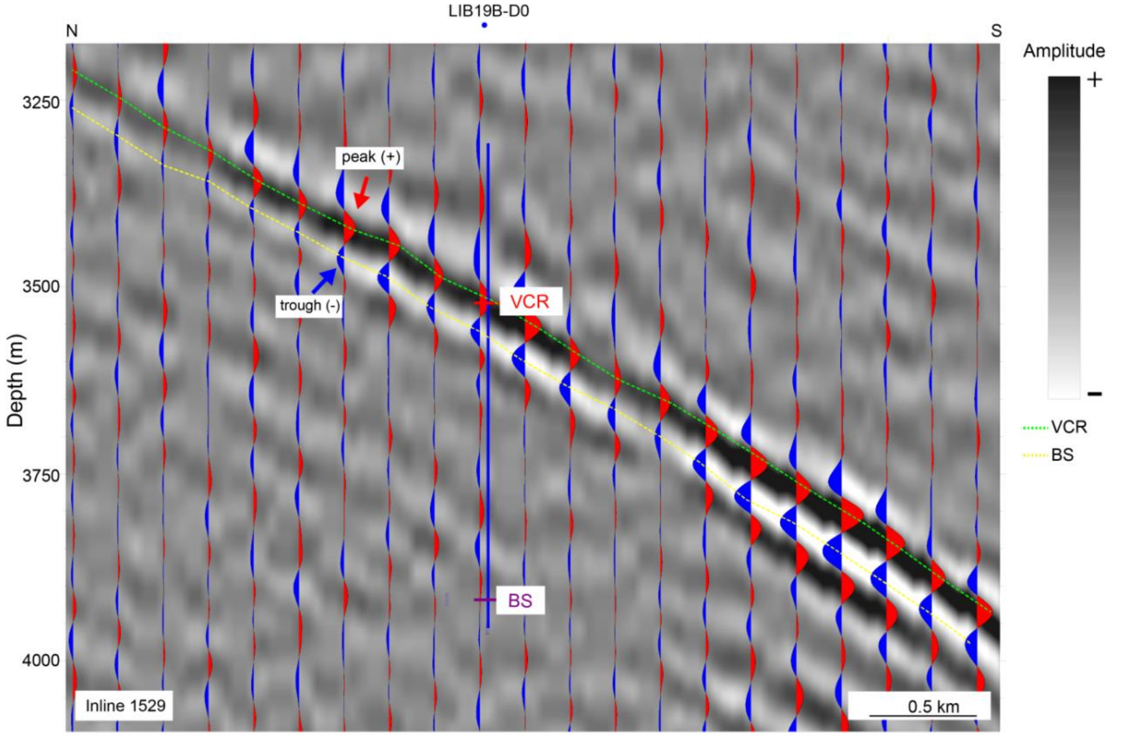

Figure 5.3: Inline 1529 showing the seismic response of the Booysens Shale (BS) and Ventersdorp Contact Reef (VCR). The shift from overlying quartzites and conglomerates above the BS to the shale layer is characterized by an increase in seismic velocity resulting in negative polarity (a trough). The transition from lavas above the VCR to the underlying

quartzites is characterized by a decrease in the seismic velocity and is thus represented as a peak, i.e. positive polarity.

5.1.3 Fault interpretation

The structural complexity of the Witwatersrand Basin offers an interesting and challenging means of fault interpretation. Brittle geological structures in the West Wits Line Goldfield range from regional (km-size fault displacement) to micro-scale (cm-size fracture sets). The structures that could be imaged in the seismic data are limited on the lower end of the scale. Faults in seismic data are identified as interruptions/discontinuities along the seismic reflector. Due to vertical resolution limits in seismic data, the mapping a fault along a seismic reflector is requires that the throw of the fault be equal to or greater than one quarter of the dominant wavelength (Yilmaz, 1987). In the case of the WUDLs 3D seismic data, faults with throws of a minimum of 25 m can be detected along seismic reflectors (Manzi, et al., 2012). Faults that visibly intersected the BS as well as the VCR were picked. In some instances, there were faults that appeared to intersect only the BS and some, only the VCR, and were picked accordingly. Fault interpretation was done on Petrel. Each fault was picked along inline and crossline intersections until it could no longer be seen on the seismic section indicating the end of the fault plane. The faults' surfaces were assumed to be planar as opposed to their actual slightly listric form that has been described in literature for some of the known faults.

5.1.4 Data conditioning

5.1.4.1 Filtering

Following the interpretation of the horizons, various smoothing filters were applied to the BS and VCR horizons. The combination of a mean and median filter was mainly used. These are described by Chopra and Marfurt (2007) as structure-oriented filters because they remove random noise and enhance lateral continuity of the geological feature. This is achieved by differentiating between the dip azimuth of the reflector and the noise above the reflector. When the distinction is made, the filters are then applied to improve signal along the horizon. Mean filtering removes random noise by computing the average values that fall within the chosen window of analysis. The mean filter was applied on the horizon using a sampling interval of 5 by 5 traces. A sample interval of 3 by 3 traces may be used but Chopra and Marfurt (2014) recommend using 3 by 3 traces for 2D seismic data and 5 by 5 traces for 3D seismic data. The mean filter is computed as follows (Equation 5.1):

$$u_{mean}(t) = \frac{1}{J}\sum_{j=1}^{J} u_j\,(t) \tag{5.1}$$

where t is time, and $u_j(t)$ is the jth of J traces within the sampling interval.

The one disadvantage of mean filtering is that it tends to smear lateral discontinuities, but the application of median filtering reduces that effect. A median filter reduces noise without jeopardizing the edges including discrete offsets on an interpreted horizon associated with faults. The way this filter works is that it identifies samples within the chosen aperture along the local dip and azimuth and replaces the amplitude of the central sample position with the median value of the amplitudes, thus eliminating outliers (Chopra & Marfurt, 2014). The median filter is computed as follows:

$$u_{median}(t) = u_{j\left(k=\frac{[J+1]}{2}\right)}\mathrm{t} \tag{5.2}$$

where t is time, and $u_j(t)$ is the jth of J traces within the sampling interval. k is an ordering index used to order the J samples within the sampling interval.

5.1.4.2 Surface smoothing

The BS and VCR have varying degrees of continuity. This is related to the reflectivity and depth at which the horizons lie. The VCR has a more continuous and apparently smoother surface than the BS owing to the higher acoustic impedance contrast between metabasalts and quartzites than between quartzites and shales. During the picking of the shale unit, it was noted that the southwestern part of the survey area had a lower S/N (signal-to-noise) ratio than the rest of the area. This meant that for most of that portion, manual picking had to be employed. The use of manual picking is most advantageous in areas where the reflector is obscured by a poor S/N due to low fold coverage or complex geology, but the method has its disadvantages. The continuous use of manual picking tends to create spikes along the surface. Smoothing (gridding) the horizon was done using the Kriging method. Kriging is a spatial interpolation method that is widely used in the interpolation of the extent of geological bodies. The Kriging method uses a weighted average of neighbouring samples to determine an unknown value at a particular location. The interpolation and smoothing method makes a good estimation of the trend of the data, so that, if there were any mis-picks (marked random spikes or dips), Kriging would attempt to average that point based on the values of the surrounding data (Figure 5.4). Once the BS horizon was filtered, smoothed, and contoured, the complex trace attributes were applied whose applications are outlined in Chapter 4.4.1.

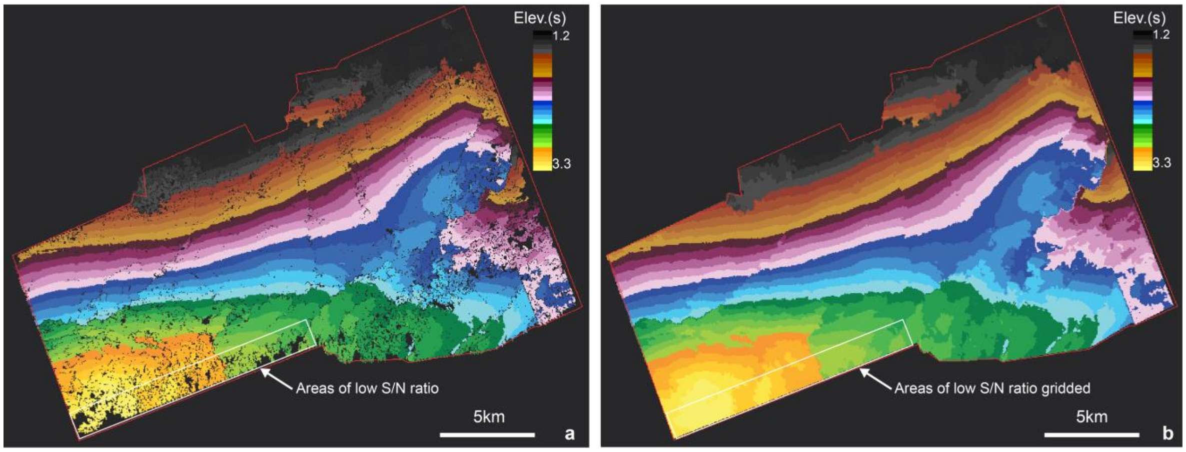

Figure 5.4: Booysens Shale horizon before (a) and after (b) gridding using the Kriging method. The gridding method has interpolated and smoothed areas of sparse data.

5.2 Time-to-depth conversion

The results in Chapters 6 and 7.2 are given in time. The application of the ant-tracking attribute and incorporation of methane gas sampling points required that the data be converted from the time to depth domain. Time-to-depth conversion was done using the domain conversion feature in Petrel software. This was done by creating a velocity model then using the model as the input for the domain conversion tool. The interval velocities inputted for the VCR and BS horizons to create the velocity model were 5600 and 5900 m/s, respectively. These interval velocities are lower than those reported by Gibson (1997) which are 5899 m/s for the VCR and 6300 m/s for the BS. The velocities are, however, based on a best-fit velocity model that provided the most accurate depth converted volume. The interval velocities for the BS and the VCR were used for the conversion of the seismic data from time to depth domain and the resulting volume was calibrated with borehole data. Given a seismic reference datum of 1400 m, discrepancies between borehole data and seismic markers averaged ~150 m following conversion. These were accordingly adjusted to align with the prominent seismic markers, i.e. the VCR and BLR. UD12 was one of the boreholes used to correlate the positions of the VCR, BS, and the BLR (Figure 5.5).

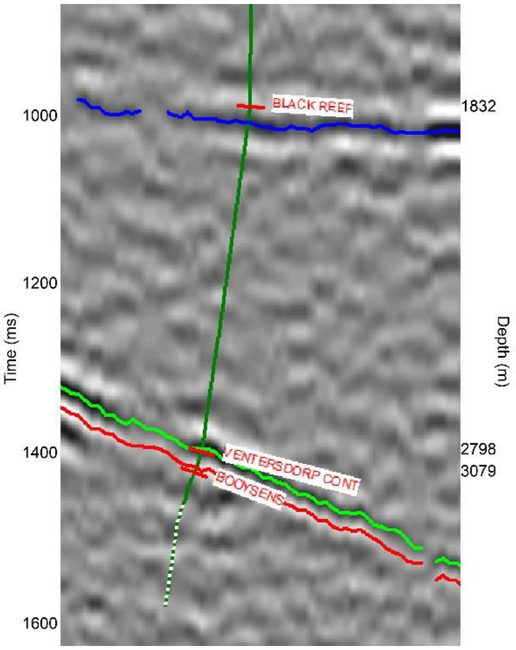

Figure 5.5: Borehole correlation of the time-to-depth conversion using borehole UD12.

5.3 The application of horizon-based and volumetric attributes

5.3.1 Horizon-based attributes

Fault and fracture characterization at the West Wits Line Goldfield is crucial in understanding the mechanisms and sources from which the methane identified at depth has migrated. A number of seismic attributes were used for structural analysis of the BS and VCR. The use of different seismic attributes increases confidence in the structural delineation and reduces the bias often associated with the interpretation of structural features in seismic data. The varied use of attributes also increases the reliability of the interpretation and allows for the interpretation of a range of different types of faults. For structural interpretation the dip and dip azimuth, edge-detection, and ant-tracking attributes were used.

The original, filtered but not smoothed BS and VCR horizons was imported into Petrel and edge-detection, dip and dip azimuth attributes were applied to them. As mentioned earlier, dip and dip azimuth are geometric attributes that are generally used as measures to reduce the S/N ratio while preserving discontinuities such as faults and unconformities in seismic volumes (Chopra & Marfurt, 2005). A full description of how dip and dip azimuth attributes work is given in Chapter 4.4.2.

5.3.2 Volumetric attributes

As previously stated, application of seismic attributes to the original 3D seismic data increases interpretation confidence. The ant-tracking attribute, in particular, improves the delineation of spatial discontinuities in a 3D seismic volume. This increases the confidence with which the interpreter can characterize the types, distribution, and orientation of subtle or complex faults within the seismic volume. The ant-tracking workflow is divided into four main parts namely, data conditioning, edge-detection, edge enhancement and interpretation (Khair, et al., 2012; Wang, et al., 2014).

Ant-tracking works well on conditioned data, where noise has been reduced using different filters. To improve the structural mapping resolution, dip-corrected and structural-oriented smoothing was applied to the 3D seismic volume using the Petrel software. Structure-oriented filtering reduces the artefacts created when attributes are extracted along vertical traces; therefore, the dip-guided with edge-enhancement filter option was chosen for these data (Hale, 2009; Petrel, 2015). This was done in consideration of the 20-25° average dip of the stratigraphy as well as to enhance faults with different orientations. Structural smoothing first computes the dip and azimuth of the data to determine local structure. Thereafter, the Gaussian filter, a filter that enhances faults, is then applied parallel to the orientation of the local structures, which reduces the noise and thus improves the quality of the data. The filter is applied in the x (σ_x), y (σ_y) and z (σ_z) directions. The parameters varied from filter sizes of 1.0, 1.5, and 2.0 for σ_x, σ_y, and σ_z, respectively, and represent the standard deviation of the Gaussian filter (Baytok, 2010). There was no significant change with a filter size of 1.0 compared to the original amplitude map. Setting the value at 2.0 smeared the edges of the smaller faults. A mid-value of 1.5

provided a good balance between noise reduction and the maintenance of structural integrity (Figure 5.6).

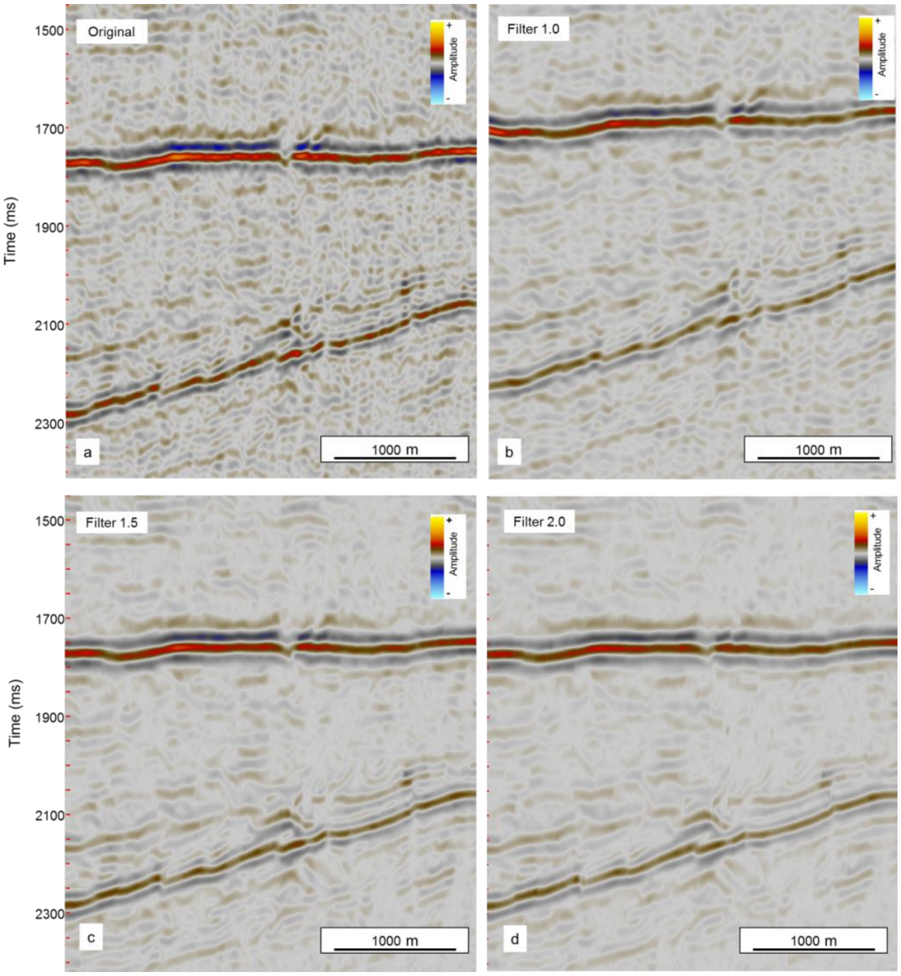

Figure 5.6: Amplitude display (a) with structural smoothing filter size of (b) 1.0, (c) 1.5, and (d) 2.0. The filter size of 1.5 (c) best preserves vertical resolution and enhances lateral continuity. There is also a significant decrease in noise at this filter size compared to the original amplitude display.

The edges in the data can be detected using variance and chaos measurements. Finding the most fitting variables to detect some edges was a process of testing different filter parameters and comparison between seismic attributes (Figures 5.7 and 5.8). For variance, two iterations were performed with the first run having an inline and crossline range of 3, vertical smoothing at 14 with dip correction on. On the other hand, the chaos attribute was tried with the filter sizes of 1.0, 1.5, and 2.0 for the x-, y- and z-directions, respectively, and 1.5 was found to be best suited for the data. Of the two edge-detection attributes, which are not vastly different in their output for these data, chaos with a filter size of 1.5 was best suited because it seemingly provided more structural detail.

Edge enhancement using the ant-tracking technique is achieved by distributing the ants within the chaos input volume. The final stage involves the extraction of surface segments and fault patches derived from the ant-tracking attribute (Randen, et al., 2001; Khair, et al., 2012). The ant-tracking attribute is poor when not coupled with other fault enhancing attributes such as variance and chaos. Variance coupled with ant-tracking provides high resolution mapping of major faults (Ngeri et al., 2015; Farghal & Zoback, 2014). Figure 5.8 is a schematic workflow of the ant-tracking process. The ant-tracking volume underwent two more runs (iterations) which enabled better fault identification, the results of which are detailed in Chapter 7.3.1 (Figure 5.9).

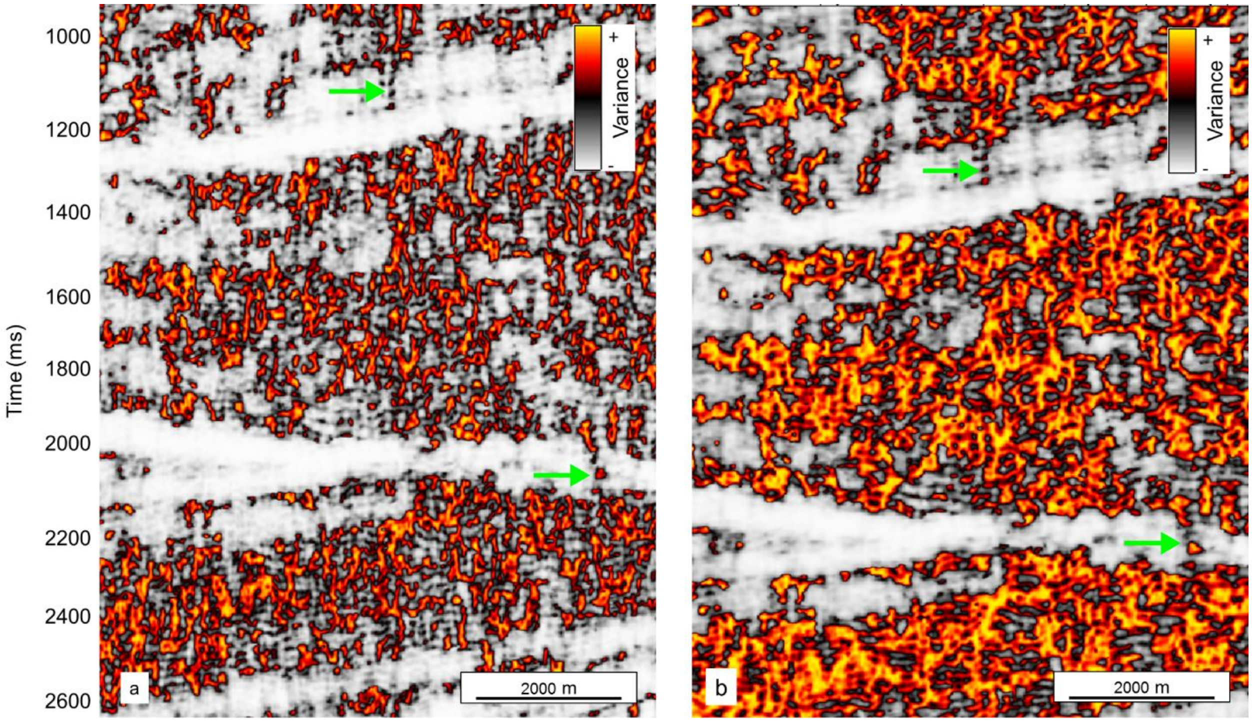

Figure 5.7: Variance attribute of a) 3-3-14, and b) 4-4-14 inline range, crossline range, vertical smoothing parameters used. It is evident that the 3-3-14 combination is better than

4-4-14 because more structural detail (green arrows) has been resolved using the 3-3-14 combination of values.

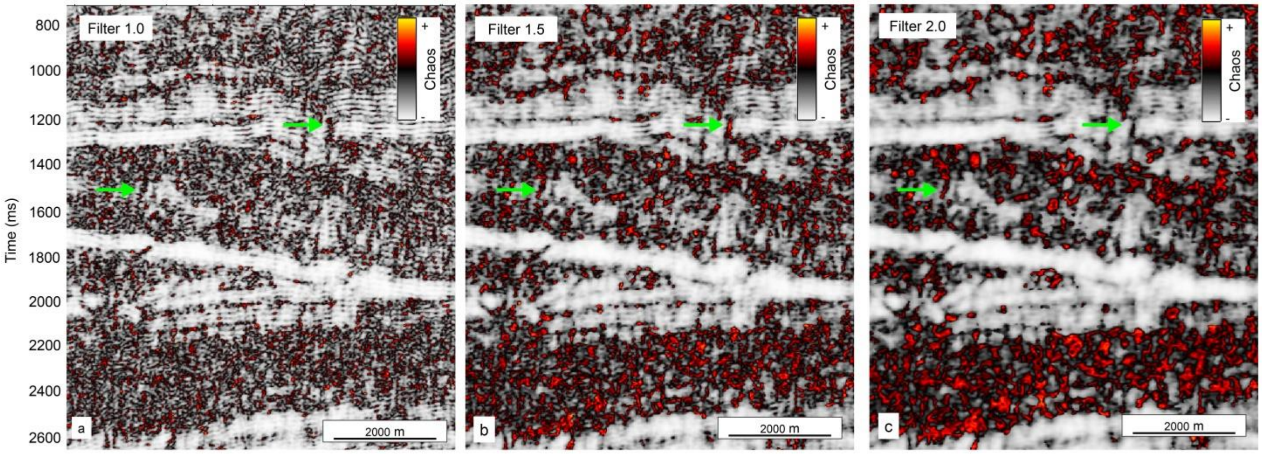

Figure 5.8: Chaos attribute using filter sizes a) 1.0, b) 1.5, and c) 2.0. A filter size of 1.5 was chosen. The green arrows indication the resolution of faults from one filter size to the next.

The ant-tracking attribute was iterated three times to assess optimal conditions. Several boundary parameters were set for the ants. The definitions of these parameters are tabulated below (Table 5.1). A stereonet filter may be used to filter out unwanted seismic events such the acquisition footprint and processing artefacts. This is done by limiting the dip and azimuths in which the ants can track (Baytok & Pranter, 2013). The stereonet filter, however, was not applied to the seismic data in order to detect not only vertical but also lateral discontinuities as well. The effects of not applying the filter are described in Chapter 7.3.

Table 5.1: The parameters and functions of those parameters used in creating the ant tracked volume.

Parameter	Function
Initial ant boundary	Defines the initial distribution of agents by putting a territorial radius around each agent.
Ant-track deviation	Controls the maximum allowed deviation of each agent from a local maximum as it tracks.
Ant step size	Defines the number of voxels an agent advances for each

	increment within its searching step.
Illegal steps allowed	Defines how far an agent’s track can continue without finding an acceptable edge value.
Legal steps required	Defines the extent of connectivity of the detected edge to distinguish it from the noise.
Stop criteria	Defines the percentage of illegal steps allowed through a single agent’s life.

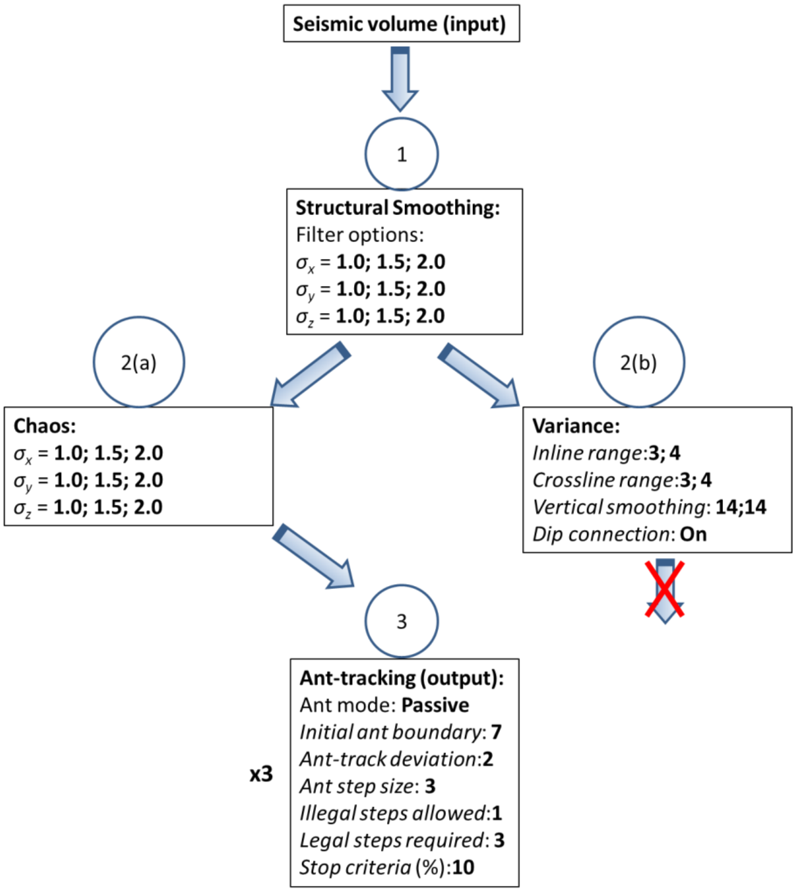

Figure 5.9: The ant-tracking workflow with the four main steps (structural smoothing, variance, chaos, and ant-tracking) as well as the parameters used at each step. Both variance and chaos were run for edge-detection but only the chaos volume was used as the input for the ant-track volume.

6. SCIENTIFIC CONTRIBUTIONS

6.1 Authorship Statement

The following chapter presents one of the research questions of this study. Chapter 6.2 gives details of the work done by the candidate as well as summary of the publication.

6.2 Manuscript

Mkhabela, M., Manzi, M. 2017. Detection of potential methane gas pathways in deep South African gold mines. **Published.** *Journal of Geophysics and Engineering.* ***14,*** *pp. 960-974*

The candidate was responsible for the following:

- Loading the 1995 Western Ultra Deep Levels (WUDLs) 3D seismic data in the SEGY format into the IHS Kingdom Suite seismic interpretation software using the LO27 (Cape Datum) South African coordinate system.
- Uploading a culture file of the mines of the West Wits Line Goldfield.
- Modifying and creating a base map that included only the mines of interest in the goldfield.
- Identifying and picking of the Booysens Shale (BS) and Ventersdorp Contact Reef (VCR) horizons on the western portion of the 3D seismic survey. This was done in both inline and crossline sections.
- Data conditioning which entailed the smoothing and filtering of the horizons in preparation for the application of seismic attributes.
- Applying the complex trace attributes, instantaneous phase, instantaneous frequency, and envelope to the BS horizon and reporting the results.
- Exporting the conditioned horizons from the IHS Kingdom Suite software to the Petrel seismic interpretation and modelling software.

- Applying the dip, dip azimuth, and edge-detection horizon-based attributes on the gridded horizons, the BS and VCR horizons.
- The interpretation of the Pretorius Fault including 1) mapping its vertical displacement (throw) as well as 2) the orientation of the fault.
- The interpretation of other structures identified from the application of seismic attributes.
- Creation and editing of all imagery was carried out by the candidate.
- Reporting and interpretation of the results was done by the candidate and the supervisor; Dr. Musa Manzi assisted by giving pointers regarding scientific writing where necessary.
- Dr. Musa Manzi also assisted in the journal selection process, procedures for uploading the manuscript and gave insight on the journal review process.

6.3 Summary of publication

At a number of gold mines in the South Africa, the presence of methane gases has been encountered when drilling into faults and/or dyke structures extending to depths beyond 7000 m. Methane gas is reported to migrate up through structures from within the basin to the mine working environments (~3000 m depths) and cause explosions. The Booysens Shale is considered one of the possible source rocks for hydrocarbons and it forms the footwall to the gold-bearing Ventersdorp Contact Reef (VCR, ~ 1.5 m thick). The Booysens Shale is a 65-125 m thick (thickens towards the west) argillaceous stratigraphic marker that is prevalent throughout the Witwatersrand Basin. This work was a first-hand opportunity to apply seismic attributes (instantaneous and geometric) on prestack time-migrated data to determine:

- The seismic character of the Booysens Shale.
- Structures propagating between the Booysens Shale, a possible source of hydrocarbons in the Witwatersrand Basin and methane found at mining levels, i.e. the VCR.

The instantaneous attributes included phase, frequency, envelope and the geometric attributes applied were dip, dip azimuth, and edge-detection. These attributes were computed for the Booysens Shale and Ventersdorp Contact Reef horizons. These attributes successfully mapped the sub-crop position of the Booysens Shale against the Ventersdorp Contact Reef and structures (faults and dykes) that have displaced both the Ventersdorp Contact Reef and Booysens Shale horizons. The edge-detection attributes were particularly useful in delineating faults with throws below the traditional seismic resolution criteria (e.g., a quarter of the dominant wavelength) that were not visible in the conventional seismic interpretation. The structural analysis of the Booysens Shale and Ventersdorp Contact Reef using seismic attributes gives a new visual representation of geological structures that may be probable conduits for hydrocarbons, particularly methane, migrating from depth to mining levels.

The paper is presented according to journal article standards.

Detection of potential methane gas pathways in deep South African gold mines

Mbali Mkhabela[1], Musa Manzi[1]

1. School of Geosciences, University of the Witwatersrand, Private Bag 3, 2050 Wits, South Africa

mbali.mkhabela@students.wits.ac.za; musa.manzi@wits.ac.za

ABSTRACT

At a number of gold mines in South Africa, the presence of methane gases has been encountered when drilling into faults and/or dyke structures extending to depths beyond 7000 m. These have been reported to have migrated up through structures from within the basin to the mine working environments (~3000 m depths) and caused explosions. The Booysens Shale is considered one of the possible source rocks for hydrocarbons and it lies beneath the gold-bearing Ventersdorp Contact Reef (VCR, ~ 1.5 m thick). The Booysens Shale lies at depths between 3500 m and 4500 m below the surface and can be best described as a base of the divergent clastic wedge, hosting the quartzite and conglomerate units that sub-crop against the VCR towards the west of the gold mining areas. Geometric attributes (dip and dip azimuth) and instantaneous attributes (phase, frequency and envelope) computed for the Booysens Shale and Ventersdorp Contact Reef horizons interpreted from 3D prestack time migrated data, acquired for gold exploration, provide insight into structures that extend from the Booysens Shale into the overlying mining level (i.e. Ventersdorp Contact Reef). These attributes successfully mapped the structures (faults and dykes) that have displaced both the Ventersdorp Contact Reef and Booysens Shale horizons. The edge-detection attributes were particularly useful in delineating faults with throws below the traditional seismic resolution criteria (e.g., a quarter of the dominant wavelength) that were not visible in the conventional seismic interpretation. The structural analysis of the Booysens Shale and Ventersdorp Contact Reef using seismic attributes gives a new visual representation of geological structures that may be probable conduits for hydrocarbons, particularly methane, migrating from depth to mining levels.

Keywords: Booysens Shale, Ventersdorp Contact Reef, Seismic Attributes, Witwatersrand Basin, Hydrocarbons

INTRODUCTION

The Witwatersrand Basin hosts some of the largest and deepest gold mines in the world. The gold derived from the Witwatersrand Basin is extracted from narrow, tabular conglomerate placers termed “reefs.” These reefs vary from a few centimetres to up to 5 m in thickness and are mined at depths of between 500 m and 4200 m below the surface of the Earth (Safonov and Prokof'ev 2006, Viljoen 2009). The Ventersdorp Contact Reef (VCR) is one of the most economically significant auriferous conglomerates in the basin. Until the late 1980s, geological and mine models were largely based on underground mapping and exploration drilling. The acquisition of the first 3D seismic reflection surveys in 1980s in the Witwatersrand Basin provided new, enhanced means of mapping these reefs, which ultimately created more reliable geomodels for exploration and mine development. The 3D seismic reflection method has since played an integral role in gold exploration, mine development, and safety in the basin. In 1995, AngloGold Ashanti Ltd. acquired 3D seismic data covering the Western Ultra Deep Levels (WUDLs) mining district of an area of approximately 300 km^2. The survey successfully imaged key horizons in the region, particularly the VCR and Black Reef (BLR) (Jolley *et al* 2004, Pretorius *et al* 2006, Dehghannejad *et al* 2012, Manzi *et al* 2012a, 2012b, 2014 and 2015, Ahmadi *et al* 2013, Malehmir *et al* 2014). The strong, continuous reflection associated with the VCR, is a result of an acoustic impedance contrast between the quartzites of the Central Rand Group and the overlying flood basalts of the Klipriviersberg Group. The quality of the seismic data made it possible to study the form and extent of the auriferous conglomerate bed (and other economic reefs such as the BLR). These data have since been used to extend the geological model for use in current and future mine development (Gibson 2000, Manzi *et al* 2013, 2015).

A significant amount of methane gas has been encountered in some of the gold mines in South Africa (Cook 1998; du Plessis and van Greuning 2011, Breytenbach 2016).

The methane, which emits from deep-seated sources within geological features such as faults, fissures, and dykes, is unlocked during normal mining operations and released into the mining levels (e.g., VCR horizon) where it causes explosions. The gas is a major safety hazard underground and despite continuous efforts to keep methane levels under control, methane explosions have occurred in numerous mines in the region and caused a series of injuries and deaths.

Faults also act as conduits for the migration of water and methane gas to the mining levels (Cook 1998; Manzi *et al* 2012a, Wanger *et al* 2012). The intersection of faults, and particular those that are prone to fluid transmission, affect the productivity of a mine and the safety of mine personnel, and can lead to substantial financial shortfalls for the affected mine. Thus, fault delineation using the seismic reflection method becomes an integral part of ensuring mine development and extending the life of a mine.

Several authors (Gray *et al* 1998, Spanenberg and Frimmel 2001, England *et al* 2002) largely attribute the sources of methane to carbon seams of algal mats deposited concomitently with placer development in the basin as well as to inter-basinal shales such as the Booysens Shale (BS) underlying the VCR. This shale unit, considered a possible hydrocarbon source rock, varies in thickness and is pervasive throughout most of the basin. The proposed general idea is that methane migrates from the source to mine workings through faults and fractures as a gas or dissolved in saline ground water (Cook 1998, Baldassare *et al* 2014).

Source rocks for hydrocarbons are described as fine-grained sedimentary rocks that contain carbon and hydrogen-rich matter such as the shales of the Witwatersrand Basin. A study by Gray *et al*. (1998) on the nature and origin of 'carbon' in the Witwatersrand Basin revealed the BS was a likely source of hydrocarbon in the basin. The authors pointed to TOC (Total Organic Carbon) values characteristic of a post-mature hydrocarbon source rock. They also identified microscopic pyrobitumen particles in the BS that were interpreted as residual liquid hydrocarbons retained in the source rock. In addition to this, hydrocarbon fluid inclusion, microscopy and spectrometry studies confirm the theory of basin-derived hydrocarbons (Spanenberg and Frimmel 2001, England *et al* 2002, Wanger *et al* 2012).

The BS is also truncating the VCR, the distance between the two horizons increasing from the east to the west. The thickness (65 to 125 m) of the BS, as well as its considerable acoustic impedance contrast with the surrounding quartzite and conglomerate units, make it a strong seismic reflector.

The purpose of this study is to map geological structures (faults and dykes) intersecting the VCR mining level and the underlying BS using instantaneous and geometric attributes. Various seismic attributes (e.g., edge-detection, dip and azimuth attributes) have been used to enhance the detection of faults and fault continuity that affect mine safety and productivity in the Witwatersrand goldfields (Stuart *et al* 2000, Manzi *et al* 2012b, 2013). Instantaneous attributes have previously applied to other datasets acquired in the Witwatersrand Basin as is in Stuart *et al*. (2000) and Manzi *et al*. (2013). It is, however, a first-hand attempt at applying these attributes to the shale unit as mapped in the time domain data of the 1995 WUDLs 3D seismic volume.

The horizon-based attributes include instantaneous phase, instantaneous frequency, and envelope. They have been applied to the BS as an initial attempt to determine the effectiveness of the attributes to delineate structural and stratigraphic features. Dip, dip azimuth, and edge-detection attributes were then applied to both the BS and VCR to delineate and compare structures that propagate between the two horizons that may act as conduits for fluid migration from the hydrocarbon source (BS) to mining level (VCR). The mapping of these structures is critical for the mines as they may provide migration pathways for methane gas from BS to the mining levels (VCR) and/or represent losses of mineable ground and potential safety hazards. They may also cause instabilities in the hanging wall leading to poor ground conditions.

The study further demonstrates how recent improvements in seismic attributes can enhance the detection of subtle faults (with throws less than ~25 m) that fall below the traditional seismic resolution limits. In terms of exploration, the detailed interpretation of the BS will enable mines in the West Wits Line Goldfield to better understand the structural framework of the mining area at depths between 3500 m and 4500 m below the surface. This will result in a coherent model for further development of the region and some indication of the prospectivity of unmined ground.

STUDY AREA

The mines investigated in this study are located in the central and western parts of the West Wits Line Goldfield, which lies on the northern end of the Witwatersrand Basin (figure 1). Mponeng gold mine is located approximately 65 km west of Johannesburg and, along with Savuka and TauTona gold mines, forms part of the West Wits Operations operated by AngloGold Ashanti. This mine, the deepest in the world, makes use of a twin-shaft system to mine the Carbon Leader Reef (CLR) and VCR at depths between 2800 m and 4200 m. The WUDLs lies south of Mponeng and is currently under exploration and development (AngloGoldAshanti 2014, Manzi *et al* 2015). The Kusasalethu gold mine, operated by Harmony Gold (Ltd.). It is located 90 km southwest of Johannesburg and lies west of the Mponeng gold mine. This mine comprises two vertical shafts, a rock/ventilation and man/material shaft, as well as two sub-vertical rock/service and ventilation shafts. Mining of the VCR occurs between 2200 m and 3300 m below the Earth's surface (Handley *et al* 2000, Harmony 2014) (figure 2).

THE GEOLOGY OF THE WEST WITS LINE GOLDFIELD

The Archaean Witwatersrand Supergroup is a 300 km by 200 km wide, 7000-8000 m thick meta-sedimentary basin. It was deposited between 2985 and 2849 Ma. The basin is divided into the lower West Rand Group and Central Rand Group and is exposed along the northern and western margins of the basin. The lower West Rand Group comprises shale and quartzite units deposited in fluvio-deltaic and shoreface to offshore environments that are also comprising the basaltic andesite of the Crown Formation (Stanistreet and McCarthy 1991, Coward *et al* 1995, McCarthy 2006). The upper Central Rand Group, deposited between 2894 and 2714 Ma (Robb and Meyer 1995), is approximately 2800 m thick towards the centre of the basin, and is divided into the Johannesburg and subsequent Turffontein Subgroups. The Johannesburg Subgroup is characterised by alternating quartzite and conglomerate units deposited in a fluvial braid-plain environment. The BS, which overlies the Johannesburg Subgroup, is a laterally extensive argillaceous stratigraphic marker that extends throughout most of the Witwatersrand Basin.

The BS horizon has an approximate age of deposition of 2894 ± 7 (Kositcin and Krapez 2004) marks the transition from the lower Johannesburg Subgroup to the overlying Turffontein Subgroup, a time of basin-wide subsidence. Described as a thick, interbedded mudstone and siltstone meta-sedimentary package, it represents one of the transgressive sequences deposited during Central Rand deposition. The BS dips towards the south-east, ranging in thickness between 65 and 125 m from the east towards the west in the study area (Carstens 2007, Myers *et al* 1992). The BS and Turffontein Subgroup, underwent deformation, tilting and erosion, followed by the deposition of the VCR (Manzi *et al* 2013). The thickness of the BS and the acoustic impedance (the product of density and seismic velocity) contrast between the BS (~2.83 g/cm^3 and ~6300 m/s) and the overlying quartzites (2.75 g/cm^3 and 5899 m/s) makes it a strong seismic reflector (Gibson *et al* 2000, Manzi *et al* 2015) (figure 3).

The VCR, unconformably underlain by the Central Rand Group, is mined throughout the northern collar of the Witwatersrand Basin. The VCR, deposited approximately 2729 Ma, dips at an angle of 20-25° to the southeast with a strike of approximately 072° east. It conformably underlies the basaltic rocks of the overlying Klipriviersberg Group. The acoustic impedance contrast at the interface between the high-velocity, dense ultramafic lavas (6457 m/s, 2.98 g/cm^3) of the Ventersdorp Supergroup and low-velocity, less dense quartzites (5899 m/s, 2.75 g/cm^3) of the Central Rand Group creates a strong seismic reflector that correlates with the VCR horizon (Tankard *et al* 1982, Pretorius *et al* 1997, Gibson, 1997).

STRUCTURAL SETTING

The West Wits Line Goldfield underwent multiple phases of extensional and contractional tectonics. This is evident in the structural complexity of the mining region (Coward *et al* 1995, Dankert and Hein 2010, Manzi *et al* 2013).

Sediments of the West Rand Group were deposited on a post-rift thermal sag, in a tectonically stable environment that was preceded by Dominion-age rifting. Thrust tectonics affected the upper part of the West Rand as well as the Central Rand Group and have been related to the development of a foreland basin and associated north-western-trending hinterland. In the West Wits Line region, sediment deposition of the Central Rand Group was influenced by the Rand Anticline to the north and the Bank Fault to the east (Coward *et al* 1995, Gibson *et al* 2000). Sustained uplift of the anticline resulted in the deformation and tilting of the Turffontein Subgroup and BS alongside the western limb of the fault. This was truncated by the deposition of the VCR, forming a gently dipping angular unconformity between the Turffontein Subgroup and BS, and the VCR.

Structural deformation has a significant effect on reef continuity. Up -or downthrown fault blocks, as well as dyke and sill intrusions, result not only in reduced mine productivity but also adversely affect the safety of mine personnel and mine development. The goldfield is also intersected by a number of sills and dykes of different periods of tectonism in the basin. The ages of these structures span from Ventersdorp (2.6 Ga) to the Transvaal (2.20 Ga), Pilanesberg (1.30 Ga) and Karoo volcanic events (150 Ma) (McCarthy 2006, Litthauer 2009).

3D REFLECTION SEISMIC DATA

In 1995, AngloGold Ashanti acquired one of the world's largest 3D reflection seismic surveys in the mineral industry (Pretorius *et al* 1997, Manzi *et al* 2015). The survey covers an area of approximately 300 km^2 of the West Wits Line Goldfield (figure 2). The survey was acquired by Compagnie Générale de Géophysique (CGG) and processed by Manzi *et al*. (2012a). The seismic data were initially acquired to give a better understanding of the extent and prospectivity of the most economic gold-bearing reefs (VCR and CLR) in the region. The pre-stack time-migrated seismic cube extends from 0 to 6 s two-way time (TWT) (~0-12 km). The acquisition survey was designed to image reefs and geological structures as deep as 4500 m below the surface of the Earth. The signal-to-noise ratio of the data was improved by using a fold coverage of 36, which is more than twice the amount used in the historical surveys. The data are of good quality and efficiently imaged the main reflectors, which are mostly unconformities separating the major stratigraphic units in the Witwatersrand Basin (figure 4a). The use of prestack time migrated data are particularly useful for the application of instantaneous seismic attributes. The advantage of using PSTM data is that they preserve relative amplitudes as a function of time. They are good in areas with little lateral velocity variations and steeply dipping strata, and are less susceptible to noise in comparison with depth-converted pre-stack time-migrated data (Schulte 2012, Marfurt and Alves 2015).

The dominant frequency of the WUDLs data is approximated at 65 Hz and a mean velocity of 6500 m/s has been determined during processing. Using the wave equation ($\lambda = v/f$) the dominant wavelength would be ~100 m, and a quarter of that, 25 m. This wavelength (25 m) is the minimum throw that can be resolved in seismic section using conventional interpretation tools. Gibson *et al*. (2000) have, however, proposed that faults with vertical displacements of down to 18 m can be delineated within the WUDLs seismic dataset because of its high signal-to-noise ratio (SNR). The use of seismic attributes may further enable more detailed structural interpretation with the lowest detected throw being down to 5 m (Manzi *et al* 2013, 2015).

SEISMIC ATTRIBUTES

The application of seismic attributes has a long-standing history in the delineation and enhancement of fault and fracture systems within the oil and gas industry. The use of instantaneous attributes (envelope, phase, and frequency) is defined by complex seismic trace analysis (Taner *et al* 1979). Envelope (also described as the reflection strength) is the square root of the sum of the squares of the complex and imaginary elements. It is sensitive to changes in the acoustic impedance and is hence a good indicator of changes in lithology, the presence of the fluids (gas, oil, and water), and porosity. Instantaneous phase is best for tracking the continuity of the reflector. The changes in the phase (measured in degrees ranging between -180° and 180°) along a horizon is a good indicator of the lateral continuity of stratigraphic horizons. Instantaneous frequency is described as the rate of change of the phase and sensitive to bed thickness and changes in lithology (Taner *et al* 1979, Robertson and Nogami 1984).

Dip and azimuth attributes (knows as geometric attributes) are the function of the variability in inclination and the direction of the inclination, respectively, of the time gradient from trace to trace, i.e. they are calculated for each sample of the horizon grid. Dip and azimuth attributes are useful tools in identifying subtle faults' crosscutting relationship and continuity (Dalley 2008). The edge-detection attribute, on the other hand, combines the variations in dip and azimuth that are normalized to the local noise of the interpreted horizon grid (Manzi *et al* 2012). The use of the edge-detection attribute analysis requires seismic data that has a high SNR. It enhances the detection of the slightest variations in the signal amplitudes. Colour plays an integral role in dip, azimuth, and edge-detection displays, giving an almost intuitive representation of information about the orientation and continuity of a horizon (Zhu *et al* 1999, Randen *et al* 2001, Dalley 2008).

METHODOLOGY

The BS and VCR horizons were interpreted using both 3D auto-picking and manual picking. Manual picking was used where the continuity of the horizon could not be easily tracked due to the low quality of the data, particularly in the faulted areas and at the edges of the survey area. The low SNR at the edges of the survey is attributed to low fold of coverage. Instantaneous attribute analysis was computed for the BS horizon, and the edge-detection, dip and dip azimuth attributes were computed for both the BS and VCR. The BS was picked on every single inline and crossline, as well as on time slices to enable the detail picking of geological features.

Seismic sections were initially interpreted at wide-line spacing, i.e. every tenth crossline and inline of the 3D volume (figure 4*a, b*). This was done in order to map major scale structures. Once a wide grid of picks was completed, infill picks were made at close line spacing which, enabled detailed structural interpretation. The BS horizon (covering an area of approximately 14.5 km x 7.6 km) was divided into Block

A, which covers the Mponeng/Western Ultra Deep Levels mine area, and Block B, a portion of the Kusasalethu and Deelkraal mines (see figure 1 and 2). Picking was mostly restricted to the central part of the survey because of the deterioration in the quality on the southern end of the survey area due to low fold of coverage. The position of the BS was constrained using borehole data that had intersected both the BS and the VCR horizons. Seismic event discontinuities were manually picked as faults. The completed horizon was then gridded using Kriging method and contoured at 25 m, thus providing a time structure map (figure 5). Subsequently, seismic attributes were applied on the gridded horizon to enhance seismic interpretation. Prior to the application of the edge-detection attribute, mean and median filters were applied to the horizons in order to suppress random noise without smearing faults and stratigraphic edges in the data (Chopra, 2011). These attributes were applied to both VCR and BS horizons to identify faults and fracture systems that have propagated between both horizons.

RESULTS

Conventional Interpretation

The BS is mapped as a strong seismic reflector and can be identified and tracked throughout the 3D seismic cube (figure 4*(a)*, *(b)*, and figure 5). Seismic interpretation was constrained using the surface and underground boreholes drilled at approximately > 1 km spacing. On average, boreholes drilled from underground had a good tie with the VCR and BS reflectors, although the VCR at some depths is slightly deeper than the actual depths of the borehole formation tops. The depth discrepancy between the seismically mapped reflectors and borehole positions is approximately 25-50 m (0.0125 – 0.025 s). A time structure map produced through conventional interpretation shows that the horizon spans time interval of 1.4 to 3.4 s, increasing in a southwesterly direction. The faults picked on the map can be arbitrarily divided, according to continuity, into three categories: primary, secondary, and tertiary faults. The primary fault, the Pretorius Fault (PF), extends for approximately 11.5 km in the study area and has a strike of approximately 045° towards the northeast. It is, in some instances, intersected by secondary and tertiary faults that trend in the north-westerly and north north-easterly directions, respectively (figure 5). The PF is a well-documented fault in the West Wits Line Goldfield (Manzi *et al* 2015). An inline seismic section (figure 6*(a)*) through the PF (labelled A-B in figure 5) shows that the PF displaces both the BS and VCR. The normal fault displaces both horizons by an apparent time difference of 0.007 s and 0.005 s, respectively. The section also shows that there are other faults at the footwall and hanging wall of the PF that displace the two horizons, and in some instances, only the BS.

The throw of the PF along its length is not uniform. In order to understand the variability of the throw along this major fault and how the BS is affected by this variability, a throw profile along the PF was plotted (figure 6*(b)*). The profile showed that throw along the structure ranged between 0.0205 and 0.1255 s, increasing from northeast to the southwest. There are some instances along the fault profile where the fault throw values dropped drastically. These drastic drops divide the profile into three segments and they occur at the 250m, 3500 m and 6500 m distances. The major variability of throw along the strike of PF indicates that the fault underwent a complex deformation history. This also shows that PF is not a single fault, but it is made up of a number of subordinate normal fault networks.

Instantaneous Attributes

Instantaneous attributes were applied to the BS horizon to detection subtle geological features or sub-seismic faults. Prior to the application of the seismic attributes, the BS horizon was smoothed using different structural smoothing filters (e.g., median, mean and Laplacian filters) in order to eliminate noise and increase the SNR of the horizon. This enabled the detection of structures not previously seen on the time structure map. Figure 7*(a)* is the instantaneous phase map computed for the BS surface covering the Block A region. The instantaneous phase map has identified a number of subtle linear features that were clearly invisible on the time structure map (see figure 5). The most dominant feature mapped on the phase attribute, not readily seen on the structure map, is a distinct north-northeast trending linear feature near the eastern edge of the survey. This feature is characterised by a distinct positive to negative phase response and it is interpreted as the sub-crop position of the BS against the VCR (see figure 4*(a)* and *(b)*). The reason for the poor mapping of sub-crop position by the amplitude attribute is due to severe destructive interference resulting from overlapping wavelets between the overlying VCR and the BS reflectors, and because the thickness between the BS and VCR approaches zero, which is below the seismic resolution limit.

Although the instantaneous phase, an amplitude-independent attribute, successfully highlighted the BS sub-crop position against the VCR, the continuity of the sub-crop could not be tracked with high confidence owing to the sensitivity of instantaneous phase to noise. There are a couple of reasons why the mapping of the sub-crop position is important for mining purposes**:** (1) the gold grade on the VCR horizon is lower at the position where it intersects the shale units, and (2) if the shale unit is the source of methane gas at the mining levels (i.e. VCR level), the sub-crop position is where the shale layer is closest to the VCR horizon (i.e. the vertical separation between the BS and VCR is almost zero).

To further enhance detection of the sub-crop position, we computed the instantaneous frequency for the BS horizon (figure 7*(b)*). This attribute provides a degree of continuity along the length of the sub-crop position, which was not identified by the phase attribute. On the frequency map, the sub-crop position is a clearly defined feature, characterised by a decrease in frequency (from approximately 12.8 to 10.4 Hz) on the surface. Like all the derivative maps, instantaneous frequency is very sensitive to noise associated with low amplitude anomalies, as shown in figure

7*(b)*. Instantaneous frequency is more chaotic and exhibits less continuous signatures than amplitude map, particularly in most structurally complex areas.

Seismic attributes computed for the BS horizon in Block B reveal a greater degree of structural variability compared to Block A, which is less structurally complex. In Block B, most of the subtle faults (less than 25 m throws) detected in the phase map are not clearly mapped by the frequency attribute. Lineaments trending in the northwest-southeast directions can also be traced along the BS horizon throughout the block (figure 8). The black arrows demarcate a northeast-southwest trending structure that is most prominent on the instantaneous frequency map. This structure is more pronounced and marked by a low-frequency signature (figure 9*(a)*). A section through the linear feature affirms the existence of a low-angle thrust dipping towards the northwest at angles between 10-15° detaching from the BS as seen in figure 9*(b)*. The fault becomes undetectable as we move along strike in the time structure map, but the instantaneous phase and frequency displays clearly show the extent of the thrust fault. This further confirms that the instantaneous attributes can enhance the detection of the subtle faults that cannot be mapped by conventional amplitude interpretations.

Comparing Blocks A and B, the envelope (reflection strength) attribute (figure 10) successfully identified the variability in the acoustic impedance response of the BS with the surrounding rocks. The attribute is sensitive to variations in the amplitude due to acoustic impedance contrasts between the target and the host rock and is, in this study, useful in identifying areas such as mine stopes where there is a significant difference in acoustic properties between the mined-out areas and surrounding solid rock. Block A exhibits two distinct features: the sub-crop position and high amplitude anomaly labelled as bright-spot in Figure 10. There is no mine infrastructure data available at present to verify whether the high seismic amplitude anomaly could represent the shaft or mine stope position.

Inline 1088 in Block B is predominantly characterized by complex reverse faulting, thus confirming the existence of structural complexity mapped on the envelope attribute map. Faulting appears to have propagated between the VCR and BS horizons (figure 11*(a)*). A seismic section (inline 1534) across Block A provides further evidence for the close proximity of the BS to VCR (figure 11*(b)*).

Structural propagation between BS and VCR

In order to further enhance the mapping of minor faults that crosscut the BS and VCR, geometric attributes such as dip and dip azimuth attributes were applied to both horizons (figure 12). These attribute displays provide much better information about the connectivity and continuity of the structures when compared to instantaneous attributes.

According to dip and dip azimuth maps, the BS and VCR have an average dip of about 20° towards the southeast across the survey areas. The dip and dip azimuth attributes computed for VCR and BS horizons show a high-resolution delineation of normal faults that have dips between 60° and 85° and reverse faults with dips no greater than 40° (figure 12*(a)*-*(d)*). These faults have been mapped with high confidence at both VCR and BS levels, providing evidence for the possible methane gas pathways between the BS and the VCR mining level. Outstanding examples of fault networks that have propagated between the two horizons include the PF, K1, K2, T1 and T2 faults. The PF is a major, northeast trending normal fault zone (with a maximum throw of ~ 0.1275 s) that cuts through the central vicinity of the study area. PF is also well mapped on the time structure map, owing to its major vertical displacement. The K1 and K2 fault zones, on the other hand, are small northwest trending normal faults with throws up to 0.025 s that truncate the PF southwest of the map (figure 12*(a)*-*(d)*). These two faults were not well mapped on the conventional interpretation maps due to their throws that are approaching the vertical seismic resolution limit (25 m or 0.0125 s). Most interestingly, these attributes have demonstrated a degree of structural complexity that was not observed with conventional interpretation. For example, these maps show that the PF crosscuts the T1 fault demonstrating that the fault system pre-dates the PF. The crosscutting relations indicate that methane gas may be transported from one fault system to the other, if and only if these structures are open and are prone to gas migration. This type of structural connectivity and crosscutting relationship was not revealed on the instantaneous attribute maps (see figures 7 to 10). Although the relation of the T1 and PF can be seen on both the dip and dip azimuth maps of both horizons, the fault intersection is best illustrated in the dip map of the VCR (figure 12c). This may imply that these faults have displaced the VCR with relatively higher vertical displacements than the BS horizons. This demonstrates that the dip azimuth map shows a better degree of structural continuity and connectivity than the dip maps. This is probably because these faults have apparent dip directions that are different to that of the horizons (Zhu *et al* 1999, Randen *et al* 2001, Dalley, 2008).

To further enhance the detection of subtle faults that crosscut both VCR and BS, we gridded the surfaces and computed the edge-detection attributes. Edge-detection maps exhibit a series of northeast trending faults with significantly low throws that could not be mapped by both dip and azimuth maps (figures 13 and 14). Most importantly, the inter-connectivity nature of these faults, as observed on the edge-detection attribute maps, suggests that they were active after the deposition of the VCR and BS horizons. Generally, edge-detection attributes have provided a delineation of subtle faults that fall below the seismic resolution limit (0.0125 s). Their effectiveness was enhanced through the smoothing of the horizon using low-pass filters such as the combination of mean and median filters to remove noise introduced during manual picking. However, there are still areas that are characterized by the low SNR, particularly at the edges of the surveys. The effects of structural complexity and the deterioration in the seismic resolution of the horizon are also more evident in most of the southern and southwestern parts of the study area. This could be due structural complexity and low fold of coverage in these areas. In the northern areas, the low SNR could be due to dolomite outcrop that hampered the seismic acquisition. Overall, the amount of structural detail that the edge-detection attribute offers is significantly greater than the dip, dip azimuth, and conventional interpretation. The detection of the vertical structural continuity, in particular, between the VCR and BS horizons has been greatly enhanced.

DISCUSSION

In this study, we have applied seismic attributes to old high-resolution 3D seismic data to: (1) enhance detection of subtle faults and (2) understand methane gas migration pathways between a hydrocarbon source rock (BS) and the mining levels (VCR) in deep gold mines of the Witwatersrand Basin. Although the VCR had been identified and interpreted in seismic data before (Manzi *et al* 2014), the detailed seismic interpretation of the BS using instantaneous attributes is reported here for the first time. Results attained from the use of seismic attributes for structural interpretation illustrate the advantages of using more than one attribute to derive information from a chosen horizon.

One of the key points of the study is that most subtle faults observed on the seismic sections across the survey areas do not appear to crosscut both BS and VCR horizons. However, seismic attribute maps demonstrate that these faults have throws below the vertical seismic resolution to be detected and tracked on the seismic sections. Further analysis on the attributes shows that these faults crosscut and offset the VCR and BS horizons by throws as small as 5 m. At major scale, the seismic data show the mapping of one dominant northeast trending structure, PF, which crosscuts and offsets the VCR and BS horizons with variable throws (~ 0.01 - 0.125 s). Our interpretation of this fault concurs with conclusions made by Gibson *et al*. (2000) that reduction in the throw along the plane indicates the intersection of the fault with other sub-vertical subordinate structures. Most of the fault segments emanating from the PF zone are cataclasitic and have been linked to fault reactivation in the Pretorius fault zone. The geometry, depth positions, and apparent dips of some of these structures have been confirmed by underground mapping and drilling (Dankert and Hein 2010). Future mine development plans may need to be updated to consider these new structural parameters, since this horizon is proximal to commercial gold deposits (namely the VCR).

At a minor scale, seismic attributes have enhanced the detection of subtle faults that displace the BS horizon and VCR with throws far below the seismic resolution limit. This information derived from seismic attributes introduces a novel representation of the interconnectivity of faults between the two horizons, but most importantly, the possible upward migration of methane gas to the mining levels. Instantaneous phase, instantaneous frequency, and envelope delineated structural features that were not previously identified by conventional interpretation. Structural definition and stratigraphic changes were largely dependent on the quality of the seismic data. Of the three complex trace attributes, the low SNR areas had the most significant effect on the phase and frequency displays. Noise in the data affects the seismic attribute output, which may result in poor quality and reduced reliability in seismic interpretation. In the instantaneous phase displays, phase changes (particularly negative changes) occurred at discontinuities and areas with random noise. The noisy and discontinuous areas in the instantaneous frequency maps were marked by low-frequency interference.

The northern portion of the survey area (which accounts for up to 8% of the entire survey area) has a particularly low SNR. The significant noise deterioration in that area is due to karst weathering of the dolomites of the overlying Transvaal

Supergroup that is known to cause scattering of seismic energy (Manzi *et al* 2012b). Although the seismic data used for interpretation are of good quality, the application of filters (mean and median – which preserve both amplitude and structural integrity) proved only partially useful in reducing the noise associated with both poor resolution and picking errors.

The sub-crop identified by all three instantaneous attributes marks a stratigraphic position where the reef thins resulting in the accumulation of characteristically low-grade gold (Manzi *et al* 2013). This sub-crop position is a zone where the unconformable sequence is possibly at its mechanically weakest; where there is less adhesion between the shales and quartzites. The BS is described as highly laminated and undergoes a significant amount of horizontal stress during mining operations west of the survey area (Carstens 2007). This point is crucial when considering possible mechanisms for lateral migration of fluids and gas in the basin. The close proximity of the shale unit to the VCR also means that if there are any structures intersecting the source rock at this position, the likelihood of them also affecting the reef is much higher.

Edge-detection attributes have mapped a series of subtle faults that seem to have propagated between the VCR and BS. Some of these faults are new and were never mapped in the previous studies previously identified by Manzi *et al*. (2012a) as part of a series of horsts and grabens extending from the adjacent goldfield in the east, across into the West Wits Line Goldfield. These normal fault networks (which appear as polygons in map view) are interpreted to have formed during a major Platberg extensional regime (Manzi *et al* 2013). The highly fragmented nature of the faults within the graben does not appear random. Tracing the faults on the dip azimuth maps confirmed that there is a certain pattern analogous to the types of faults known as polygonal faults seen in a number of offshore sedimentary and continental margin basins (Cartwright 1996, 2011, Sonnenberg and Underwood 2012). These faults are defined as "an array of layer-bound extensional faults within a mainly fine-grained stratigraphic interval that exhibit a diverse range of fault strikes that partially or fully intersect to form a polygonal pattern in map view" (Cartwright *et al* 2003).

The migration of methane from depth to mining levels

The most critical clue leading to deciphering the sources of methane in the Witwatersrand Basin is the carbonaceous material found in reef packages. Carbon in the basin occurs either as stratiform carbon seams or as pyrobitumen. Carbon is closely linked to gold precipitation in the basin and in most cases, this gold of a high grade. There are two theories regarding the presence of carbon (and associated hydrocarbons) in the basin. The first theory is that the carbon was derived from algal mats that were attached to the gold reefs (Mossman *et al* 2008, Spanenberg and Frimmel 2001). Evidence for this includes isotopic data that associates the carbonaceous material to the insoluble organic matter and fractures that offset the carbon seams. The second theory is that the carbon was derived from liquid hydrocarbons that migrated through fractures and faults in the basin. The source of these hydrocarbons may be attributed to the alteration of the carbon seams and basin-internal shales such as the BS. The type of methane found at depth might give an integral clue about the source of that methane.

Sherwood Lollar *et al*. (2006) reported that most of the methane in the basin was abiogenic. Samples collected from fissure water at depths of up to 3400 m show that a significant amount of mixing has occurred between the microbial and abiogenic end-members (Sherwood Lollar *et al* 2006). A few deductions/assumptions can be made from these observations. The meta-sedimentary rocks of the Witwatersrand Basin are low porosity and permeability rocks (Barnard and Baran 2000) therefore mixing had to have occurred through the presence of an interconnected fracture and fault system(s). Seismic data provide the possible migration mechanism by which the biotic and abiotic methane can mix at greater depths. Considering the distance that these gases have to be migrated both vertically and laterally, it is worth noting that the most effective agents of transportation are hydrothermal fluids (Staude *et al* 2009, Burisch *et al* 2016).

With all this information derived from the use of seismic attributes to map structural propagation between the BS and VCR horizons, it is also possible that not all the mapped-out structures may be labelled as conduits for the present-day methane detected at mining levels. There are a number of conditions that have to be met for a fracture or fault to be considered an effective pathway for fluid migration. For example, fault reactivation in sedimentary basin settings is considered an active agent in either closing or opening up pathways for fluid migration (Sherwood Lollar et al 2006). The purpose of this is to demonstrate that 3D seismic data integrated with seismic attributes can provide high resolution mapping of the faults, dykes and fracture systems that may provide methane gas pathway to the mining levels. The work provides an important step towards resolving a long-standing controversy of the gas migration mechanism in the Witwatersrand Basin.

CONCLUSION

The history of methane explosions in the Witwatersrand gold mines has given cause for investigation of the source of this methane. The ability to seismically image and structurally interpret a possible source of methane in the basin may give new insight into the fault mechanisms that act as conduits transmitting methane from depth up into the mining VCR levels.

Seismic attribute analysis in hard rock environments has gained momentum in its effectiveness to delineate structures that affect mine planning and development. The conventional interpretation of the BS outlined some of the major faults intersecting the horizon. The use of instantaneous phase, frequency, and reflection strength took the seismic interpretation process a step further by delineating the seismic character of the shale. All three attributes are successful in highlighting the shoreline position where the BS sub-crops against the VCR. The data showed that discontinuities are generally characterised by abrupt phase changes, low frequencies, and strong reflections, particularly in the western portion of the goldfield. The application of dip, dip azimuth, and edge-detection maps provide a good correlation between structures found at both the BS and overlying VCR. This information may now be used to give further insight and a visual representation of structural controls of methane gas in the Witwatersrand Basin. In order to fully understand the nature and modes of structural control of the methane migration from depth, an integration of different datasets such as borehole and gas compositional data is required. This means that the structural interpretation of the BS and VCR is only part of a bigger puzzle of the occurrence and mobility of methane gas. Such an integrated system would shed more light into the hydrocarbon enigma of the Witwatersrand Basin.

REFERENCES

Ahmadi, O. Juhlin, C Malehmir, A. and Munck, M. (2013) 'High-resolution 2D seismic imaging and forward modeling of a polymetallic sulfide deposit at Garpenberg, central Sweden', *Geophysics*, **78**, pp. 339-350. doi**.** http.//dx.doi.org/10.1190/geo2013-0098.1

AngloGoldAshanti, (2014) 'Mineral Resource and Ore Reserve Report'. Available at www.aga-reports.com/16/download/AGA-RR14.pdf ; Accessed 30/03/2016

Bacon, M. Simm, R. and Redshaw, T. (2007) 'Geological Interpretation', in *3-D Seismic Interpretation*, 3rd edition, Cambridge**.** Cambridge University Press.

Baldassare, F.J. McCaffrey, M.A. and Harper, J.A. (2014) 'A geochemical context for stray gas investigations in the northern Appalachian Basin**.** Implications of analyses of natural gases from Neogene-through-Devonian-age strata', *AAPG Bulletin*, **98**, no. 2, pp. 341-372. doi**.** http.//dx.doi.org/10.1306/06111312178

Barnard, H.C. and Baran, E., (2000) *1:500 000 Hydrogeological map series of the Republic of South Africa: Johannesburg 2526*. Pretoria: Department of Water Affairs and Forestry.

Barnicoat, A.C. Jolley, S.J. Phillips, G.M. Freeman, S.R. Gibson, M. and Hewitt, T. (2000) 'Structural controls on gold mineralisation in the Ventersdorp Contact Reef, Witwatersrand Basin, South Africa', pp. 1-4.

Breytenbach, M. (2016) *Creamer Media's Engineering News*, 10 June, [Online], Available**.** http.//www.engineeringnews.co.za/article/free-state-gas-potential-to-pioneer-helium-natural-gas-production-for-sas-local-gas-economy-2016-06-10 [18 June 2016].

Burisch, M. Walter, B. F. Walle, M. Markl, G. (2016), ‘Tracing fluid migration pathways in the root zone below unconformity-related hydrothermal veins: Insights from trace element systematics of individual fluid inclusions’, *Chemical Geology*, **429**, pp. 44-50 https://doi.org/10.1016/j.chemgeo.2016.03.004

Carstens, A. (2007) 'Development of a Support Strategy for Cleaning Slushers Situated in Booysen's Shale at Mponeng Gold Mine', Symposium - Redefining Boundaries Part 2, Free State,pp. 123-135.

Cartwright, J.A. (1996) 'Polygonal fault systems**.** A new type of fault structure reavealed by 3-D seismic data from the North Sea Basin', in Weimer, P. and Davis, T.L., eds. *AAPG Studies in Geology No. 42,* and *SEG Geophysical Development Series No. 5*, pp. 225-230

Cartwright, J.A. James, D. and Bolton, A. (2003) 'The genesis of polygonal fault systems**:** a review', *Geological Society, London, Special Publications*, **216**, pp. 223-243. doi**.** http://dx.doi.org/10.1144/GSL.SP.2003.216.01.15

Cartwright, J.A. (2011) 'Diagenetically induced shear failure of fine-grained sediments and the development of polygonal fault systems', *Marine and Petroleum Geology*, **28**, no. 9, pp. 1593-1610. doi**.**10.1016/j.marpetgeo.2011.06.004

Chopra, S. (2011) 'Extracting meaningful information from seismic attributes', *Canadian Society of Exploration Geophyscists Recorder*, **36**, no. 3, pp. 9-12.

Cook, A.P. (1998) 'The occurrence, emission and ignition of combustible strata gases in Witwatersrand gold mines and Bushveld platinum mines, and means of ameliorating related ignition and explosion hazards'. Safety in Mines Research Advisory Committee. Project Report

Coward, M.P. Spencer, R.M. and Spencer, C.E. (1995) 'Development of the Witwatersrand Basin, South Africa', in Coward, M.P. and Ries, A.C. (ed.) *Early Precambrian Processes*, 1st edition, London**.** Geological Society of London Special Publications. doi**.** http://dx.doi.org/10.1144/GSL.SP.1995.095.01.15

Dalley, D. (2008) 'Value of visual attributes**.** revisiting dip and azimuth displays for 3D seismic interpretation', *First Break*, **26**, no. 4, pp. 87-91.

Dankert, B.T. and Hein, K.A.A. (2010) 'Evaluating the structural character and tectonic history of the Witwatersrand Basin', *Precambrian Research*, **177**, pp. 1-22. doi**.** 10.1016/j.precamres.2009.10.007

Dehghannejad, M. Malehmir, A. Juhlin, C. and Skytta, P. (2012) '3D constraints and finite-difference modeling of massive sulfide deposits**.** The Kristineberg seismic lines revisited, northern Sweden', *Geophysics*, **77**, pp. 69-79.
doi**.** http.//dx.doi.org/10.1190/geo2011-0466.1

du Plessis, J.J.L. and van Greuning, D.C. (2011) 'Destruction of underground methane at Beatrix Gold Mine', *The Journal of The Southern African Institute of Mining and Metallurgy*, **111**, pp. 887-894.

England, G. Rasmussen, B. Krapez, B. and Groves, D. (2002) 'Archaean oil migration in the Witwatersrand Basin of South Africa ', *Journal of the Geological Society*, **159**, pp. 189-201. doi**.** http.//dx.doi.org/10.1144/0016-764900-197

Gibson, M.A. (1997) 'The Western Deep Levels gold mine 3-D seismic survey', 5th SAGA Binnial Conference and Exhibition, Swakopmund, Namibia, pp.34-36.

Gibson, M.A.S. Jolley, J. and Barnicoat, C. (2000) 'Interpretation of the Western Ultra Deep Levels 3-D seismic survey', *The Leading Edge*, pp. 730-735. doi**.** http.//dx.doi.org/10.1190/1.1438704

Gray, G.J. Lawrence, S.R. Kenyon, K. and Cornford, C. (1998) 'Nature and origin of 'carbon' in the Archaean Witwatersrand Basin, South Africa', *Journal of the Geological Society, London*, **155**, pp. 39-59. doi**.** http.//dx.doi.org/10.1144/gsjgs.155.1.0039

Handley, M.F. De Lange, J.A.J. Essrich, F. and Banning, J.A. (2000) 'A review of the sequential grid mining method employed at Elandsrand Gold Mine', *Journal of the South African Institute of Mining and Metallurgy* , pp. 1183-1194.

Harmony (2014) 'Annual Report**.** Mineral Reources and Mineral Reserves'. Available at www.har.co.za/16/download/HAR-RR146.pdf ; accessed 30/03/2016.

Jolley, S.J. Freeman, S.R. Barnicoat, A.C. Phillips, G.M. Knipe, R.J. Pather, A. Fox, P.C. Strydom, D Birch, M.T.G Henderson, H.C. and Rowland, T (2004) 'Structural controls on Witwatersrand gold mineralisation', *Journal of Structural Geology*, **26**, pp. 1067-1086. doi**.** http.//dx.doi.org/doi.10.1016/j.jsg.2003.11.011

Jolley, S.J. Henderson, H.C. Barnicoat, A.C. and Fox, P.C. (1999) 'Thrust-fracture network and hydrothermal gold mineralization**.** Witwatersrand Basin, South Africa ', *Geological Society, London, Special Publications*, **155**, pp. 153-165. doi**.** http.//dx.doi.org/10.1144/GSL.SP.1999.155.01.12

Litthauer, A. (2009) 'The Geochemistry of the Dykes in the Carletonville Goldfield' Bloemfontein**.** University of the Free State. MSc Thesis

Malehmir, A. Koivisto, E. Manzi, M. Cheraghi, S. Durrheim, R.J. Bellefleur, G. Wijns, C. Hein, A.A. and King, (2014) 'A review of reflection seismic investigations in three major metallogenic regions**.** The Kevitsa Ni–Cu–PGE district (Finland), Witwatersrand goldfields (South Africa), and the Bathurst Mining Camp (Canada)', *Ore Geology Reviews*, **56**, pp. 423-441. doi**.**10.1016/j.oregeorev.2013.01.003

Manzi, M.S.D. Hein, K.A.A. Durrheim, R. and King, N. (2014) 'The Ventersdorp Contact Reef model in the Kloof Gold Mine as derived from 3D seismics, geological mapping and exploration borehole datasets', *International Journal of Rock Mechanics and Mining Sciences* , **66**, pp. 97-113. doi**.** 10.1016/j.ijrmms.2013.12.015

Manzi, M.S.D Hein, K.A.A Durrheim, R. and King, N. (2013) 'Seismic attribute analysis to enhance detection of thin gold-bearing reefs**.**South Deep gold mine,Witwatersrand basin, South Africa', *Journal of Applied Geophysics*, **98**, pp. 212-228. doi**.** 10.1016/j.jappgeo.2013.08.017

Manzi, M. Cooper, G. Malehmir, A. Durrheim, R. and Nkosi, Z. (2015) 'Integrated interpretation of 3D seismic data to enhance the detection of the gold-bearing reef**.** Mponeng Gold mine, Witwatersrand Basin (South Africa)', *Geophysical Prospecting*, **63**, pp. 881-902. doi**.** http.//dx.doi.org/10.1111/1365-2478.12273

Manzi, M.S.D. Durrheim, R.J Hein, K.A.A. and King, N. (2012a) '3D edge detection seismic attributes used to map potential conduits for water and methane in deep gold mines in the Witwatersrand basin, South Africa', *Geophysics*, **77**, pp. 133-147. doi**.** http://dx.doi.org/10.1190/geo2012-0135.1

Manzi, M.S.D. Gibson, M.A.S. Hein, K.A.A King, N. and Durrheim, R.J. (2012b) 'Application of 3D seismic techniques to evaluate ore resources in the West Wits Line Goldfield and portions of the West Rand goldfield, South Africa', *Geophysics*, **77**, no. 5, pp. 163-171. doi**.** http://dx.doi.org/10.1190/geo2012-0133.1

Manzi, M.S.D. Hein, K.A.A King, N. and Durrheim, R.J. (2013) 'Neoarchaean tectonic history of the Witwatersrand Basin and Ventersdorp Supergroup**.** New constraints from high-resolution 3D seismic reflection data', *Tectonophysics*, **590**, pp. 94-105. doi**.** 10.1016/j.tecto.2013.01.014

Marfurt, K. and Alves, T.M. (2015) 'Pitfalls and limitations in seismic attribute interpretation of tectonic features', *Society of Exploration Geophysics and American Association of Petroleum Geologists*, **3**, pp. 5-15. doi**.** http://dx.doi.org/10.1190/INT-2014-0122.1

McCarthy, T.S. (2006) 'The Witwatersrand Supergroup', in Johnson, M.R. Anhaeusser, C.R. and Thomas, R.J. (ed.) *The Geology of South Africa*, 1st edition, Johannesburg, Pretoria**.** Geological Society of South Africa.

Mossman, D.J. Minter, W.E.L. Dutkiewicz, A. Hallbauer, D.K. George, S.C. Hennigh, Q. Reimer, T.O. and Horscroft, F.D. (2008) 'The indigenous origin of Witwatersrand "carbon"', *Precambrian Research*, **164**, pp. 173-186. doi**.** 10.1016/j.precamres.2008.04.008

Myers, R.E. Stanistreet, I.G. and McCarthy, T.S. (1992) 'Two-stage basement fault-block deformationin the development of the Witwatersrand goldfields, South Africa', in Bartholomew, M.J. Hyndman, D.W. Mogk, D.W. Mason, R. *Basement Tectonics 8*, Proceedings of the International Conferences on Basement Tectonics.

Pretorius, C.C. Muller, M.R. Larroque, M. and Wilkins, C. (2006) 'A Review of 16 Years of Hardrock Seismics on the Kaapvaal Craton', in Eaton, D.W Milkereit, B. and Salisbury, H., eds. *Hardrock Seismic Exploration*, Society of Exploration Geophysicists.

Pretorius, C.C. Trewick, W.F. and Irons, C. (1997) 'Application of 3-D Seismics to Mine Planning at Vaal Reefs Gold Mine, Number 10 Shaft, Republic of South Africa', Proceedings of Exploration 97**.** Fourth Decennial International Conference on Mineral Exploration, Toronto, pp.399-408.

Randen, T. Pederson, S. and Sonneland, L. (2001) ' Automatic extraction of fault surfaces from three-dimensional seismic data', 71st Annual International Meeting, SEG, Expanded Abstracts, Norway, pp.551-554.

Robertson, J.D. and Nogami, H.H. (1984) 'Complex seismic trace analysis of thin beds', *Geophysics*, **49**, pp. 344-352. doi**.** http.//dx.doi.org/10.1190/1.1441670

Safonov, Y. and Prokof'ev, V. (2006) 'Gold-bearing reefs of the Witwatersrand Basin**:** a model of synsedimentation hydrothermal formation', *Geology Ore Deposits*, **48**, pp. 415-447. doi**.** http.//dx.doi.org/10.1134/S1075701506060018

Schulte, B. (2012) 'Overview on the Fundamentals of Imaging', *CSEG Recorder* , p. 40.

Sherwood Lollar, B. Lacrampe-Couloume, G. Slater, G.F. Ward, J. Moser, D.P. Gihring, T.M. Lin, L.-H. and Onstott, T.C. (2006) 'Unravelling abiogenic and bigenic sources of methane in the Earth's deep subsurface', *Chemical Geology*, **226**, pp. 328-339. doi**.** 10.1016/j.chemgeo.2005.09.027

Sonnenberg , S.A. and Underwood, D. (2012) *Polygonal fault systems: A new structural style for the Niobrara Formation, Denver Basin, Colorado*, 25 June, Available at www.searchanddiscovery.com/documents/2012/50624sonnenberg/ndx_sonnenberg.pdf. Accessed 06/06/2015.

Spanenberg, J.E. and Frimmel, H.E. (2001) 'Basin-internal derivation of hydrocarbons in the Witwatersrand Basin, South Africa**.** evidence from bulk and molecular ^{13}C data', *Chemical Geology*, **173**, pp. 339-355. doi**.** 10.1016/S0009-2541(00)00283-7

Stanistreet, I.G. and McCarthy, T.S. (1991) 'Changing tectono-sedimentary scenarios relevant to the development of the Late Archaean Witwatersrand Basin', *Journal of African Earth Sciences*, **13**, pp. 65-81. doi**.** 10.1016/0899-5362(91)90044-Y

Staude, S. Bons, P.D. Markl, G. (2009) 'Hydrothermal vein formation by extension-driven dewatering of the middle crust: An example from SW Germany', Earth and Planetary Science Letters, 286, pp. 387-395, https://doi.org/10.1016/j.epsl.2009.07.012

Stuart, G.W. Jolley, S.J. Polome, L.G.B.T. and Tucker, R.F. (2000) 'Application of 3-D seismic attributes analysis to mine planning**.** Target gold deposit, South Africa', *The Leading Edge*, **19**, pp. 736-742. doi**.** http.//dx.doi.org/10.1190/1.1438706

Taner, M.T. Koehler, F. and Sheriff, R.E. (1979) 'Complex seismic trace analysis ', *Geophysics*, **44**, no. 6, pp. 1041-1063. doi**.** http.//dx.doi.org/10.1190/1.1440994

Tankard, A.J. Jackson, M. Eriksson, K.A. Hodday, D.K. Hunter , D.R. and Minter , W.E.L. (1982) *Crustal Evolution of Southern Africa: 3.8 Billion Years of Earth History*, 1st edition, New York**.** Springer-Verlag.

Viljoen, M. (2009) 'The life, death and revival of the Central Rand Goldfield ', World Gold Conference , Johannesburg.

Wanger, G. Moser, D. Hay, M. Mynent, S. Onstott, T.C. and Southam, G. (2012) 'Mobile hydrocarbon microspheres from > 2-billion-year-old carbon-bearing seams in the South African deep subsurface', *Geobiology*, **10**, no. 6, pp. 496-505.

Zhu, S. Plataniotis, K.N. and Venetsanopoulos, A.N. (1999) 'Comprehensive analysis of edge detection in color image processing', *Optical Engineering*, **38**, no. 4, pp. 612-625. doi**.** http.//dx.doi.org/10.1117/1.602105

FIGURES

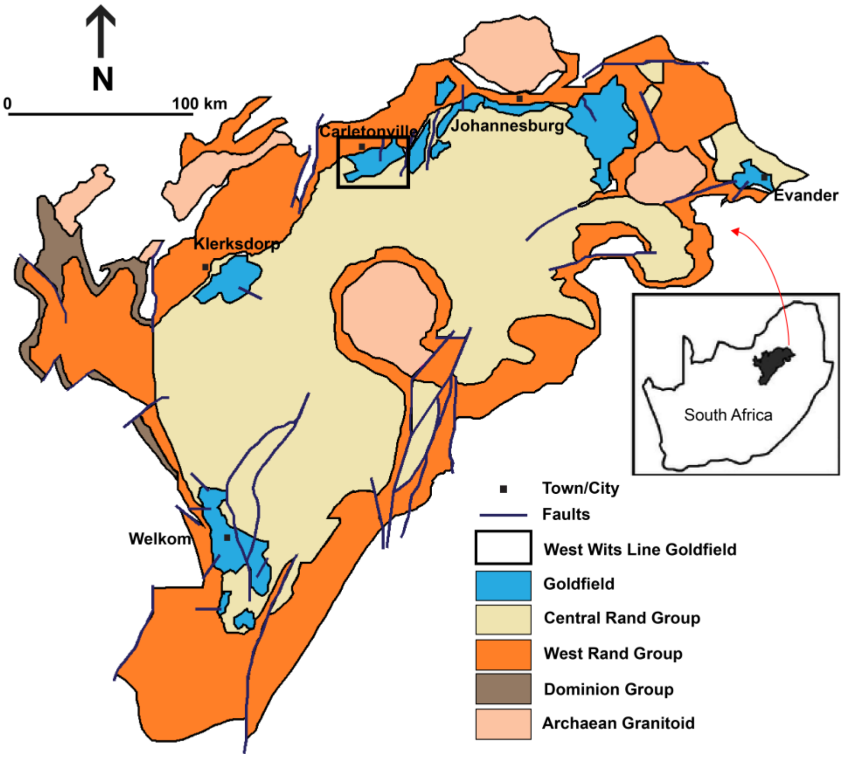

Figure 1. The geology of the Witwatersrand Basin and location of the West Wits Line Goldfield (outlined with a black rectangle) within the basin.

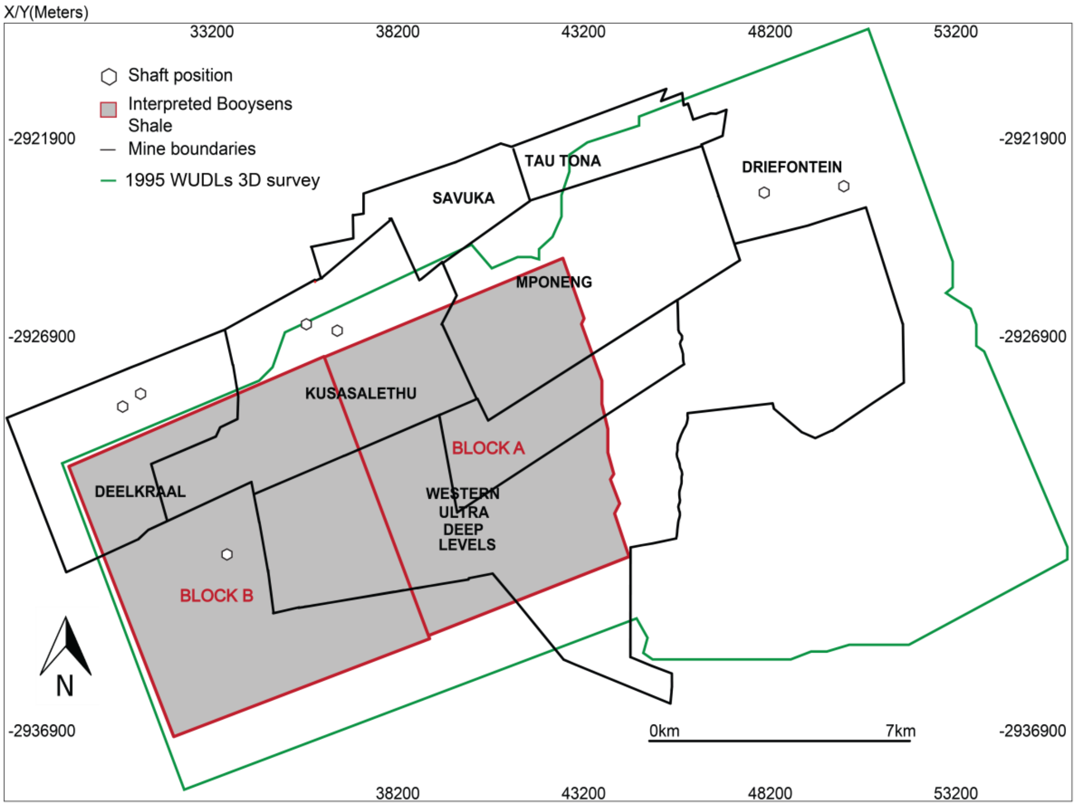

Figure 2. The WUDLs 3D seismic survey and the mines covered by the survey. The interpreted BS covers approximately half of the survey and has been divided into Block A (which covers portions of the Mponeng, Western Ultra Deep Levels and Kusasalethu mines) and Block B (which covers portions of the Kusasalethu and Deelkraal gold mines).

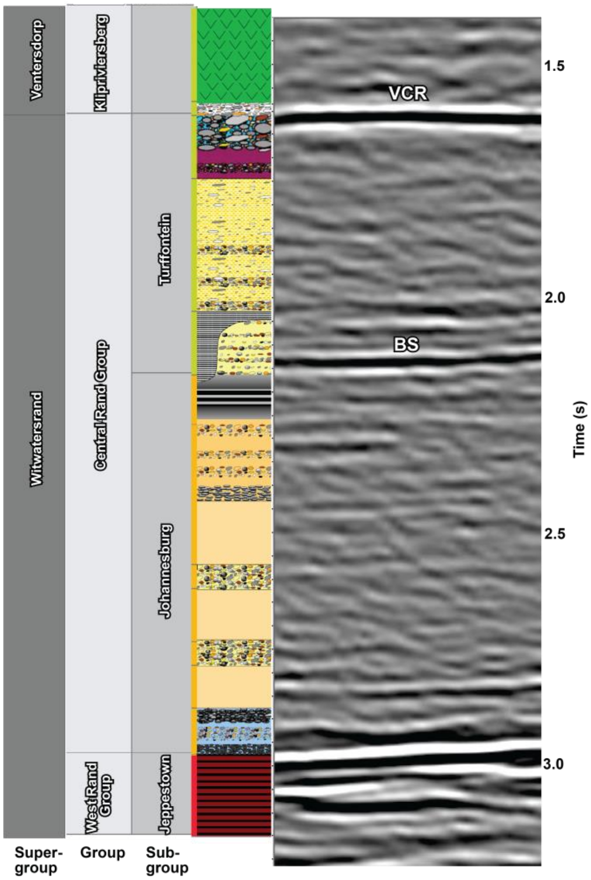

Figure 3. Stratigraphic overview of the specific area of interest within the Witwatersrand Supergroup and overlying Klipriviersberg Group of the Ventersdorp Supergroup. VCR – Ventersdorp Contact Reef; BS – Booysens Shales.

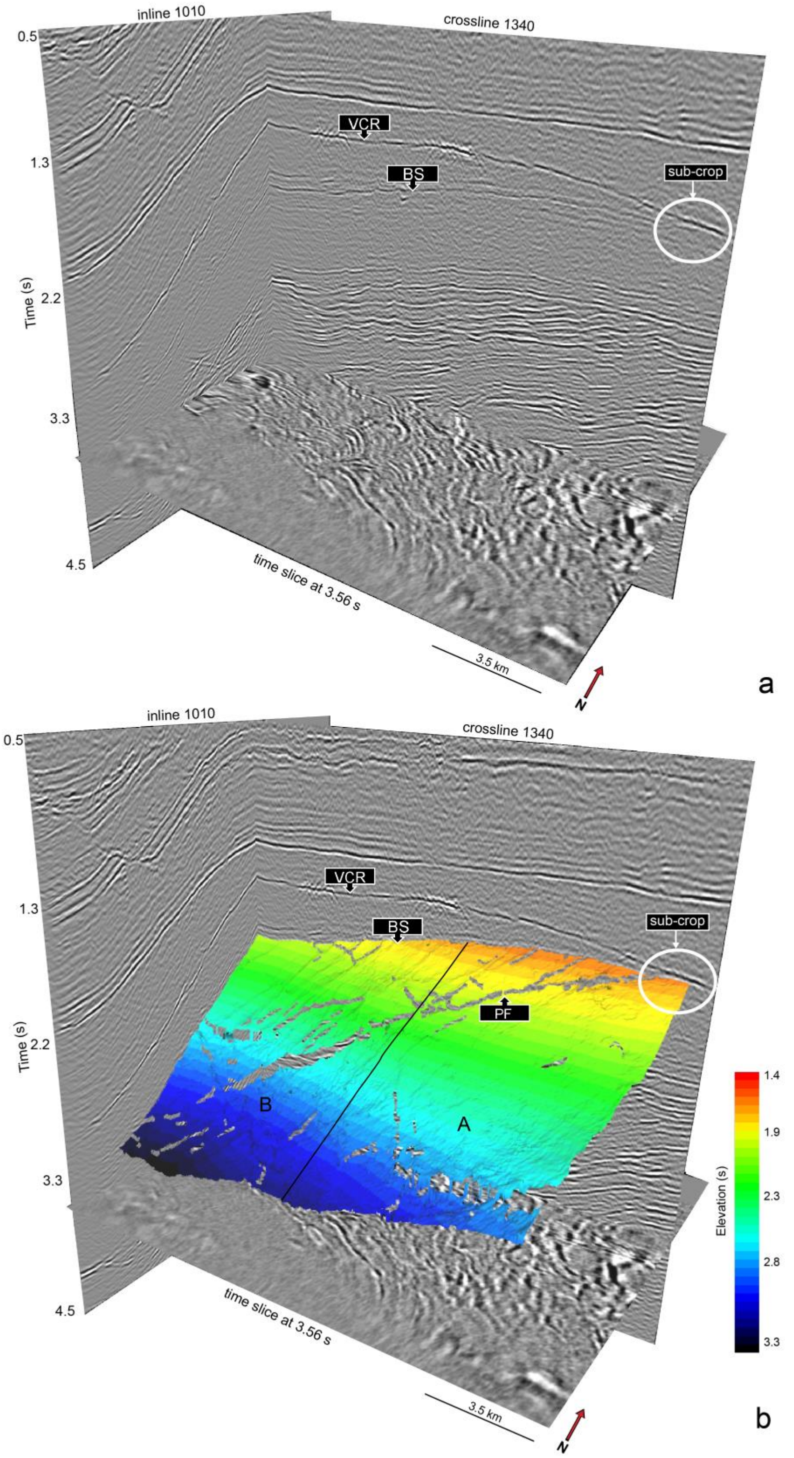

Figure 4. (a) 3D seismic cube (created from inline 1010, crossline 1340 and a time slice at 3.56 s) representative of the area of interpretation of the Booysens Shale (BS)

and Ventersdorp Contact Reef (VCR). The data are of good quality with most of the unconformities down to depth. The sub-crop position (highlighted by the white circle) can also be seen in the 3D seismic cube; (b) A picked time structure map of the BS horizon. Time increases in a southwesterly direction. The "cracks" in the horizon are fault picks where the Pretorius Fault (PF) is the most prominent fault displacing the BS.

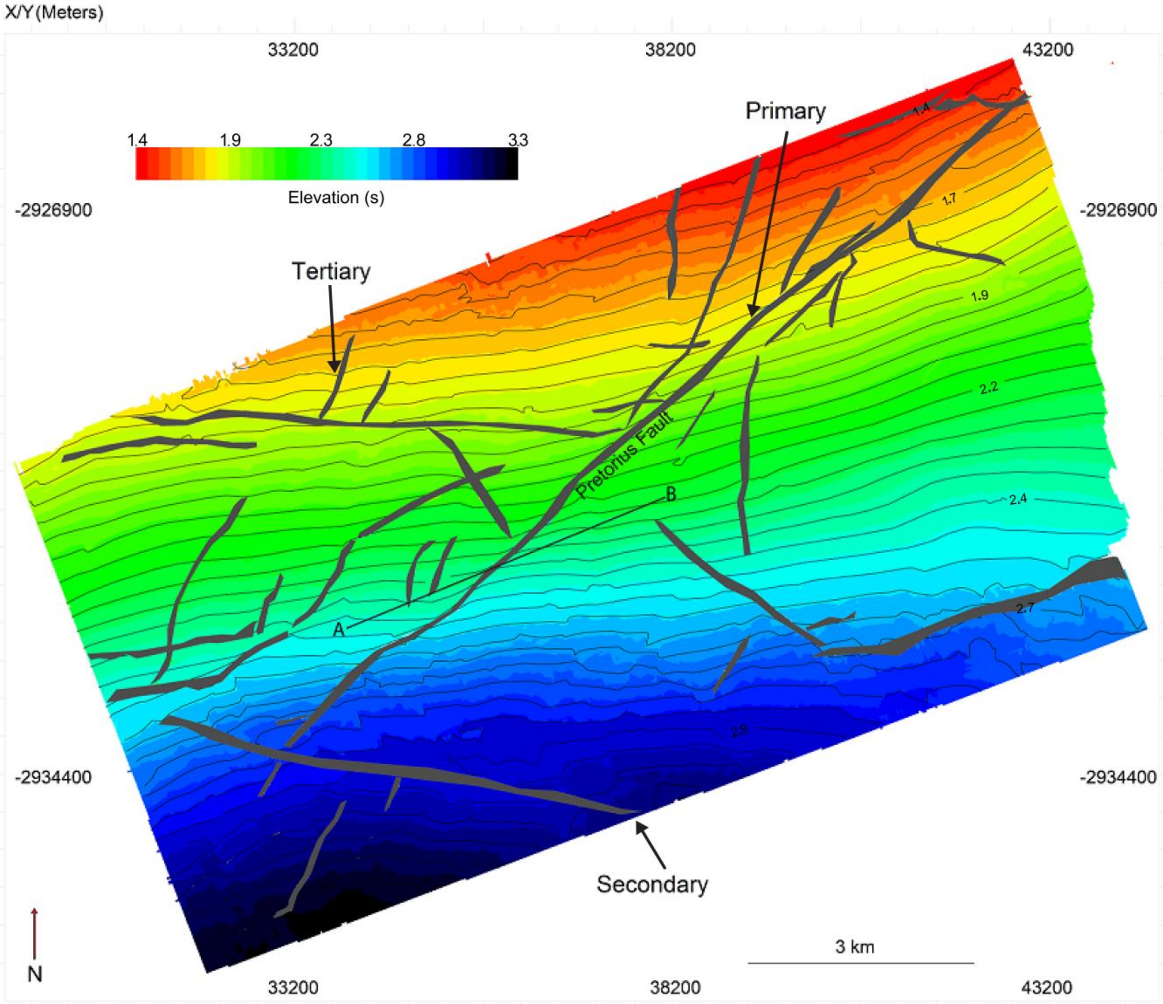

Figure 5. A time structure surface of the Booysens Shale with fault polygons. The contour interval was set at 0.5 s, showing no abrupt changes in continuity (i.e. faulting) along the horizon. A section (A-B) through the Pretorius Fault was acquired

and is presented in figure 6(*a*). Three types of faults have been identified based on their orientation and length – primary, secondary, and tertiary. The most prominent primary fault is the Pretorius Fault. The secondary faults generally trend in a NW-SE direction and the tertiary and smallest faults, in a NE-SW direction.

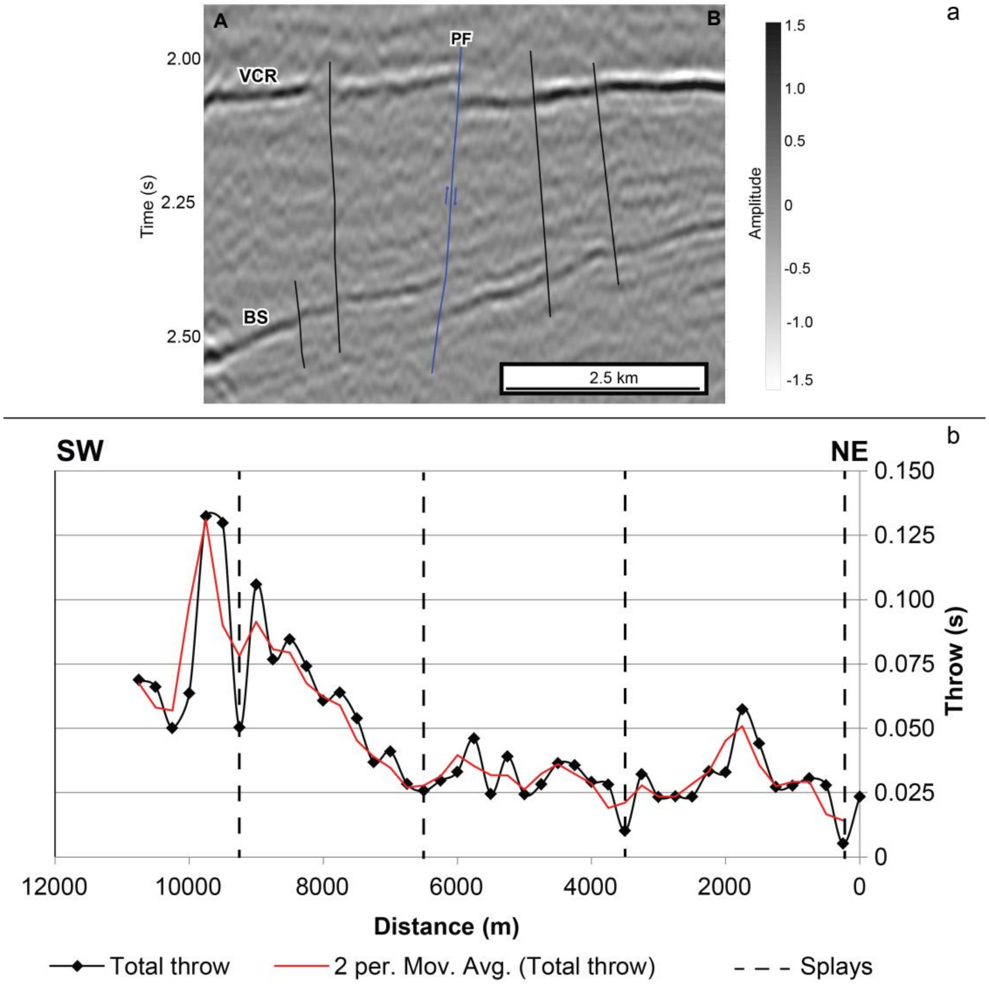

Figure 6. (a) Section A-B displaying the significant throw of the Pretorius Fault (PF). The fault displaces both the Ventersdorp Contact Reef (VCR) and the Booysens Shale (BS). The PF is flanked by faults on either side of the fault plane (b) A variable throw graph of the Pretorius Fault. Substantial peaks and dips in the trendline may be attributed to sub-ordinate faults splays (at the 250, 3500, 6500 and 9250 m marks) branching out from the Pretorius Fault.

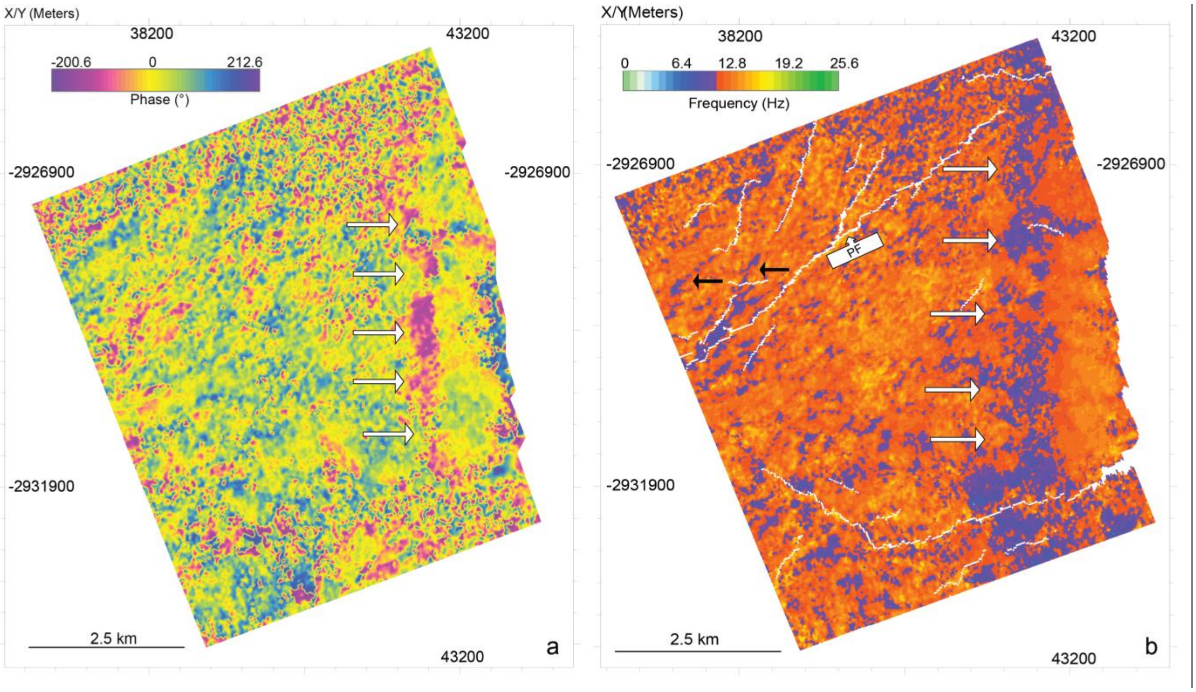

Figure 7. (a) Instantaneous phase and (b), the instantaneous frequency maps of the Booysens Shale of Block A. The white arrows, characterized by a phase change in the instantaneous phase map and a lower frequency in the instantaneous frequency map, mark the approximate location of the sub-crop position. It is evident that the extent sub-crop position can be more clearly seen on the instantaneous frequency map. The black arrows show the extension of faults where picking could not be achieved due to low seismic resolution.

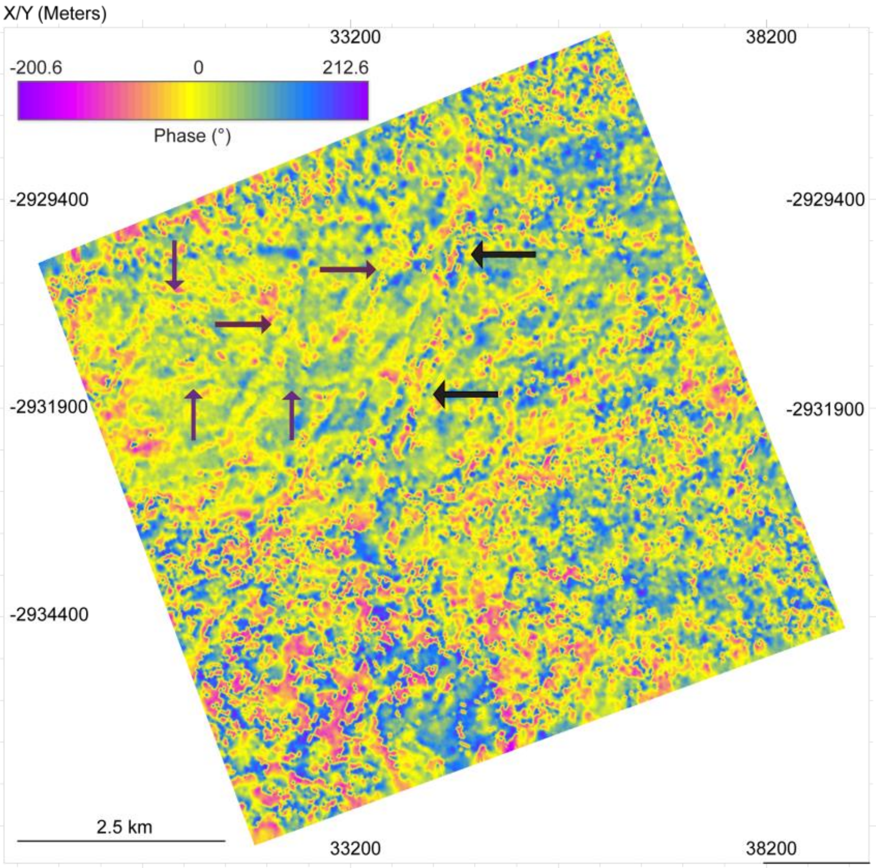

Figure 8. Instantaneous phase map of the Booysens Shale for Block B. The black arrows denote a linear north northeast-trending feature (the distinction and extension of which is best delineated in the frequency map for Block B in figure 9a). The purple arrows point to east-west trending lineaments as well as an intersecting set of north-north-east trending faults. Most of the area is significantly affected by noise, particularly the southern portion of the block.

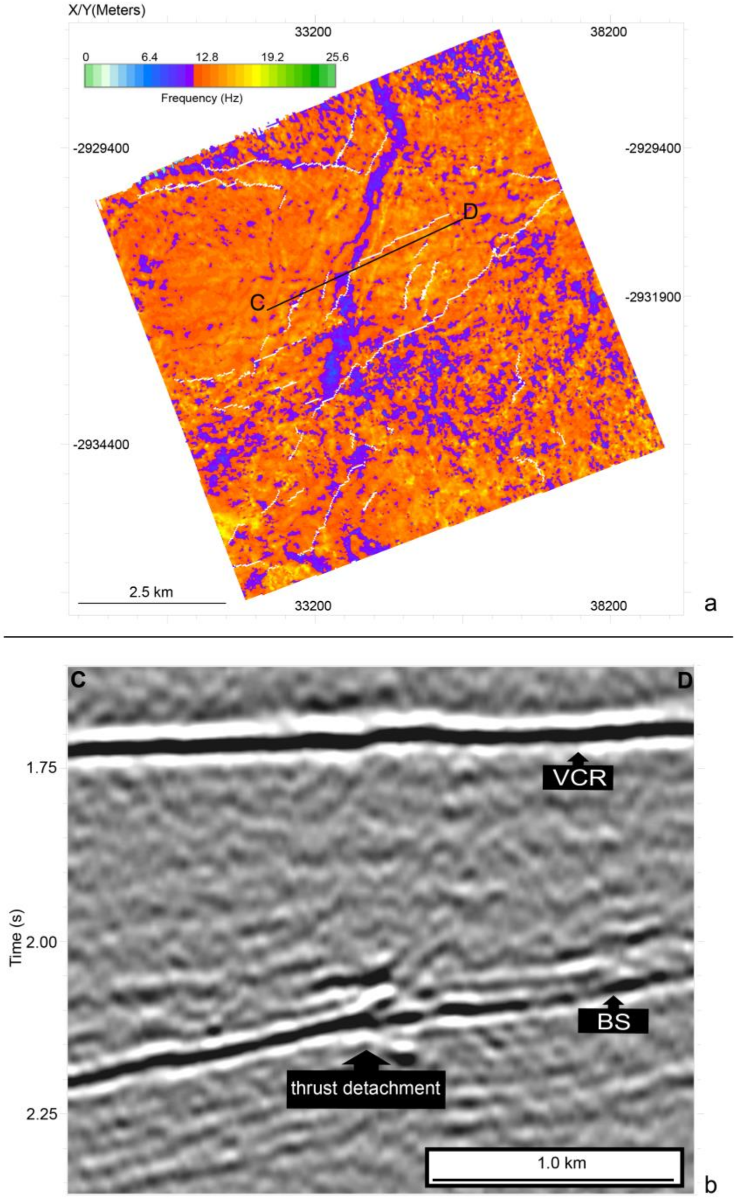

Figure 9. The instantaneous frequency map of the Booysens Shale for Block B (a) has a distinct linear, northeast trending feature that has been identified in the cross-section (b) as a thrust fault detaching from the Booysens Shale horizon. Noise on the northern and southern portions of the instantaneous map may be attributed to structural complexity and/or poor fold coverage along the edges of the survey.

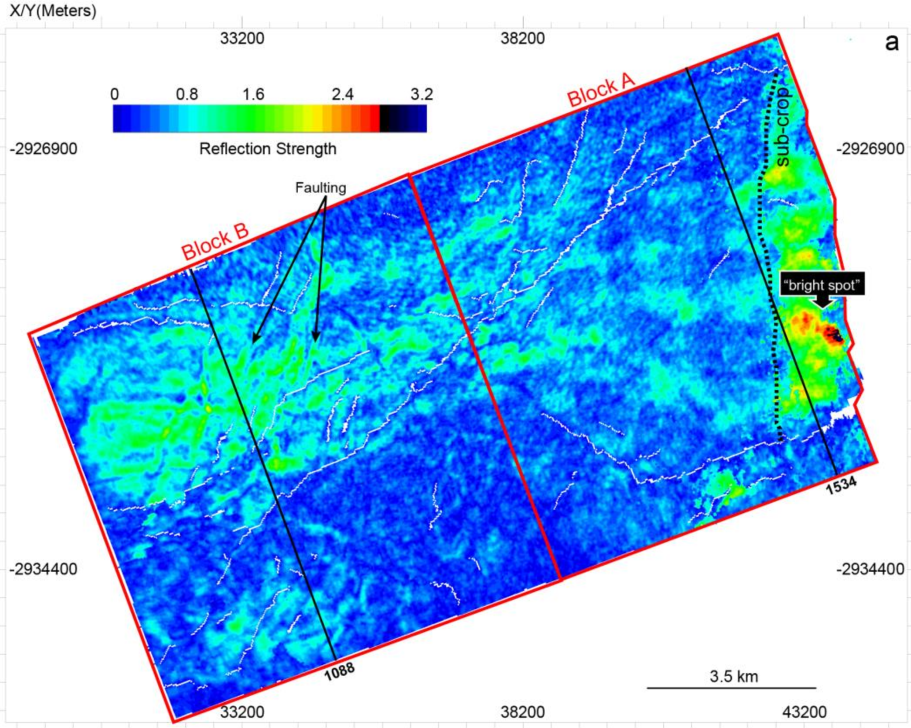

Figure 10. The envelope map of the Booysens Shale for Blocks A and B. There is variability in the reflective strength resulting from varying acoustic impedances across the horizon. Features of interest in the map include high reflectance areas related to faulting and a bright spot. Inline sections 1088 and 1534 (see Figure 11) of the different areas of interest were acquired for further interpretation within Blocks A and B.

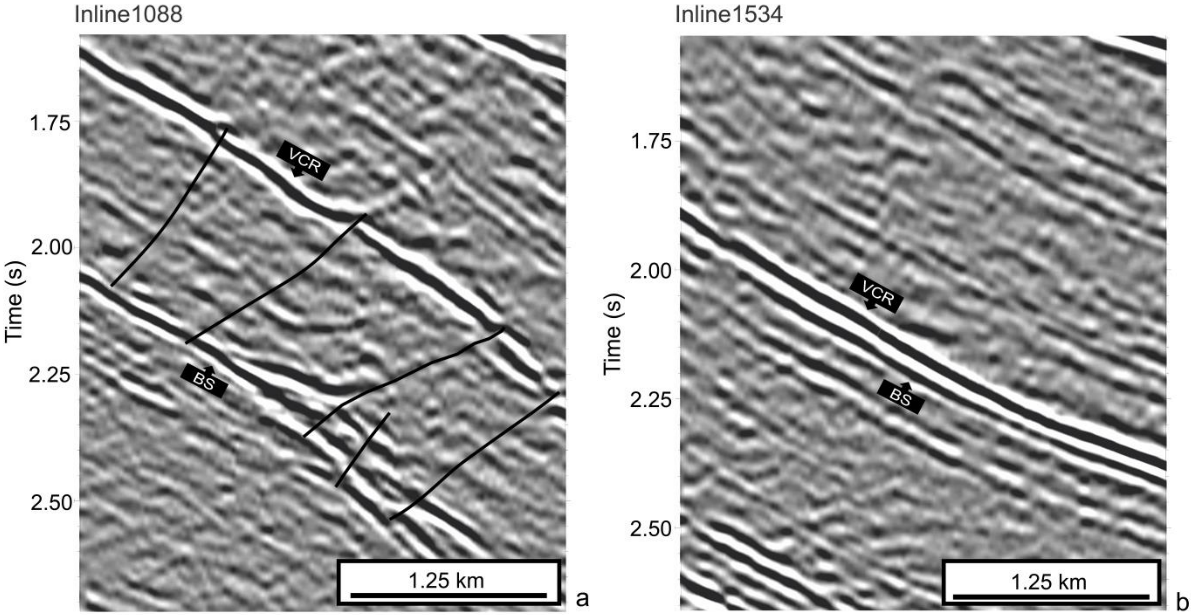

Figure 11. (a) Complex structural mapping in Block B. Faults appear to have displaced the Booysens Shale (BS) and the Ventersdorp Contact Reef (VCR) and (b) a section showing the close proximity of the Booysens Shale to the Venterdorp Contact Reef close to the sub-crop position of the Booysens Shale against the Ventersdorp Contact Reef in Block A.

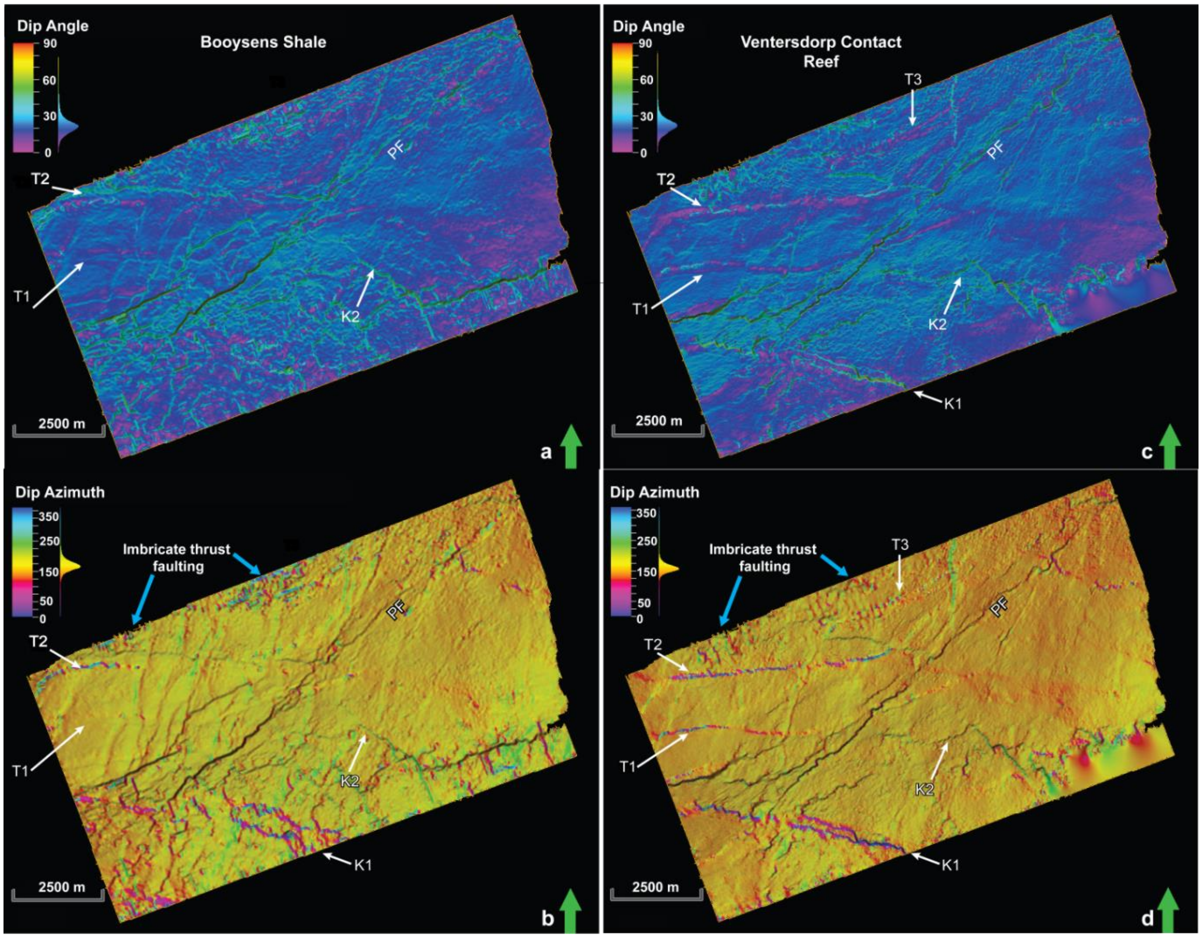

Figure 12. Dip and dip azimuth maps of the Booysens Shale (a and b) showing fault intersections and relief possibly due to folding. The dip (c) and dip azimuth (d) maps of the Ventersdorp Contact Reef show a greater amount of structural detail highlight the major structures found in the West Wits Line Goldfield. The most prominent structures include the PF, T1, T2 and T3, K1 and K2 faults and all of them appear to extend from the BS to the mining level, the VCR.

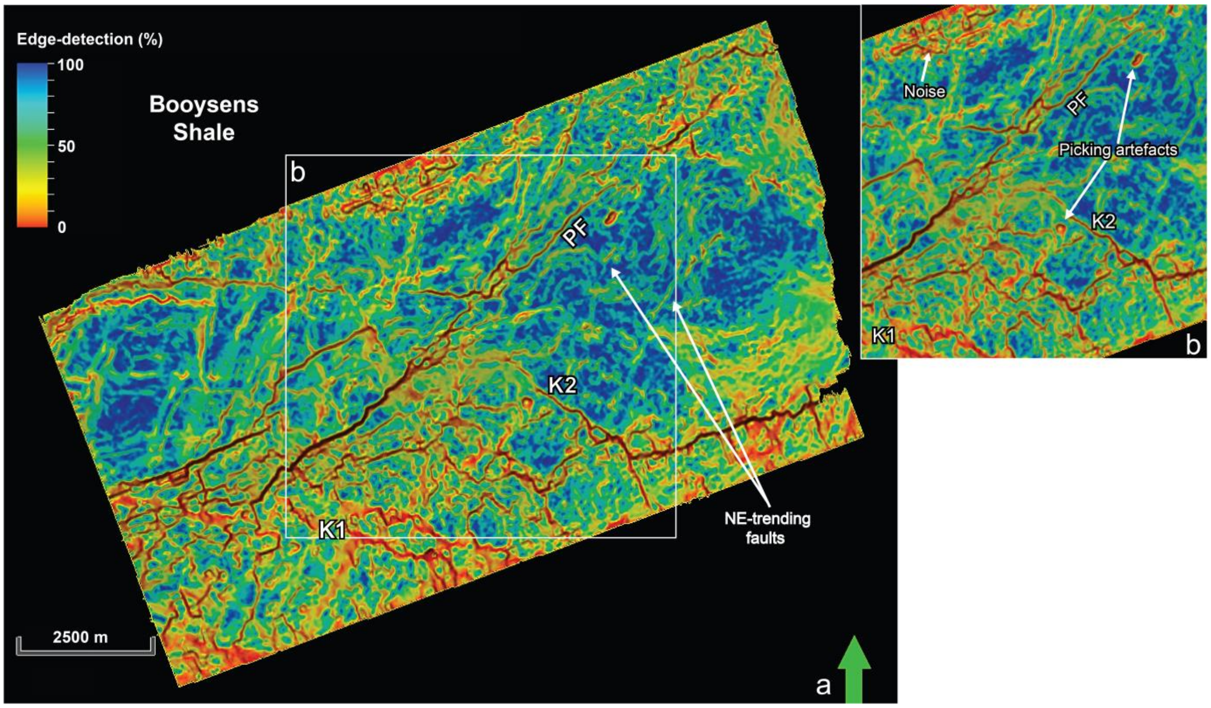

Figure 13. (a) Edge-detection attribute map of the Booysens Shale. There is a significantly degree of sub-seismic lineaments (with the example of the NE-trending faults in the west) that have been images by the attribute; (b) A close-up of some of the features such as manual picking errors and noise accentuated by edge-detection [*].

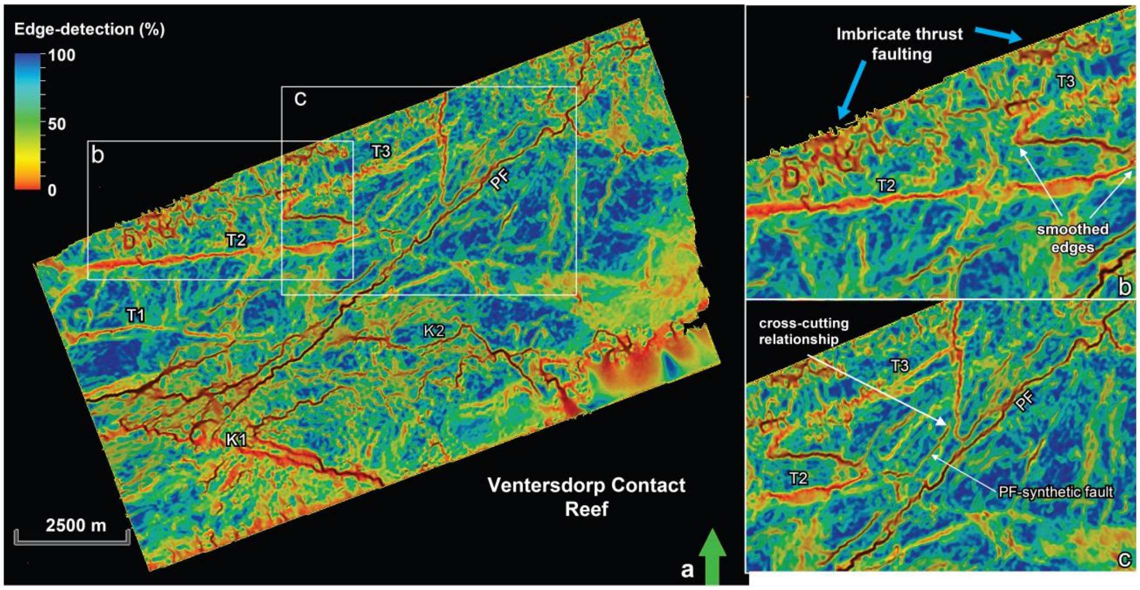

Figure 14. (a) Edge-detection display of the Ventersdorp Contact Reef. (b) Thrust imbrication north of the survey area is identified by the smeared edges(c) The crosscutting relationships between faults can clearly be observed using the edge-detection method. Values for the attributes are represented as percentages and the lower the percentage (more orange than blue), the more likely it is that it attribute has detected a lineament. It is clear to see that edge-detection has delineated a series of faults that were otherwise below the seismic resolution limit (~25 m).

7. RESULTS ON METHANE IN THE WEST WITS LINE GOLDFIELD

As previously stated, the methane found in the Witwatersrand Basin has multiple sources attributed to it. The occurrence of methane gas found at deep mining levels in the gold mines has been linked to geological structures such as faults and dykes. This chapter presents and examines the link between groundwater samples containing hydrocarbons derived from underground gold mine boreholes, and faults and dykes cross-cutting the mining horizons, which were detected by seismic attributes. This is done by comparing conventional amplitude seismic displays with seismic attributes (mainly ant-tracking) applied to the 3D seismic volume. In Chapter 6, only the western portion of the WUDLs 3D seismic survey was interpreted. In this section, due to boreholes being located further east of the survey area, structural interpretation has been extended further into the Mponeng, TauTona and Driefontein gold mines where most of the samples were collected. The localities of 15 methane borehole-sampled points are integrated into a 3D ant-tracked volume.

7.1 The biohydrogeology of fracture waters of the West Wits Line Goldfield gold mines

A significant body of literature documents the characteristics of the fracture water as well as the microbial communities that exist in deep South African gold mines (Takai, et al., 2001; Lippmann, et al., 2003, 2011; Ward, et al., 2004; Moser, et al., 2005; Sherwood Lollar, et al., 2006, 2007, 2008; Lau, et al., 2014; Borgonie, et al., 2015; Simkus, et al., 2016). The following section provides a background of the types and characteristics of the water found at these boreholes in the West Wits Line Goldfield. A synopsis of the types of waters found in the Driefontein, Mponeng, and TauTona gold mines is given and a more detailed overview of the compositional and isotopic characteristics of the borehole sites is presented.

Gas and fissure water sampling in some of the world's deepest mines is an arduous task. Sampling occurs as far down as 3 500 m below the surface of the Earth, at temperatures ranging between 20 and 60°C. The samples for this study were collected over fifteen years (1998 to 2013) by a collaborative team of scholars with the help of mine personnel in the Mponeng, TauTona, Driefontein, and Kloof gold mines. The candidate is not included in the group of scholars that collected the data, but they have made it available for use in this research. 1596 water and gas samples were acquired from 55 underground boreholes. Most of the samples were collected from fissure water at the designated borehole collars. Parameters such as temperature, air pressure and groundwater salinity were measured. Most of the samples were analysed for gas and isotope composition. Detailed descriptions of the sampling methods are outlined by Ward, et al. (2004) and Sherwood Lollar, et al. (2006). The main purpose of the studies has been to characterize the groundwater emanating from the boreholes as well as understanding the types of life forms that have been found at these sites (Moser, et al., 2005; Sherwood Lollar, et al., 2006). At some of the borehole positions, geological structures, i.e. faults and dykes, were identified. The presence of fissure water is generally accompanied by considerable amounts of hydrocarbon gases, and understanding the character and spatial relation of the groundwater at the different sampling sites gives clues as to how structurally interconnected (or isolated) the groundwater systems are.

There have been over 100 samples collected from gold mines in the northern and eastern parts of the Witwatersrand Basin, however, this study will focus only on 16 borehole samples collected from the three aforementioned gold mines; Driefontein, Mponeng, and TauTona. DR546 BH1, DR548 FW, DR5IPC, DR638 FW, DR938 CH, DR9IPC, DR938 H3, and DR940 FW were collected from Sibanye's Driefontein gold mine. Samples collected from Mponeng were MP104 and MP10, and TT100, TT107, TT109, and TT118 were collected from TauTona gold mine. The groundwater and gas samples were collected between 1998 and 2011 at depths between 896 and 3 550 mbls (meters below land surface). The temperature of the groundwater collected from the boreholes ranged between 20 and 60°C, with MP104 having the highest recorded temperature (Table 7.1).

Table 7.1: The samples collected from the Driefontein (DR), Mponeng (MP), and TauTona (TT) gold mines including the sampling date, depth, temperature, and gas compositions.

				Mole (%)						
Sample name	**Sample Date(mo-dy-yr)**	**Sample Depth (mbls.)**	**T°C**	**H_2**	**He**	**O_2**	**N_2**	**CH_4**	**C_2H_6**	**C_3H_8**
DR548 FW [a]	09-04-01	3 300	41,6	10,34	3,05	6,18	23,61	56,31	2,67	0,220
DR5IPC [c]	07-15-11	1 050	26,8	0,000434	0,15	19,11	75,25	1,93	0,0027	n.d.
DR546 BH1 [d, e]	12-01-98	3 213	37,0	3,19	2,77	0,03	3,34	84,50	3,18	0,325
DR638 FW	11-01-98	2 700	45,0	0,0134	4,29	0,18	34,90	28,00	1,24	0,108
DR938 CH [a]	09-12-02	2 712	20,0	n.d.	0,42	16,77	73,59	4,70	0,12	0,020
DR9IPC [a]	10-16-02	896	26,0	n.d.	2,75	3,77	101,78	11,62	n.d.	n.d.
DR938 H3 (D3)	07-12-02	3 350	42,5	0,32	4,64	4,95	28,60	61,40	2,45	0,260
DR938 H3 (D2) [a]	11-11-01	2 716	43,0	0,74	5,98	0,55	13,98	76,03	3,15	0,319
DR938 H3 (D1) [b]	10-24-01	2 825	54,0	0,0127*	n.m.	n.m.	n.m.	61,09*	n.m.	n.m.
DR940 FW	09-26-02	2 812	20,0	n.d.	1,17	19,31	73,05	10,18	0,30	0,040
MP104 [a]	09-16-02	2 825	60,0	9,85	9,11	6,12	29,31	41,96	3,30	0,480
MP109 [a]	10-17-01	3 000	50,0	3,30	9,06	4,77	28,14	53,83	2,47	0,360
TT100 [e]	08-27-02	3 025	46,5	n.d.	0,25	18,70	76,70	2,50	0,04	n.d.
TT107 [c]	07-04-05	3 049	48,7	0,11	3,98	0,96	38,89	16	0,87	0,13
TT109 [c]	07-04-05	3 137	52,1	0,011	4,46	0,04	28,28	61,9	2,58	0,37
TT118	05-30-07	3 550	55,0	2,4	8,8	3,3	29,2	53,4	3,25	0,38

Source: a. Sherwood Lollar, et al. (2006); b. Duane, et al. (2005); c. Simkus, et al. (2016); d. Moser, et al. (2003); e. Onstott, et al. (2006).

mbls: metres below land surface; n.m – not measured; n.d. – not detected

*Measurement based on results from Residual Gas Analyser/Flame Ionization Detector (RGA/FID) analysis; for the other samples, FID was used.

A plot of temperature versus methane gas concentration shows that CH_4 concentration generally increases with increasing temperature and depth (Figures 7.1 and 7.2). The Driefontein samples have a wide temperature range (20 - 54°C) compared to the samples collected from the other gold mines but like the other mines, show a positive linear trend in increasing methane concentration with increasing depth. An exception is DR938 H3 (D2), which has the highest recorded CH_4 concentration at 76.03 mol% of the total gas composition with a coinciding temperature of 26°C. The lowest recorded value for CH_4 was 1.93 mol% from borehole DR5IPC. Samples at depths between 2 700 and 2 830 mbls have temperatures ranging between 20 and 26.8°C. The groundwater temperatures above 40°C coincide with depths greater than 2 500 mbls. The Mponeng gold mine samples, MP104 and MP109, have the coolest and warmest temperatures with a slight change in CH_4 mol% content of 11%. The TauTona data are clustered in a narrow range of temperature of 10°C. The TT109, TT118, and MP109 cluster has temperatures above 50°C, occurring at depths between 2 700 and 3 550 mbls and CH_4 concentrations reflecting those depths and temperatures (Figures 7.1 and 7.2). This is significant because, although organic decomposition required to produce oil and gas may occur at temperatures up to 150°C, effective hydrocarbon generation within appropriate geological timescales occurs at temperatures below 80°C (Wilhelms , et al., 2001; Stopler , et al., 2014). Other gases comprising the borehole water are also presented in Table 7.1. The gases worth noting are hydrogen (H_2) and the higher hydrocarbons, ethane (C_2H_6) and propane (C_3H_8) due to their explosive nature. The boreholes with the greatest amounts of H_2, which has an explosive limit ranging between 4 and 75 mol% of total gas composition (Yaws & Braker, 2001), are DR548 FW (10.34 mol%), MP104 (9.11 mol%), and MP109 (9.06 mol%). The percentage of higher hydrocarbons increases with increasing CH_4. This is exemplified in samples DR546 BH1 and DR938 H3 (D2), where high CH_4 concentrations have correspondingly relatively high C_2H_6 (3.18 and 3.15 mol%) and

C_3H_8 (0.325 and 0.319 mol%) values, respectively. The explosive limits for C_2H_6 range between 3 and 12.4 mol% and between 2.1 and 9.5 mol% for C_3H_8 of the total gas composition (Figure 7.1).

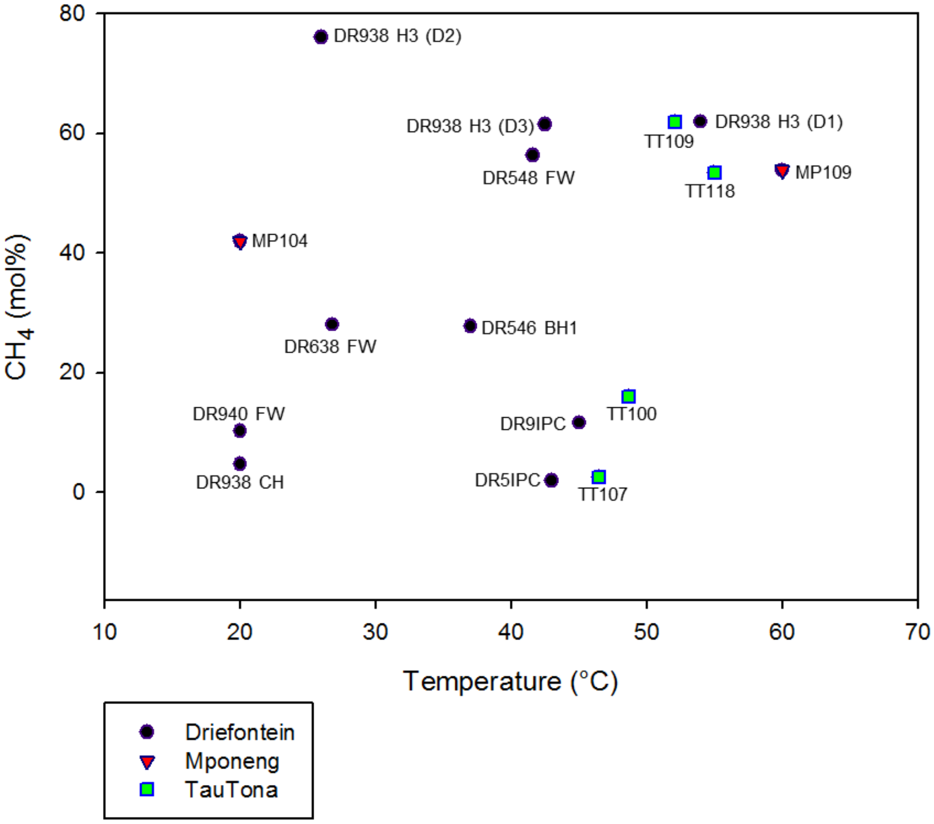

Figure 7.1: A plot of temperature versus CH_4 concentration. The plot shows that higher CH_4 concentrations are generally associated with higher temperatures showing a positive linear trend.

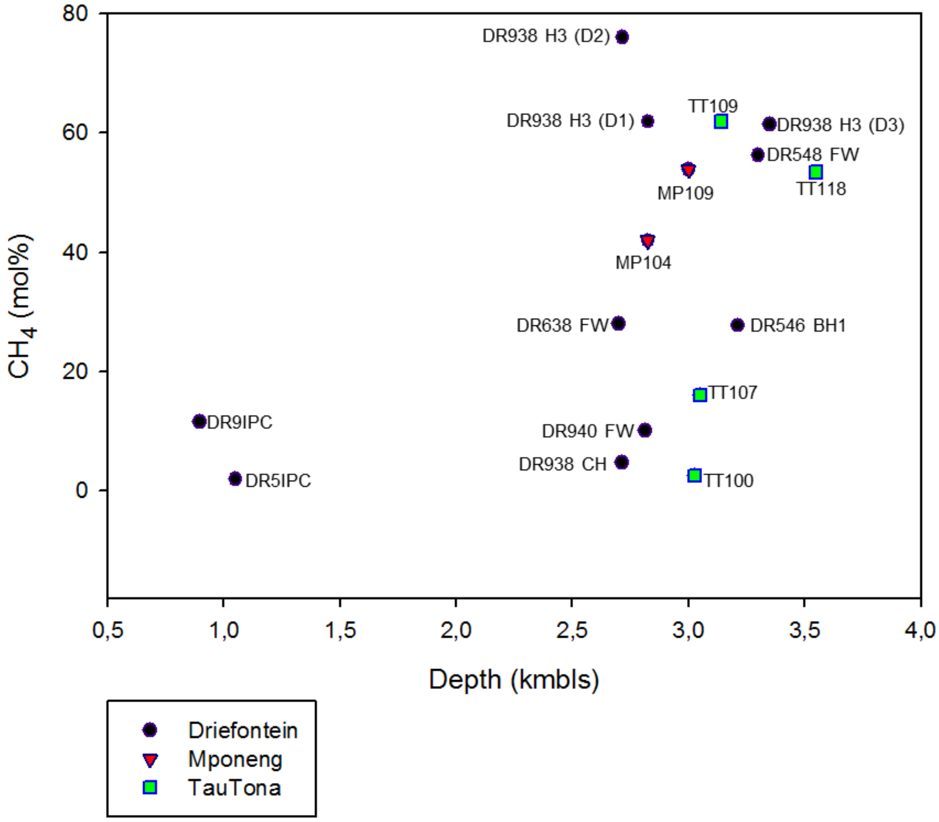

Figure 7.2: A plot of the relationship between depth and CH_4 concentration. The samples from the Driefontein, Mponeng, and TauTona gold mines samples generally have increasing methane concentration with increasing depth. DR - Driefontein, MP - Mponeng, TT- TauTona.

Groundwater is a significant mode of mobility for the gases found at depth. Stable isotope analysis of δ^2H and δ^{18}O gives a good indication of the possible source and type, whether meteoric or hydrothermal, of groundwater found within a sedimentary basin (Blasch & Bryson, 2007; Heilweil, et al., 2009). The relative proportions of δ^2H and δ^{18}O contained in water are shown as an indication of the deviation from the global meteoric water line (GMWL). The stable isotope analyses were run for some of these boreholes the results are summarized in Table 7.2. The values were then plotted against the GMWL and the local meteoric water line (LMWL) of Pretoria. The GMWL is an equation, formulated by Craig (1961), that expresses the worldwide average relationship between hydrogen and oxygen ratios in natural terrestrial water. The

GWML has a regression line of $\delta^{2}H = 8.0*\delta^{18}O+10$. The LMWL, on the other hand, is the regression line derived from data collected from a local site and may differ from the GMWL. The LMWL has a line regression line of $\delta^{2}H = 6.7*\delta^{18}O + 7.2$ (IAEA/WMO, 2017). Pretoria has been used as the LMWL because it is one of two Global Network for Isotopes in Precipitation (GNIP) stations in South Africa. Apart from Cape Town, which is located at the southernmost tip of South Africa, Pretoria has an extensive collection of rainfall and stable, environmental isotope data that dates back to the 1960s (West, et al., 2014).

Except for four samples from the Mponeng and Driefontein gold mines, the samples generally cluster along the meteoric water line (Figure 7.3). The Driefontein samples, DR546 BH1 and DR548 FW, on the far left of the LMWL, are comparatively enriched in $\delta^{2}H$ and depleted in $\delta^{18}O$ relative to the LMWL. These were both collected at depths greater than 3 000 mbls within the Ventersdorp Supergroup. There are three possibilities for these observed values. The first possible explanation is that the precipitation coming from a higher altitude than Pretoria, a reference point based on LMWL data which is located 55 km north of Johannesburg, may have resulted in the lighter isotopic signature. The other possibility is that the depleted $\delta^{18}O$ signature may represent palaeometeoric water that precipitated during either warmer climate or may have been affected by magmatism associated with the extrusion of the lavas of the Ventersdorp Supergroup. This is because $\delta^{18}O$ content changes as temperatures fluctuate (Duane, et al., 1997; Hoefs, 2009). This is palaeometeoric, fissure water is described by Lippmann, et al. (2003) as ranging in age between 1-100 Ma dated using dissolved noble gas, ^{36}Cl, $\delta^{2}H$, $\delta^{18}O$ data. A third possibility is the effect that the geological formation along which the water flows has on the isotopic signature of that water. That is, the two boreholes lie within the Ventersdorp Supergroup lavas and the more positive $\delta^{2}H$ values may be the result of isotope exchange with surrounding rock or hydration (Lippmann, et al., 2003). Isotopic exchange between carbonates and silicates may produce reduced values for $\delta^{18}O$ without affecting the $\delta^{2}H$. The possibility of such an isotopic exchange occurring within quartzites is small because the rock does not readily exchange at temperatures below 100°C (Matthews & Beckinsale, 1979). The other, and most likely possibility, is the hydration of the Ventersdorp lavas that would result in more $\delta^{18}O$-depleted, $\delta^{2}H$-enriched water as seen in samples DR546 BH1 and DR548 FW (Onstott, et al., 2006). Clark and Fritz (1997) proposed that such observed values might be the result of hydrothermal fluid undergoing isotopic exchange with rock strata at temperatures between ~250 and 300°C. This is likely considering that the Witwatersrand Basin has undergone metamorphism, with which the hydrothermal fluid is associated that raised temperatures up to 350 ± 50°C (Phillips & Law, 1994). The water would have cooled over time to the present day recorded temperatures, exhibiting the more negative $\delta^{18}O$ and more positive $\delta^{2}H$ isotopic signatures (see Table 7.2).

Table 7.2: Stable $\delta^{18}O$ and $\delta^{2}H$ isotope data of fracture water collected from boreholes in the Driefontein (DR), Mponeng (MP), and TauTona (TT). Apart from samples DR546 BH1 and DR548 FW, which have the most negative $\delta^{18}O$ values, the data ranges between approximately -4 ‰ and -7‰. The $\delta^{2}H$ values range between -24‰ and -34‰, where DR548 FW is the only exception with a $\delta^{2}H$ recording of -10.30‰. A plot of $\delta^{18}O$ and $\delta^{2}H$ in Figure 7.3 shows that most of the samples lie along or close to the meteoric water line.

Borehole name	δ^{18}O-**H$_2$O** **(‰)**	δ^{2}H-**H$_2$O** **(‰)**	**Geological Formation**
DR546 BH1[a]	-13,14	-24,38	VL
DR548 FW[b]	-12,28	-10,30	VL
DR5IPC[c,d]	-4,44	-24,26	TD
DR638 FW	-6,19	-33,96	VL
DR938 H3 (D3) [e]	-5,64	-26,93	CRQ
DR938 H3 (D2)	-5,01	-27,87	VL
DR938 H3 (D1)	-5,80	-27,71	VL
DR940 FW	-4,78	-27,20	VL
MP104[b]	-6,82	-29,13	VL
MP109	-6,95	-30,44	CRQ

TT100	-4,89	-25,69	CRQ
TT107[c, d]	-4,78	-24,42	CRQ
TT109[c, d]	-5,02	-25,29	CRQ
TT118	-5,19	-31,32	CRQ

Source: a. Lippmann, et al. (2003); b: Silver, et al. (2012); c. Simkus, et al. (2016); d: Lau, et al. (2014); e. Moser, et al. (2003). Samples that do not have accompanying superscript have not been previously reported. VL – Ventersdorp Lavas, TD – Transvaal Dolomites, CRQ – Central Rand Quartzites.

DR5IPC was collected from the dolomitic aquifer of the Transvaal Supergroup, and the observed δ^{2}H and δ^{18}O values are consistent with recharge originating from modern surface precipitation, which in turn is reflected by its position along the Local Meteoric Water Line (LMWL). The water derived from the DRIPC samples has been described as hypoxic palaeometeoric water with an approximate age of 12 300 years based on δ^{14}C and ^{3}H analyses (Borgonie, et al., 2015).

The DR938 H3 borehole is probably one of the most documented boreholes in the gold mines of the West Wits Line Goldfield. DR938 H3 has a collar depth of 2 712 mbls and samples have been collected down to a depth of 3 350 mbls – the borehole spanning a total length of 748 m. The sample names DR938 H3 (D1), DR938 H3 (D2), DR938 H3 (D3) denote the different times at which they were collected. DR938 H3 (D1) was collected in October 2001 at a depth of 2 825 mbls and less than a month later a second sample, DR938 H3 (D2), was collected in November 2001 at a depth of 2 716 mbls. The last sample, DR 938 (D3), was collected in July 2002 at 3 350 mbls. The stable isotope data derived from the different sampling depths, collected at different times, exhibit a noteworthy trend pertaining to the groundwater springing from the borehole. In order for a change in isotopic data to be considered significant, there has to be a change that is greater than 0.5‰ of the previous, comparative reading (Bense & Hiscock, 2014). The δ^{18}O and δ^{2}H readings for DR938 H3 (D1) were -5.80‰ and -27.71 ‰, respectively. The second sample, DR938 H3 (D2), was collected approximately 100 m above the first sample point along the borehole and yielded values of -5.06‰ for $\delta^{18}O$ and -27.87‰ for $\delta^{2}H$. A comparison between samples DR938 H3 D1 and DR938 H3 D2 shows that there is not much of a change in the $\delta^{2}H$, but there is a notable difference in the $\delta^{18}O$ value – a 0.74‰ increase. The water in the borehole appears to have become more $\delta^{18}O$ – enriched, and while DR938 H3 (D1) lies to the left of the LMWL, the second sample, DR938 H3 (D2), lies right along the LMWL. Eight months later, at a depth of 3 350 mbls, sample DR938 H3 (D3) was collected: the isotopic analysis shows the water comprises -5.64‰ of $\delta^{18}O$ and -26.93‰ of $\delta^{2}H$. The $\delta^{18}O$ value for this sample is closer to that of the first sample, which had a reading of -5.80‰. The variable $\delta^{18}O$ may be an indication of either a recharge of the more palaeometeoric water by modern precipitation via fractures and faults in the bedrock as noted by Moser, et al. (2005), or may be an indication of the variability of the type of water found along the length of the borehole.

The TT118 of the TauTona samples lies along the LMWL, generally becoming more depleted in $\delta^{2}H$ and $\delta^{18}O$ with increasing depth. TT118, the deepest sampling point (3 550 mbls), lies on the GMWL, giving an indication of water that may have precipitated at an earlier time, in a warmer climate. This sample also attests to the observation that water at greater depths is more depleted in $\delta^{18}O$ (Bense & Hiscock, 2014). The variability of the gas composition of the samples gives an indication of the behaviour of methane as it migrates upwards. As previously stated, the methane content increases with increasing depth, and this is the case with the TauTona samples. This upwards reduction in the methane concentration, from deeper to shallower depths, may be an indication of the 1) diffusion of the gas from a high- to a low-pressure area, and/or 2) lower temperatures as one moves up the mining levels.

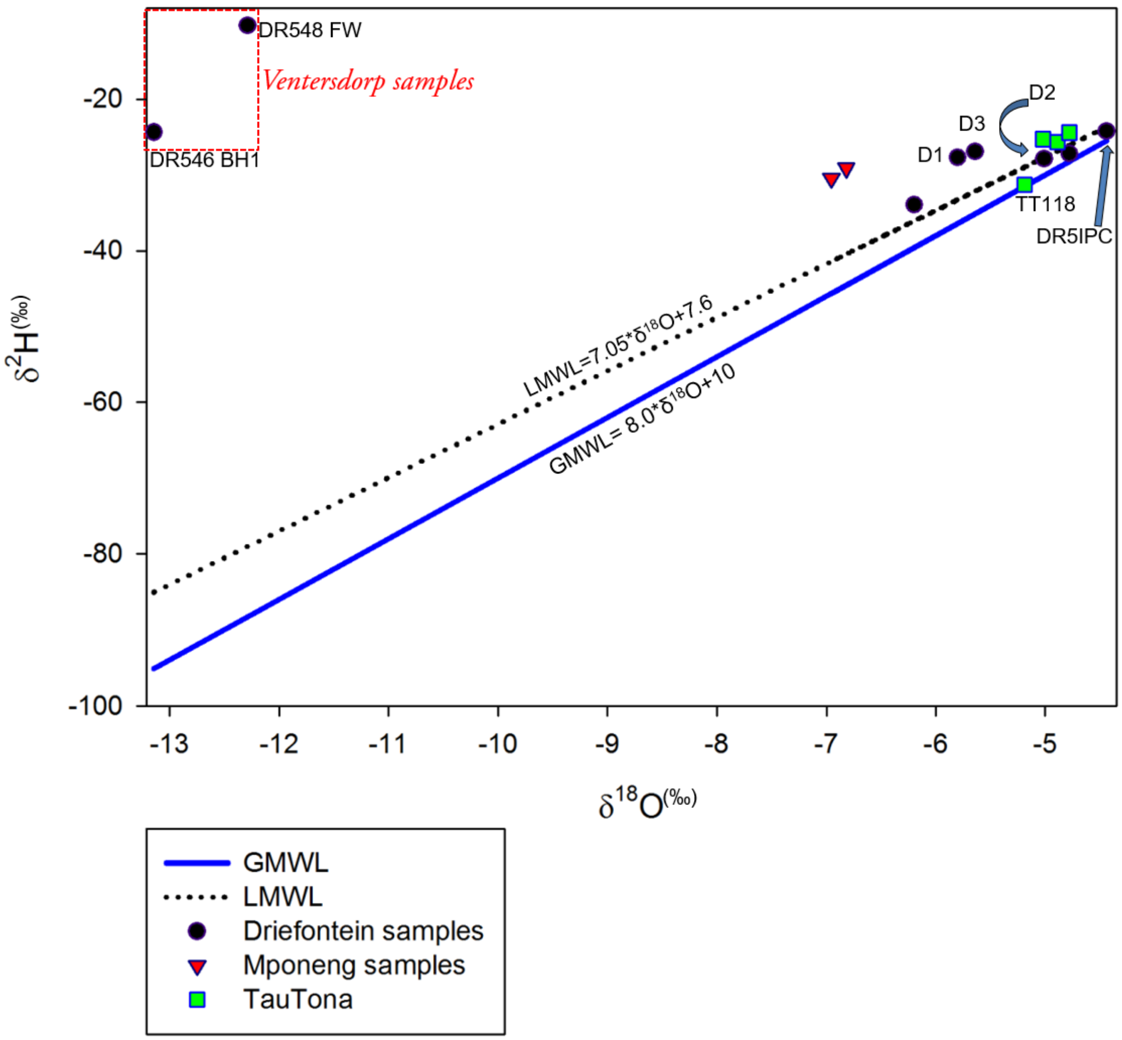

Figure 7.3: $\delta^{18}O$ and $\delta^{2}H$ plot of the samples collected from the 16 boreholes. Most of the samples cluster along the meteoric water lines, except the Mponeng gold mine samples (inverted triangles) as well as samples from borehole DR546 BH1 and DR548 FW (enclosed by red square), which were the only two samples collected from the Ventersdorp lavas. Although from the same borehole, D1, D2, D3 of borehole DR938 H3 have distinctly differing values. LMWL – Local Meteoric Water Line; GMWL – Global Meteoric Water Line.

7.2 3D fault detection and visualization

One of the integral components of this study was to identify faults and dykes that intersect the potential source of hydrocarbons in the BS and the auriferous VCR. The BS and VCR, described in detail in Chapter 6, are seismically delineated throughout the survey area. As previously mentioned, in seismic data interpretation, faults are identified as areas where reflector continuity is interrupted by poor resolution resulting from the vertical displacement of the reflector (Bacon, et al., 2007). Faults offsetting the aforementioned horizons were identified along inline and crossline sections across the entire seismic survey. These faults were above the seismic resolution limit (above a quarter of a dominant wavelength, i.e. 25 m for these data) and thus could be detected. Several major faults transect both the BS and the VCR but there are faults that appear to crosscut only the underlying BS.

In Chapter 6.3, fault interpretation was mostly done for the Kusasalethu, Deelkraal and some portion of Mponeng and TauTona gold mines. Due to the location of most of the borehole sampling points, interpretation has been extended into the rest of the Mponeng, TauTona and the Driefontein gold mines. The process of horizon picking and identifying faults along the BS and VCR is detailed in Chapter 5.1.2 and 5.1.3, and in the methodology section of Chapter 6, and will hence not be reiterated in this section. For the purposes of identifying faults that were below the seismic resolution limit, the edge-detection method was applied to the extended portions of the BS. Although previously interpreted by Manzi, et al. (2012, 2014), the VCR horizon was also included, and the attribute applied for the purpose of comparison between the two horizons for this particular study (Figure 7.4).

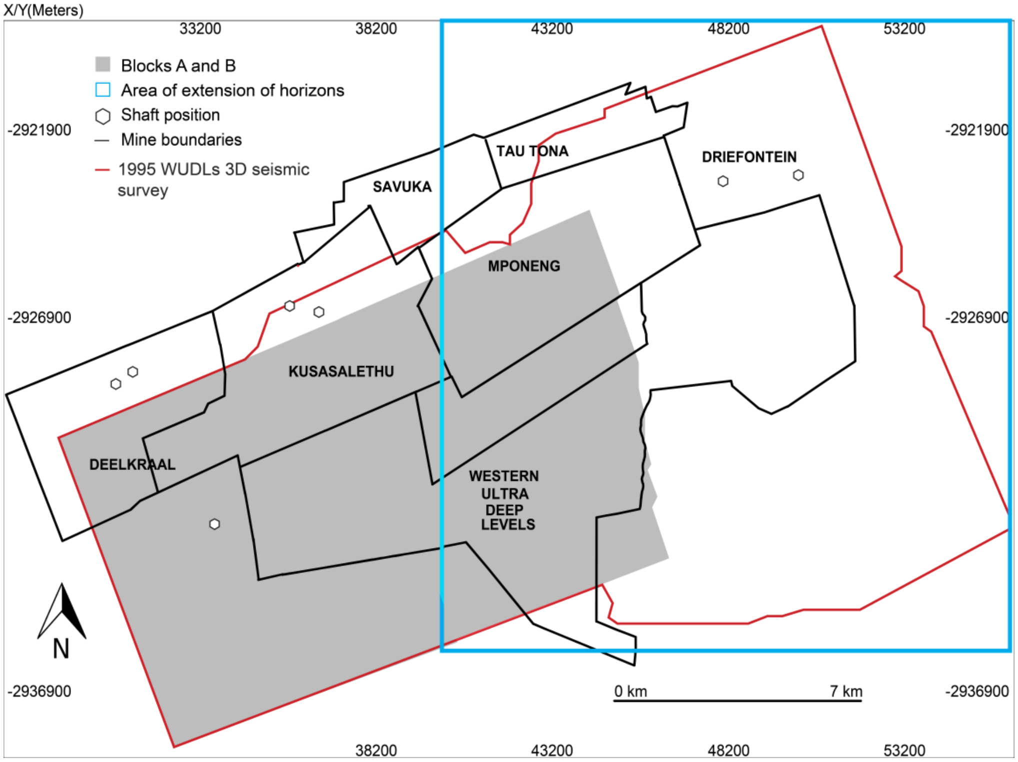

Figure 7.4: A map of the WUDLs 3D seismic survey area. The shaded area are blocks A and B of the previously interpreted BS and VCR in Chapter 6. The area of the survey shows the extent of the extension of the interpretation of the survey; this extension includes most of the Mponeng gold mine as well as including the Driefontein and TauTona gold mines.

In Figures 7.5 and 7.6, the edge-detected horizons reiterate the point that gold mining in the region occurs in the structurally complex collar of the Witwatersrand Basin. The edge-detected surfaces of the BS and VCR show that the area has undergone a considerable amount of structural deformation, particularly in the Driefontein gold mining area as well as in most of the southern portions of the goldfield (outlined in white rectangles in Figure 7.5). Two key factors have previously been noted as limitations in high confidence interpretation of horizons in the mentioned areas and these are, 1) poor seismic imaging due to the dolomite aquifers of the Transvaal Supergroup that directly overlie the rocks of the Witwatersrand Supergroup in the Driefontein area and 2) structural complexity (refer to Chapter 6).

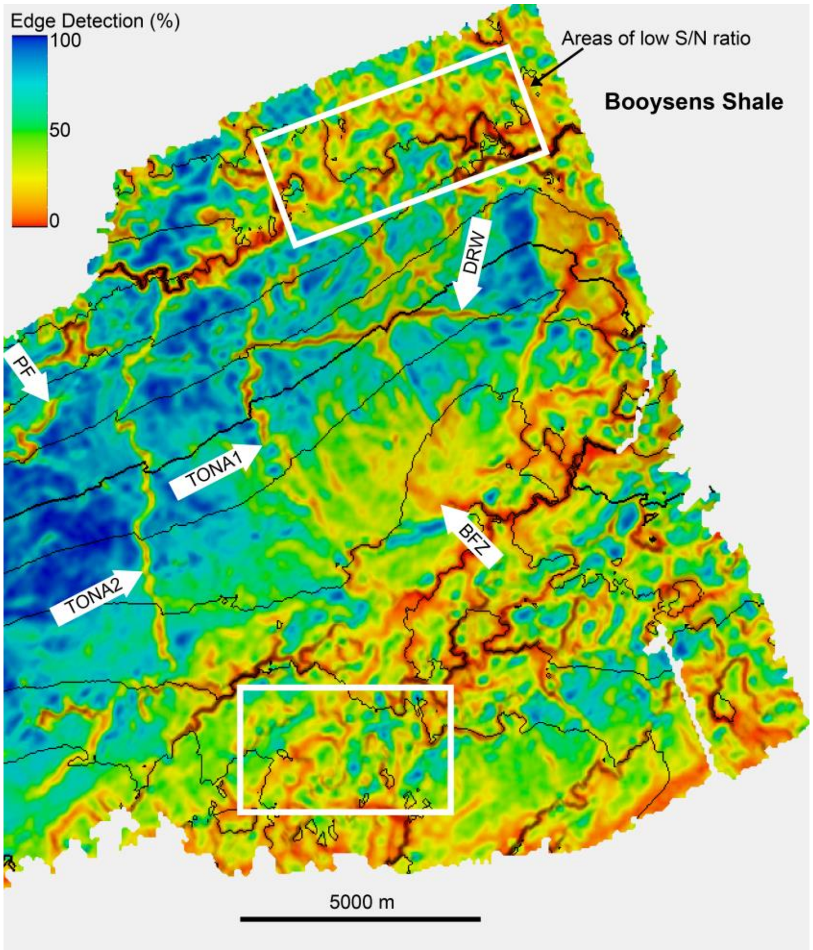

Figure 7.5: Edge-detection map of the Booysens Shale (BS). The major faults intersecting the horizon have been identified. These are the Bank Fault Zone (BFZ), the DRW (Driefontein West) Fault, Tona 1 and 2 Faults and the Pretorius Fault (PF). Areas of low signal-to-noise (S/N) are also marked (white rectangles) on the map.

The faults interpreted vary in size from first-order scale, which are faults that have throws between 2.5 km and 400 m, to second-order (400 m to 25 m), and third-order scale faults that have throws below 25 m (Manzi, et al., 2013a). Considering that the seismic data being used for this study are in the time domain with a total vertical span of 6 seconds (or 6 000 ms) which equates to approximately 12 km. The 3D seismic data used in this study has been previously used first-order faults would have displacement between 1250 ms and 200 ms, second-order faults, displacement between 200 ms and 12.5 ms, and third-order faults, displacement below 12.5 ms. The main faults that have been identified along the BS horizon are the Bank, DRW, Tona 1 and Tona 2, and Pretorius faults (Figure 7.5). The two horizons have many shared structures between them; however, Tona 2 does not appear to intersect the VCR (Figure 7.6).

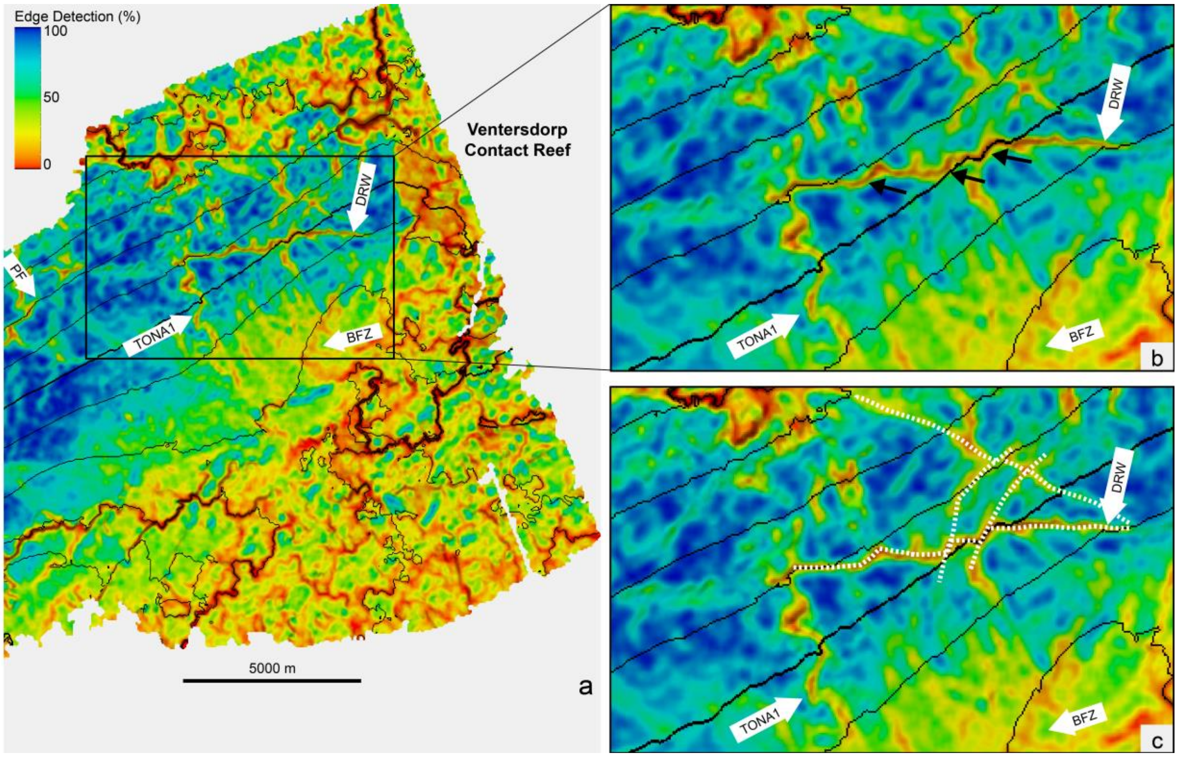

Figure 7.6: a) An edge-detection map of the Ventersdorp Contact Reef (VCR) shows that apart from Tona 2, all the faults intersecting the Booysens Shale (BS) in Figure 7.5 intersect the VCR as well. A close-up of a portion of VCR (b) highlights that the DRW Fault has been crosscut by a set of left-lateral strike-slip faults (the planes of displacement are indicated by the black arrows and outlined in white dashed lines in (c)).

The Bank Fault is the only first-order fault that has been identified within the seismic survey area. It is situated on the eastern edge of the West Wits Line Goldfield, separating the goldfield from the adjacent West Rand Goldfield, which lies further east, beyond the boundary of the survey area. The Bank Fault is a north-northeast trending, normal listric fault with a maximum throw of approximately 1250 ms (2.5 km) that dips between 65-75° westward (Figure 7.7). The fault may have formed during the extrusion of the Platberg Group of the Ventersdorp Supergroup, which occurred between 2.70 and 2.64 Ga, characterized as a major rifting event with concurrent heating of the lithosphere by a mantle plume (Stanistreet & McCarthy, 1991; Manzi, et al., 2013a). The seismic data in Manzi, et al. (2013a) show that faulting extends from depth through the Witwatersrand and Ventersdorp Supergroups but is truncated at the base of the Transvaal Supergroup and with a proposed age of normal faulting activity ranging between 2.71 and 2.58 Ga. Fault throw mapping done by Manzi, et al. (2013a) shows that the Bank Fault has a variable throw along its length with throw values increasing towards the north-northeast. Clockwise block rotation during listric normal faulting was followed by the formation of a rollover anticline (McCarthy, 2006; Manzi, et al., 2013a).

Figure 7.5 shows a number of second- and third-order faults that extend from the main fault in the hanging wall and footwall, and those along with the Bank Fault, make-up the Bank Fault Zone (BFZ). Unlike the main fault, which trends in the northeast direction, these sub-ordinate faults trend in a northwest-southeast direction relative to the Bank Fault and extend for approximately 3 km into the gold mines that lie northwest of the BFZ.

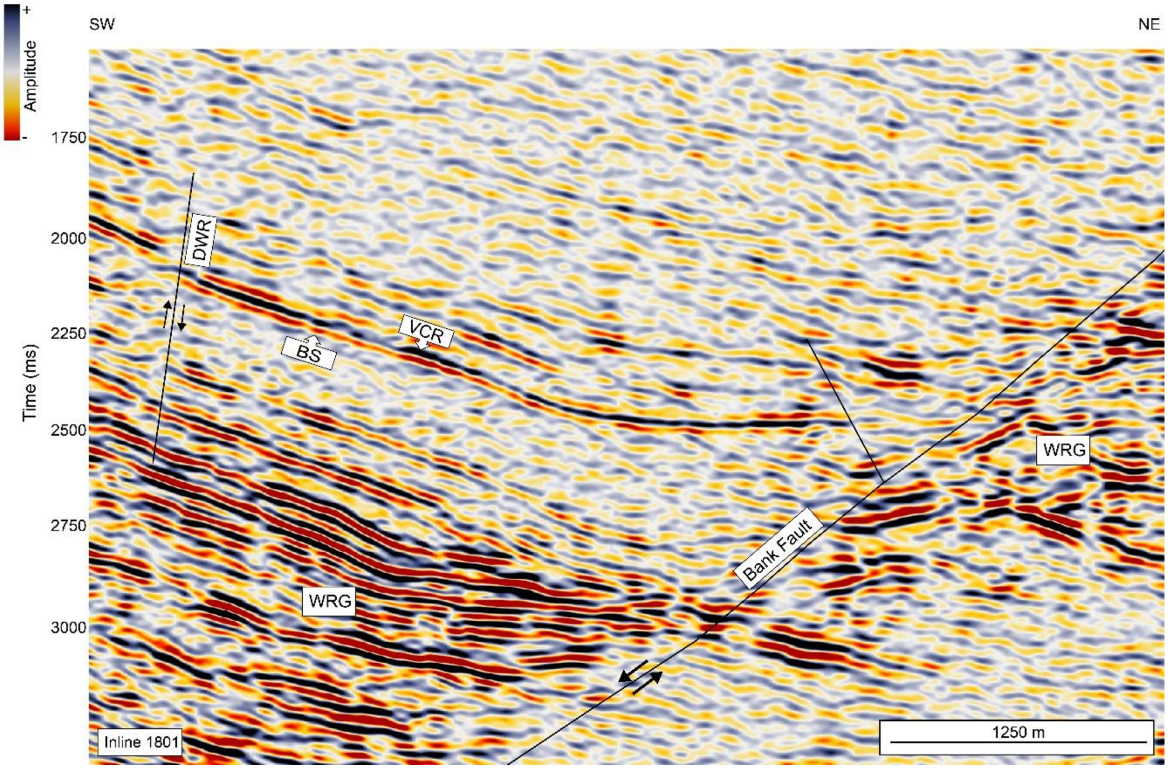

Figure 7.7: Inline 1801 showing the degree of displacement of the rocks of the West Rand Group (WRG) by the Bank Fault. The rocks of the West Rand Group (WRG) are significantly displaced by the Bank Fault by approximately 1 500 ms. The DRW Fault extends from the WRG and displaces the Booysens Shale (BS) and Ventersdorp Contact Reef (VCR) reflectors by about 150 ms.

The DRW fault is a normal fault that trends in an east-west direction, steeply dips towards the south at an angle between 75-80°, and has an approximate maximum vertical displacement of 100 ms (Figure 7.7). The fault displaces West Rand Group stratigraphy, intersects both the BS and VCR and, according to edge-detection mapping by Manzi, et al. (2012), it also displaces the base of the Transvaal Supergroup. The fault forms a graben between itself and the Bank Fault. The DRW fault appears to terminate at the Bank Fault and displaces thrust faults in the West Rand Group related to compression during the emplacement of the Klipriviersberg Group (Stanistreet & McCarthy, 1991). The fault is not continuous along its length (see Figures 7.5 and 7.6) but is cut by left-lateral strike-slip faulting which is more prominent on the VCR horizon (Figure 7.6b). Shearing planes are characteristically areas of major partings associated with bedding-parallel faults such as is seen in the altered Booysens and Green Bar shales. In the case of the Driefontein gold mine, stick-slip motion that occurs along bedding-parallel faults has been associated with lensoid faults found in the hanging wall of the VCR (Sylvester, 1988; Roberts and Schweitzer, 1999).

The Tona 1 fault (so named after its proximity to the TauTona gold mine borehole samples) is a steeply dipping (70-80°) reactivated fault that extends from the BS, through the VCR and all the way up to the contact between the Ventersdorp Supergroup and the base of the Transvaal Supergroup – the BLR (Figure 7.8). This northwest trending second-order fault has a throw of between 25 and 50 ms. There is significant amplitude attenuation along the BS reflector in the hangingwall and footwall of the Tona 1 fault that extends from depth up to the BLR. The disturbance is more pronounced along the BLR and such a disturbance of reflector continuity is generally characteristic of dyke intrusions in seismic data (Bacon, et al., 2007). The Tona 1 fault also exhibits characteristics of a fault reactivation where the upper BLR has a different sense of displacement than the lower BS and VCR horizons.

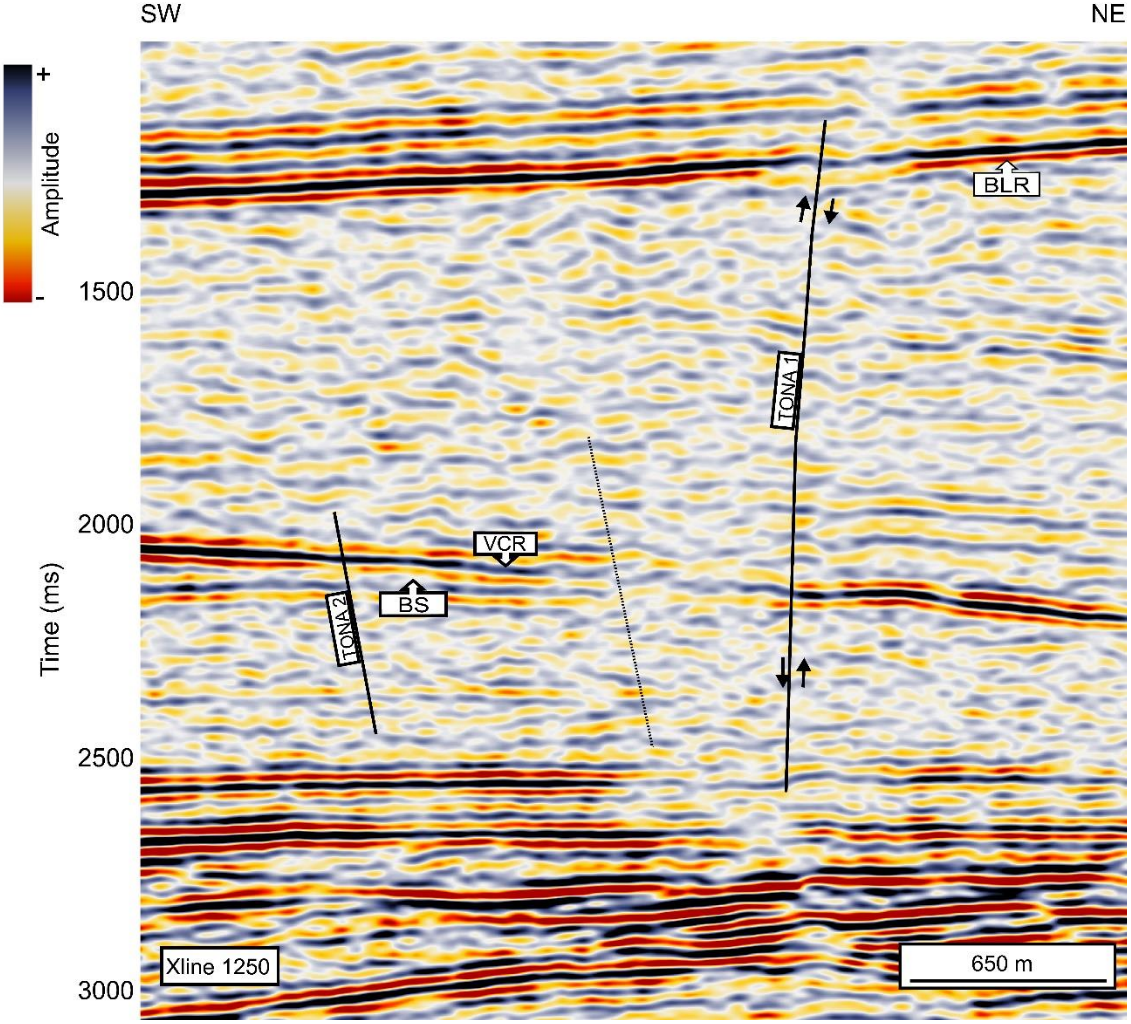

Figure 7.8: Crossline 1250 showing the Tona 1 and Tona 2 faults. Tona 1 intersects the West Rand Group (WRG) rocks, the Ventersdorp Contact Reef (VCR) and even beyond the Black Reef (BLR). The fault has a differing sense of displacement in the WRG than it does along the VCR and BLR. It is therefore considered to have undergone reactivation. The dashed line illustrates the extent of a possible dyke swarm. Tona 2 normally displaces only the Booysens Shales (BS) but leaves the VCR undisturbed.

It appears that the lower horizons have undergone compressional deformation where, as described by Williams, et al. (1989), the hangingwall of the horizon has been displaced above the pre-deformational regional elevation. The Tona 1 fault was initially a reverse fault that was later reactivated as a normal fault that displaced the

BLR. Fault reactivation in the West Wits Line Goldfield has played a crucial role in fluid flow and gold mineralization (Phillips & Law, 1994; Jolley, et al., 2004). Tona 1 fault is a significant fault because, as will be discussed in detail in the following section, three of the four TauTona samples were collected in close proximity to this fault. Tona 2 dips towards the east at an angle of approximately 70-80°. Like the Tona 1 Fault, Tona 2 is a normal fault that has a throw of no more than 100 ms.

The Pretorius Fault is the largest fault intersected at the Mponeng and TauTona gold mines. A full description of the characteristics of the fault and associated fault zones is given in Chapter 6.

7.3 The application of the volumetric attributes - ant-tracking attribute

7.3.1 The ant-tracking attribute

The following section introduces the application of the volumetric seismic attribute (namely ant-tracking). Based on the workflow presented in Chapter 5.3.2, parameters were applied to an edge-enhanced volume to produce an ant-tracked seismic volume. The ant-tracking algorithm was run three times on an edge-enhanced volume in order to enhance fault, as well as sub-horizontal, discontinuity detection. A comparison of the original amplitude display seismic volume with the first- and third-run ant-tracked volumes (Figures 7.9 to 7.11) shows the significant differences between the three volumes. All three iterations have different characteristics as seen in Figures 7.12 and 7.13; however, the first and third iterations show the greatest degree of structural variations and are described in more detail below.

Prior to the discussion of the results of the comparison between conventional seismic amplitude display and application of the ant-tracking attribute, it is worth noting the challenges faced in the interpretation process:

- Confident seismic interpretation using attribute analysis is dependent on the quality of the seismic data. Data that are of high quality yield good results, but confident interpretation is hampered in areas of low signal-to-noise ratio.
- The stereonet filter is used in the ant-tracking workflow to filter the orientation of the structures that the interpreter wants highlighted. The choice not to apply a stereonet filter introduced artefacts. The effect of lineaments such as the acquisition footprint being detected as pseudo-structures was reduced by correlating known information about the orientation of the structures intersected by the boreholes. Despite the drawback of not applying the filter, faults and fractures could still be confidently detected by the ant-tracking attribute, and the edge-enhancement method remains one of the best seismic attributes for fault enhancement.
- Although the spatial data for the samples were provided, the borehole deviation surveys were not. Thus, most of the boreholes are represented as points. In instances where the borehole orientation and deviation are noted, the information is derived from literature and the authors are noted.

The best indicator of the presence of a fault along a horizon is the reduction of reflector's amplitude strength because of vertical displacement of the reflector. This is how faults (and sometimes dykes) are interpreted in amplitude display as seen in Figure 7.9. The shortfall with relying on basic amplitude display is that there may be some ambiguity regarding fault continuity and connectivity. The use of the ant-tracking attribute reduces that ambiguity and even highlights structures that were not apparent before. Figure 7.10 is the result of the first-run of the edge-enhanced volume through the ant-tracking attribute. Several faults and fractures (and their connectivity) that were not apparent in the amplitude display are now evident in the ant-tracked volume as marked by red arrows in all three volumes. The stereonet filter was not applied in order to constrain the search of the intelligent "ants" to particular orientations, thus the attribute has also identified bedding-parallel discontinuities.

These are marked by the blue rectangles in all three figures (Figures 7.9 to 7.11); the discontinuities are identified as high amplitude areas in the amplitude display. The continuity of some of the fracture zones that was not discernible in the amplitude display is enhanced in the first run; refer to pink ellipses in Figures 7.9 to 7.11.

The first-run is characterized by small-scale faulting and fracturing as well as what may be considered fractured rock zones. There appears to be variability in the distribution of the fracture zones based on the key lithologies that have been identified in the study area; that is dolomite (or carbonates), lavas, quartzites and conglomerates (see stratigraphic column in Chapter 2.1). The density of the fracture zones is much greater in the dolomites of the Transvaal Supergroup and this coincides with the hydrogeological nature of the rock as a highly permeable aquifer. The Ventersdorp Supergroup and Central Rand Group have similar clusters of fracturing and faulting as observed in the Transvaal Supergroup. The one of the causes for the intensity of fracturing in these rocks is mining activity, which involves blasting and drilling (Riemer & Durrheim, 2011).

Milev and Spottiswoode (2001) also found that the different rock types found in the mining district, particularly those that are the hanging and footwalls to the VCR experience different degrees of structural disturbance caused by mining induced seismicity. The frequency of fracturing and the isolated fracture zones decreases downwards towards the sediments of the West Rand Group. There are two possible explanations for the dispersal of these fracture zones and lack thereof in the West Rand Group. The first possibility is the extent and effect of mining and mine seismicity in the Witwatersrand Basin. A large proportion of the gold mining in the basin occurs in the Central Rand Group and due to the depth of any possible minable reefs, subsides in the West Rand Group. There exist both natural as well as mine-induced fractures and faults in the gold mines and the West Rand Group appears to be dominated by natural structural deformation (Reches, et al., 2006; Riemer &

Durrheim, 2011). The second possibility is frequency filtering; seismic signals are highly attenuated as they propagate deeper into the Earth (Bacon, et al., 2007). This is less likely because the initial run of the ant-tracking attribute (Figure 7.9b) highlights the fractured nature of the basement, which precedes the West Rand Group, quite well. It must be noted that some of the strong reflectors are traced faintly but they are discernible from this run. One disadvantage of the first run is that there are instances where fault extension is quite poor. Therefore, the form and extent of them diminishes instantaneously and is even often lost in the “chaos” of any fracture zones it intersects.

In the third-run volume (Figure 7.11), the major discontinuities are emphasized, and the resolution of the smaller faults and fractures is diminished. There are instances where major faults have been highlighted by the ant-tracking attribute. The zones of concentrated fracture systems are now also absent from this iteration. The third run on the other hand is different from the first one in that it is the least representative of the structural features that are observed on the amplitude map. The run shows poor visibility and continuity of horizons. Although, some pseudo-structural features preserve their general dip direction in the inline. Most of these pseudo-structures cannot be correlated to the structural features observed in the 3D amplitude map or in the first run ant-tracking map. In summary, none of the features that were highlighted in the amplitude display (Figure 7.9) or first ant-track run (Figure 7.10) are observed in the third run of the ant-tracking inline and crossline sections (Figure 7.11). Under the set parameter conditions, these observations suggest that the ant-track attribute may not be reliable beyond the third iteration. While this is the case in the crossline and inline directions, the depth slices (Figure 7.12) give a different and more useful indication. As seen in Figure 7.13b, the third run ant-track volume fares well in the z-direction as discontinuities are well defined. A good example of this is in the northeastern corner of the survey where amplitude and first-run ant track displays show poor mapping of faults compared to the higher-run iterations, which shows significant improvement in fault detection.

On this run, it is evident that the ants preferentially track strong reflectors (with high amplitudes) in comparison to faults (with lower amplitudes) that intersect the reflectors (Figures 7.12b to d). This means that the more the ant-attribute is computed to an already ant-tracked volume, the more the ants will pick the signal of the stronger discontinuity, i.e. the reflector in this case (as highlighted by the pink squares on the ant-tracked depth slices in Figure 7.12). This is not always the case and the way the ants decide on which discontinuity to enhance is still unclear.

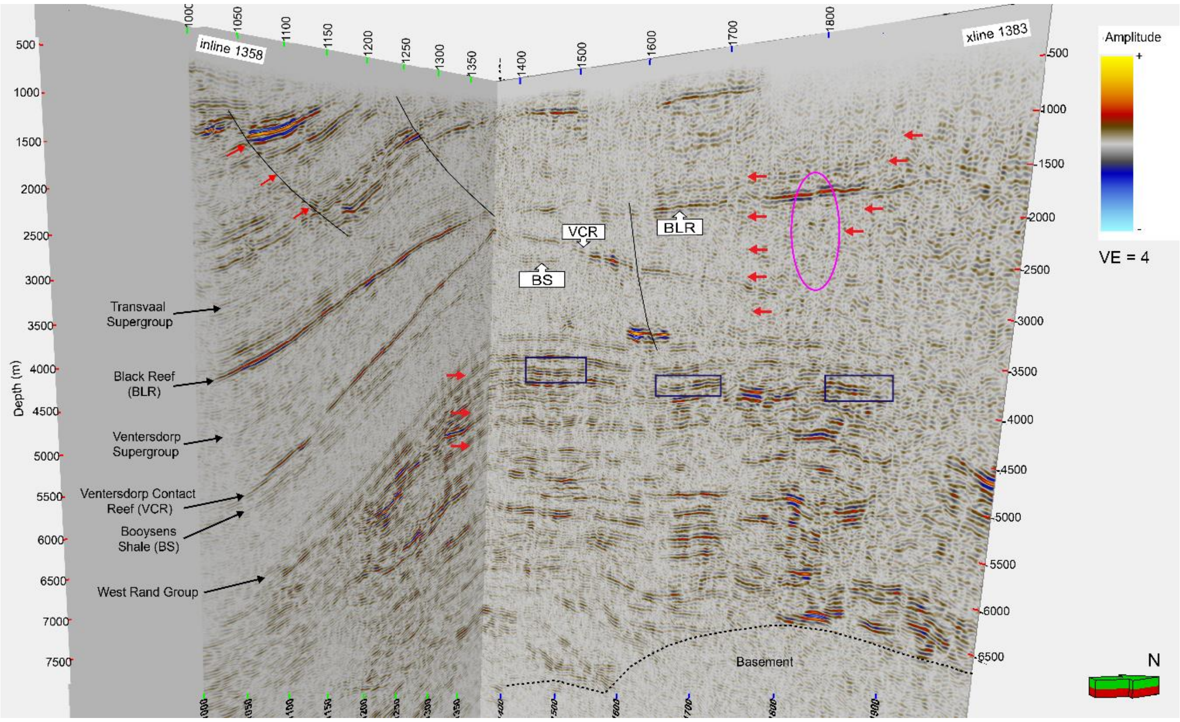

Figure 7.9: A 3D representation of inline 1358 and crossline 1383 of the amplitude display. There are a number of faults (marked by red arrows) and reflectors such as the Booysens Shale (BS), Ventersdorp Contact Reef (VCR), and Black Reef (BLR) that can be identified in the amplitude display. A fault that distinctly displaces the BLR is outlined by the pink ellipse. The blue rectangles highlight areas that have been identified as definitive sub-horizontal discontinuities in the ant-tracking volume in Figure 7.10. The approximate position of the basement is indicated by a dashed line.

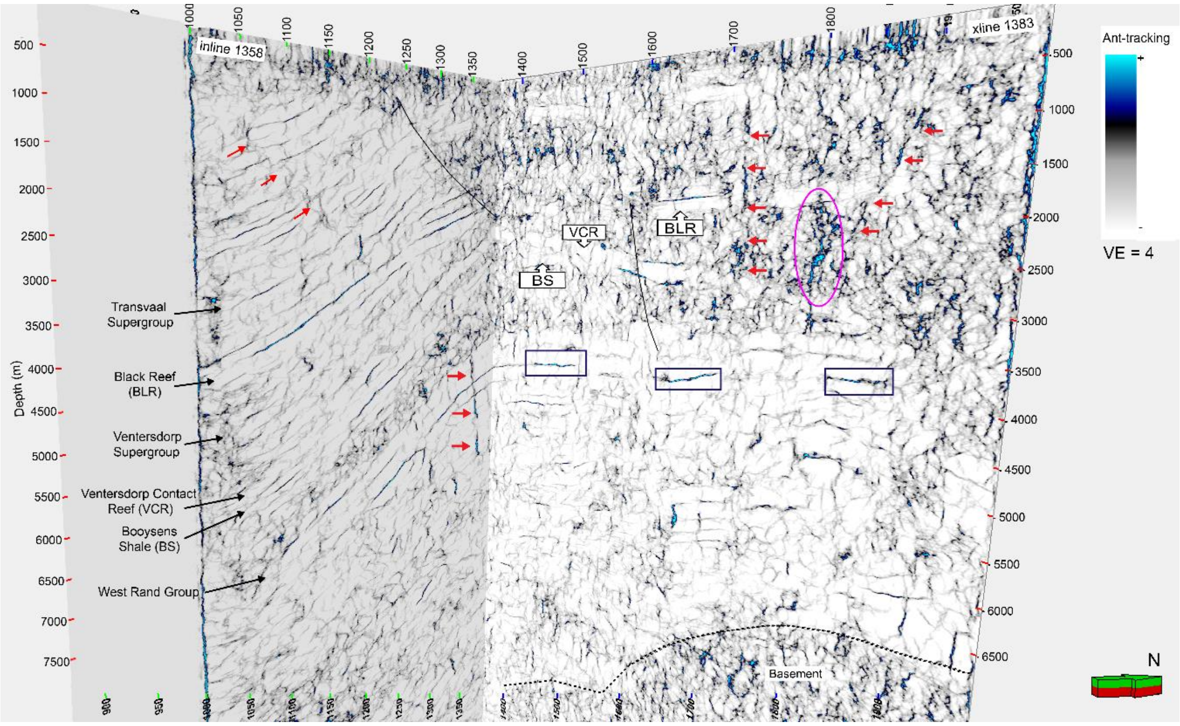

Figure 7.10: A 3D representation of inline 1358 and crossline 1383 of the first-run ant-tracking volume. There are a number of faults, marked by red arrows that have been enhanced by the ant-tracking attribute. Sub-horizontal reflectors such as the Booysens Shale (BS), Ventersdorp Contact Reef (VCR), and Black Reef (BLR) are identifiable in the ant-tracked display as well. The visibility and continuity of some of these sub-vertical faults as well as sub-horizontal discontinuities (outlined by blue rectangles) are enhanced using the first ant-tracking attribute. A fault that distinctly displaces the BLR and previously identified in Figure 7.9 is outlined by the pink ellipsoid. The extension of the fault is now visible using the ant-tracking attribute. The approximate position of the basement is indicated by a dashed line.

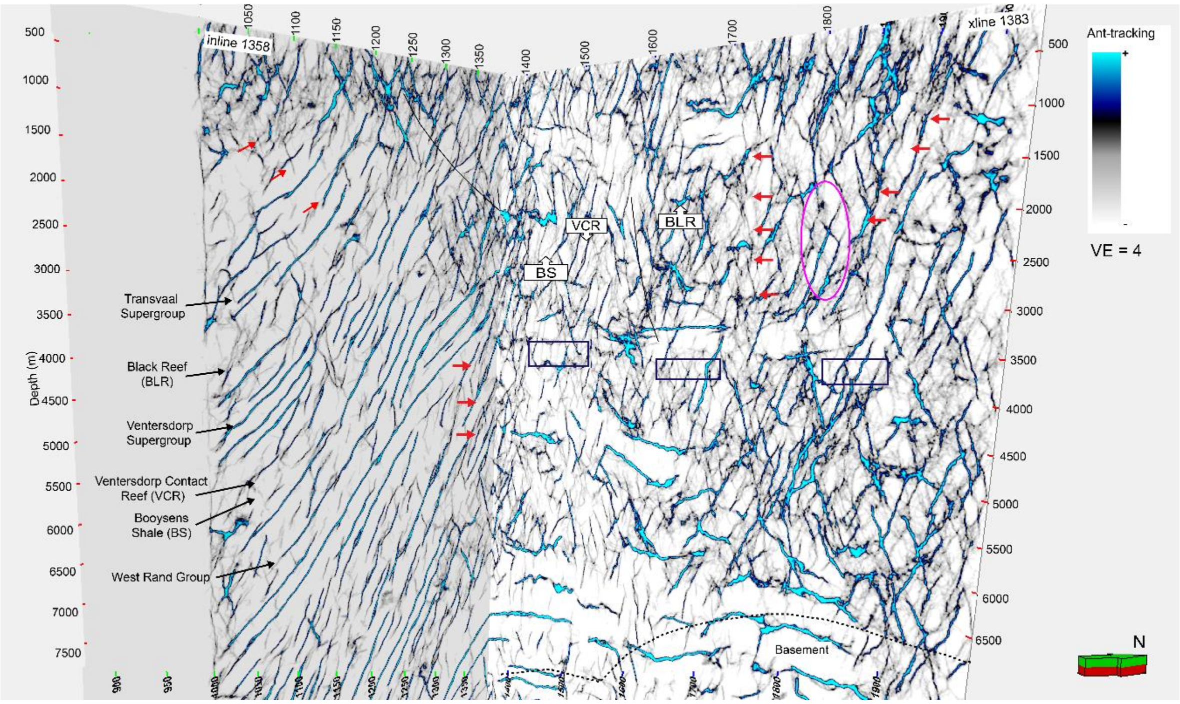

Figure 7.11: A 3D representation of inline 1358 and crossline 1383 of the third-run ant-tracking volume. A set of northwest dipping, sub-vertical lineaments and lateral discontinuities are apparent in the crossline (xline) and inline directions, respectively. Unlike in the amplitude and first-run ant-track displays (Figures 7.9 and 7.10), the faults (marked by red arrows) are no longer apparent. The continuity of the reflectors such as the Booysens Shale (BS), Ventersdorp Contact Reef (VCR), and Black Reef (BLR) is also not evident. The pink ellipsoid marks a visible fault in the amplitude and first-run displays that has not been mapped by this run. The approximate position of the basement is indicated by a dashed line.

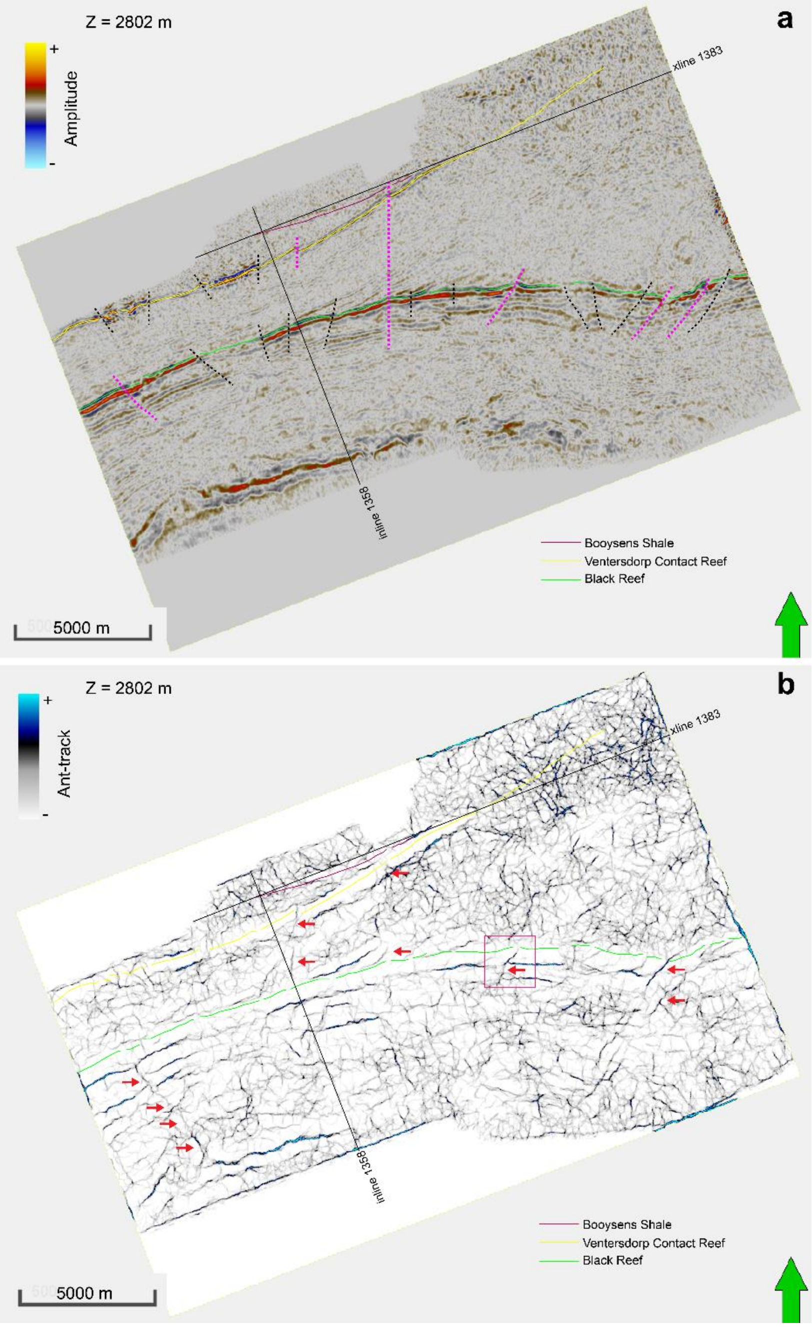

Figure 7.12: Depth slices of an (a) amplitude display and the first run (b) ant-tracking attribute displays in fault detection. The faults picked in the pink dotted line on the amplitude display depth slice are highlighted by the red arrows on the ant-tracking attribute displays.

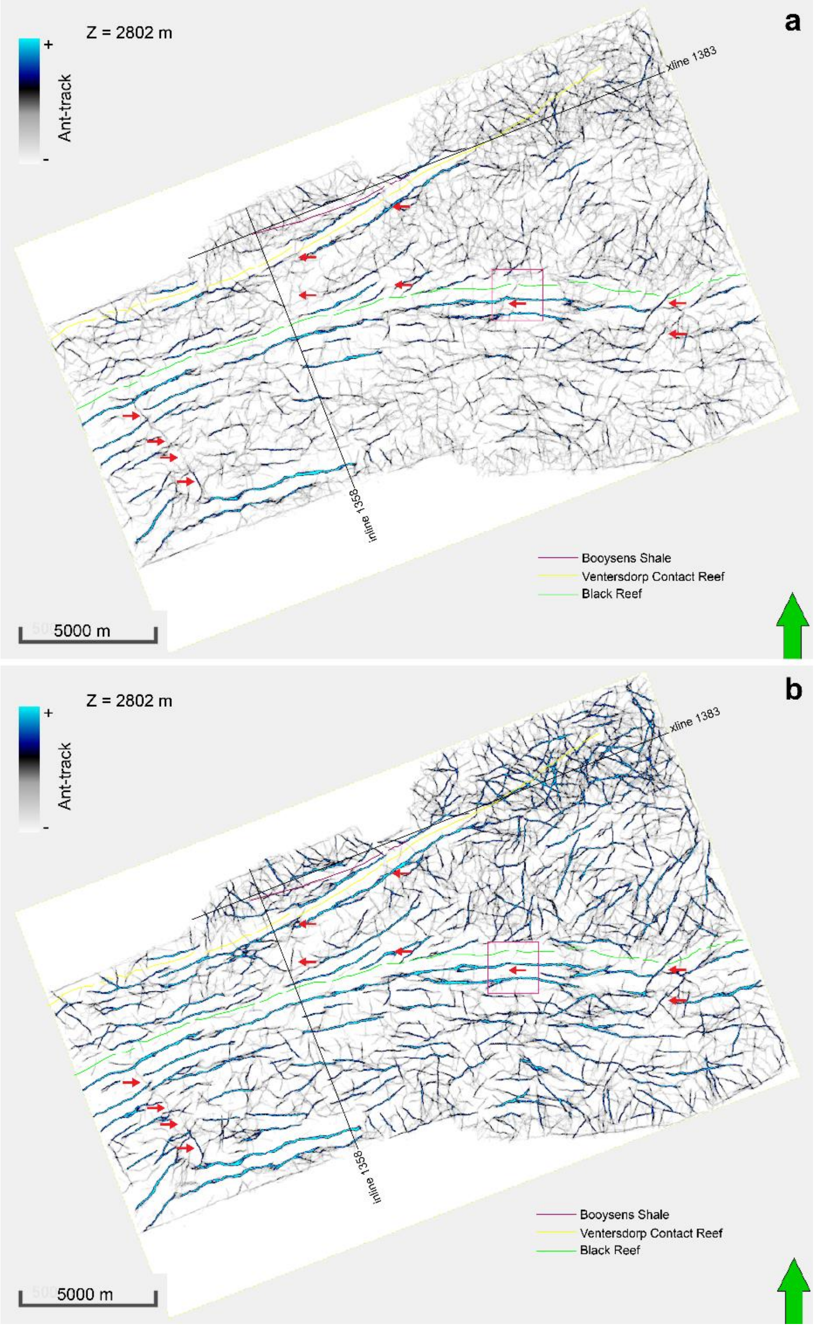

Figure 7.13: Depth slice of the differences between a) second-run and b) third–run ant-tracking attribute displays in fault detection. Faults detected in the first-run generally become more enhanced as the number of iterations increase, i.e. from the first-run to the third-run slice.

7.3.2 Correlation of fault networks and methane data

The use of seismic attributes in the detection of fault networks has proven successful in the 1995 WUDLs 3D seismic data. The main objectives of this study have been to not only see how well the attributes work on PSTM data but mostly importantly, to identify any structures related to the methane gas that has been intersected in the deep gold mines of the Witwatersrand Basin. The previous sections of this chapter (7.1 to 7.3.1) looked at the compositional and isotopic data of the methane gas as well as a general overview of the major structures found at the Driefontein, Mponeng, and TauTona gold mines. The following section gives a visual representation of the methane sampling points within the 3D seismic volume to identify any structures that may be linked to methane gas transmission.

The methods by which most of the samples were collected are documented by Ward, et al. (2004) and Sherwood Lollar, et al. (2008) in the Driefontein, Mponeng, and TauTona gold mines. For the purposes of this study, only the results from 15 of the samples collected will be reported for this section (Appendix A). These are samples whose methanogenic origin has been determined and/or a geological structure was associated with them at the time of sample collection. Table 7.3 is a list of all the samples that have been plotted within the seismic volume along with information about the formations in which they are found, the origin of the methane, geological structures that were intersected, as well as water and gas flow rates. The samples are represented as points rather than boreholes unless otherwise stated. These points represent the actual points where samples were derived along the borehole.

Table 7.3: A table of the samples collected from the Driefontein (DR), Mponeng (MP), and TauTona (TT) gold mines. The formations in which the samples are located, sample depth, types of methane, geological structures, and gas and water flow rates from the boreholes samples are noted.

Sample name	Sample Depth (m)	Formation	Type of methane	Geological Structure	Water Flow Rate (ml/min)	Gas Flow Rate (ml/min)
DR5IPC	1 050	Transvaal Dolomite	Microbial[a]	-	n.m.	n.m.
DR546 BH1	3 213	Ventersdorp Lavas	Abiogenic[b]	Snake Dyke	16.66[e]	4
DR548 FW	3 300	Ventersdorp Lavas	Abiogenic[c]	-	5 000 000	15 000 000
DR938 CH	2 712	Ventersdorp Lavas	Abiogenic[c]	Spotted Dick Dyke	1 300	250
DR9IPC	896	Transvaal Dolomite	Microbial[c]	-	26 087	160
DR938 H3 (D3)	3 350	Central Rand Group Quartzite	Abiogenic[c]*	-	3 317	45
DR938 H3 (D2)	2 716	Ventersdorp Lavas	Abiogenic[c]	-	4 448	2 298
DR938 H3 (D1)	2 825	Ventersdorp Lavas	Abiogenic[c]	-	120	15
DR940 FW	2 812	Ventersdorp Lavas	Unknown	Spotted Dick Dyke	7 500	450
MP104	2 825	Ventersdorp Lavas	Abiogenic[c]	-	40 000	2 400
MP109	3 000	Central Rand Group Quartzite	Abiogenic[c]	Post-Ventersdorp dyke	1 000	100
TT100	3 025	Central Rand Group Quartzite	Unknown	CLA Dyke	150 376	100
TT107	3 049	Central Rand Group Quartzite	Abiogenic[a, d]	Jeans Dyke; Pretorius Fault[a]	n.m.	n.m.
TT109	3 137	Central Rand Group Quartzite	Abiogenic[a]	Jean Dyke[a]	n.m.	n.m.
TT118	3 550	Central Rand	Unknown	Pretorius	2 240	1 920

Group Quartzite	Fault

Source: a. Simkus, et al. (2016); b. Moser, et al. (2005); c. Sherwood Lollar, et al. (2006); d. Magnabosco, et al., 2016; e. Moser, et al. (2003).

n.m – not measured

The borehole sample points lie on the northeastern quadrant of the 3D seismic survey area (Figure 7.14). Apart from samples DR5IPC and DR9IPC, which have predominantly microbial sources of methane, most of the samples are dominated by abiogenetically produced methane. The boreholes from which the samples were collected are located within the Malmani dolomites of the Transvaal Supergroup, lavas of the Ventersdorp Supergroup and the quartzites of the Witwatersrand Supergroup, and specifically, the Central Rand Group (Figure 7.15). The Ventersdorp lavas generally have the highest recorded water and gas flow rates, followed by the Transvaal dolomites, then the Central Rand Group quartzites. The only exception to the Central Rand Group quartzites having the overall lowest water and gas flow rates is borehole TT100, which had flow rates of 150 376 ml/min for water and 100 ml/min for gas. As previously stated in Table 7.1, the samples were collected at mining levels between 895 and 3 550 m.

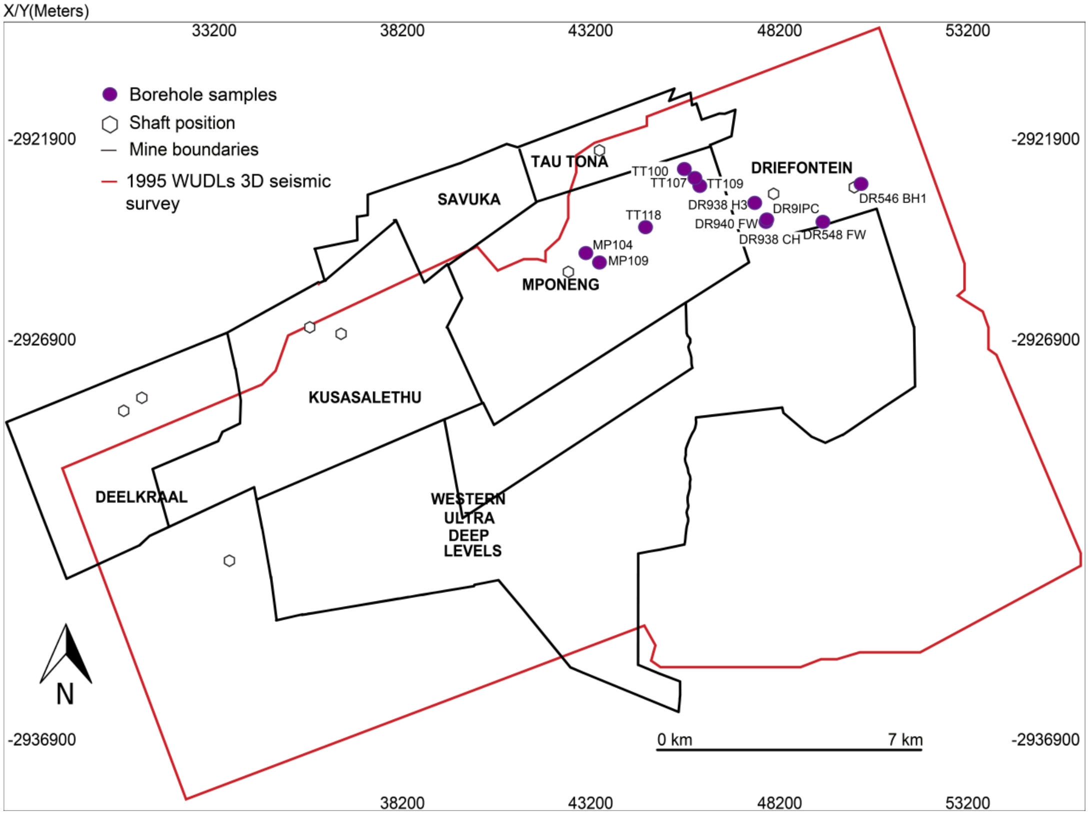

Figure 7.14: The geographic location of the samples (purple circles) from the Driefontein (DR), Mponeng, (MP), and TauTona (TT) gold mines that have had structures associated with them. The samples all cluster in the north-eastern part of the WUDLs 3D seismic survey (outlined in red).

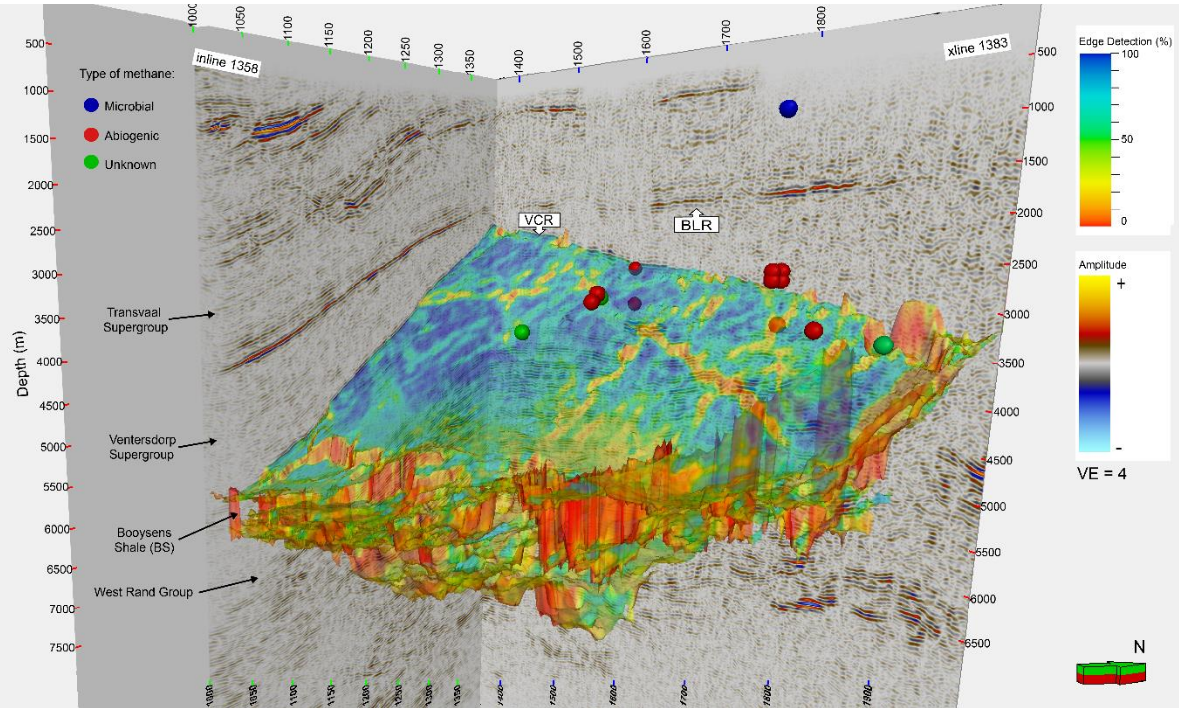

Figure 7.15: A 3D amplitude display of the samples from the Driefontein, Mponeng, and TauTona. The sources of methane have been identified as either microbial (blue sphere), abiogenic (red sphere), or unknown (green sphere). Most of the samples lie a few hundred milliseconds above and below the Ventersdorp Contact Reef (VCR), whose edge-detected surface has been included. The Black Reef (BLR) above the VCR is also noted.

7.3.2.1 Driefontein Gold Mine

Eight samples were collected from six boreholes at the Driefontein gold mine. DR5IPC and DR9IPC are the only samples that contain predominantly microbially generated methane and are located in the Transvaal dolomites. The other boreholes have been drilled into the Ventersdorp Supergroup lavas, with the highest water and gas flow rates recorded at borehole DR548 FW – 5 000 000 and 15 000 000 ml/min respectively. DR938 H3 (D3) is the deepest sample (3350 m) collected from the gold mine and the only one sampled from within the Central Rand Group quartzites. The low water (120 ml/min) and gas (5 ml/min) flow rates recorded at the site may be an indication of the hydraulic conductivity of the rocks of the Witwatersrand Basin. The samples were acquired from fracture water and only dykes at two of the eight sampling points were recorded during the sampling process. The seismic volumes from the standard seismic display and the ant-tracking attributes are presented in Figures 7.16 to 7.24 and provide insight into the observed flow rates and possible associated structures.

7.3.2.1.1 DR9IPC – DR938 CH – DR940 FW

These three boreholes have the same collar coordinates but occur at different mining depths. DR9IPC, located within the Transvaal dolomite, was sampled within the intermediate pumping chamber (IPC) of the mine. This is a borehole whose water, drawn from the dolomitic aquifer, has been used for mining operations. The flow rates reflect the position of the borehole within the aquifer. At 896 m, DR9IPC is the shallowest sample collected at the Driefontein gold mine. Due to the position of the borehole within the dolomites of the Transvaal Supergroup, not much is discernible in the amplitude display and the area surrounding the sampling point appears noisy.

The use of the ant-tracking attribute in mapping faults proves advantageous. Faults and fracturing around the sampling point are clearly denoted by the attribute (Figures 7.16 and 7.17). Further down, at depths of 2 712 and 2 812 mbls, samples DR938 CH and DR940 FW were collected (Figure 7.16). The Spotted Dick Dyke was the geological structure intersected during the collection of samples DR938 CH and DR940 FW. The differing water and gas flow rates may be an indication of the source of the water intersected at these boreholes. DR938 CH measured 1 300 ml/min for water and 250 ml/min for gas. The water flow rate at borehole DR940 FW, 100 m below DR938 CH, was five times higher at 7 500 ml/min. The gas flow rate also increased from 250 ml/min at DR938 CH to 450 ml/min at DR940 FW.

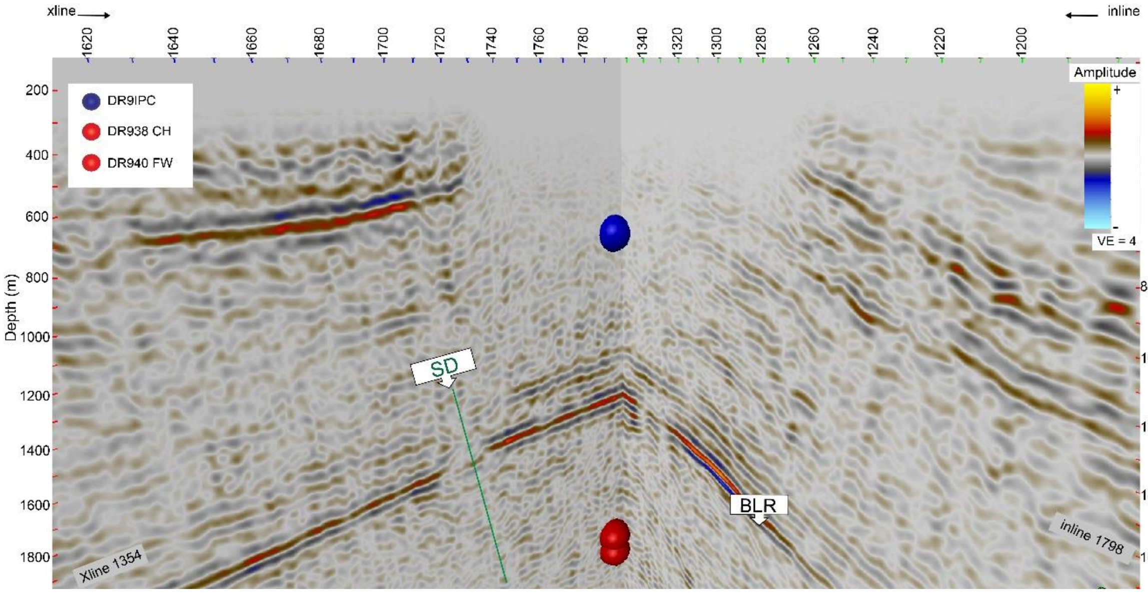

Figure 7.16: A 3D amplitude display with the location of samples DR9IPC, DR938 CH, and DR940 FW. Sample DR9IPC is located within the Transvaal Supergroup and the other two samples DR938 CH and DR940 FW are located within the Ventersdorp Supergroup; the stratigraphic marker separating the two supergroups is the Black Reef (BLR). DR9IPC is represented as a blue dot because of the microbial origin found at its location while the other two samples are marked as red dots because of abiogenic methane observed at the boreholes. SD – Snake Dyke.

An interpretation of the seismic sections (amplitude display) suggests that the samples are located between a set of steeply dipping normal faults (black lines in Figure 7.17a and b). The amplitude display also shows that the samples lie a few hundred meters from the proposed Spotted Dick Dyke, the structure reported to have been intersected by boreholes DR938 CH and DR940 FW. The Spotted Dick Dyke is a metamorphosed dolerite dyke that forms part of a network of dykes in the Driefontein gold mine (Ilgner, 2006). The extension of the dyke at the TauTona gold mine has been reported to be associated with a horst system, and the dyke is seismically active (Scheepers, 2004). There are areas along the VCR and BS horizons where the amplitude has been attenuated, but the BLR is mostly undisturbed except for some minor faulting. This may suggest that there may have been volcanics that extruded into the Ventersdorp Supergroup that pre-date the deposition of the Transvaal

Supergroup. The corresponding ant-tracking seismic section highlights the inhomogeneity of the area where the Spotted Dick Dyke has been outlined. At VCR and BS levels, a fault that flanks the eastern side of the dyke is accentuated (Figure 7.17c). There are instances where faults were enhanced by the ant-tracking attribute along a horizon (highlighted by pink arrows in Figure 7.17d). DR940 FW is located above a planar discontinuity not previously noticeable on the amplitude display but apparent on the ant-tracked seismic section (Figure 7.17b and d). Based on its position just above the VCR, the discontinuity may either be an unconformity, the periphery of a mining stope or a bed-parallel fault. The latter option may be a repository for fluids and possibly help explain the higher water and gas flow rates observed at borehole DR940 FW versus those recorded at DR938 CH. This could imply a deeper source of water migrating from the Witwatersrand Basin into the mining levels within the Ventersdorp Supergroup.

Depth slices at the three sampling points highlight the northwest trending fault into which the Spotted Dick Dyke intrudes (Figure 7.18). The depth slices also confirm that the steeply dipping normal faults mapped in the crossline and inline sections in Figure 7.17 are north northwest trending, and are most apparent at the DR940 FW sampling point versus the overlying sampling points (Figure 7.18c).

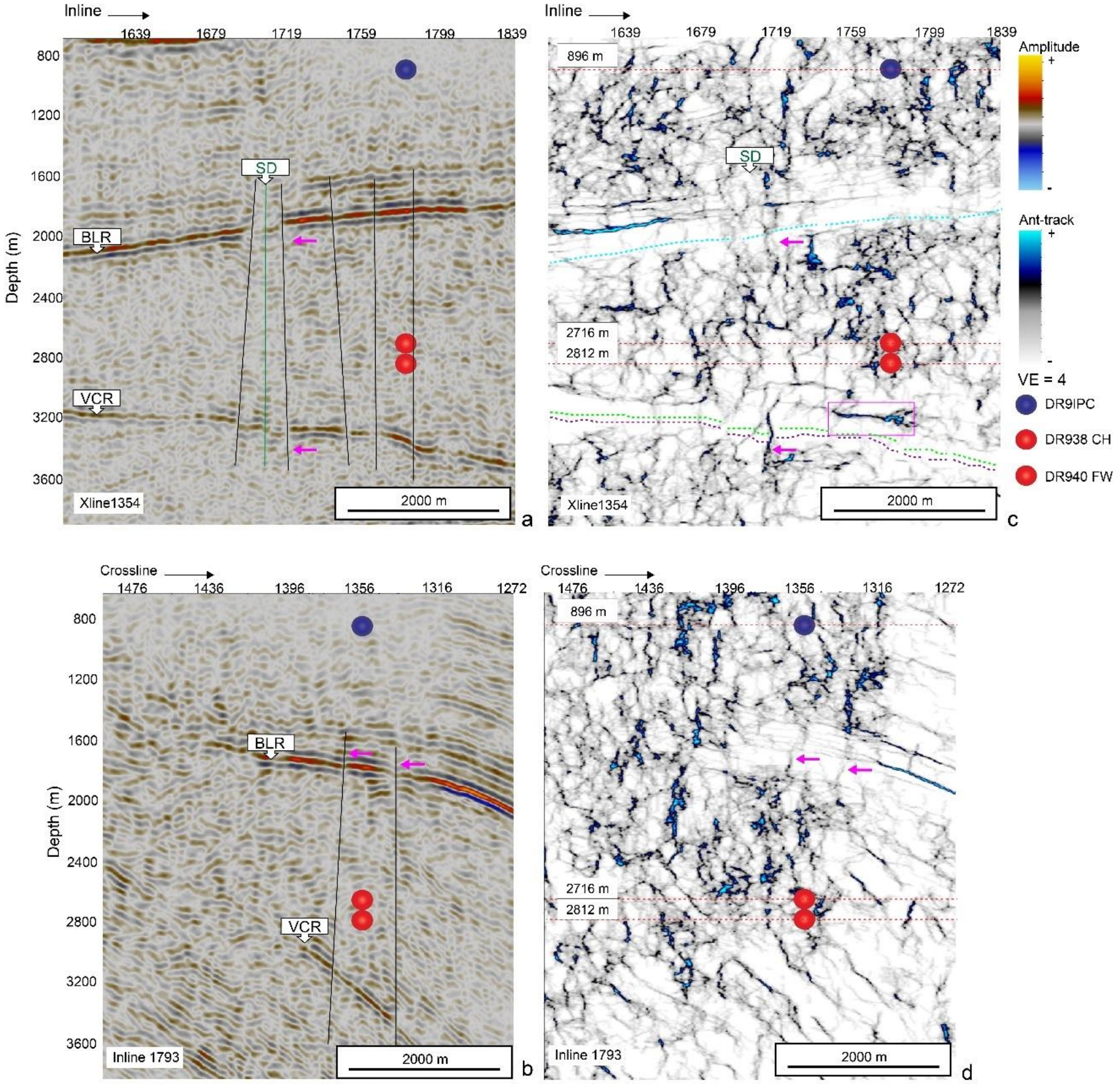

Figure 7.17: Crossline 1354 and Inline 1793 showing structures related to samples DR9IPC, DR938 CH, and DR940 FW including the Spotted Dick (SD) Dyke (green line). The pink arrows show where faults are detected in the amplitude display (a and b) and ant-tracking (c and d) seismic sections, and the green sub-vertical line denote the edges of dyke intrusions. The faults (denoted by black lines) that are detected displacing the Black Reef (BLR) are clearly enhanced in the ant-tracked sections but disappear into the chaotic Ventersdorp Lavas and seem to reappear at the Ventersdorp Contact Reef (VCR) horizon. The dashed lines represent the horizons where blue is the BLR, green is for the VCR and purple is the Booysens Shale (BS). The red dashed lines represent depth slices 896, 2716, and 2812 m interpreted in Figure 7.18.

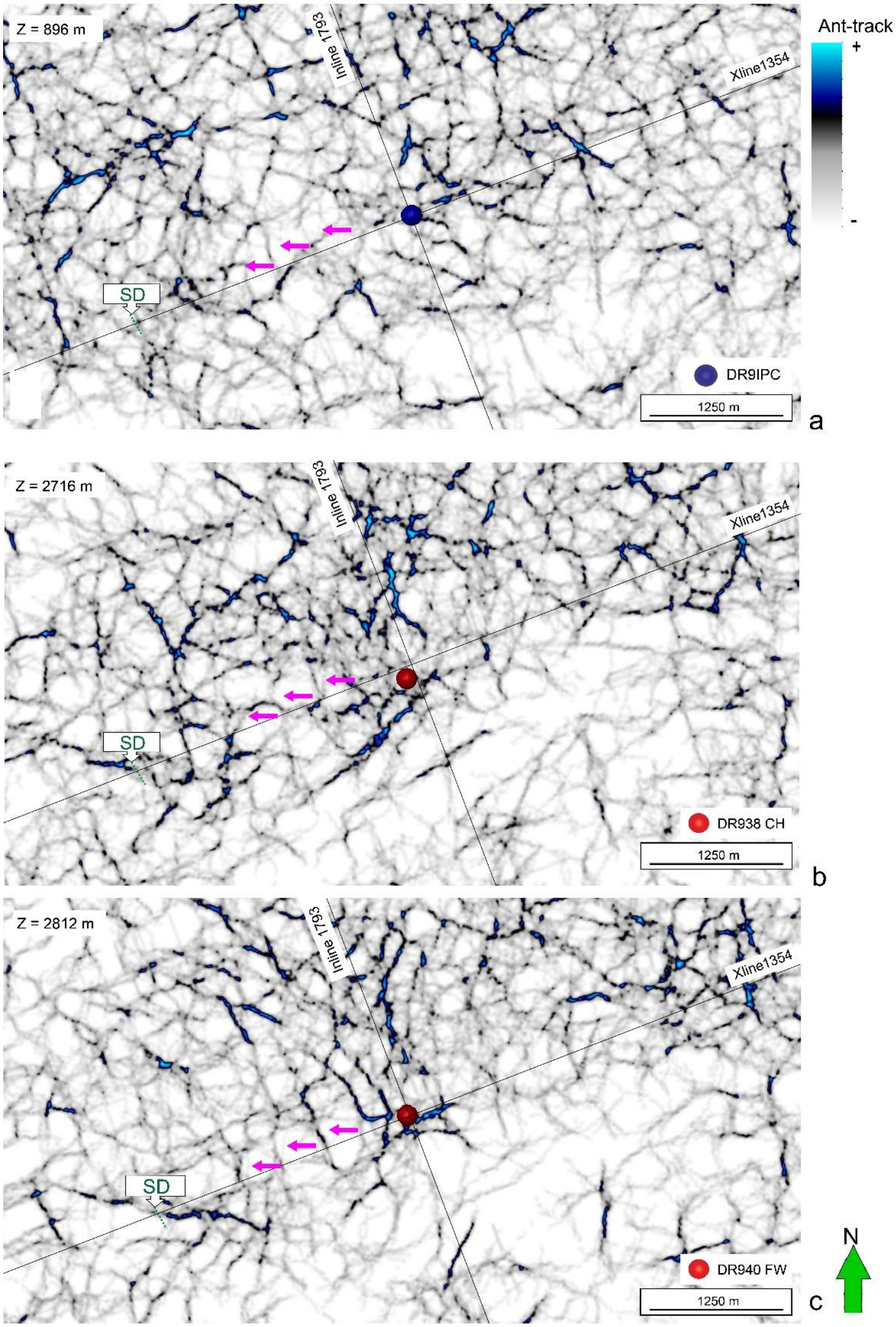

Figure 7.18: Depth slices at 896, 2712 and 2812 m across the a) DR9IPC, b) DR938 CH, and c) DR940 FW samples, respectively. The northwest trending fault into which

the Spotted Dick Dyke intruded is evident at b) and at c). The northeast-striking faults in proximity to the Driefontein samples are also well emphasized at a depth slice of 2812 m where DR940 FW was collected. SD – Spotted Dick Dyke.

7.3.2.1.2 DR938 H3

Borehole DR938 H3 is located approximately 900 m northwest of boreholes DR9IPC, DR938 CH, and DR940 FW, and the methane gas produced in the borehole is abiogenic in origin (Sherwood Lollar, et al., 2006). The samples (D1-D3) were collected at varying depths along its ~750 m length of the borehole and no structure was recorded as being associated with the borehole. Sample DR938 H3 (D1) was the first sample collected at a depth of 2 825 m and has the lowest recorded water and gas flow rates – 120 and 15 ml/min, respectively. The reduced flow rates may reflect the comparatively lower hydraulic conductivity of the quartzites in the Witwatersrand Basin compared to that of the Transvaal dolomites and Ventersdorp lavas (Barnard & Baran, 2000). DR938 H3 (D2) was recorded approximately one month later, 109 m above the first sample, and had the highest water (4 448 ml/min) and gas (2 298 ml/min) flow rates. The last sample, DR938 H3 (D3) was collected at 3 350 m and recorded flow rates measuring 3 317 ml/min for water and 45 ml/min for gas. Of all the Driefontein samples, this sample was the only sample located within the Central Rand Group quartzites. The reduction in flow rates between the second and last flow rates may be an indication of stabilization of fluid flow over time and reduced input from the groundwater source, but the puzzle lies with the first sample, which is located between DR938 H3 (D2) and DR938 H3 (D3). One possibility is that there may have been replenishment of the borehole from the source in between the sampling periods. Another possibility is that the low flow rates could be an indication of an error in the equipment used during the sampling process resulting in a mis-reading.

A comparison of the amplitude and ant-track attribute displays shows that the ant-tracking attribute has successfully enhanced the detection of several faults and fracture zones within the vicinity of the sampling points that were not apparent in the amplitude display (Figure 7.19a and b). The samples lie a few hundred meters east of the Spotted Dick Dyke. The intrusion of the dyke (which can also be tracked along the edge-detected map of the VCR incorporated into the 3D display) is characterized by seismic attenuation along the BLR reflector in Figure 7.19a. A comparison with the ant-tracked volume gives more information about the possible permeability and conductivity of the dyke. A structure that diagonally intersects the dyke, which is not apparent in the amplitude display, is clearly mapped by the ant-tracked volume. This raises the possibility of the dyke being a conduit rather than an impervious water barrier. The use of seismic attributes gives a visual confirmation of a study by Omar, et al. (2003) proposing that dykes intersecting the gold mine play a crucial role in distributing fluid carrying temperature sensitive microbes throughout the Witwatersrand, Ventersdorp, and Transvaal Supergroups. These dykes would have played both a conduit role for groundwater flow as well as affecting temperatures in the basin, which in turn affected the metabolic and respiratory processes of these organisms (Omar, et al., 2003).

Based on the ant-tracking attribute results, fracture intensity around the borehole in the Ventersdorp Lavas is greater than within the rocks below the VCR horizon and those above the BLR horizon (Figure 7.20a and b). There is evidently less structural deformation down-dip and a few bed-parallel discontinuities can be seen. Depth slices at 2716, 2825, and 3350 m of the ant-tracked volume (Figure 7.20 a to c) show that the borehole is located within a set of northwest trending faults, which are prominent and clearly correlate with the sampling point DR938 H3 (D3) (Figure 7.21c).

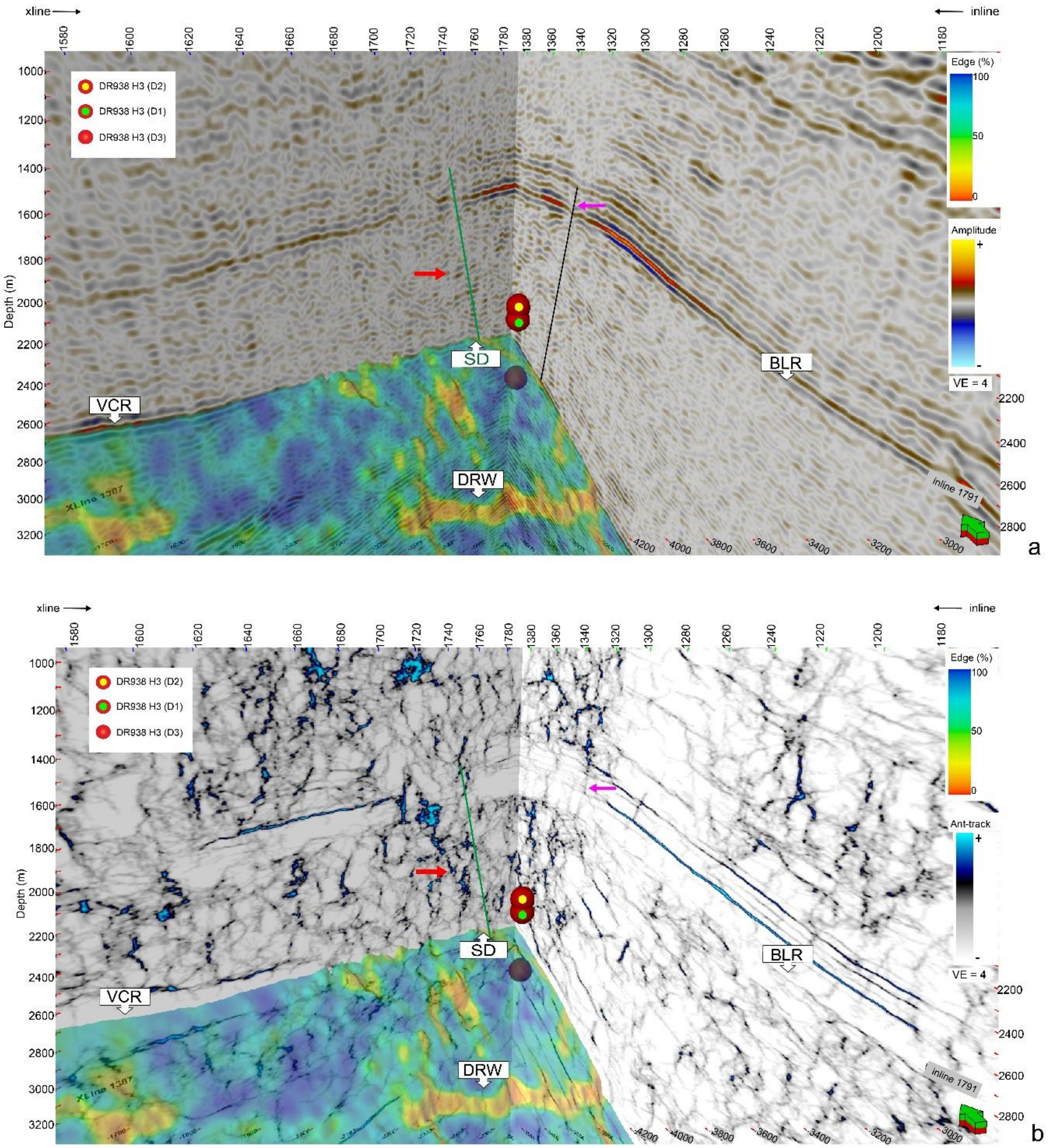

Figure 7.19: Crossline 1387 and inline 1791 of the a) amplitude, and b) ant-tracking displays demonstrating a projection of the DR938 H3(D2), DR938 H3(D1), and DR938 H3(D3) locations along borehole DR938 H3, in the order in which they were sampled. The borehole is located close to the Spotted Dick (SD) Dyke, made evident by the attenuation of the signal at the Black Reef (BLR) horizon (a), and confirmed with the use of the edge-detected Ventersdorp Contact Reef (VCR) horizon. It is evident on the ant-tracked crossline that the extent where the SD has been outlined is not as uniform as it appears. DRW – Driefontein West Fault. The red arrow marks a fault intersecting the SD.

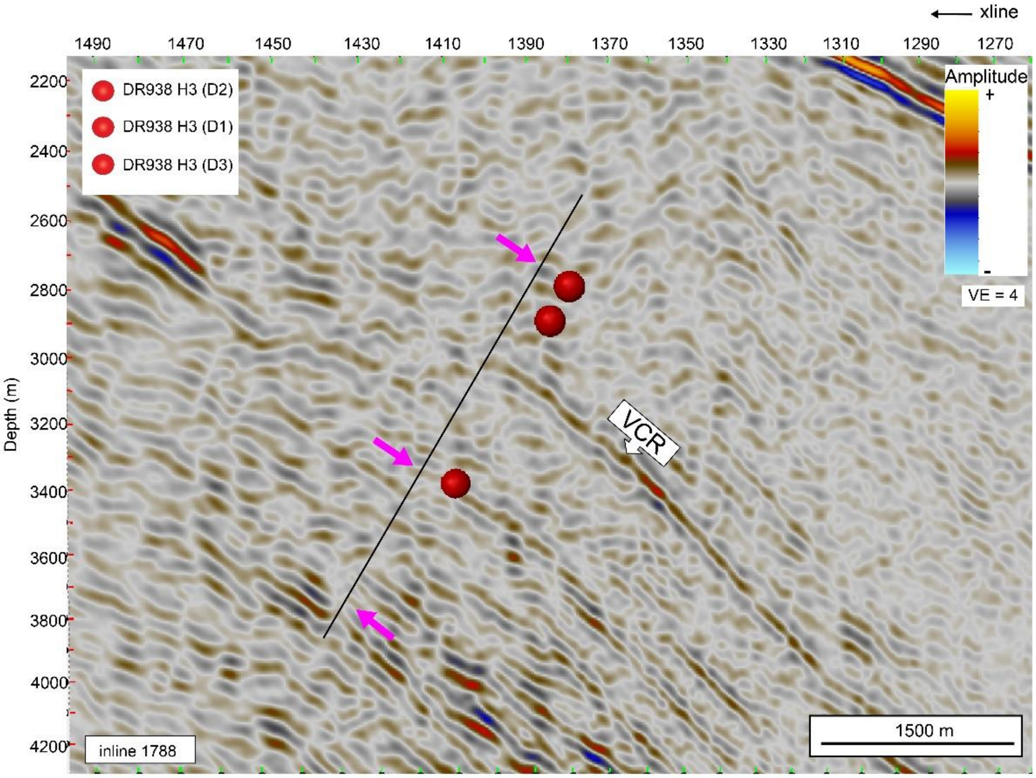
xline
1490
1470
1450
1430
1410
1390
1370
1350
1330
1310
1290
1270
DR938 H3 (D2)
DR938 H3 (D1)
DR938 H3 (D3)
Amplitude
+
-
VE = 4
Depth (m)
2200
2400
2600
2800
3000
3200
3400
3600
3800
4000
4200
VCR
inline 1788
1500 m

a

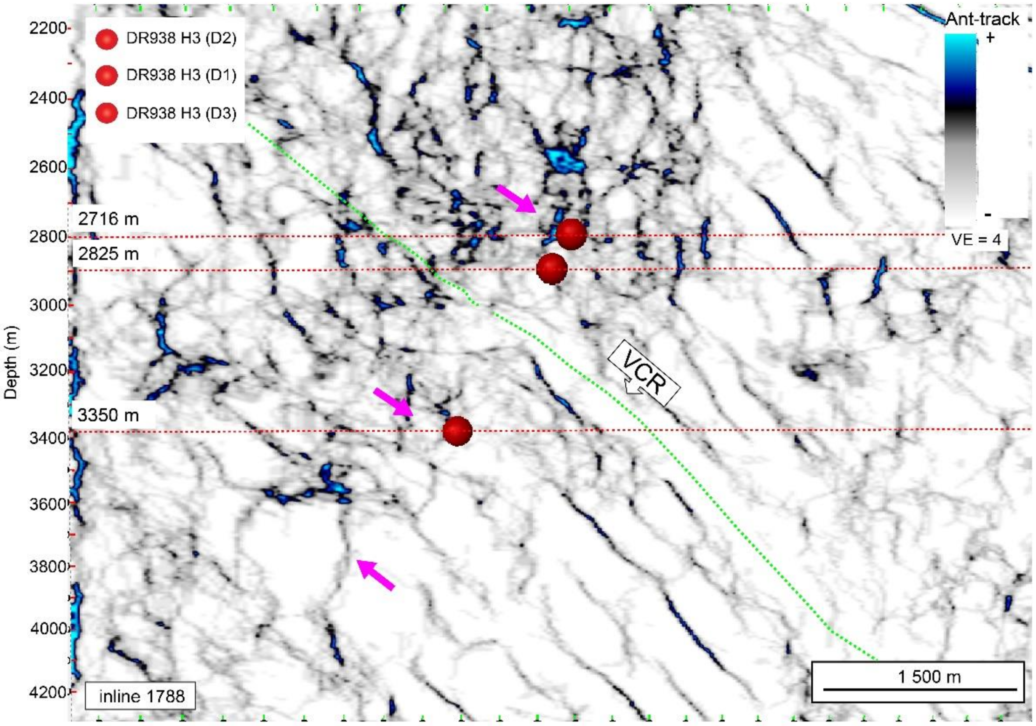
DR938 H3 (D2)
DR938 H3 (D1)
DR938 H3 (D3)
Ant-track
+
-
VE = 4
2716 m
2825 m
3350 m
Depth (m)
2200
2400
2600
2800
3000
3200
3400
3600
3800
4000
4200
VCR
inline 1788
1 500 m

b

Figure 7.20: Sampling points DR938 H3 (D1-D3) collected along borehole DR938 H3. The borehole dips at a 60° from the horizontal and is approximately 750 m in length. A fault can be seen displacing the Ventersdorp Contact Reef (VCR) in the amplitude display (a). In the ant-tracked section (b), the first two sampling points that lie within the Ventersdorp Supergroup lavas appear to be located in a section of what might be an inhomogeneous rock mass and faults on the section are indicated by the pink arrows. DR938 H3 (D3) appears to be intersected by a fault. The red dashed line denotes the location of the depth slices from the ant-tracked volume in Figure 7.21.

The mine borehole name given for borehole DR938 H3 is D8A (Figure 1, Appendix B). A study done by Moser, et al. (2005) describes the borehole as having been drilled at a 60° angle from the horizontal, i.e. mine tunnel. The borehole intersects the VCR at 400 m and the Carbon Leader Reef (CLR) at 720 m. Based on the corresponding core samples, faults were intercepted at depths of 620 and 650 m. Studies by Moser et al. (2003) on geochemical and isotopic data suggest that the fracture water derived from the borehole originates from within the Central Rand Group quartzites rather than Ventersdorp Supergroup lavas. This ancient meteoric water is dated at 4 – 53 million years (Moser, et al., 2003).

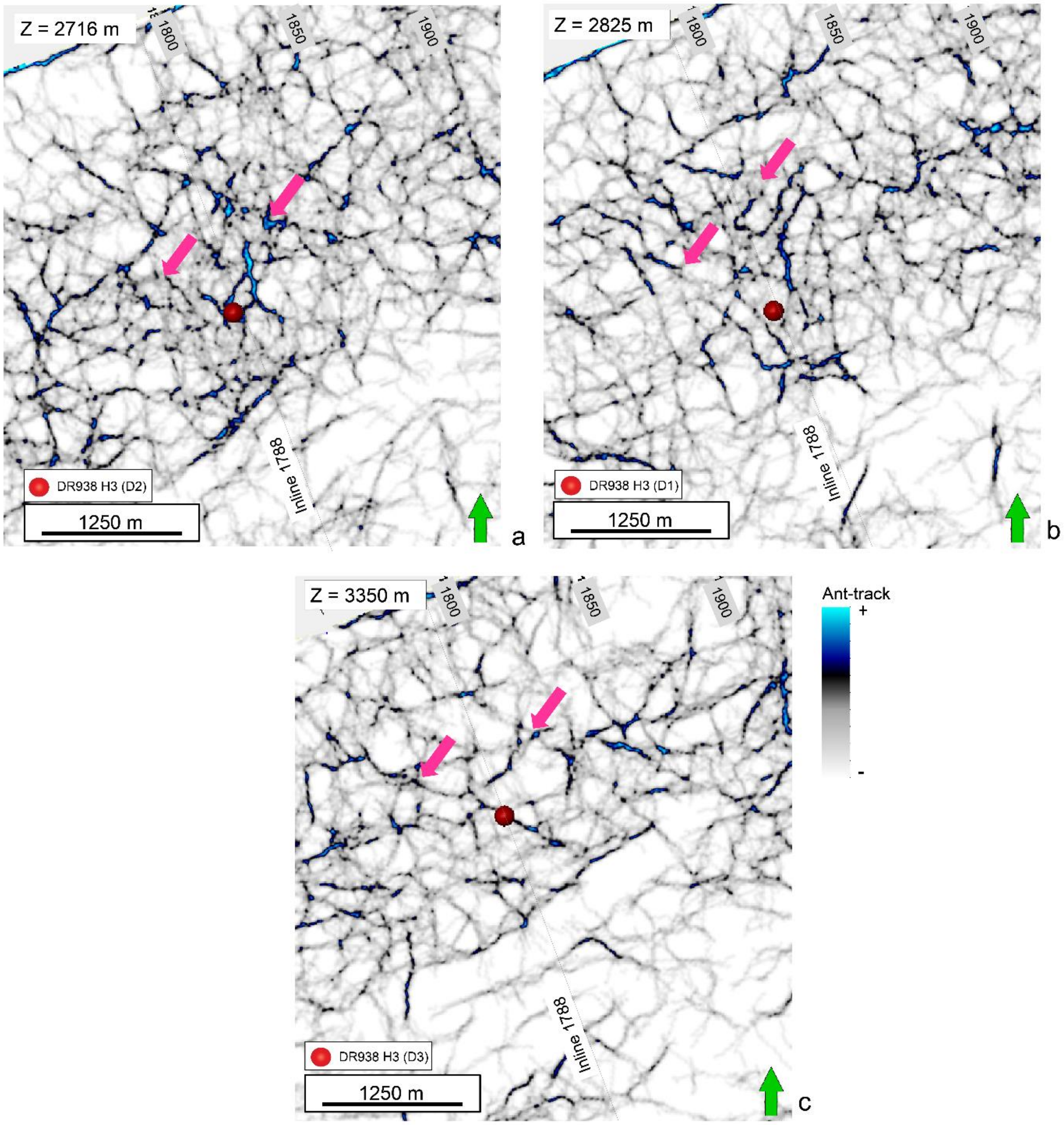

Figure 7.21: Ant-tracking depth slices along the samples collected for the borehole DR938 H3 at a) sample DR938 H3(D2) at 2716 m, b) sample DR938 H3(D1) at 2825 m, and c) sample DR938 H3(D3) at 3350 m. The pink arrows indicate a set of northwest trending faults, one of which intersects sample DR938 H3(D3).

7.3.2.1.3 DR546 BH1 and DR548 FW

Boreholes DR546 BH1 and DR548 FW are located at Shaft 5 in the Driefontein gold mine. Isotopic data suggests an abiogenic source of methane largely as a result of water-rock interaction. DR546 BH1 is located approximately 3 km east of DR938 H3 and 3 km northeast of DR548 FW. The flow rates at borehole DR548 FW were the highest recorded amongst the samples with 5 000 000 ml/min for water and 15 000 000 ml/min for gas. Borehole DR546 BH1 is a 120 m long horizontal borehole drilled into the Ventersdorp Supergroup lavas with the water and gas flow rates measured at 16.66 ml/min and 4 ml/min respectively (Moser , et al., 2003). The Snake Dyke, the geological structure intersected by the borehole, forms part of a series of dykes that have intruded into the Driefontein gold mine. The fracture water derived from the borehole is interpreted to be emanating from a hypersaline, hydrogeologically isolated water "pocket" within the Ventersdorp Supergroup that has undergone a considerable amount of water-rock interaction with the surrounding lavas (Lippmann, et al., 2003; Moser , et al., 2003).

DR546 BH1 is located within a syncline dubbed the Driefontein Syncline by Dankert and Hein (2010) (Figure 7.22). The Snake Dyke is evident on both the amplitude and ant-tracked sections (Figure 7.22a and b). The faults associated with the Snake Dyke appear to extend from depth through the VCR horizon and into the overlying BLR horizon. These faults have been mapped by the ant-tracking attribute at the BS, VCR, and BLR horizons level but are not traceable through the chaotic Ventersdorp Supergroup lavas. Although the ant-tracking attribute does not detect dyke intrusions, it may detect faults into which the dykes have intruded. Depth slices at a 3212 and 3300 m clearly illustrates the northeast trending fault associated with the Snake Dyke (Figure 7.22).

Fracture water collected from DR548 FW was dated, using ^{4}He analysis, to have an age of 15 million years (Silver, et al., 2012). Despite the observed flow rates, no geological structure is noted as having been intersected by the borehole. 3D seismic data do, however, indicate that the borehole is located between two northwest trending, steeply dipping (>80°) normal faults, F548(1) and F548(2) (Figure 7.23a). Assuming sub-horizontal borehole orientation, DR548 FW would intersect a northeast-trending, southeast-dipping normal fault (F548(3)). This fault runs parallel to F548(4), which has a normal sense of displacement and may have undergone fault reactivation (Figure 7.23b). A depth slice at an elevation of 3300 m shows that faults, F548(1) and F548(2), intersect the northeast trending F548(3) and F548(4) fault set. The ant-tracked depth slices 3212 and 3300 m further show that F548(3) and F548(4) crosscut the fault associated with Snake Dyke (Figure 7.24). The fault connections, a means by which fracture water mixing can occur, may begin to explain the similar δ^{18}O and δ^2H values for samples DR548 FW and DR546 BH1 observed in Chapter 7.1.

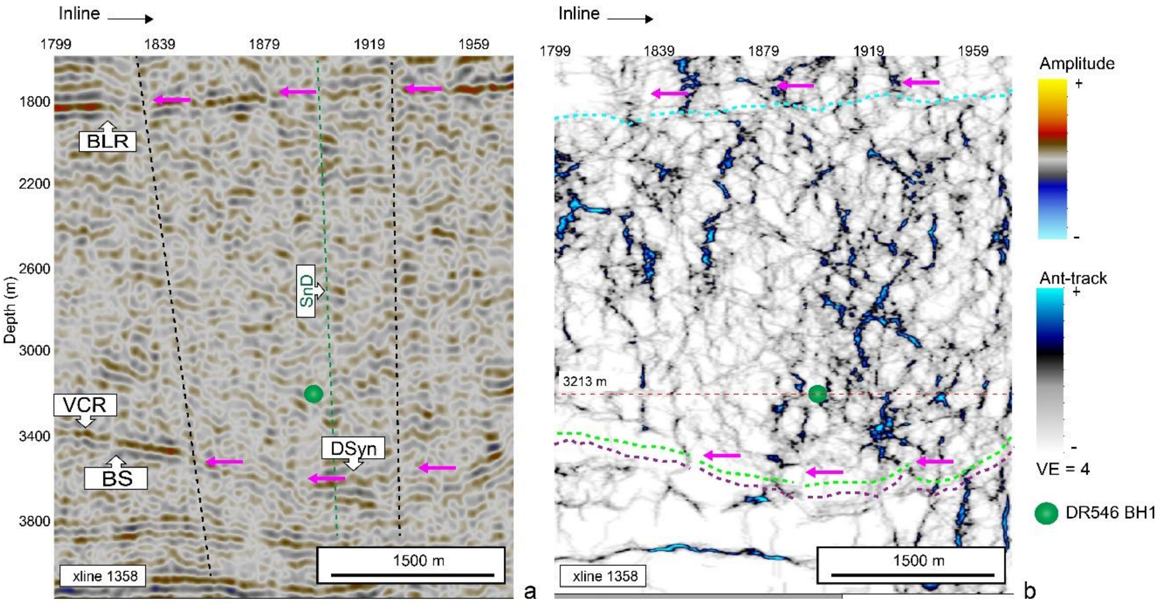

Figure 7.22: Crossline 1358 showing the location of sampling point DR546 BH1 in a) amplitude, and b) ant-tracked seismic section. The dark green sub-vertical line denotes the Snake Dyke (SnD) and the sampling point is located within the Driefontein Syncline (DSyn). The Booysens Shale (BS – purple dashed line), Ventersdorp Contact Reef (VCR- light green dashed line), and Black Reef (BLR – light blue dashed line) are intersected by faults (black dashed lines) displacing the horizons and are enhanced in the ant-tracked section (highlighted by pink arrows). The red dashed line denotes the location of the depth slices from the ant-tracked volume in Figure 7.24.

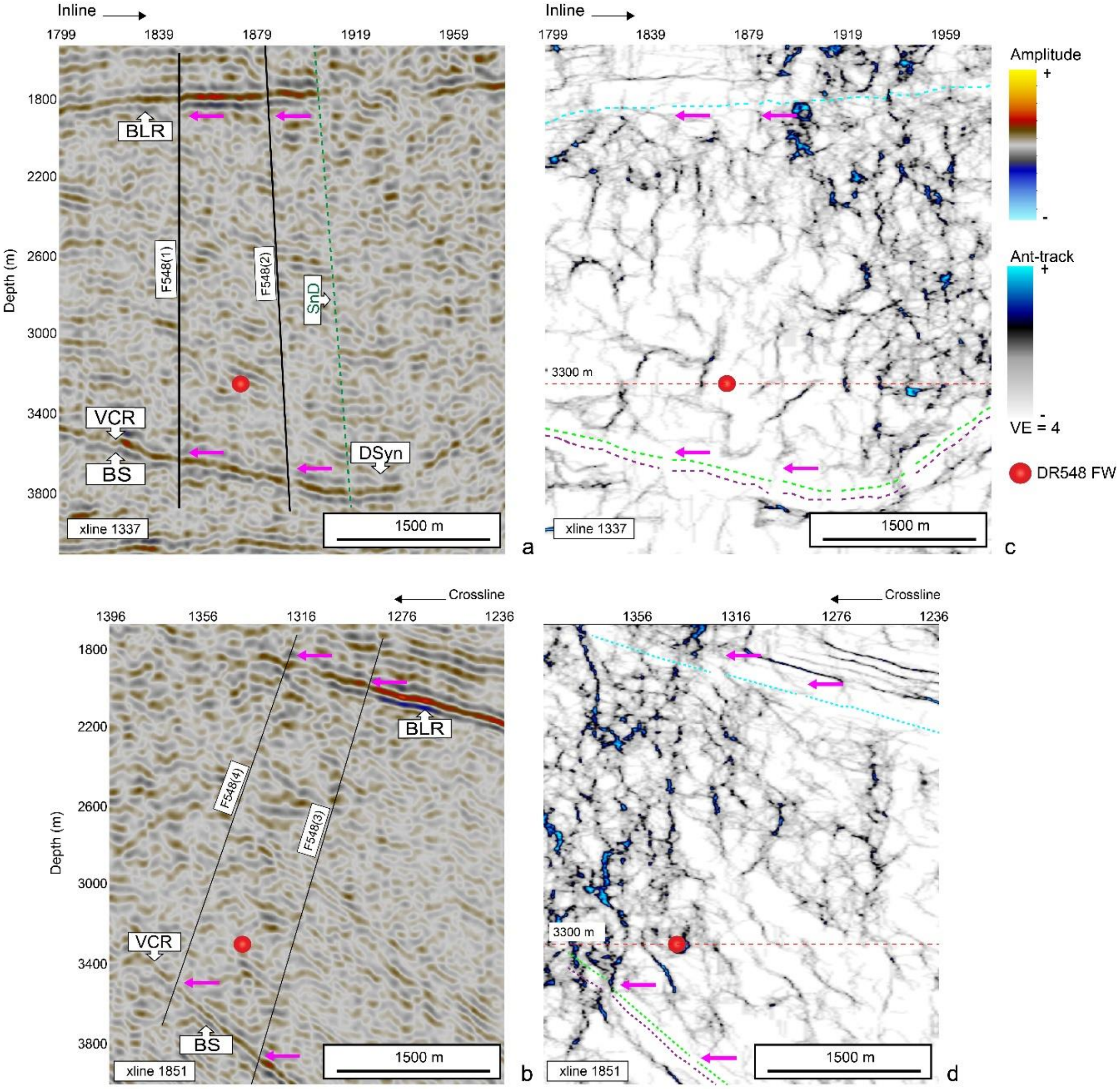

Figure 7.23: Amplitude (a and b) and ant-tracking (c and d) displays showing the location of borehole DR548 FW. Faults F548(1), F548(2), F548(3), and F548(4) flank the sampling point. The faults displace the Booysens Shale (BS), Ventersdorp Contact Reef (VCR), and Black Reef (BLR). The pink arrows highlight the possible position of the faults in the ant-tracking attributes. The Booysens Shale (BS) horizon is denoted as a purple dashed line, the Ventersdorp Contact Reef (VCR) by a light green dashed line, and the Black Reef (BLR), by a light blue dashed line. The Driefontein Syncline (DSyn) is also prominent on the eastern side of the sampling point. The dark green dashed line denotes the Snake Dyke (SnD). The depth slice of 3300 m, marked as a red dashed line, can be seen in Figure 7.24b.

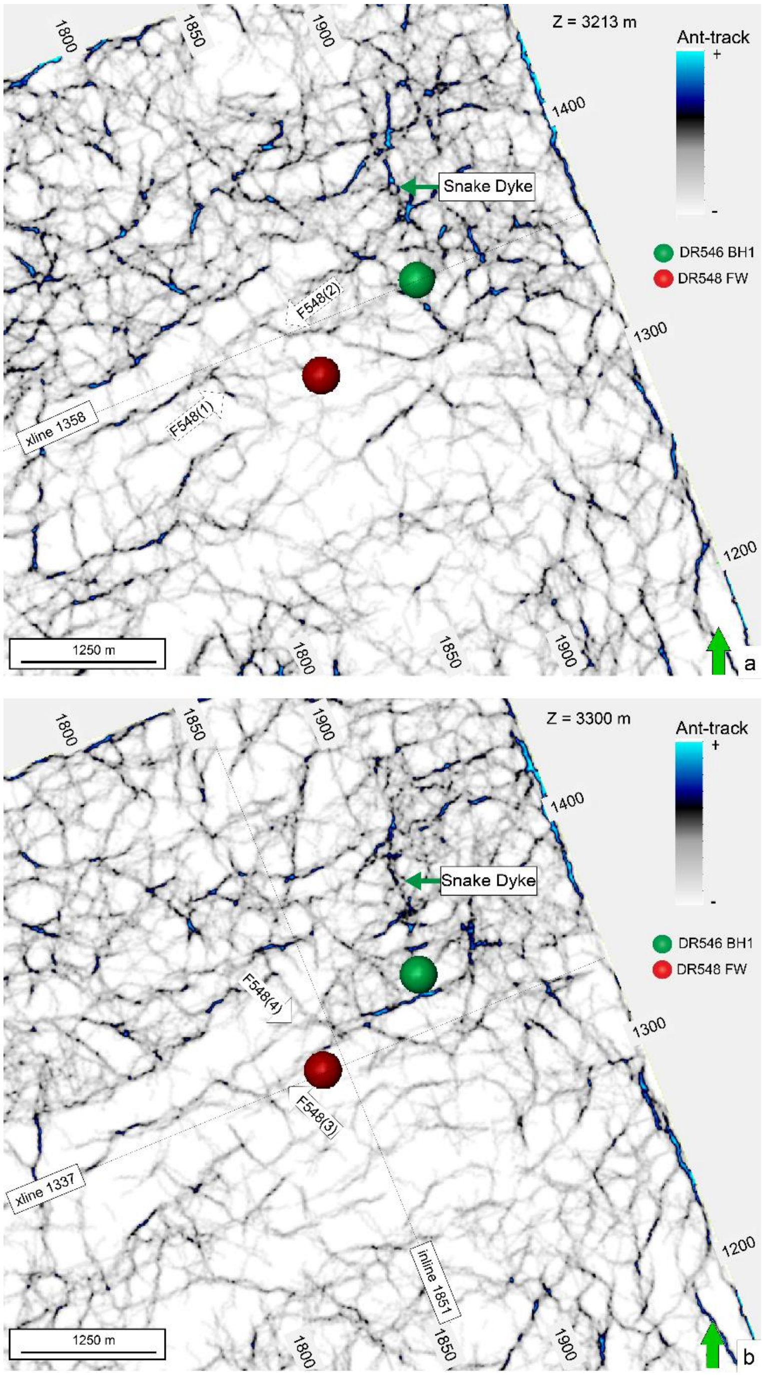

Figure 7.24: Depth slices of ant-tracked volume at 3213 m at borehole DR546 BH1 (a) and at 3300 m at borehole DR548 FW (b). The F548 faults have been mapped by the ant-tracking attribute. F548(3) intersects the fault associated with the Snake Dyke, which clearly intersects sample DR546 BH1. DR546 BH1 is located at an intersection between the northwest trending Snake Dyke and a northwest trending fault.

7.3.2.2 Mponeng Gold Mine

The two samples collected from the Mponeng gold mine, MP104 and MP109, are located within the Ventersdorp Supergroup lavas and Central Rand Group quartzites, respectively. Both sites have predominantly abiogenic methane detected within the fracture water (Sherwood Lollar, et al., 2006) and despite a post-Ventersdorp dyke being noted as the structure intersected at MP109, the borehole had considerably lower water and gas flow rates than those observed at borehole MP104. While the water and gas flow rates for MP109 were measured at 1000 and 100 ml/min, respectively, fracture water collected from MP104 was emanating at a rate of 40 000 ml/min and the gas reading was 2 500 ml/min (Table 7.3).

A few geological features are discernible on the seismic amplitude display. The VCR, BS, and BLR are identifiable and continuous with a number of high amplitude areas present in close proximity to samples MP104 and MP109 (Figure 7.25). Amplitude display also shows the imaging of faults near the Mponeng gold mine samples (Figure 7.25). The seismic data also show that MP104 intersects a north-northeast dipping normal fault labelled F1 in Figure 7.26a and b. The fault (F1), along with faults F2, F3, and F4, are visible in both the amplitude and ant-tracked sections (Figure 7.26). One thing that stands out in the ant-tracked sections, which is not apparent on the amplitude display, is the planar discontinuity located just beneath sample MP104 (Figure 7.26c and d). The discontinuity is most likely bed-parallel faulting or shearing that has been identified by Jolley, et al. (2004) in the mining area, along the VCR.

Dyke intrusions in seismic data may cause amplitude attenuation along laterally continuous horizons in seismic data. Interpretation along the amplitude displays suggest that the dyke imaged by seismics may be associated with the post-Ventersdorp dyke identified during the sampling at borehole MP109 (Figure 7.27a and b). It is unclear however, whether the attenuation near the sample is the said post-Ventersdorp dyke. A look at the ant-tracked section where MP109 was collected, located 300 m southeast of MP104, shows that the planar discontinuity noted at borehole MP104 is more pronounced and appears to be connected to a distinct set of faults (Figure 7.27c and d). These vertical and lateral fault connections may help explain the increased influx of water and gas at borehole MP104 rather than MP109. There is a high amplitude anomaly seen at both sampling localities in the amplitude displays. These are most likely a mining stopes; stopes are mining levels that which have been identified by Pretorius, et al. (2006) in seismic data and their locations have been confirmed using underground mine data from the gold mines in the region. The strong seismic reflection is a result of the significant acoustic impedance contrast between air and the surrounding rock mass. The ant-tracking attribute has successfully detected faults as well as planar discontinuities that occur close to and are intersected by MP104 and MP109 (Figures 7.26 and 7.27). A series of faults intersect the sampling points and for some, their continuity is apparent but for most, positively discriminating between individual faults is not easy.

MP104 was sampled four times over the course of two months. Although the water flow rates significantly decreased with each sampling excursion, the gas flow rates remained relatively stable. The temperature decreased from 60 to 52°C from the first sample to the subsequent samples that were collected, and methane concentration increased over the observed period. Lin, et al. (2006) also conducted some isotope studies to determine the origin of the fracture water at MP104. Isotope analysis shows that water derived from the Mponeng samples lies to the side of the LMWL and model ages using noble gas analyses place the age of the water between 15 – 25 ± 3.8 million years. The age of this water is either an indication of the true residence time or mixing between old (up to 2.5 billion years old), saline water enriched in reduced gases and younger palaeometeoric water not as saline and/or as enriched in H_2 and hydrocarbon gases. The observed decrease in temperature from the initial to the last sample and $\delta^{18}O$ and $\delta^{2}H$ analysis incorporated with thermal conductivity and heat flow data of the rocks of the Witwatersrand Basin indicate fracture water from depths between 2 400 and 4 200 mbls. The strong correlation between geological structures (faults and dykes) and methane/water sampling points, as shown by ant-tracking attribute results, support the possibility of water coming from depth, but also, the ingress of water from above the borehole.

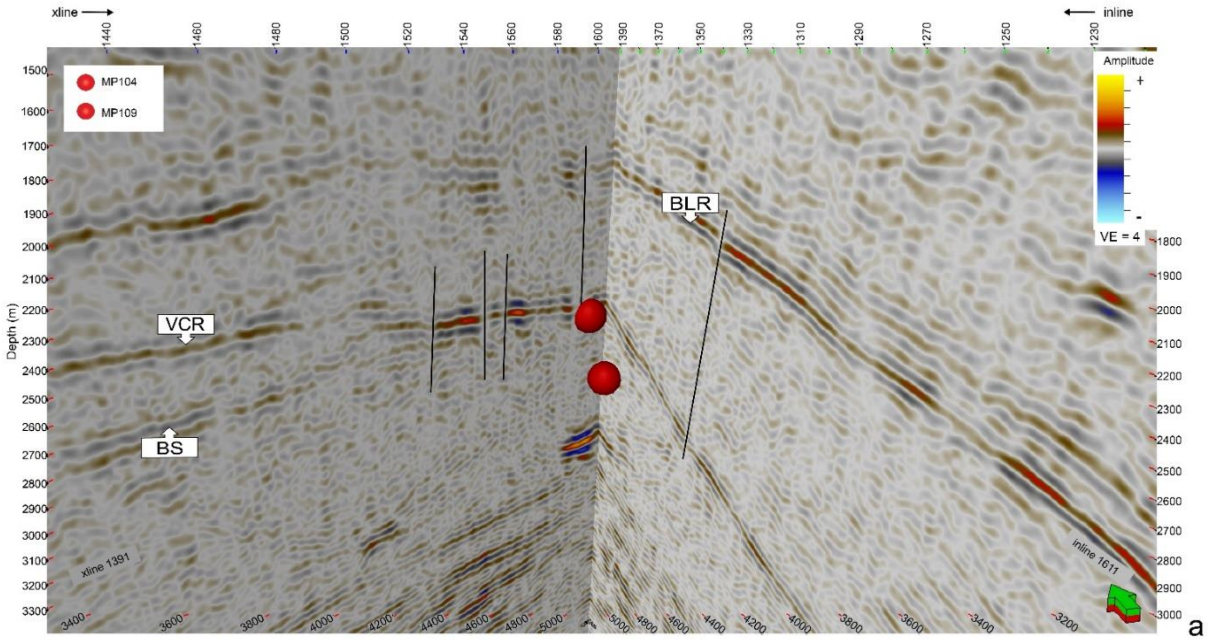

Figure 7.25: Crossline 1391 and inline 1611 of the amplitude display showing samples MP104 and MP109. MP104 lies just above the Ventersdorp Contact Reef (VCR) and the MP109 within the Central Rand Group quartzites, above a mine stope (high amplitude reflection below the sample). The samples lie close to and are intersected by faults (black lines). BS – Booysens Shale; BLR – Black Reef.

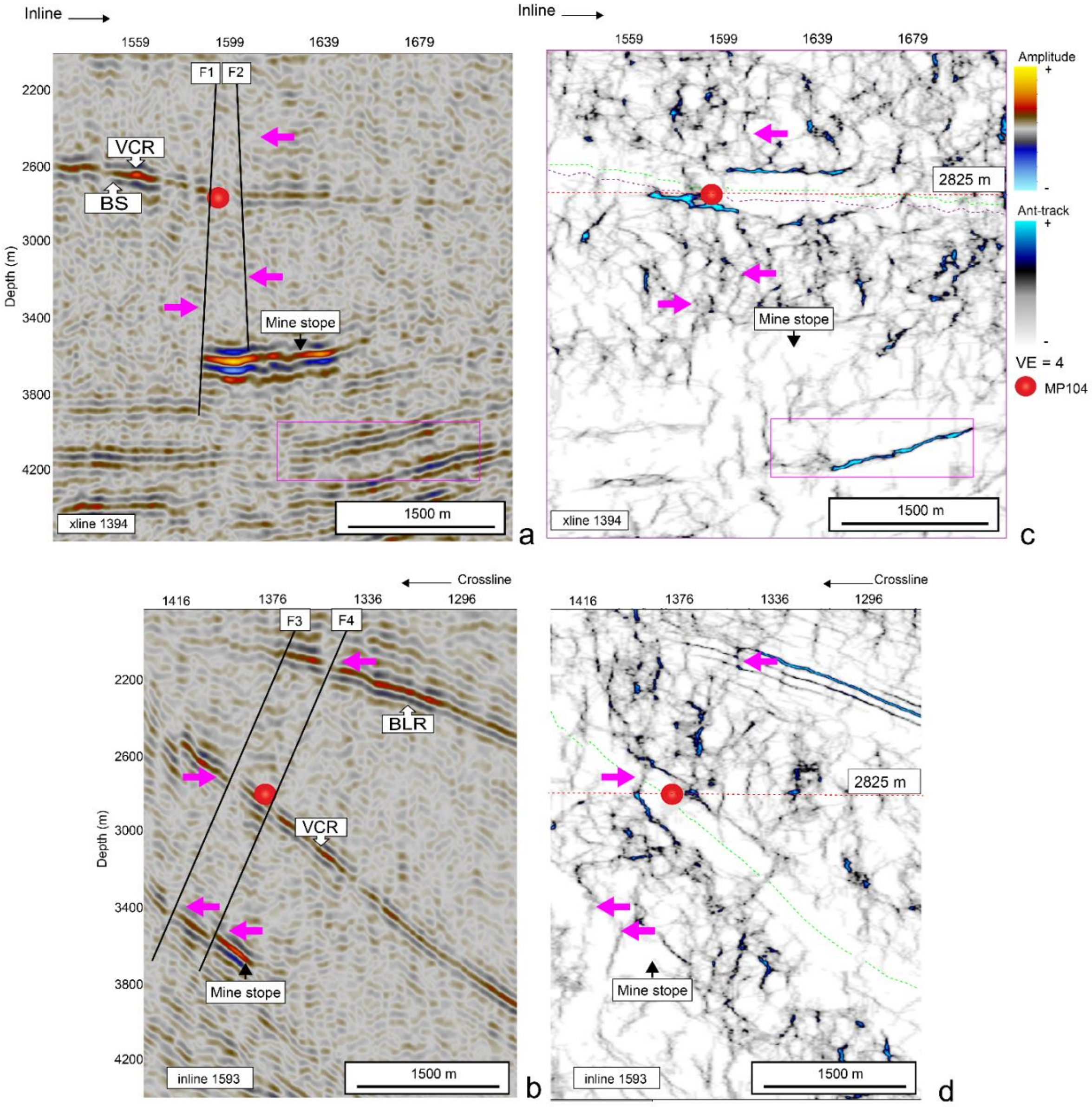

Figure 7.26: Crossline 1394 and inline 1593 of amplitude (a and b) and ant-tracking (c and d) displays in proximity to sample MP104. Faults F1 to F4 are noted in both amplitude and ant-tracking (denoted by pink arrows) displays and displace the Ventersdorp Contact Reef (VCR) and Black Reef (BLR). Other features such as the high amplitude area in the amplitude display below MP104 are noted as a mine stope and planar discontinuities (pink rectangle), enhanced by the ant-tracking attribute.

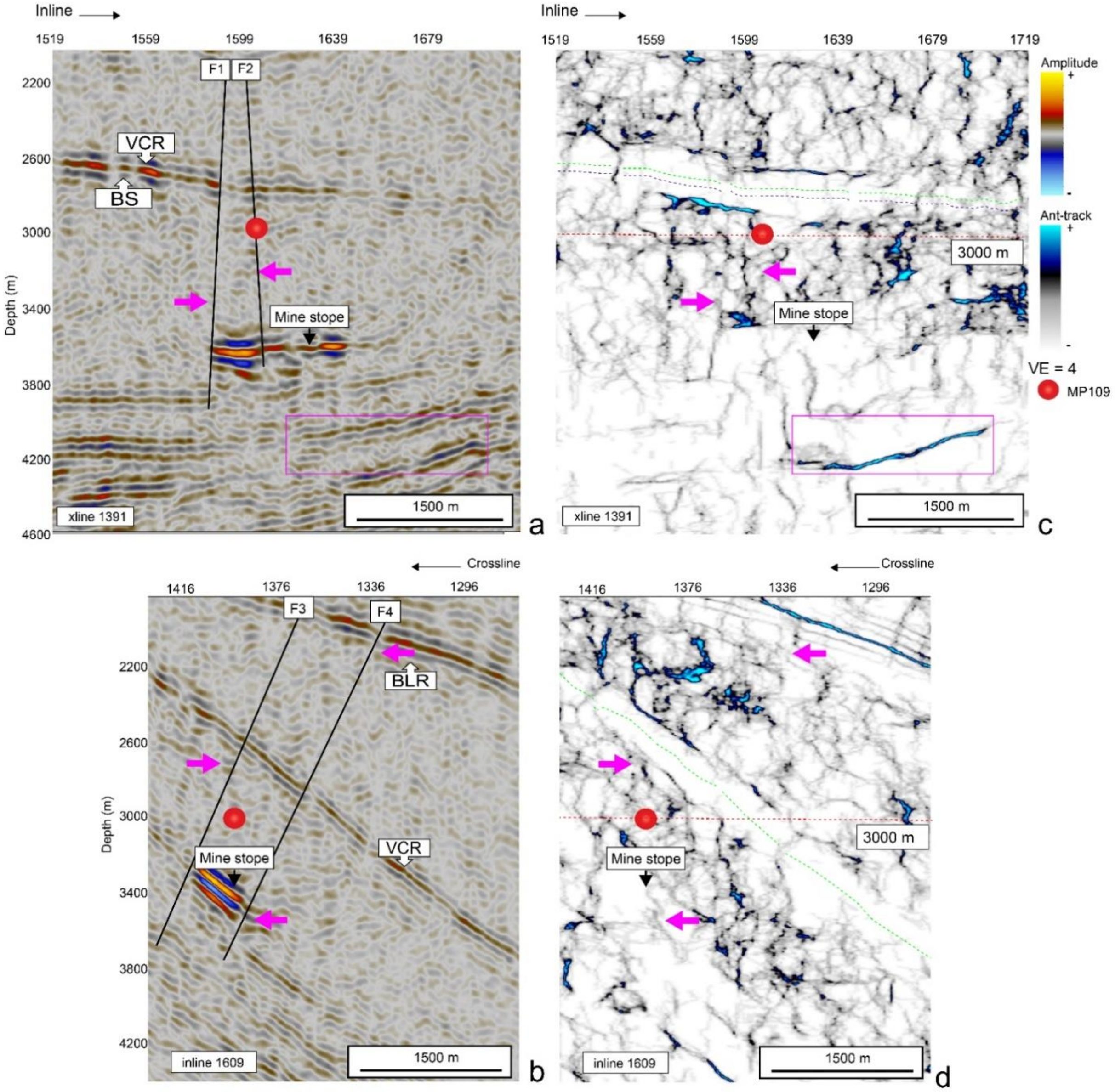

Figure 7.27: Crossline 1391 and inline 1609 of amplitude (a and b) and ant-tracking (c and d) sections in proximity to sample MP109. Faults F1 to F4 are noted in both amplitude and ant-tracking (denoted by pink arrows) displays and displace the Ventersdorp Contact Reef (VCR) and Black Reef (BLR); F2 in particular, intersects borehole MP109. Other features such as the high amplitude area in the amplitude display below M104 are noted as a mine stope and planar discontinuities (pink rectangle) are enhanced by the ant-tracking attribute.

7.3.2.3 TauTona Gold Mine

The TauTona samples are located northeast of MP104 and MP109, within the Central Rand Group quartzites at depths greater than 3 000 mbls. Of the four boreholes, only TT107 and TT109 were determined to have a predominantly abiogenic source of methane (Simkus, et al., 2016). The flow rates for the two boreholes were not recorded, but for the other two, TT100 and TT118, the recorded water flow rates were 150 376 and 2 240 ml/min and gas flow rates of 100 and 1 920 ml/min, respectively (Table 7.3). Although the sources of methane for boreholes TT100 and TT118 are unknown, there were structures that were encountered during sampling.

TT118 was drilled down-dip, towards the south of the mining operations and intersects the Pretorius Fault (PF) approximately 50 m along the length of the borehole. TT118 (known in the mine as LIC118 – Figure 2, Appendix B) is a 900-m sub-horizontal borehole that intersects a number of faults and dykes along its length including the PF (Heesakkers, et al., 2011). The fracture water sample collected from the borehole was collected at a depth of 3550 m. 3D seismic visualization of the amplitude and ant-tracking displays confirm the intersection of the PF with borehole TT118 (Figure 7.28a and b). Despite the sampling point being in a structurally dense portion of the seismic survey, as highlighted by the ant-tracking attribute in Figure 7.28b, the flow rates are consistent with average flow rates observed in the samples derived from the Central Rand Group quartzites (Table 7.3).

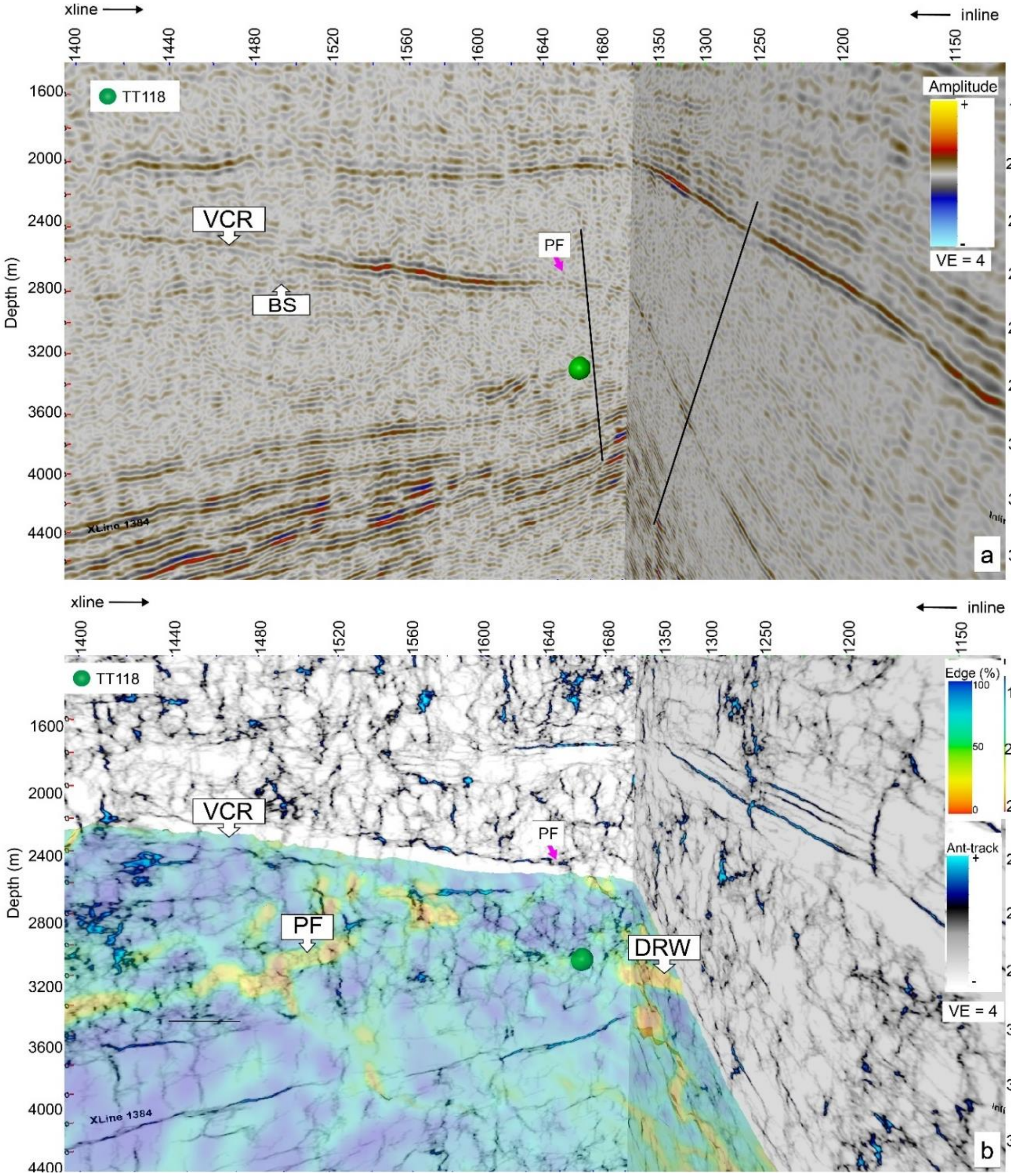

Figure 7.28: Crossline 1384 and inline 1701 of the a) amplitude and b) ant-tracking displays and the location of borehole TT118. The Pretorius Fault (PF), also shown in the edge-detected VCR horizon, shows a strong correlation with a fault at TT118 in both the amplitude and ant-tracking displays. BS – Booysens Shale.

Borehole TT100 is located at 3025 m and intersects the CLA Dyke. The dyke is described by Litthauer (2009) as a mafic Bushveld-aged intrusion comprising mainly plagioclase, epidote, sphene, and quartz that has undergone a significant amount of alteration. According to the mine structural map of AngloGold Ashanti Ltd. (Figure 3, Appendix B), the dyke is northwest trending and is crosscut and displaced by the PF. A study by Simkus, et al. (2016) noted the Jean Dyke and Pretorius Fault as the main structures intersected by the sub-horizontal boreholes TT107 and TT109. TT107 is a 400-m long borehole located at 3049 m that crosscuts the Pretorius Fault as well as intersects the border of the north-northeast trending Jean Dyke. Borehole TT109 is located approximately 100 m northeast of TT107, is 100 m long, and intersects the Jean Dyke. Based on the geochemical analyses conducted by Litthauer, et al. (2009), the dyke is possibly of Ventersdorp age. The dyke comprises chlorite as the main mineral with epidote, plagioclase that has mostly been altered to calcite, and quartz.

A comparison of amplitude and ant-tracked displays of sample points TT100, TT107, and TT109 outline a number of different features. While the overlying BLR and underlying West Rand Group shales have strong reflections, the VCR is a poor seismic reflector in between the two horizons. The reason for poor imaging of the VCR in this area is not known. Amplitude display shows that TT100, TT107, and TT109 lie right within the vicinity of mine stopes represented as the high amplitude areas (Figure 7.29 a, c, and e). In the ant-tracked sections (Figure 7.29b, d, and f), the samples are evidently intersected by a number of dykes and faults, and sample TT100, in particular, appears to be located in an area of structural complexity.

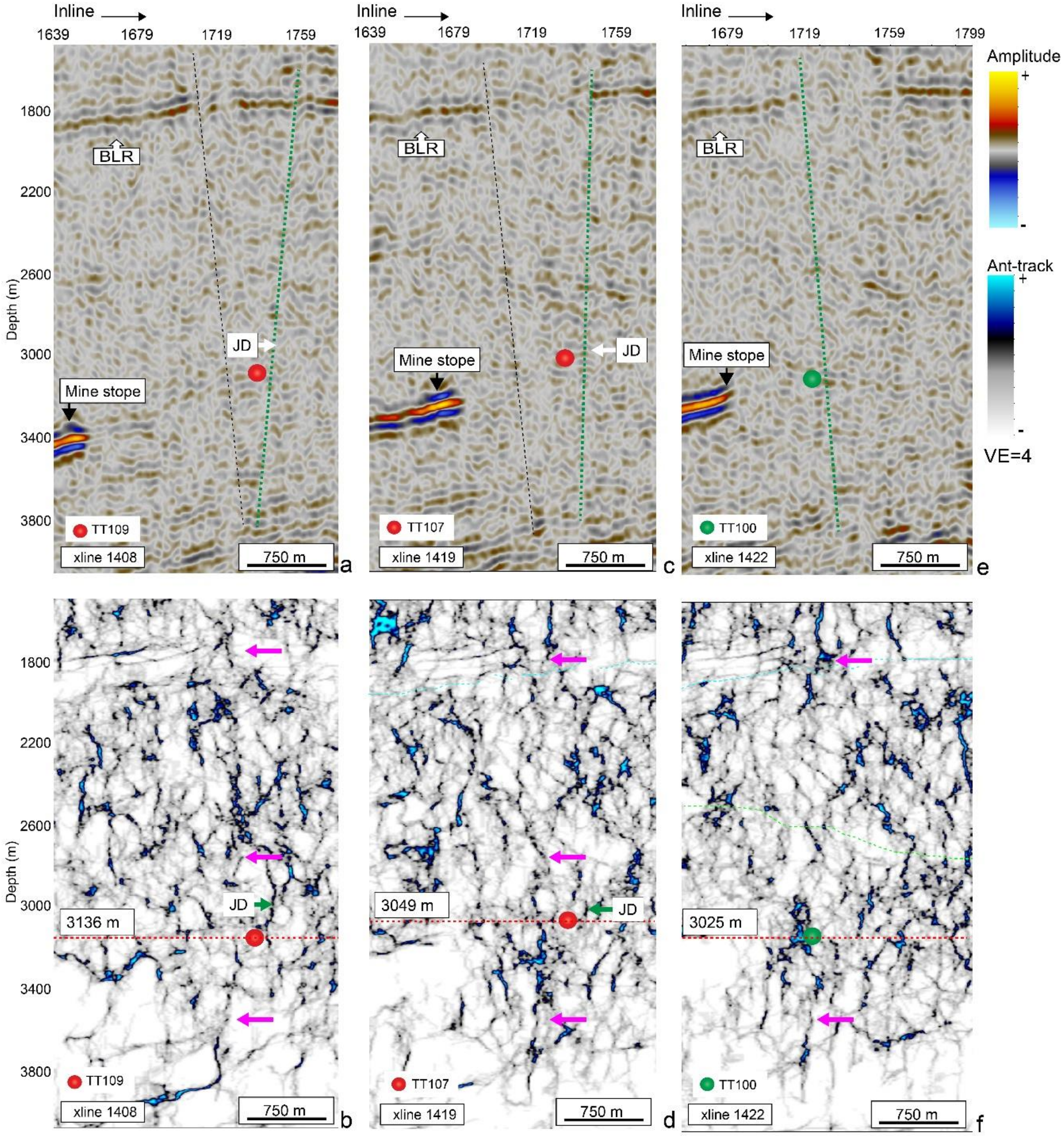

Figure 7.29: Amplitude and ant-tracked displays along samples TT109 (a and b), TT107 (c and d) and TT100 (e and f). The samples are located close to the Jean Dyke (JD; green dashed line). There is a fault (traced by pink arrows) mapped by the ant-tracking attribute that visibly stems from depth and crosscuts the Black Reef (BLR). Mine stopes are also noted in the amplitude display seismic sections of all the samples.

Structural interpretation at the TauTona gold mine using the conventional amplitude display was challenging. Two factors have resulted in the low signal-to-noise ratio observed in the gold mine. The first is the location of the mine along the periphery of the 3D seismic survey where there is low fold coverage, which affects the quality of the acquired seismic data. The other factor is the structural complexity at this portion of the West Wits Line Goldfield that hampers imaging of subsurface features using the seismic reflection method. Despite this, the possible dykes as well as faults reported as being intersected by the boreholes could be noted. The ant-tracking attribute even enhanced faults emanating from depth, intersecting boreholes TT107 and TT109.

The reported geological structures and their orientations was confirmed by depth slices taken at 3025, 3049, 3137, and 3550 m where the four samples were located. The depth slices show that the TT100, TT107, and TT109 boreholes are located within a set of north northeast trending faults (Figure 7.30a to c). The depth slice 3550 m where borehole TT118 is located (Figure 7.30d), a northeast fault that is mostly likely the PF intersects not only TT118 but TT107, confirming the report of both boreholes intersecting the PF as reported by Heesakkers, et al. (2011) and Simkus, et al. (2016).

Integration of standard amplitude seismic display and the ant-tracking displays show the mapping of faults and dykes associated with fracture waters containing methane gas. The results share insightful information into the degree of structural complexity and connectivity of geological structures that may be conduits in the West Wits Line Goldfield.

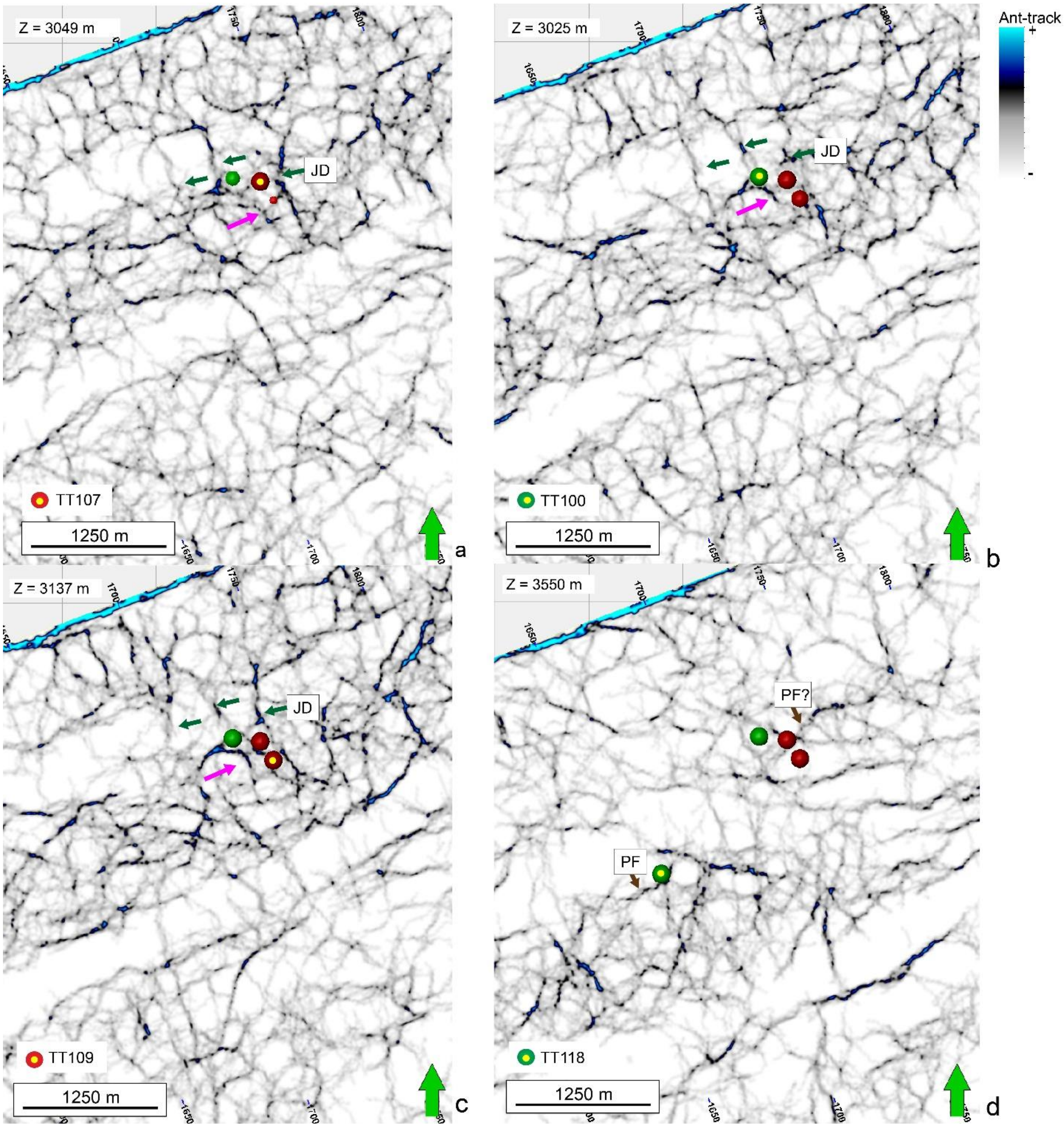

Figure 7.30: Times slices of ant-tracked volume of sample a) TT107 at 3049 m, b) TT100 at 3025 m, c) TT109 at 3137 m, and d) TT118 at 3550 m. At elevations between TT107(a) and TT109 (c) the proposed Jean Dyke (JD) as well other NNW-trending faults (marked with the green arrows) that run parallel to the dyke. The pink arrows point to a NW-trending intersecting sample TT100. The Pretorius Fault (PF) can be seen intersecting sample TT118 (d) and the fault appears to extend and intersect TT107.

8. DISCUSSION

In this study, the 1995 WUDLs 3D seismic data from the West Wits Line Goldfield were used to determine the structural controls of the occurrence of hydrocarbons, particularly methane, in the gold mines within the goldfields. A comparison of the structures intersecting the mining reef, the Ventersdorp Contact Reef (VCR), and potential source of hydrocarbons in the Witwatersrand Basin, the Booysens Shale (BS) was carried out. This was done by first, using conventional seismic data and then applying seismic attributes analysis to enhance faults and fractures in the data set that are undetected using conventional seismic amplitude interpretation. Data from 16 samples collected from Driefontein, Mponeng, and TauTona gold mines in the West Wits Line Goldfield were incorporated into the 3D seismic data to study the relationship between methane/water sampling positions, rock formations, gas compositional and stable isotope, and seismically mapped geologically structures. The data collected from the boreholes included spatial information (x-, y- and z-coordinates) that could be used to map the locations of the samples. Geological information such as the rock formations, the structures that intersected the boreholes, and gas compositional and stable isotope data from fissure water analysis was included.

8.1 Conventional seismic display versus seismic attribute analysis

Prior to the development of the numerous seismic attributes available for structural interpretation today, the interpreter relied mainly on a standard amplitude display, the manipulation of the colour display colour, and some experience and knowledge to interpret structures encountered at the subsurface (Chopra & Marfurt, 2005; Herron, 2011). The quality and confidence with which the interpretation would be (and in some instances still is) carried out would depend on the quality of the seismic data.

Acquisition of the WUDLs 3D seismic data proved successful in mapping geological targets such as the VCR and BLR and the data are thus considered to be of good quality (Pretorius, et al., 2006; Malehmir, et al., 2014). The high acoustic impedance contrast between the quartzites of the Witwatersrand Supergroup and metabasalts of the Ventersdorp Supergroup resulted in good imaging of the VCR, which lies at the base of the Ventersdorp Supergroup. Imaging of the BS was also successful based on its acoustic impedance with the overlying Central Rand Group quartzites.

An interpretation of the BS and VCR horizons using 3D seismic showed that the depth at which they can be intersected increases basinward, away from the collar of the Witwatersrand Basin. The VCR occurs at depths between approximately 1 300 and 6 300 mbls and the BS forms the immediate footwall to the VCR in the Driefontein gold mine and reaches maximum depths of 6 600 mbls within the 3D seismic survey. The BS and VCR horizons are seismically mapped throughout most of the survey area; however, there were factors that hindered confident interpretation of the horizons. The first hindrance was poor resolution along the periphery of the survey due to low fold coverage. The general range for the fold coverage of 3D seismic surveys is between 10 and 120 (10 being the lowest and poorest coverage, and 120, the highest and best) (Ashton, et al., 1994). In most 3D seismic surveys acquired from the Witwatersrand Basin, fold coverage ranged between 16 and 20 and the WUDLs survey fell within that range. Increasing the fold coverage to 36 was a means to improve the imaging of the key stratigraphic horizons in the basin (Pretorius, et al., 1989; Pretorius, et al., 2006; Manzi, et al., 2015).

Another problem encountered during the interpretation process was the poor imaging of seismic horizons in the north and northeastern portions of the survey. This has been attributed to the scattering of seismic energy due to karst weathering of the Transvaal dolomites that overlay the Witwatersrand Basin. The highly fractured nature of the carbonate rocks creates the intense heterogeneity that can be seen on the seismic section, particularly in the Driefontein gold mine area (Manzi, et al., 2012; Doetsch, et al., 2015). While the first option may be true for MP104, the theory may not hold for sample MP109. The strong seismic reflections below sample MP109 suggest a significant acoustic impedance contrast between two mediums - presumably air and the surrounding rock type. Pretorius, et al. (2006) have previously correlated seismic data with underground mine data from gold mines and identified such high amplitude areas as mine stopes. The likelihood of the high amplitude anomaly being a mine stope is also supported by Heersakkers, et al. (2011).

Fault detection between the BS and VCR using various interpretation techniques has been done with a high amount of confidence. Interpretation of the western portion of the survey was done by Manzi, et al. (2012) but no interpretation had yet been done in the eastern part of the seismic survey (namely the Kusasalethu and Deelkraal mines). The faults that could be identified in conventional seismic amplitude display were those with throws above a quarter of the dominant wavelength (i.e. 25 m). Although interpreting faults using seismic amplitude display is a good basic step in fault interpretation, the method falters in areas of low signal-to-noise ratios caused by structural complexity or poor fold coverage. Confident interpretation is also low in areas where faults have undergone block rotation resulting in variable throw along the length of the fault. One such example is the Pretorius Fault (PF) whose maximum throw was measured at 7 ms towards the west of the survey and a minimum of 5 ms further east where the fault throw was above seismic resolution. The application of seismic attributes proved valuable in defining not only faults under-sampled by conventional seismic display for horizon interpretation but also highlighted the continuity and connectivity of faults in volumetric seismic attribute analysis.

The work done in this dissertation involved the application of both horizon-based and volumetric attributes. Because the BS had never been interpreted before, three basic attributes were applied to the horizon: instantaneous phase, instantaneous frequency, and envelope. These three attributes (collectively known as complex trace attributes) gave a first-hand understanding of the stratigraphic and structural character of the BS. The dip, dip azimuth, and edge-detection attributes were also applied to both the BS and VCR, and the structural relationship between the two horizons was determined.

The application of the horizon-based seismic attributes, particularly the instantaneous attributes, emphasized areas of noisy data, which reiterated the importance of data conditioning prior to the application of the attribute. Data conditioning involved smoothing along both the horizons as well as the entire 3D seismic volume. Using dip-corrected, structure-oriented smoothing filters as described by Hale (2009) ensured that the structural integrity of the fault was preserved and variations in orientation and coherence along the horizon and within the seismic data are accounted for. Smoothing filters such as median and mean filters were applied to the seismic data used in this study. These filters not only reduce noise and enhance structural features but if not applied correctly, may result in smearing along edges as was demonstrated when different filter sizes were applied to the 3D seismic volume. Deciding on the correct level of smoothness is at the discretion of the interpreter and depends on what features the user would like to be preserved (Hale, 2009; Herron, 2011; Chopra & Marfurt, 2014). The process of data conditioning set the precedent for fault mapping using seismic attribute application and analysis.

The application of the volumetric ant-tracking attribute involved a four-step process of 1) data conditioning, 2) edge-detection, 3) edge enhancement, and 4) fault interpretation. The ant-tracking attribute successfully highlighted faults and fault intersects as well as fractures in the 3D seismic data. In some few areas, seismic attributes were not as successful due to poor signal-to-noise ratio. These could be attributed to acquisition footprints and processing artefacts. Cheret, et al., (2010) point out that the noise, which appears as discontinuities, may be coherent and non-coherent, attributed to the acquisition footprint identified as vertical discontinuities following the acquisition direction or processing artefacts. An example of the effects of noise because of the enhancement of the acquisition footprint was the result derived from running the ant-tracking volume 3 times in an attempt to accentuate structural detail. Although the acquisition footprint was stark in the third-run ant-track volume, there had to be a compromise between the quality of the extraction and the magnitude of the faults enhanced. This meant that in instances where particular faults of interest were identified in the third-run ant-track volume, this had to be correlated with the first-run ant-tracking volume, which was less affected by noise caused by the acquisition footprint.

Overall, the application of seismic attributes for structural interpretation was successful. The attributes shed new light on faults displacing the economic VCR and associated source of hydrocarbons in the Witwatersrand Basin, the BS. The ant-tracking attribute also highlighted likely structural controls of methane gas as well as groundwater finding its way to mining operations in the gold mines of the West Wits Line Goldfield.

8.2 Structural controls of methane gas and the associated fracture water

One of the key objectives of this study was to determine any links between the types of methane, whether biogenic or abiogenic, found at mining levels and faults or dykes that are associated with the boreholes where fracture water and gas samples were collected. The samples presented were collected from the Driefontein, Mponeng, and TauTona gold mines. This research forms a branch of a larger body of work where numerous authors have identified and attempted to characterize microbial life found in the deep, high temperature gold mines across the Witwatersrand Basin (Takai, et al., 2001; Moser, et al., 2003; Omar, et al., 2003; Ward, et al., 2004; Kieft, et al., 2005;

Moser, et al., 2005; Sherwood Lollar, et al., 2006, 2007, 2008; Lau, et al., 2014; Magnabosco, et al., 2016; Simkus, et al., 2016). The findings have been correlated with the categories of fracture waters emanating from boreholes located in the Central Rand Group quartzites, Ventersdorp Supergroup lavas, and Transvaal dolomites (Duane, et al., 1997; Lippmann, et al., 2003; Lippmann-Pipke, et al., 2011).

8.2.1 The character of fracture waters in the West Wits Line Goldfield

The 15 samples that were collected from the Driefontein, Mponeng, and TauTona gold mines and analysed for compositional, isotopic, and geochemical data were all fracture water. As recognized by Manzi, et al. (2012), the occurrence of methane gas in the Witwatersrand gold mines is intimately tied to groundwater intersected during mining operations. This is also the case in other Precambrian Shields in Canada, Finland, Sweden, and the United States of America (Kietavainen & Purkamo, 2015). The boreholes were located in the dolomites of the Transvaal Supergroup, the Ventersdorp lavas, and the Central Rand Group quartzites. Only the samples collected from the Transvaal dolomites were described as having a predominantly microbial methanogenic signature. The other sampling locations in the Ventersdorp Supergroup lavas and Central Rand Group quartzites were noted as having abiogenically produced methane (Sherwood Lollar, et al., 2006; Simkus, et al., 2016). Numerous authors (Moser, et al., 2003; Onstott, et al., 2006; Duane, et al., 1997) have categorized the fracture water found in the gold mines into two categories. The first is younger (up to 15 Ma), saline palaeometeoric water with temperatures ranging between 30 and 40°C, that has lower concentrations of CH_4 gas of microbial origin. Waters derived from samples DR5IPC and DR9IPC collected within the Transvaal dolomites exhibited these characteristics – they had the lowest recorded CH_4 concentrations at 1.93 and 11.62 mol%, respectively. The other category is hypersaline hydrothermal fluid that is older than 2 Ga with current day temperatures ranging between 45 and 60°C. Onstott, et al. (2006) proposes that these fluids formed at temperatures between 250 and 300°C and as the fluid cooled, O and H isotopic exchange occurred, a phenomenon that has been witnessed in gold mines in Canada (Holland, et al., 2013). This helps explain the low $\delta^{18}O$ and $\delta^{2}H$ values observed in fracture water derived from boreholes DR546 BH1 and DR548 FW. The samples had abiogenically generated CH_4 that pointed to extensive water-rock interaction. In particular, according to Lippmann, et al. (2003), the observed stable isotope values are a result of the hydration of the surrounding rock minerals, specifically the alteration of silicates to clay minerals on the condition that the water-to-rock ratio is low.

Although these categories have been defined, Sherwood Lollar, et al. (2008) found that most of the fracture water collected at these gold mines, both in South Africa and Canada, had undergone a significant degree of mixing – the palaeometeoric water mixing with hydrothermal fluid. The mixing has resulted in CH_4 and hydrocarbon signatures that represent heterogeneous fluid pathways within the rocks of the Witwatersrand and Ventersdorp supergroups.

8.2.2 Abiogenic CH_4 production in the Witwatersrand Basin

All samples collected in the three gold mines had a predominantly abiogenic methane signature excluding those collected from the intermediate pumping chambers (IPCs) of Shafts 5 and 9 of the Driefontein gold mine. For most of the samples with an abiogenic signature, the presence of methanogens, i.e. methane producing microbes, generally accounted for less than 10% of the total methane observed at the boreholes. One particular study by Lin, et al. (2006) looking at sulphide-reducing microbes and CO_2-utilizing methanogens at borehole MP104 to determine the metabolic and respiratory patterns of these microbes, highlights the previous statement. Lin, et al. (2006) observed that while the methanogens were present in these deep subsurface conditions, their impact, based on the size of the methanogenic community (which made up approximately 10%), was smaller than that of the sulphide-reducing microbes. δ^2H and $\delta^{13}C$ isotopic analysis of the hydrocarbons found in the fractures from Mponeng gold mine have isotopic signatures similar to methane found at the adjacent Driefontein and Kloof gold mines and other Precambrian Shield sites in Canada (Sherwood Lollar, et al., 2006). The methane gas production in these rocks has been attributed to water-rock interactions.

It was noted that abiogenic CH_4 found in the Witwatersrand Basin, as well as in other sites in Canada and Finland, was isotopically lighter than that of mantle CH_4 (Sherwood Lollar, et al. 1993; 2005). This reflects sources of carbon from within the basin supporting similar postulates made by Mossman, et al. (2008). Abiogenic methane production is attributed to extensive gas-water-rock in the basin. Geological processes such as serpentinization, Fischer-Tropsch synthesis, which involves the reaction of H_2 with CO to produce CH_4 and H_2O, and the metamorphism of carbonaceous-graphite containing rocks have been known to produce abiogenic methane (Schoell, 1988; Etiope & Sherwood Lollar, 2013). An alternative study by Bons and Gomez-Rivas (2013) postulates that variable isotopic signatures from shallower depths to deeper reservoirs are the result of gravitational fractionation.

The geochemistry of the dykes that the boreholes intersected give some light about the processes that may be responsible for the abiogenic production of CH_4 and mobility of fracture water containing CH_4. Dykes in the West Wits Line Goldfield are known to compartmentalize the rocks of the dolomites of the Transvaal Supergroup (Schrader & Winde, 2015). The dykes are of different ages and may act as conduits for water or may impede the flow of fluid. Litthauer (2011) carried out geochemical analyses to determine the origin of the dykes at the Mponeng and TauTona gold mines. The study included samples from the CLA Dyke intersected by TT100 and the Jean Dyke, intersected by the TT107 and TT109 boreholes. Another petrographic study was done by Ilgner (2006) of the Spotted Dick Dyke, intersected by boreholes

DR938 CH and DR940 FW. All the dykes were described as mafic and of Ventersdorp-age (Jean and Spotted Dick Dykes) and Bushveld Complex-age (CLA Dyke). Both these studies showed that all these samples comprised more than 10% chlorite, an alteration mineral of greenschist metamorphic grade. Other key metamorphic minerals that were found were quartz and calcite, an alteration mineral of plagioclase. These secondary minerals play a crucial role in the availability of components for the production of CH_4 and the migration of fluids within the basin. Secondary minerals such as chlorite, quartz, and calcite, as well as tectonic activity may control the opening and closing of fractures thus controlling fluid flow (McNutt, et al., 1990). According to Grasemann and Tschegg (2012), the formation of secondary minerals in fault rocks reduces the friction coefficient value thus effectively weakening the fault. The formation of the secondary minerals increases the permeability of the fault zone. This facilitates additional influx of fluid. Fluid influx is dependent on the tectonic stability of the fault zone and water-rock reaction rates that form the secondary minerals (Wästeby, et al., 2014).

Numerous processes may result in the production of H_2 exist within the Witwatersrand Basin. The hydrolysis of olivine would produce H_2 but none of the dykes intersected by these boreholes contains olivine, which alters to serpentine, an important component in the production of CH_4. The alteration of Fe^{2+}-bearing olivine produces serpentine and hydroxides, combined with the oxidation of Fe^{2+}, produce magnetite and H_2 (Neubeck, et al., 2014). Lin, et al. (2005) suggests that although the mineral assemblages of the Ventersdorp- and Bushveld Complex-aged dykes, shales of the Witwatersrand Basin such as the BS and the rocks of the Ventersdorp Supergroup contain some Fe, these are unlikely candidates for the production of H_2. The study, which investigated the production of H_2 in the Witwatersrand Basin, found that the most likely source of H_2 would be the interaction of water with the radiogenic elements U, Th, and K that have been identified and studied in the rocks of the Witwatersrand Supergroup. According to Wronckiewicz and Condie (1987) shales of the Central Rand Group such as the BS are low in Fe^{2+} and Mg^{2+} but those of the West Rand Group are enriched in these elements. Some of the shale units in the West Rand Group are even described as magnetite-rich. This means that while the chances of the BS being a source of abiogenic hydrocarbons is slim, the shales of the West Rand Group may be a more likely candidate.

Another study by Lippmann, et al. (2011) showed that at level 118 at the TauTona, where borehole TT118 is located and intersects the PF, the amount of geogas components such as H_2, CH_4, and CO_2 present at mining levels peaked during mine blasting and drilling operations. These results point to the major role mining activity plays in the occurrence and transmission of flammable gases such as CH_4 and H_2 at mining levels.

8.2.3 Fluid and CH_4 migration in the Witwatersrand and Ventersdorp supergroups

One of the main aims of this research was to not only attempt to determine the structural characteristics of a possible hydrocarbon source relative to a key gold-bearing horizon, i.e. a mining level, but also to distinguish any faults related to methane gas that could be imaged using conventional seismic amplitude and enhanced using the ant-tracking attribute. The following section conveys the possible implications of structures identified by seismic amplitude sections and enhanced by the ant-tracking attributes.

Fluid migration and the presence of hydrocarbons in the Witwatersrand Basin has been intimately tied to the occurrence of gold found in the basin. The link between the two is that where enrichment in hydrocarbons was encountered, any associated gold, whether along the reefs or in veins, would be of a high grade (Jolley, et al., 2004). The migration of fluids in this meta-sedimentary basin is a result of the complex structural history of the Witwatersrand Basin.

The ant-tracking attribute highlighted that the three stratigraphic packages had distinctly different structural characters. Varying degrees of what have been described as “fracture zones” were identified along stratigraphy with the frequency of these bodies decreasing from the upper Transvaal Supergroup dolomites through the Ventersdorp Supergroup lavas to the lower Central Rand Group quartzites. The zones may be attributed to noise, fracturing and faulting occurring naturally or exacerbated by blasting occurring during mine operations, or in the case of the Transvaal dolomites, might represent the highly porous nature of the aquifer. The presence of these observed fracture zones supports the model by Sherwood Lollar, et al. (2007) of mixing between less saline palaeometeoric water and hydrogeologically isolated pockets of water, predominantly hydrothermal fluid in the basin. A concept originally derived from McNutt, et al. (1994) and adapted to the case of the isotopic signatures observed in the fracture waters of the Witwatersrand Basin, the authors point out the role played by secondary minerals such as calcite and quartz as well as tectonic activity in the opening and closing of fractures to control fluid flow.

Amplitude seismic display successfully showed that the faults that were associated with the sampling points were mainly normal faults that intersected the BS, VCR, and the BLR. The structures were NNW, NW, or NE-trending with dips greater than 75°. The structures are attributed to different compressional and extensional tectonics that has been documented in the Witwatersrand Basin. Although the tectono-sedimentary history of the Witwatersrand Basin and overlying Ventersdorp Supergroup are well documented, a summary of the tectonic events that has been encountered at the West Wits Line Goldfield is presented by Dankert and Hein (2010).

The Snake Dyke (and associated fault), Jean Dyke, Pretorius Fault and faults F548 (3) and F548 (4) are the northeast trending geological structures identified in the study. The orientation of the faults coincides with a time in the tectonic history of the volcano-sedimentary basin characterized by the deposition of the VCR, extrusion of the Klipriviersberg metabasalts, and tectonic inversion of the Bank Fault (Berlenbach, 1993). The extrusion of the Klipriviersberg Group lavas would have resulted in the introduction of CO_2, H_2O and other gases associated with magmatic extrusion into the Witwatersrand Basin (Gonnermann & Manga, 2012).

Tectonic inversion would have resulted in fault reactivation as seen in the Pretorius Fault Zone. The Pretorius Fault is a steeply dipping normal fault that has a variable throw along its length. The fault system is also characterized by three fault zones with faults and fractures that have varying orientations and slips within each zone. The fault segments (which are connected to the variable throw of the main fault) are attributed to increased seismicity due to mining operations in the TauTona and Mponeng gold mines. Seismic interpretation shows that the fault extends much further (approximately 2 km more than the originally proposed 10 km) and the throw increases towards the southwest extension of the fault (Gibson, et al., 2000; Heesakkers, et al., 2011). The timing of activity of a structure implies that an originally normal fault undergoes compressional reactivation. Such is the case with the PF where the VCR has a normal sense of displacement whereas the fault has undergone compressional reactivation in upper BLR. As stated by Sibson (1995), and later reiterated by Bonini, et al. (2012), steeply dipping normal faults that have undergone reactivation may form crucial structural traps for hydrocarbons.

North northwest and northwest- trending structure such as the Spotted Dick Dyke is related to a compressional event that came before the intrusion of the Bushveld Complex approximately 2.06 Ga. This coincides with the categorization of the CLA

Dyke by Litthauer (2006) as a Bushveld-aged intrusion. The orientation of the Spotted Dick Dyke may indicate the change from the compressional regime into which the Klipriviersberg Group extruded to the rifting event characterized by the extrusion of the Platberg Group as suggested by Stanistreet and McCarthy, et al. (1991).

Another key structural feature identified in the seismic data was thrust imbricate faulting at VCR level in the Mponeng and Kusasalethu gold mining areas. Extensive structural mapping done by Jolley, et al. (1999, 2004) show that the thrust planes (which linked to form imbricate systems and were oriented in an north northwest and north westerly directions) found in the Kusasalethu gold mine are characterized by ultracataclasitic fault rocks. The cataclasitic material comprised within these fault rocks is described as having undergone fluidized granular flow that formed laminar bands within the thrust planes and focused fluid movement (Jolley, et al., 1999). These fault rocks would have low cohesion and show evidence of hydrothermal fluid flow. These thrust faults are associated with steeply dipping fracture systems (which were formed in the reef) that not only contain gold and uranium minerals, but mesophase hydrocarbons as well. An investigation of the fracture systems by Jolley, et al. (2004) and their relationship to gold mineralization revealed that most of the fractures that were mapped were closely associated with fault rocks. The study showed that, based on their position and form along the fractures, the hydrocarbons had to have migrated from source via faults and into the gold bearing reefs through the fractures. That said, there are limitations to the migration of hydrocarbons. Not all faults and fractures found in a sedimentary basin are conduits for gas and water transmission. This is particularly true in crystalline, metamorphosed sedimentary basins such as the Witwatersrand Basin that has a complex deformation history. Sibson (1994) explains that differential stresses acting within a tectonic regime affect the permeability of the rock mass and thus modulate fluid flow in the crust. The study shows that while faults and extensional fractures affect the permeability of the surrounding rocks, fluid flow in these faults and fracture systems is episodic. Fluid flow within a fault zone like the

PFZ that has undergone intermittent rupturing in the TauTona gold mine, is controlled by a number of mechanisms (Heesakkers, et al., 2011). These mechanisms, which include, dilatancy due to shearing, mean stress changes during fault growth and the discharge of overpressurized fluids in sections of the crust, act to either increase permeability or create impermeable barriers in the rock-mass (Sibson, 1995; Frape, et al., 2014).

The results show that although there were numerous faults that transacted the BS and VCR, not all of them would carry methane gas from depth. Apart from the structural information that was noted during the extraction of fracture water from the gold mines of the West Wits Line Goldfield, seismic attribute analysis revealed that the basin is characterized by a degree of structural complexity that cannot be observed using traditional interpretation methods.

9. CONCLUSION

South Africa is home to some of the deepest gold mines in the world. 3D seismic surveys have been acquired since the 1980s in order to delineate and effectively map key economic horizons such as the Ventersdorp Contact Reef. The use of these surveys has proven to be successful over the years for not only mine development but remote structural mapping of these reefs. One problem that is yet to be solved regarding mine production is the occurrence of methane gas and subsequent explosions associated with them. This research applied conventional as well as enhanced (through seismic attribute analysis) seismic interpretation techniques in order to understand a possible source of this methane gas. The use of instantaneous phase, frequency, and envelope as well as geometric attributes dip, dip azimuth and edge-detection showed that there are structures that propagate between the Booysens Shale and the mining levels (i.e. VCR). The process was taken a step further and ant tracking (an edge enhancement attribute) was applied to the 3D seismic volume. Methane data points were also plotted in the seismic volume and depth slices through the survey revealed that the methane occurrences in the Witwatersrand Basin are largely structurally controlled. Results showed that there was variation in methane concentration that was a function of the temperature and the proximity of these methane data points to faults. The study concluded that although most of the sampling points (which were either gas or groundwater samples) were structurally related, not all the structures were near the sample locations. The study has shown that the integration of different datasets is useful in helping to understand the mechanism of fluid and gas transmission in the mining region. The study also found a link between the abiogenic sources of methane and the structures with which they were associated. Faults and dykes play an integral part in fluid flow that allows for gas-water-rock interactions, the mechanism by which most of the methane found in the study area is generated. The research confirmed postulations that the sources of the methane found at mining levels may not only come from depth but from more localized sources.

10. REFERENCES

Ahmadi, O., Juhlin, C., Malehmir, A. & Munck, M., 2013. High-resolution 2D seismic imaging and forward modeling of a polymetallic sulfide deposit at Garpenberg, central Sweden. *Geophysics,* Volume 78, pp. 339-350.

AngloGold Ashanti Limited, 2015. *West Wits, South Africa - Operation Profile,* Johannesburg

AngloGold Ashanti Limited, 2013. *Exploration Review,* Johannesburg: AngloGold Ashanti Limited.

Anhaeusser, C. R., 2006. Ultramafic and mafic intrusions of the Kaapvaal Craton. In: M. R. Johnson, C. R. Anhaeusser & R. J. Thomas, eds. *The Geology of South Africa.* 1st ed. Johannesburg, Pretoria: Geological Society of South Africa, Council of Geosciences, pp. 95-134.

Armstrong , R. A., et al., 1991. Zircon ion microprobe studies bearing on the age and evolution of the Witwatersrand. *Precambrian Research ,* Volume 53, pp. 243-266.

Ashton, C. P., et al., 1994. 3D Seismic Survey Design. *Oilfield Review,* Volume 6, pp. 19-32.

Bacon, M., Simm, R. & Redshaw, T., 2007. Common techniques for quantitative seismic interpretation. In: *3-D Seismic Interpretation.* 3rd ed. Cambridge: Cambridge University Press, pp. 168-211.

Bacon, M., Simm, R. & Redshaw, T., 2007. Geological interpretation. In: *3-D Seismic Interpretation.* 3rd ed. Cambridge: Cambridge University Press, p. 225.

Barnard, H. C. & Baran, E., 2000. 1:500 000 Hydrogeological map series of the Republic of South Africa: Johannesburg 2526. Pretoria: Department of Water Affairs and Forestry.

Baytok, S., 2010. Seismic investigation and attribute analyisis of faults and fractures within a tight-gas sandstone reservior: Williams Fork formation, Mamm, Piceance Basin, Colorado. Kocaeli University, Turkey. MSc Thesis.

Baytok, S. & Pranter, M. J., 2013. Fault and fracture distribution within a tight-gas sandstone reservoir: Mesaverde Group, Mamm Creek Field, Piceance Basin, Colorado, USA. *Petroleum Geoscience,* Volume 19, pp. 203-222.

Bense, V. F. & Hiscock, K. M., 2014. Environmental isotope hydrogeology. In: *Hydrogeology: Principles and Practice.* 2nd ed. Wiley, p. 564.

Berlenbach, J. W., 1993. The mechanics of bedding-parallel faulting associated with the Ventersdorp Contact Reef on the Kloof Gold Mine, Johannesburg: Rand Afrikaans University. PhD Thesis.

Biffi, M. & Cook, A. P., 2002. A combined analysis of investigations into recent flammable gas explosions in South Africa gold mines. Kingston, Canada, CRC Press, pp. 511-518.

Blasch, K. W. & Bryson, J. R., 2007. Distinguishing sources of ground water recharge by using δ2H and δ18O. *Groundwater,* Volume 45, pp. 294-308.

Borgonie, G., et al., 2015. Eukaryotic opportunists dominate the deep-subsurface biosphere in South Africa. *Nature Communications,* pp. 1-12.

Bowen, T. B., Marsh, J. S., Bowen, M. P. & Eales, H. V., 1986. Volcanic rocks of the Witwatersrand Triad, South Africa: description, classification and geochemical stratigraphy. *Precambrian Research ,* Volume 31, pp. 297-324.

Brink, M., Waanders, F., Bisschoff, A. & Gay, N. C., 2000. The Foch Thrust–Potchefstroom Fault structural system, Vredefort, South Africa: a model for impact-related tectonic movement over a pre-existing barrier. *Journal of African Earth Sciences,* Volume 30, pp. 99-117.

Brown, A., 1996. Seismic attributes and their classification. *The Leading Edge,* Volume 15, p. 1090.

Bonini, M., Sani, F., Antonielli, B., 2012. Basin inversion and contractional reactivation of inherited normal faults: A review based on previous and new experimental models. *Tectonophysics*, Volume 522-523, pp. 55-88.

Buck, S. G. & Minter, W. E. L., 1985. Placer formation by fluvial degradation of an alluvial fan sequence: the Proterozoic Carbon Leader placer, Witwatersrand Supergroup, South Africa. *Journal of the Geological Society of London,* Volume 142, pp. 757-764.

Carstens, A., 2007. Development of a support strategy for cleaning slushers situated in Booysen's Shale at Mponeng Gold Mine. Free State, South African National Institute of Rock Engineering, pp. 123-135.

Cawthorn, R. G., 2015. The geometry and emplacement of the Pilanesberg Complex, South Africa. *Geological Magazine,* Volume 152, pp. 802-812.

Cawthorn, R. G., Davies, G., Clubley-Armstrong, A. & McCarthy, T. S., 1981. Sills associated with the Bushveld Complex, South Africa: an estimate of the parental magma composition. *Lithos,* Volume 14, pp. 1-15.

Cawthorn, R. G., et al., 2006. The Bushveld Complex. In: M. R. Johnson , C. R. Anhaeusser & R. J. Thomas , eds. *The Geology of South Africa.* 1st ed. Johannesburg, Pretoria: Geological Society of South Africa, Council of Geosciences, pp. 261-281.

Cawthorn, R. G. & Walraven, F., 1998. Emplacement and crystallization time for the Bushveld Complex. *Journal of Petrology,* Volume 39, pp. 1669-1687.

Cheret, T., Long, J. & Turner, J., 2010. Comparison between faults extracted from seismic and Elastic Dislocation Modelling. *Canadian Society of Exploration Geophysicists Recorder,* pp. 32-34.

Chopra, S. & Marfurt, K., 2005. Seismic attributes - A historical perspective. *Geophysics,* Volume 70, pp. 3-28.

Chopra, S. & Marfurt, K., 2014. Causes and appearance of noise in seismic volumes. *Geophysical Corner: An AAPG article*, October.

Chopra, S. & Marfurt, K. J., 2007. Structure-oriented filtering and image enhancement. In: *Seismic Attributes for Prospect Identification and Reservoir Characterization.* Tulsa, USA: SEG Books, pp. 187-218.

Chopra, S. & Marfurt, K. J., 2007. Volumetric curvature-attribute applications for detection of fracture lineaments and their calibration. *Geohorizons,* pp. 27-31.

Clark, I. & Fritz, P., 1997. *Environmental isotopes in Hydrogeology.* Florida: Lewis Publishers.

Cook, A. P., 1998. The occurrence, emission and ignition of combustible strata gases in Witwatersrand gold mines and Bushveld platinum mines, and means of ameliorating related ignition and explosion hazards. Itasca Africa (Pty) Ltd.

Cook, P. G., 2003. A guide to regional groundwater flow in fractured rock acquifers. 1st ed. Adelaide, Australia: CM Digital.

Coward, M. P., Spencer, R. M. & Spencer, C. E., 1995. Development of the Witwatersrand Basin, South Africa. *Special Publications of the Geological Society of London,* Volume 95, pp. 243-269.

Cox, S., Flatten, A. & Beck, D., 2015. Dynamics of fluid pathways and fluid flow in intrusion-related hydrothermal systems: Insights from Ore Deposits, Seismicity, and Numerical Modeling. Hobert, Tasmania, Society of Economic Geologits, pp. 1-2.

Cox, T. & Sietz, K., 2007. Ant tracking seismic volumes for automated fault interpretation. Calgary, Alberta

Craig, H., 1961. Isotopic variations in meteoric waters. *Science,* Volume 133, pp. 1702-1703.

Crow, C. & Condie, K. C., 1987. Geochemistry and origin of late archaean volcanic rocks from the Rhenosterhoek Formation, Dominion Group, South Africa. *Precambrian Research,* Volume 37, pp. 217-229.

Crow, C. & Condie, K. C., 1988. Geochemistry and origin of late archean volcanics from the Ventersdorp Supergroup, South Africa. *Precambrian Research,* Volume 42, pp. 19-37.

Dalley, D., 2008. Value of visual attributes: revisiting dip and azimuth displays for 3D seismic interpretation. *First Break,* Volume 26, pp. 87-91.

Dalley, R. M., et al., 1989. Dip and azimuth displays for 3D seismic interpretation. *First Break,* Volume 7, pp. 86-95.

Dankert, B. T. & Hein, K. A. A., 2010. Evaluating the structural character and tectonic history of the Witwatersrand Basin. *Precambrian Research,* Volume 177, pp. 1-22.

Davies, R. J., et al., 2004. 3D seismic technology: are we realising its full potential?. In: *3D Seismic Technology: Application to the Exploration of Sedimentary Basins.* London: The Geological Society of London, pp. 1-9.

De Wit, M. J., et al., 1992. Formation of an archean continent. *Nature,* Volume 357, pp. 553-562.

Dehghannejad, M., Malehmir, A., Juhlin, C. & Skytta, P., 2012. 3D constraints and finite-difference modeling of massive sulfide deposits: The Kristineberg seismic lines revisited, northern Sweden. *Geophysics,* Volume 77, pp. 69-79.

Department of Mineral Resources, South Africa., 2013. *Annual Report,* Pretoria

Doetsch, J., Robertsson, J. O. A., Manukyan, E. & Maurer, H., 2015. Understanding the impact of karst on seismic wave propagation - A multi-method geophysical study. Spain, EAGE, pp. 1-5.

Drennan, G. R. & Robb, L., 2006. The nature of hydrocarbons and related fluids in the Witwatersrand Basin, South Africa: Their role in metal redistribution. *Geological Society of America Special Papers,* Volume 405, pp. 353-385.

Duane, M. J., Pigozzi, G. & Harris, C., 1997. Geochemistry of some deep gold mine waters from the western portion of the Witwatersrand Basin, South Africa. *Journal of African Earth Sciences,* Volume 1, pp. 105-123.

Duddy, I. R., Green, P. F., Bray, R. J. & Hegarty, K. A., 1994. Recognition of the thermal effects of fluid fow in sedimentary basins. *Geological Society, London, Special Publications,* Volume 78, pp. 325-345.

Duncan, A. R. & Marsh, J. S., 2006. The Karoo Igneous Province. In: M. R. Johnson , C. R. Anhaeusser & R. J. Thomas, eds. *The Geology of South Africa.* 1st ed. Johannesburg, Pretoria: Geological Society of South Africa, Council of Geosciences, pp. 501-520.

Einsele, G., et al., 1980. Intrusion of basaltic sills into highly porous sediments, and resulting hydrothermal activity. *Nature,* Volume 283, pp. 441-445.

Els, B. G., van den Berg, W. A. & Mayer, J. J., 1995. The Black Reef Quartzite Formation in the western Transvaal: sedimentological and economic aspects, and significance for basin evolution. *Mineralium Deposita,* Volume 30, pp. 112-123.

Eriksson, P. G. & Altermann, W., 1998. An overview of geology of the Transvaal Supergroup dolomites (South Africa). *Environmental Geology,* Volume 36, pp. 179-188.

Etgen, J., Samuel, H. G. & Zhang, Y., 2009. An overview of depth migration imaging in exploration geophysics. *Geophysics,* Volume 74, pp. WCA5-WCA17.

Etiope, G. & Sherwood Lollar, B., 2013. Abiotic methane on Earth. *Review Gephysics,* Volume 51, pp. 276-299.

Farghal, S. M. & Zoback, D. M., 2014. Utilizing ant-tracking to identify slowly slipping faults in the Barnett shale. Stanford, California, pp. 1-5.

Flectcher, P. & Gay, N. C., 1971. Analysis of gravity sliding and orogenic translation: Discussion. *Geological Society of America Bulletin,* Volume 9, pp. 2667-2682.

Frape, S. K., et al., 2014. Deep fluids in the continents. In: *Treatise on Geochemistry.* 2nd ed. Oxford: Elsevier, pp. 516-554.

Frimmel, H. E. & Minter, W. E. L., 2002. Recent developments concerning the geological history of the Witwatersrand gold deposits, South Africa. In: R. Goldfarb & R. L. Nielsen, eds. *Global Exploration 2002 — Integrated Methods for Discovery: Special Publication, 9.* Littleton: Society of Economic Geologists, pp. 17-45.

Fruh-Green, G. L., Scambelluri, M. & Vallis, F., 2001. O-H isotope ratios of high pressure ultramafic rocks: implications for fluid sources and mobility in the subducted hydrous mantle. *Contributions to Mineralogy and Petrology,* Volume 141, pp. 145-159.

Gibson, M. A., 1997. *The Western Deep Levels goldmine 3-D seismic survey.* Swakopmund, Namibia, South African Geophysical Association, pp. 34-36.

Gibson, M. A. S., Jolley, S. J. & Barnicoat, A. C., 2000. Interpretation of the Western Ultra Deep Levels 3-D seismic survey. *The Leading Edge,* Volume 19, pp. 730-735.

Gibson, R. L. & Jones, M. Q. W., 2002. Late Archean to Palaeoproterozoic geotherms in the Kaapvaal craton, South Africa: constraints on the thermal evolution of the Witwatersrand Basin. *Basin Research,* Volume 14, pp. 169-181.

Godfrey, R. & Ran, B., 2008. Seismically guided fracture characterization. *CSEG RECORDER,* March.pp. 30-36.

Gonnermann, H. M. & Manga, M., 2012. Dynamics of magma ascent in the volcanic conduit. In: S. A. Fagents, T. K. P. Gregg & M. C. Rosaly, eds. *Modelling Volcanic Processes: The Physics nad Mathematics of Volcanism.* 1st ed. Cambridge: Cambridge University Press, pp. 55-84.

Gray, G. J., Lawrence, S. R., Kenyon, K. & Cornford, C., 1998. Nature and origin of carbon in the Archaean Witwatersrand Basin, South Africa. *Journal of the Geological Society,* Volume 155, pp. 39-59.

Grove, D. & Harris, C., 2010. O- and H-isotope study of the Carbon Leader Reef at the TauTona and Savuka Mines (Western Deep Levels), South Africa: Implications for the origin and evolution of Witwatersrand Basin fluids. *South African Journal of Geology,* Volume 113, pp. 1-14.

Hale, D., 2009. Structure-oriented smoothing and semblance. *CWP Report,* Volume 635, pp. 1-10.

Hallbauer, D. K. & van Warmelo, K. T., 1974. Fossilized plants in thucholite from Precambrian rocks of the Witwatersrand, South Africa. *Precambrian Research,* Volume 1, pp. 199-212.

Hall, D. L. & Bodnar, R. J., 1990. Methane in fluid inclusions from granulites: a product of hydrogen diffusion?. *Geochimica et Cosmochimica Acta,* Volume 54, pp. 641-651.

Hall, R. C. B., Els, B. G. & Mayer, J. J., 2004. The Ventersdorp contact reef; final phase of the Witwatersrand Basin, independent formation, or precursor to the Ventersdorp Supergroup. *South African Journal of Geology,* Volume 100, pp. 213-222.

Harmony Gold Mining Company Limited, 2015. *Integrated Annual Report,* Randfontein

Heesakkers, V., Murphy, S. & Reches, Z., 2011. Earthquake rupture at focal depth, part I: Structure and rupture of the Pretorius Fault,. *Pure and Applied Geophysics,* Volume 168, pp. 2395-2425.

Heilweil, V. M., Solomon, D. K., Gingerich, S. B. & Verstraeten, I. M., 2009. Oxygen, hydrogen, and helium isotopes for investigating groundwater systems of the Cape Verde Islands, West Africa. *Hydrogeology Journal,* Volume 17, pp. 1157-1174.

Herron, D. A., 2011. Chapter 2: Seismic Response. In: R. Latimer, ed. *First steps in seismic interpretation.* No. 16 ed. Tulsa, Oklahoma: Geophysical Monograph Series: Society of Exploration Geophysicists, p. 217.

Herron, D. A., 2011. Data Quality and Management. In: R. B. Latimer, ed. *First Steps in Seismic Interpretation.* Tulsa, Oklahoma: Society of Exploration Geophyscists, pp. 153-159.

Hobbs, P. & Cobbing, J., 2007. The hydrogeology of the Krugersdorp Game Reserve area and implications for the management of mine water decant, Johannesburg: CSIR.

Hoefs, J., 2009. *Stable isotope Geochemistry.* 6th ed. Berlin Heildelberg: Springer-Verlag.

Holland, G., et al., 2013. Deep fracture fluids isolated in the crust since the Precambrian era. *Nature,* Volume 497, pp. 357-360.

Horita, J. & Berndt, M. E., 1999. Abiogenic methane formation and isotopic fractionation under hydrothermal conditions. *Science,* Volume 285, pp. 1055- 1057.

IAEA/WMO, 2017. *Global Network of Isotopes in Precipitation. The GNIP Database.* [Online] Available at: http://www.iaea.org/water [Accessed 25 September 2017].

Ilgner, H. J., 2006. *Electric rock breaking for South African ore bodies,* Johannesburg: University of the Witwatersrand. MSc Dissertation.

Jenden, P. D., Kaplan, I. R. & Craig, H., 1994. Abiogenic hydrocarbons and mantle helium in oil and gas fields. In: G. H. David, ed. *The Future of Energy Gases.* United States of America: United States Geological, pp. 31-56.

Jolley, S. J., et al., 2004. Structural controls on Witwatersrand gold mineralisation. *Journal of Structural Geology,* Volume 26, pp. 1067-1086.

Jolley, S. J., Henderson, I. H. C., Barnicoat, A. C. & Fox, N. P. C., 1999. Thrust-fracture network and hydrothermal gold mineralization: Witwatersrand Basin, South Africa. *Geological Society, London, Special Publications,* Volume 155, pp. 153-165.

Jones, M. Q. W., 2003. Thermal properties of stratified rocks in the Witwatersrand gold mining areas. *The Journal of South African Institute of Mining and Metallurgy,* pp. 173-186.

Kalkomey, C. T., 1997. Potential risks when using seismic attributes as predictors of reservoir properties. *The Leading Edge,* Volume 16, pp. 247-251.

Kearey, P., Brooks, M. & Hill , I., 2002. Geophysical Data Processing. In: *An Introduction to Geophysical Exploration.* 3rd ed. Oxford: Blackwell Science Limited, p. 262.

Khair, A. H., et al., 2012. Subsurface mapping of natural fracture networks; A major challenge to be solved. Case study from the shale intervals in the Copper Basin, South Australia. Stanford, California, pp. 1-14.

Kieft, T., et al., 2005. Geochemically Generated, Energy-Rich Substrates and Indigenous Microorganisms in Deep, Ancient Groundwater. *Geomicrobiology Journal,* Volume 22, pp. 325-335.

Kietavainen, R. & Purkamo, L., 2015. The origin, source and cycling of methane in deep crystalline rock biosphere. *Frontiers in Microbiology ,* Volume 6, pp. 1-16.

Kingsley, C. S., 1987. Facies changes from fluvial conglomerate to braided sandstone of the early Proterozoic Welkom Goldfield,Witwatersrand,South Africa. *Society of Economic Palaeontologists and Mineralogists Special Publications,* Volume 39, pp. 359-370.

Kositcin, N. & Krapez, B., 2004. Relationship between detrital zircon age-spectra and the tectonic evolution of the Late Archean Witwatersrand Basin, South. *Precambrian Research,* Volume 129, pp. 141-168.

Kotelnikova, S., 2001. Microbial production and oxidation of methane in deep subsurface. *Earth-Science Reviews,* Volume 58, pp. 367-395.

Lau, M. C. Y., et al., 2014. Phylogeny and phylogeography of functional genes shared among seven terrestrial subsurface metagenomes reveal N-cycling and microbial evolutionary relationships. *Frontiers in Microbiology,* Volume 5, pp. 1-17.

Lin, L.-H. ,et al., 2006. Long-term sustainability of a high-energy, low-diversity crustal biome. *Science,* Volume 314, pp. 479-482.

Lippmann, J., et al., 2003. Dating ultra-deep mine waters with noble gases and 36Cl, Witwatersrand Basin, South Africa. *Geochimica et Cosmochimica Acta,* Volume 67, pp. 4597-4619.

Lippmann-Pipke, J., et al., 2011a. Geogas transport in fractured hard rock – Correlations with mining seismicity at 3.54 km depth, TauTona gold mine, South Africa. *Applied Geochemistry,* Volume 26, p. 2134–2146.

Litthauer, A., 2009. *The geochemistry of the dykes in the Carletonville Goldfield,* Bloemfontein: University of the Free State. MSc Dissertation.

Maake, L., et al., 2013. Gold One Cooke Four Underground operation, Gauteng, South Africa, Independent Technical Report, Johannesburg: Gold One International Limited.

Magee, C., McDermott, K. G., Stevenson, C. E. T. & Jackson, C., 2014. Influence of crystallised igneous intrusions on fault nucleation and reactivation during continental extension. *Journal of Structural Geology,* Volume 62, pp. 183-193.

Magnabosco, C., et al., 2016. A metagenomic window into carbon metabolism at 3 km depth in Precambrian continental crust. *International Society for Microbial Ecology,* Volume 10, pp. 730-741.

Malehmir, A., et al., 2014. A review of reflection seismic investigations in three major metallogenic regions: The Kevitsa Ni–Cu–PGE district (Finland), Witwatersrand goldfields (South Africa), and the Bathurst Mining Camp (Canada). *Ore Geology Reviews,* Volume 56, pp. 423-441.

Manzi, M. et al., 2015. Integrated interpretation of 3D seismic data to enhance the detection of the gold-bearing reef: Mponeng Gold mine, Witwatersrand Basin (South Africa). *Geophysical Prospecting,* Volume 63, pp. 881-902.

Manzi, M. S. D., Durrheim, R. J., Hein, K. A. A. & King, N., 2012. 3D edge detection seismic attributes used to map potential conduits for water and methane in deep gold mines in the Witwatersrand Basin, South Africa. *Geophysics,* Volume 77, pp. 133-147.

Manzi, M. S. D., Hein, K. A. A., Durrheim, R. J. & King, N., 2014. The Ventersdorp Contact Reef model in the Kloof Gold Mine as derived from 3D seismics, geological mapping and exploration borehole datasets. *International Journal of Rock Mechanics and Mining Sciences,* Volume 66, pp. 97-113.

Manzi, M. S. D., Hein, K. A. A., Durrheim, R. & King, N., 2013b. Seismic attribute analysis to enhance detection of thin gold-bearing reefs:South Deep gold mine,Witwatersrand basin, South Africa. *Journal of Applied Geophysics,* Volume 98, pp. 212-228.

Manzi, M. S. D., Hein, K. A. A., King, N. & Durrheim, R. J., 2013a. Neoarchaean tectonic history of the Witwatersrand Basin and Ventersdorp Supergroup: New constraints from high-resolution 3D seismic reflection data. *Tectonophysics,* Volume 590, pp. 94-105.

Marsh, J. S., 2006. The Dominion Group. In: M. R. Johnson, C. R. Anhaeusser & R. J. Thomas, eds. *The Geology of South Africa.* 1st ed. Johannesburg, Pretoria: Geological Society of South Africa, Council of Geosciences, p. 691.

Matthews, A. & Beckinsale, R. D., 1979. Oxygen isotope equilibration systematics between quartz and water. *American Mineralogist,* Volume 64, pp. 232-240.

McCarthy, T. S., 2006. The Witwatersrand Supergroup. In: M. R. Johnson, C. R. Anhaeusser & R. J. Thomas, eds. *The Geology of South Africa.* 1st ed. Johannesburg, Pretoria: Geological Society of South Africa.

McNutt, R. H. et al., 1990. The ^{87}Sr/^{86}Sr values of Canadian Shield brines and fracture minerals with applications to groundwater mixing, fracture history, and geochronology. *Geochimica Cosmochimica Acta,* Volume 54, pp. 205-215.

Meier, D. L., Heinrich, C. A. & Watts, M. A., 2009. Mafic dikes displacing Witwatersrand gold reefs: Evidence against metamorphic-hydrothermal ore formation. *Geological Society of America,* Volume 37, pp. 607-610.

Milev, A. M. & Spottiswoode, S. M., 2002. Effect of the rock properties of mining-induced seismicity around the Ventersdorp Contact Reef, Witwatersrand Basin, South Africa. *Pure and Applied Geophysics,* Volume 159, pp. 165-177.

Milkereit, B. & Eaton, D., 1998. Imaging and interpreting the shallow crystalline crust. *Tectonophysics,* Volume 286, pp. 5-18.

Moon, C. J., Whateley, M. K. G. & Evans, A. M., 2006. *Introduction to Mineral Exploration.* 2nd ed. Oxford: Blackwell Publishing.

Moser, D. P., et al., 2003. Temporal shifts in the geochemistry and microbial community structure of an ultradeep mine borehole following isolation. *Geomicrobiology Journal,* Volume 20, pp. 517-548.

Moser, D. P. et al., 2005. Desulfotomaculum and methanobacterium spp. dominate a 4- to 5-kilometer-deep fault. *Applied and Enviromental Microbiology,* Volume 71, pp. 8773-8783.

Moser, D. P. et al., 2003. Temporal shifts in the geochemistry and microbial community structure of an ultradeep mine borehole following isolation. *Geomicrobiology Journal,* Volume 20, pp. 517-548.

Mossman, D. J. et al., 2008. The indigenous origin of Witwatersrand "carbon". *Precambrian Research,* Volume 164, pp. 173-186.

Myers, R. E., McCarthy, T. S. & Stanistreet, I. G., 1990. A tectono-sedimentary reconstruction of the development and evolution of the Witwatersrand Basin, with particular emphasis on the Central Rand Group. *South African Journal of Geology,* Volume 93, pp. 180-201.

Neubeck, A., 2014. Olivine alteration and H2 production in carbonate-rich, low temperature aqueous environments. *Planetary and Space Science*, Volume 96, pp. 51-61

Neumann, E.-R., Svensen, H., Galerne, C. Y. & Planke, S., 2011. Multistage evolution of dolerites in the Karoo Large igneous Province, Central South Africa. *Journal of Petrology,* Volume 52, pp. 1-26.

Ngcobo, T. A., 2006. The risks associated with mines in dolomitic compartments. *The Journal of The South African Institute of Mining and Metallurgy,* Volume 106, pp. 251-264.

Ngeri, A. P., Tamunobereton-ari, I. & Amakiri, A. R. C., 2015. Ant-tracker attributes: An effective approach to enhancing fault identification and interpretation. *Journal of VLSI and Signal Processing (IOSR-JVSP),*Volume 5, pp. 67-73.

Omar, G. I., Onstott, T. C. & Hoek, J., 2003. The origin of deep subsurface microbial communities in the Witwatersrand Basin, South Africa as deduced from apatite fission track analyses. *Geofluids,* Volume 3, pp. 69-80.

Onstott, T. C. et al., 2006. The origin and age of biogeochemical trends in deep fracture water of the Witwatersrand Basin, South Africa. *Geomicrobiology Journal,* Volume 23, pp. 369-414.

Petrel, 2015. *Structural smoothing,* Houston, Texas: Schlumberger.

Phillips, N. G. & Law, J. D. M., 1994. Metamorphism of the Witwatersrand gold fields: A review. *Ore Geology Reviews,* Volume 9, pp. 1-31.

Pretorius, C. C., Jamison, A. & Irons, C., 1989. *Seismic exploration in the Witwatersrand Basin, Republic of South Africa.* Ontario, Ontario Geological Survey, pp. 241-253.

Pretorius, C. C., Muller, M. R., Larroque, M. & Wilkins, C., 2003. A review of 16 years of hardrock seismics on the Kaapvaal Craton. In: D. W. Eaton, B. Milkereit & M. H. Salisbury, eds. *Hardrock Sesimic Exploration.* Geophysical Developments No.10. Tulsa: Society of Exploration Geophysicists, pp. 247-268.

Randen, T., Pederson, S. & Sonneland, L., 2001. *Automatic extraction of fault surfaces from three-dimensional seismic data.* Norway, Society of Exploration Geophysics, pp. 551-554.

Reches, Z., DASFAM & NELSAM teams, 2006. Building a natural earthquake laboratory at focal depth (DAFSAM-NELSAM Project, South Africa). *Scientific Drilling,* Volume 3, pp. 30-33.

Rice, D. D. & Claypool, G. E., 1981. Generation, accumulation and resource potential of biogenic gas. *American Association for Petroleum Geology Bulletin,* Volume 65, pp. 5-25.

Riemer, K. L. & Durrheim, R. J., 2011. Mining seismicity in the Witwatersrand Basin: monitoring mechanisms and mitigation strategies in perspective. *Journal of Rock Mechanics and Geotechnical Engineering,* Volume 3, pp. 250-259.

Rijks, E. J. H. & Jauffred, J., 1991. Attribute extraction: An important application in any detailed 3-D interpretation study. *The Leading Edge,* Volume 10, pp. 11-19.

Robb, L. J., 2005. *An introduction to ore-forming processes.* 1st ed. London: Blackwell Publishing.

Robb, L. J., Brandl, G., Anhaeusser, C. R. & Poujol, M., 2006. Archean granitoid intrusions. In: M. R. Johnson, C. R. Anhaeusser & R. J. Thomas, eds. *The Geology of South Africa.* 1st ed. Johannesburg, Pretoria: Geological Society of South Africa, Council for Geosciences, pp. 57-94.

Robb, L. J., Landias, P., Drennan, G. R. & Dubessy, J., 1997. Petrographic, chemical and spectroscopic studies of carbonaceous matter in the Wiwatersrand Basin, South Africa. *Economic Geology Research Unit Information Circular*, August, pp. 1-30.

Robb, L. J. & Meyer, F. M., 1995. The Witwatersrand Basin, South Africa: Geological framework and mineralization processes. *Ore Geology Reviews,* Volume 10, pp. 67-94.

Roberts, M. K. & Schweitzer, J. K., 1999. Geotechnical areas associated with the Ventersdorp Contact Reef, Witwatersrand Basin, South Africa. *The Journal of the South African Institute of Mining and Metallurgy,* pp. 157-166.

Roberts, P. J., Gize, A. P., Duane, M. J. & Verhagen, B. T., 1993. Precambrian hydrocarbon residues associated with Mississippi Valley-type mineralization in the Transvaal Sequence, South Africa. *South African Journal of Geology,* Volume 96, pp. 57-60.

Rojey, A., 1997. *Natural gas : production, processing, transport.* 1st ed. Paris: Editions Technip.

Salisbury , M. H. et al., 1997. Physical properties and seismic imaging of massive sulphides. *Proceedings of Exploration 97: Fourth Decennial International Conference on Mineral Exploration,* pp. 383-390.

Scheepers, L. J., 2004. *Stability of access ways in ultra high stress – The next step.* Potchefstroom, South African National Institute of Rock Engineering, pp. 23-29.

Schmitz, M. D., Bowring, S. A., de Wit, M. J. & Gartz, V., 2004. Subduction and terrane collision stabilize the western Kaapvaal craton tectosphere 2.9 billion years ago. *Earth and Planetary Science Letters,* Volume 222, pp. 363-376.

Schoell, M., 1984. Recent advances in petroleum isotope geochemistry. *Organic Geochemistry,* Volume 6, pp. 645-663.

Schoell, M., 1988. Multiple orgins of methane in the Earth. *Chemical Geology,* Volume 71, pp. 1-10.

Schrader, A. & Winde, F., 2015. Unearthing a hidden treasure: 60 years of karst research in the Far West Rand, South Africa. *South African Journal of Science,* Volume 111, pp. 1-7.

Schweitzer, J. & Kroner, A., 1985. Geochemistry and petrogenesis of early Proterozoic intracratonic volcanic rocks of the Ventersdorp Supergroup, South Africa. *Chemical Geology,* Volume 51, pp. 265-288.

Sherwood Lollar, B. et al., 1993. Abiogenic methanogenesis in crystalline rocks. *Geochimica et Cosmochimica Acta,* Volume 57, pp. 5087-5097.

Sherwood Lollar, B. et al., 2006. Unravelling abiogenic and biogenic sources of methane in the Earth's deep subsurface. *Chemical Geology,* Volume 226, pp. 328-339.

Sherwood Lollar, B. et al., 2008. Isotopic signatures of CH_4 and higher hydrocarbon gases from Precambrian shield sites: A model for abiogenic polymerization of hydrocarbons. *Geochimica et Cosmochimica Acta,* Volume 72, pp. 4778-4795.

Sherwood Lollar, B., O'Nions, R. K. & Ballentine , C. J., 1994. Helium and neon isotope systematic in carbon dioxide-rich and hydrocarbon-rich gas reservoirs. *Geochimica et Cosmochimica Acta,* Volume 58, pp. 5279-5290.

Sherwood Lollar, B. et al., 2007. Hydrogeologic controls on episodic H_2 release from Precambrian fractured rocks—energy for deep subsurface life on Earth and Mars. *Astrobiology,* Volume 7, pp. 971-986.

Sibanye Gold, 2012a. *Driefontein Gold Mine,* Johannesburg

Sibanye Gold, 2012b. *Kloof Gold Mine,* Johannesburg

Sibson, R. H., 1995. Selective fault reactivation during basin inversion: potential for fluid redistribution through fault-valve action. *Geological Society, London, Special Publications,* Volume 88, pp. 3-19.

Silver, B. J. et al., 2012. The origin of NO3 and N2 in deep subsurface fracture water of South Africa. *Chemical Geology,* Volume 294-295, pp. 51-62.

Simkus, D. N. et al., 2016. Variations in microbial carbon sources and cycling in the deep continental subsurface. *Geochimica et Cosmochimica Acta,* Volume 173, pp. 264-283.

Simm, R. & Bacon, M., 2014. *Seismic Amplitude: An interpreter's handbook.* Cambridge, United Kingdom: Cambridge University Press.

Spanenberg, J. E. & Frimmel, H. E., 2001. Basin-internal derivation of hydrocarbons in the Witwatersrand Basin, South Africa: evidence from bulk and molecular 13C data. *Chemical Geology,* Volume 173, pp. 339-355.

Stanistreet, I. G. & McCarthy, T. S., 1991. Changing tectono-sedimentary scenarios relevant to the development of the Late Archaean Witwatersrand Basin. *Journal of African Earth Sciences,* Volume 13, pp. 65-81.

Stevenson , F., Higgs, R. M. A. & Durrheim, R. J., 2003. Seismic imaging of precious and base-metal deposits in Southern Africa. In: D. W. Eaton, B. Milkereit & M. H. Salisbury , eds. *Hardrock Seismic Exploration.* Geophysical Developments No. 10. Tulsa: Society of Exploration Geophysicists, pp. 141-156.

Stopler, D. A. et al., 2014. Formation temperatures of thermogenic and biogenic methane. *Science,* Volume 344, pp. 1500-1503.

Stuart, G. W., Jolley, S. J., Polome, L. G. B. T. & Tucker, R. F., 2000. Application of 3-D seismic attributes analysis to mine planning: Target gold deposit, South Africa. *The Leading Edge,* Volume 19, pp. 736-742.

Subrahmanyan, D. & Rao, P., 2008. *Seismic attributes: a review.* Hyderabad, SPG, pp. 398-404.

Sylvester, A. G., 1988. Strike-slip faults. *The Geological Society of America Bulletin,* Volume 100, pp. 1666-1703.

Takai, K. et al., 2001. Archaeal Diversity in Waters from Deep South African Gold Mines. *Applied and Environmental Microbiology,* Volume 67, pp. 5750-5760.

Taner, M. T., Koehler, F. & Sheriff, R. E., 1979. Complex seismic trace analysis. *Geophysics,* Volume 44, pp. 1041-1063.

Taner, T., 2001. Seismic attributes. *CSEG Recorder,* pp. 48-56.

Trickett, J.-C., Duweke, W. A. & Kock, S., 2005. Three-dimensional reflection seismics: its worth in weight in platinum. *The Journal of the South African Institute of Mining and Metallurgy,* May/June, Volume 105, pp. 357-363.

van der Westhuizen, W. A., de Bruiyn, H. & Meintjies, P. G., 2006. The Ventersdorp Supergroup. In: M. R. Johnson, C. R. Anhaeusser & R. J. Thomas, eds. *The Geology of South Africa.* 1st ed. Johannesburg, Pretoria: Geological Society of South Africa, Council for Geosciences, pp. 187-208.

van der Westhuizen, W. A., de Bruiyn, H. & Meintjies, P. G., 1991. The Ventersdorp Supergroup: an overview. *Journal of African Earth Sciences,* Volume 13, pp. 83-105.

Veeken, P. H. C., 2007. Seismic stratigraphy, basin analysis, and reservoir characterisation. In: K. Helbig & S. Treitel, eds. *Handbook of Geophysical Exploration: Seismic Exploration.* 1st ed. The Netherlands: Elsevier, pp. 7-109.

Verweij, J. M., 1993. *Hydrocarbon migration systems analysis.* Amsterdam: Elsevier Science Publishers.

Verwoed, W. J., 2006. The Pilanesberg Alkaline Complex. In: M. R. Johnson, C. R. Anhaeusser & R. J. Thomas, eds. *The Geology of South Africa.* 1st ed. Johannesburg, Pretoria: Geological Society of South Africa, Council for Geosciences, pp. 381-393.

Viehmann, S. et al., 2015. The reliability of ~2.9 Ga old Witwatersrand banded iron formations (South Africa) as archives for Mesoarchean seawater: Evidence from REE and Nd isotope systematics. *Journal of African Earth Sciences,* Volume 111, pp. 322-334.

Vogt, D. & van Schoor, M., 2010. The rise of Geophysics for in-mine imaging in South Africa's gold and platinum mines. In: J. F. Brune, ed. *Extracting the Science: A Century of Mining Research.* Littleton, Colorado: Society of Mining, Metallurgy, and Exploration, p. 544.

Wang, Z. et al., 2014. Automatic fault tracking across seismic volumes via tracking vectors. *IEEE- ICIP,* pp. 5851-5855.

Ward, J. A. et al., 2004. Microbial hydrocarbon gases in the Witwatersrand Basin, South Africa: Implications for the deep biosphere. *Geochimica et Cosmochimica Acta,* Volume 68, pp. 3239-3250.

Weatherby, B. B., 1940. The history and development of seismic prospecting. *Geophysics,* Volume 5, pp. 215-230.

West, A. G., February, E. C. & Bowen, G. J., 2014. Spatial analysis of hydrogen and oxygen stable isotopes (“isoscapes”) in ground water and tap water across South Africa. *Journal of Geochemical Exploration,* Volume 145, pp. 213-222.

Whiticar, M. J., Faber, E. & Schoell, M., 1986. Biogenic methane formation in marine and freshwater environments: CO2 reduction vs. acetate fermentation—Isotope evidence. *Geochimica et Cosmochimica Acta,* Volume 693–709, p. 50.

Whiticar, M. J., 1999. Carbon and hydrogen isotope systematics of baterial formation and oxidation of methane. *Chemical Geology,* Volume 161, pp. 291-314.

Wilhelms, A. et al., 2001. Biodegradation of oil in uplifted basins prevented by deep-burial sterilization. *Nature,* Volume 411, pp. 1034-1037.

Williams, G. D., Powell , C. M. & Cooper, A., 1989. Geometry and kinematics of inversion tectonics. *Geological Society, London, Special Publications,* Volume 44, pp. 3-15.

Wronkiwicz, D.J., Condie, K.C., 1987. Geochemistry of Archean shales from the Witwatersrand Supergroup, South Africa: Source-area weathering and provenance. *Geochimica et Cosmochimica Acta*, Volume 51, pp. 2401-2416.

Yaws, C. L. & Braker, W., 2001. *Matheson Gas Data Book.* 7th ed. McGraw Hill Professional.

Yilmaz, O., 1987. *Seismic data processing.* Tulsa: Investigations in Geophysics, Volume 2. The Society of Exploration Geophysicists.

11. APPENDICES

Appendix A

Table 1: Compositional gas analyses using RGA/FID mole (%) of fracture water in boreholes in the Driefontein (DR), Mponeng (MP), and TauTona (TT) gold mines.

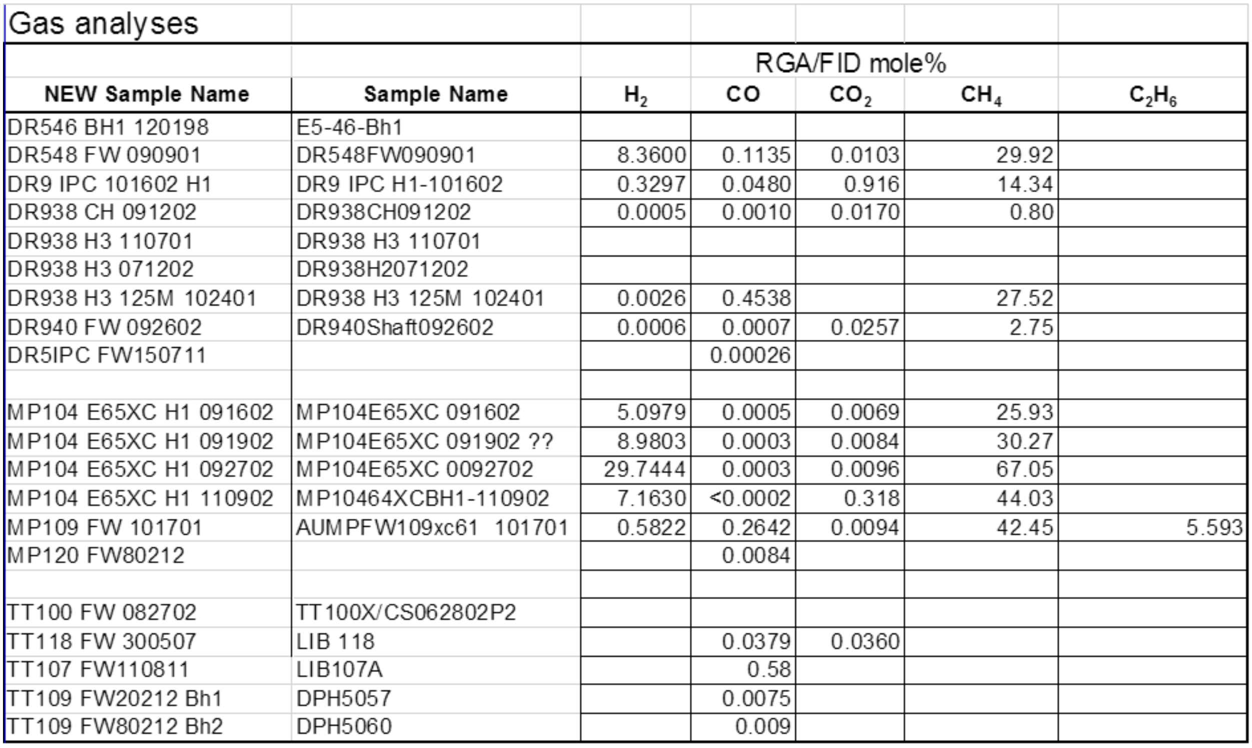

Gas analyses

			RGA/FID mole%			
NEW Sample Name	**Sample Name**	**H_2**	**CO**	**CO_2**	**CH_4**	**C_2H_6**
DR546 BH1 120198	E5-46-Bh1					
DR548 FW 090901	DR548FW090901	8.3600	0.1135	0.0103	29.92	
DR9 IPC 101602 H1	DR9 IPC H1-101602	0.3297	0.0480	0.916	14.34	
DR938 CH 091202	DR938CH091202	0.0005	0.0010	0.0170	0.80	
DR938 H3 110701	DR938 H3 110701					
DR938 H3 071202	DR938H2071202					
DR938 H3 125M 102401	DR938 H3 125M 102401	0.0026	0.4538		27.52	
DR940 FW 092602	DR940Shaft092602	0.0006	0.0007	0.0257	2.75	
DR5IPC FW150711			0.00026			
MP104 E65XC H1 091602	MP104E65XC 091602	5.0979	0.0005	0.0069	25.93	
MP104 E65XC H1 091902	MP104E65XC 091902 ??	8.9803	0.0003	0.0084	30.27	
MP104 E65XC H1 092702	MP104E65XC 0092702	29.7444	0.0003	0.0096	67.05	
MP104 E65XC H1 110902	MP10464XCBH1-110902	7.1630	<0.0002	0.318	44.03	
MP109 FW 101701	AUMPFW109xc61 101701	0.5822	0.2642	0.0094	42.45	5.593
MP120 FW80212			0.0084			
TT100 FW 082702	TT100X/CS062802P2					
TT118 FW 300507	LIB 118		0.0379	0.0360		
TT107 FW110811	LIB107A		0.58			
TT109 FW20212 Bh1	DPH5057		0.0075			
TT109 FW80212 Bh2	DPH5060		0.009			

Table 2: Compositional gas analyses of fracture water in boreholes in the Driefontein (DR), Mponeng (MP), and TauTona (TT) gold mines

Gas analyses

			TCD (mole%)					FID (mole%)					
NEW Sample Name	**Sample Name**	**Ar**	**H_2**	**He**	**O_2**	**N_2**	**CH_4**	**C_2H_6**	**C_3H_8**	**iso-C_4**	**n-C_4**	**CO_2**	**Total**
DR546 BH1 120198	E5-46-Bh1		0.003	9.98	0.03	56.50	27.70	0.27	0.024	0.002	0.005		84.23
DR548 FW 090901	DR548FW090901		10.34	3.05	6.18	23.61	56.31	2.67	0.220	0.028	0.020		102.55
DR9 IPC 101602 H1	DR9 IPC H1-101602			2.75	3.77	101.78	11.62						121.21
DR938 CH 091202	DR938CH091202			0.42	16.77	73.59	4.70	0.12	0.020				95.62
DR938 H3 110701	DR938 H3 110701		0.74	5.98	0.55	13.98	76.03	3.15	0.319	0.018	0.038		100.81
DR938 H3 071202	DR938H2071202	.	0.32	4.64	4.95	28.60	61.40	2.45	0.260	0.010	0.030		102.62
DR938 H3 125M 102401	DR938 H3 125M 102401												
DR940 FW 092602	DR940Shaft092602			1.17	19.31	73.05	10.18	0.30	0.040				104.05
DR5IPC FW150711			0.00043	0.15	19.11	75.25	1.93	0.003				0.33	
MP104 E65XC H1 091602	MP104E65XC 091602		9.85	9.11	6.12	29.31	41.96	3.30	0.480	0.030	0.080		100.24
MP104 E65XC H1 091902	MP104E65XC 091902 ??		12.08	11.94	2.40	16.69	53.00	4.21	0.620	0.040	0.100		101.08
MP104 E65XC H1 092702	MP104E65XC 0092702		11.54	12.32	3.65	21.14	49.59	3.99	0.600	0.040	0.100		102.97
MP104 E65XC H1 110902	MP10464XCBH1-110902		11.4	12.34	1.86	16.95	49.92	4.03	0.580	0.040	0.090		97.53
MP109 FW 101701	AUMPFW109xc61 101701		3.3	9.06	4.77	28.14	53.83	2.47	0.360	0.030	0.050		102.01
MP120 FW80212			23.17	7.38	0.96	6.11	53.2	3.46	0.49	0.05	0.07	1.69	
TT100 FW 082702	TT100X/CS062802P2			0.25	18.70	76.70	2.50	0.04					98.19
TT118 FW 300507	LIB 118		2.4	8.8	3.3	29.2	53.4	3.25	0.38	0.03	0.06		100.82
TT107 FW110811	LIB107A		0.11	3.98	0.96	38.89	16	0.87	0.13	0.01	0.02	0.05	
TT109 FW20212 Bh1	DPH5057		0.0035	4.17	1.33	31.85	58.58	0.09				0.05	
TT109 FW80212 Bh2	DPH5060		0.011	4.46	0.04	28.28	61.9	2.58	0.37	0.03	0.06	0.05	

Table 3: Flow rates, temperature, salinity, and O_2 concentrations of fracture water in boreholes in the Driefontein (DR), Mponeng (MP), and TauTona (TT) gold mines

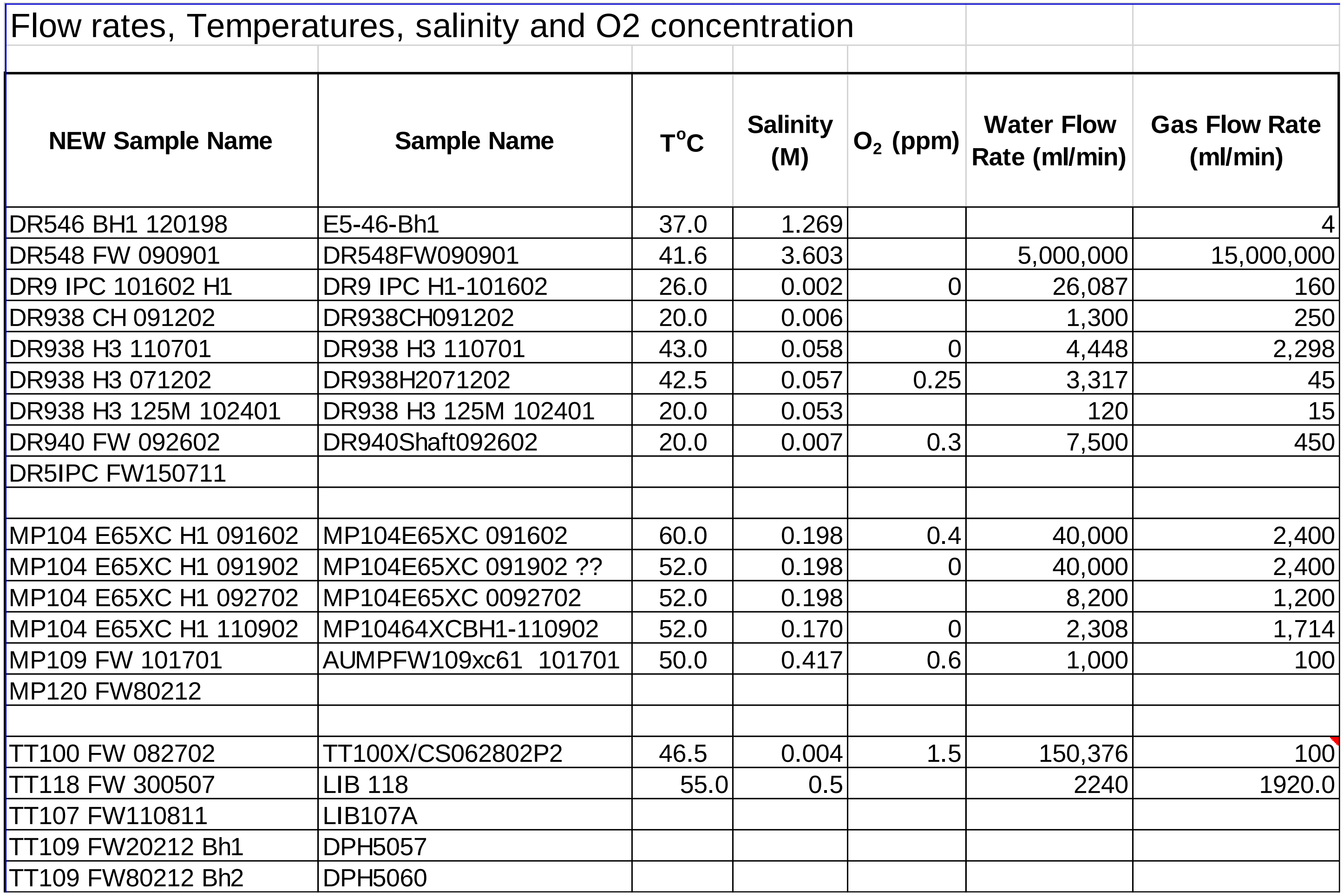

Flow rates, Temperatures, salinity and O2 concentration

NEW Sample Name	Sample Name	T°C	Salinity (M)	O_2 (ppm)	Water Flow Rate (ml/min)	Gas Flow Rate (ml/min)
DR546 BH1 120198	E5-46-Bh1	37.0	1.269			4
DR548 FW 090901	DR548FW090901	41.6	3.603		5,000,000	15,000,000
DR9 IPC 101602 H1	DR9 IPC H1-101602	26.0	0.002	0	26,087	160
DR938 CH 091202	DR938CH091202	20.0	0.006		1,300	250
DR938 H3 110701	DR938 H3 110701	43.0	0.058	0	4,448	2,298
DR938 H3 071202	DR938H2071202	42.5	0.057	0.25	3,317	45
DR938 H3 125M 102401	DR938 H3 125M 102401	20.0	0.053		120	15
DR940 FW 092602	DR940Shaft092602	20.0	0.007	0.3	7,500	450
DR5IPC FW150711						
MP104 E65XC H1 091602	MP104E65XC 091602	60.0	0.198	0.4	40,000	2,400
MP104 E65XC H1 091902	MP104E65XC 091902 ??	52.0	0.198	0	40,000	2,400
MP104 E65XC H1 092702	MP104E65XC 0092702	52.0	0.198		8,200	1,200
MP104 E65XC H1 110902	MP10464XCBH1-110902	52.0	0.170	0	2,308	1,714
MP109 FW 101701	AUMPFW109xc61 101701	50.0	0.417	0.6	1,000	100
MP120 FW80212						
TT100 FW 082702	TT100X/CS062802P2	46.5	0.004	1.5	150,376	100
TT118 FW 300507	LIB 118	55.0	0.5		2240	1920.0
TT107 FW110811	LIB107A					
TT109 FW20212 Bh1	DPH5057					
TT109 FW80212 Bh2	DPH5060					

Appendix B

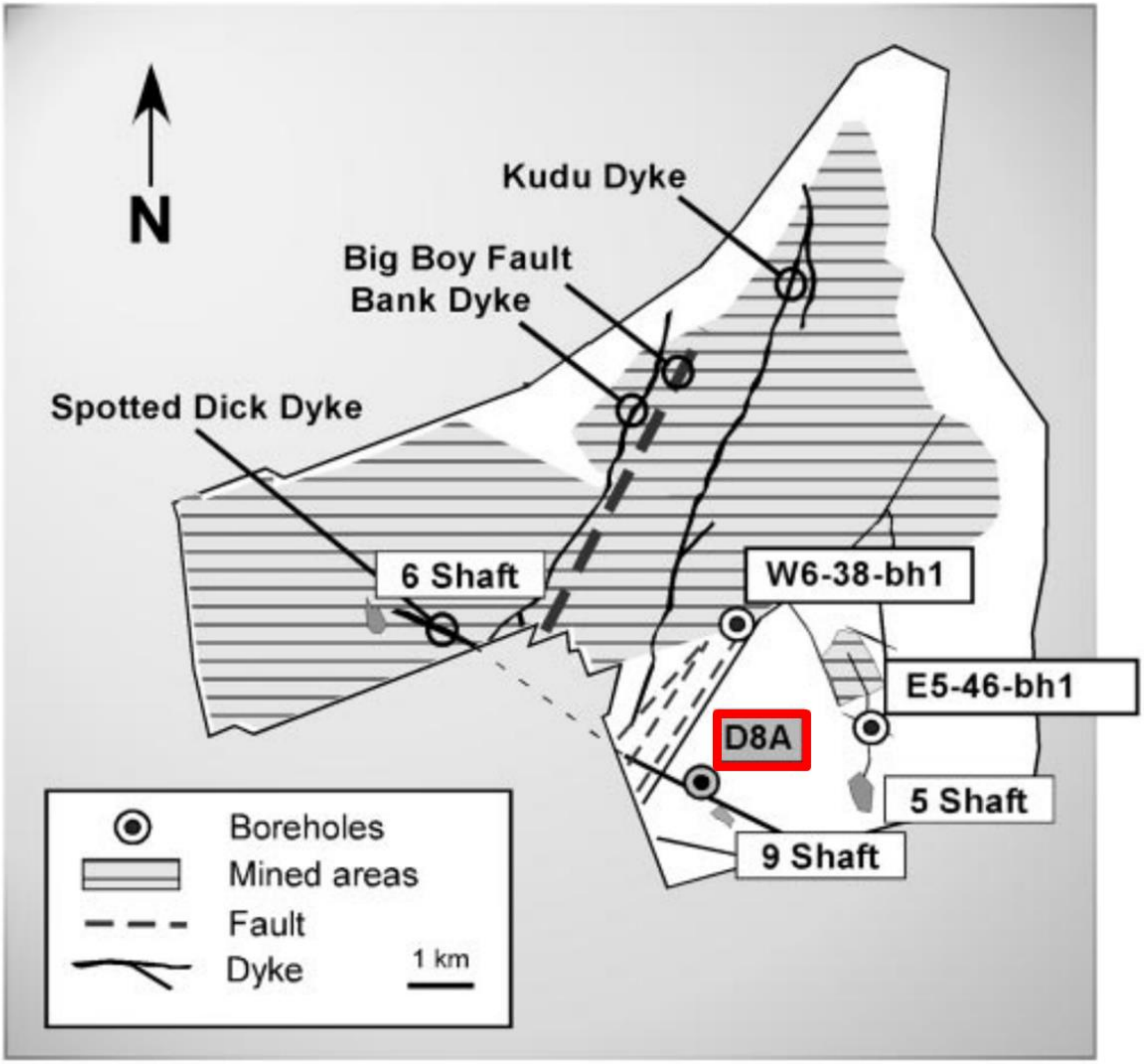

Figure 1: Driefontein gold mine map showing the D8A borehole (highlighted in red). The borehole clearly intersects the Spotted Dick Dyke (after Moser et al., 2003).

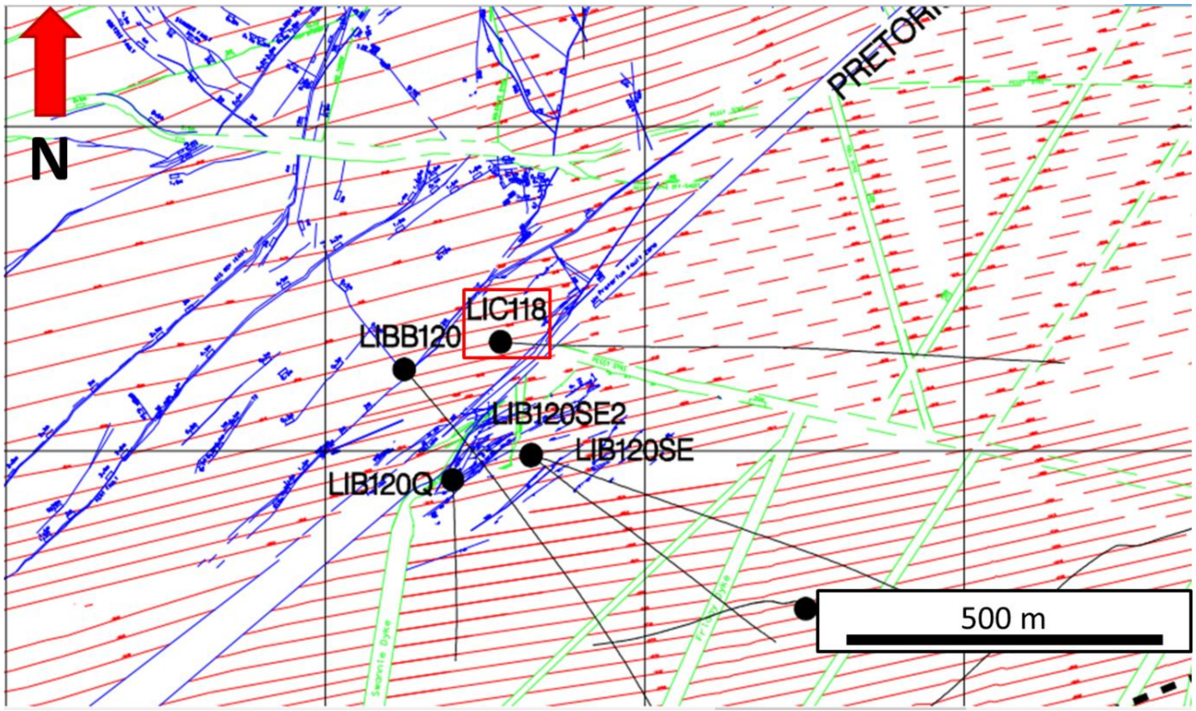

Figure 2: Location of borehole LIC 118 (TT118), outlined in red, at the TauTona gold mine (after Litthauer, 2009). The blue lines denote faults, the green lines dykes, and the red lines, contour lines at mining levels.

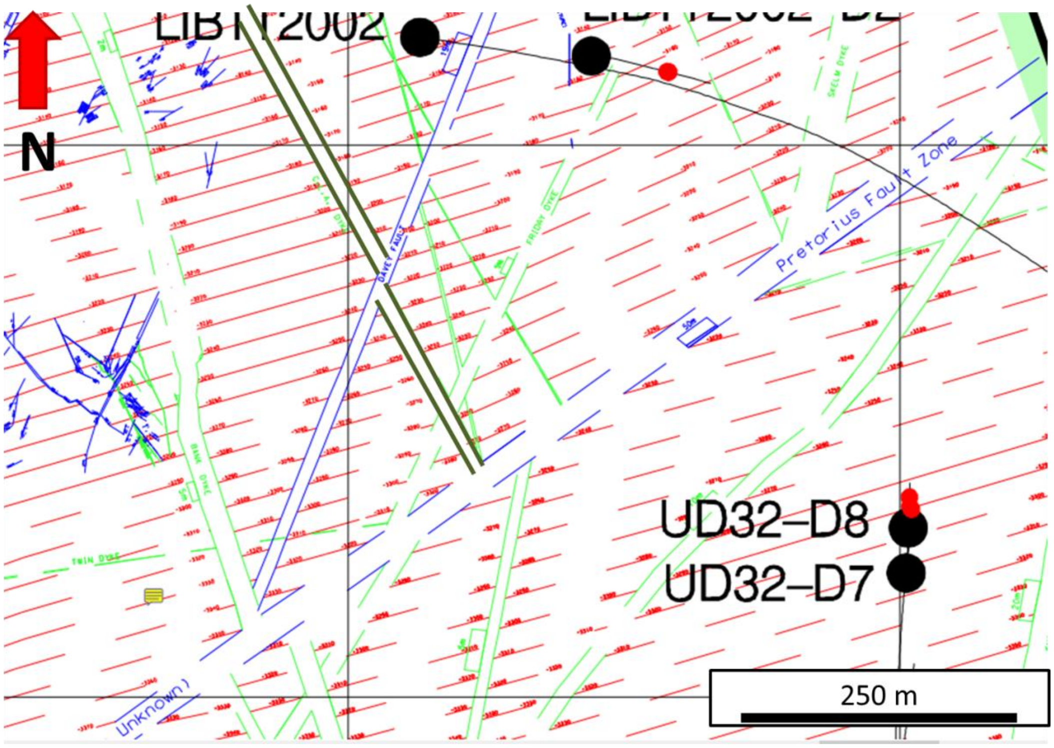

Figure 3: Location of the CLA Dyke (outlined in dark green), outlined in red, at the TauTona gold mine. The dyke is intersected by the Davey and Pretorius faults (after Litthauer, 2009). The blue lines denote faults, the green lines dykes, and the red lines, contour lines at mining levels.